PVDF piezoelectric polymers : characterization and application to thermal energy harvesting

Boris Gusarov

UNIVERSITÉ GRENOBLE ALPES

THÈSE

Pour obtenir le grade de

DOCTEUR DE L'UNIVERSITÉ GRENOBLE ALPES

Spécialité : **Génie Électrique**

Arrêté ministériel : 7 août 2006

Présentée par

Boris GUSAROV

Thèse dirigée par **Orphée CUGAT**
et codirigée par **Bernard VIALA et Leticia GIMENO**

préparée au sein du **Laboratoire de Génie Électrique de Grenoble (G2Elab)**
dans **l'École Doctorale «Électronique, Électrotechnique, Automatique et Traitement du Signal»**

PVDF polymères piézoélectriques: caractérisation et application pour la récupération d'énergie thermique

Thèse soutenue publiquement le **12 Novembre 2015**,
devant le jury composé de :

Pr Etienne PATOOR
Professeur Georgia Tech Lorraine, Président
Pr François COSTA
Professeur ENS Cachan, Rapporteur
Dr Fabrice DOMINGUES DOS SANTOS
CEO Piezotech (Arkema group), Membre
Dr Bernard VIALA
Chercheur CEA-Leti, Membre
Dr Leticia GIMENO
Maitre de conférences, UJF, Membre
Dr Orphée CUGAT
Directeur de recherche CNRS, Membre

To my father
– the most curious man I've known.

Abstract

This work is focused on the characterization of piezoelectric polymers PVDF and its composites with shape memory alloys, for thermal energy harvesting applications. First, we discuss current advancements on energy harvesting technologies as well as their economical interests. Typical values of energy that can be generated are given together with energies typically needed for applications. Particular attention is given to the functioning principles of pyroelectric and piezoelectric materials. PVDF and shape memory alloy NiTiCu are also introduced.

Custom characterization techniques are introduced to characterize PVDF piezoelectric properties relevant to generator applications and to evaluate its suitability for thermal energy harvesting. Since PVDF is a very flexible material, four-point bending, tube bending and a tensile machine experiments are used to study its piezoelectric response in quasi-static mode, as well as changes in piezoelectric properties with increased strain. Self-discharge measurements under various applied electric fields, temperatures and strains are performed to study the stability of material.

A concept of composite energy harvesting, utilizing two materials of different families, is introduced. Here, we propose the coupling of piezo-/pyroelectric material and shape memory alloy. The pure pyroelectric voltage is combined with generated piezoelectric voltage, induced by shape memory alloy transformation, to increase the total energy generated by the system during heating. The proof of concept is shown first for ceramic PZT-based semi-flexible material and then for fully flexible PVDF.

Finally, a power management circuit was designed and integrated with the PVDF energy harvester. High generated voltage peaks at heating are lowered by a two-step buck converter to a useful stable output voltage. Output energy are used to power a wireless emission card. Thus, a complete power generation chain from temperature variations to data emission is presented.

The results of this work concern a wide range of applications, especially modern autonomous wireless sensors and Internet of Things objects, with low profile, high mechanical flexibility and low maintenance costs.

Résumé

Les travaux de cette thèse portent sur la caractérisation de polymères piézoélectriques de PVDF et celle de ses composites avec un alliage à mémoire de forme, pour des applications de récupération d'énergie thermique. Tout d'abord, une discussion est donnée sur les avancées actuelles des technologies de récupération d'énergie ainsi que leur intérêt économique. Des valeurs typiques de l'énergie pouvant être générée sont estimées, ainsi que des énergies nécessaires pour certaines applications. Une attention particulière est accordée aux principes de fonctionnement des matériaux pyroélectriques et piézoélectriques. Le PVDF et l'alliage à mémoire de forme NiTiCu sont également introduits.

Des techniques de caractérisation adaptées sont introduites pour caractériser par voie directe le PVDF en tant que générateur de charges électriques, et son aptitude à la récolte de l'énergie thermique. Puisque le PVDF est un matériau très souple, la flexion à quatre points, la flexion sur tube, et la machine de traction sont utilisées pour étudier sa réponse piézoélectrique directe en mode quasi-statique, ainsi que les changements de propriétés piézoélectriques sous contrainte. Des mesures d'auto-décharge sous différents champs électriques appliqués, températures et contraintes sont effectuées pour étudier la stabilité du matériau.

Un concept de récupération d'énergie utilisant des composites de matériaux fonctionnels de familles différentes est introduit. Ici, le couplage entre un matériau piézo-/pyroélectrique et un alliage à mémoire de forme est proposé. Le voltage pyroélectrique simple est combiné avec un voltage piézoélectrique induit par la transformation de phase de l'alliage à mémoire de forme, pour augmenter l'énergie totale générée par le système en chauffant. Une preuve de concept est présentée d'abord pour un matériau semi-flexible basé sur une céramique PZT, et ensuite pour le PVDF qui est entièrement flexible.

Enfin, un circuit de gestion d'énergie a été conçu et intégré au récupérateur d'énergie en PVDF. Les hauts pics de tension générés lors du chauffage ou refroidissement sont abaissés par un convertisseur de type buck à deux étages jusqu'à une tension de sortie utile stable. L'énergie de sortie est utilisée pour alimenter une carte d'émission sans fil. Ainsi, une chaîne complète de génération d'énergie, exploitant des variations de température et allant jusqu'au l'émission de données représentatives de l'événement thermique survenu est présentée.

Les résultats de ces travaux concernent un large spectre d'applications potentielles, particulièrement les capteurs autonomes sans fil, et des objets de l'Internet of Things, avec une flexibilité mécanique élevée, une épaisseur réduite et un faible coût de maintenance.

Acknowledgments

This PhD thesis would not be possible without help and collaboration of many people. I would like to express my sincere gratitude to everyone who participated in this work, directly or indirectly, and to everyone who supported me during these years.

I would like to say first merci beaucoup to my numerous supervisors. Thank you Jérôme DELAMARE for calling me on skype that day and proposing me to come. We have done first steps together, and even though you had to leave the project quite soon, these were very important first steps. Thank you also for showing us the aerial side of Isere and for the initiation in airplane flying!

Thank you Bernard VIALA for your confidence in me and for giving me a lot of autonomy to conduct this project. Your scientific support was essential and I really appreciated our work as a team, and many discussions and ideas that we have had together.

Thank you Leticia GIMENO for everyday support, your readiness to always help and an endless flow of ideas and optimizations! Your miams were always delicious and we all appreciated our gathering and culinary discoveries.

Finally, thank you very much Orphée CUGAT for always being there even when the times were hard. You always have an alternative point of view on science, which often helps to straighten the thoughts and solve the problems. Thank you also for helping us with many household things upon our arrival to Grenoble and for the musical revelations.

I am very grateful to the jury members Etienne PATOOR, Francois COSTA and Fabrice DOMINGUES DOS SANTOS for accepting to review this work and for coming to Grenoble. Thank you for the valuable comments on the manuscript and interesting questions during the defense.

Besides my direct supervisors, there are many people in CEA and G2Elab that helped me during this work. I would like to express my sincere gratitude to:

Loïc VINCENT for making me familiar with the CIME platform and teaching to use some important set-ups.

Alain SYLVESTRE for showing me first electrostatic voltmeter measurements. Also thank you for your valuable comments during the half-defense, together with Skandar BASROUR and Romain GWOZIECKI.

Vincent MANDRILLON for letting me use the traction machine and helping with automatization.

Nicolas GALOPIN for theoretical background and calculations of different PVDF structures.

Alain HAUTCOEUR and André EBERHARD for inviting me to your lab in Metz and teaching

me stent NiTi structures.

Sébastien BOISSEAU for making pyroelectric measurements with me and your big help with electric circuit conception and components optimization.

Charles-Elie GOUJON for the help with low power emission card, essential for our wireless demonstration.

My internship students Erika VANDELLE and Bastien LOUISON for your great work on SMA switch conception and testing, and on circuit simulation and assembly.

My many thanks go to my colleagues and friends with whom we shared our office and lab: Ben WILSCH, Thomas LAFONT, Thibault RICART, Sarah DELSHADI, Guillaume BLAIRE and many others.

A word should be said about my Russian fellow scientists and friends Gor LEBEDEV, who had confidence in me and invited me for a stage in CEA many years ago, and Dmitry ZAKHAROV who greatly helped me in many aspects of my life.

I would like to thank very much my mother for helping me with the defense organization and for cooking a delicious buffet for the Pot de These.

Finally, I wish to thank my wonderful wife Elena for being such a supportive person and for your everyday help in life and in science!

CONTENTS

List of Figures

List of abbreviations

The most used textual abbreviations in this manuscript. Sorted by the order of appearance in the text.

Abbreviations	Full form
PVDF	Polyvinylidene fluoride
SMA	Shape Memory Alloy
MFC	MicroFiber Composite
PZT	$Pb[Zr_xTi_{1-x}]O_3$
k^2	Piezoelectric coupling coefficient
g_{31}, g_{33}	Piezoelectric voltage coefficients
d_{31}, d_{33}	Piezoelectric charge coefficients
ρ_Q	Pyroelectric charge coefficient
ρ_V	Pyroelectric voltage coefficient
ΔT	Temperature difference
A_s	Temperature of start of austenitic transition
A_f	Temperature of finish of austenitic transition
T or σ	Mechanical stress
S or ε	Mechanical strain
YM	Young's modulus
V	Electric voltage
E	Energy
C	Capacitance
L	Inductance
η	Conversion efficiency
LED	Light emitting diode
PCB	Printed circuit board

Chapter 1

General introduction

The most profound technologies are those that disappear. They weave themselves into the fabric of everyday life until they are indistinguishable from it.

Mark D. Weiser

1.1 General context: why energy harvesting

This thesis presents an experimental work dedicated to the harvesting of thermal energy. This work addresses a very small aspect of a much larger issue: the modern industrial world faces an increasing energy problem; fossil fuels are finite and environmentally costly, and alternative energy sources can not yet fully replace them. World consumption of energy is gradually increasing every year, and the main energy sources being consumed are non-renewable coal, gas and oil[20]. On the other hand, sustainable large-scale technologies are being developed to capture efficiently renewable ambient sources in forms of solar, wind and tide energy. At the lower scales, there are also small amounts of wasted or neglected energy that could be useful if captured. Using even a small portion of this otherwise disregarded energy can have a significant economic and environmental impact[21]. This is where energy harvesting comes in.

The concept of energy harvesting generally relates to the process of using ambient energies, which are converted primarily into electrical energy, in order to power small and autonomous electronic devices. Energy harvesting captures small amounts of energy that would otherwise be lost. This energy can be then used either to improve the efficiency of existing technologies (e.g. computing costs could be significantly reduced if waste heat were harvested and used to help power the computer), or to enable new technologies, e.g. wireless sensor networks. Energy harvesting has the potential to replace batteries for small, low power electronic devices. This will allow for maintenance free (no need to change batteries), environmentally friendly (disposal of batteries is problematic as they contain harmful chemicals and metals) and remote applications[21].

We can imagine applications of environmental monitoring of large infrastructures or distant and hardly accessible places such as glaciers or mountains, applications requiring several hundreds of wireless nodes scattered over a wide area, or implanted medical devices, where access to replace batteries is inconvenient if not impossible. Indeed, in such applications, energy harvesting solutions have clear benefits[22].

Such developing technologies require expertise from all aspects of physics, including energy capture, energy storage, metrology, material science, power management and system engineering[21]. Moreover, the socio-economic impact of energy harvesting technologies is of high importance, with an estimated market potential of €3 billion in 2020 and ample opportunity for job creation[23].

Within this context, this thesis presents an experimental work dedicated to the harvesting of

thermal energy. Energy harvester, based on a composite system consisting of piezoelectric PVDF polymer in combination with thermal shape memory alloy NiTiCu, is studied. The ultimate goal is to make low profile flexible harvester, capable of generating energy from slow and small temperature variations without need of cold source management or radiator. It would act as an autonomous thermal threshold sensor, combining sensing and energy harvesting capabilities.

1.2 Feasibility of composite thermal energy harvesting

The principle of the composite of this work relies on the fact that PVDF has naturally both piezoelectric and pyroelectric properties. When the temperature rises, the pyroelectricity generates an electric voltage in PVDF. At the same time, the shape memory alloy (SMA) undertakes a phase transformation, which induces a 2–3% strain. This strain is transferred to the PVDF and generates additional piezoelectric voltage in it. Both pyroelectric and piezoelectric effects sum up and result in a double increase of the harvester output.

As we will see further, the efficiency of thermal-to-mechanical conversion of NiTiCu can be up to 8%. In a more general case the efficiency is around 4%. This mechanical energy is in turn converted into electricity by the piezoelectric behavior of PVDF, with an efficiency characterized by the coupling coefficient k, which can be as high as 15%. Thereby, when taking into account only piezoelectric generation, the total efficiency of an SMA + piezoelectric composite harvester can be estimated at about 0.6%, which is comparable to typical pyroelectric conversion efficiency ($\approx$1%). This means that a combination of two non-pyroelectric materials can have theoretically similar efficiency as a pyroelectric material by itself in thermal-to-electric energy conversion. The efficiency estimation is illustrated in figure 1.1, with an example of 100 Joule heating of NiTiCu.

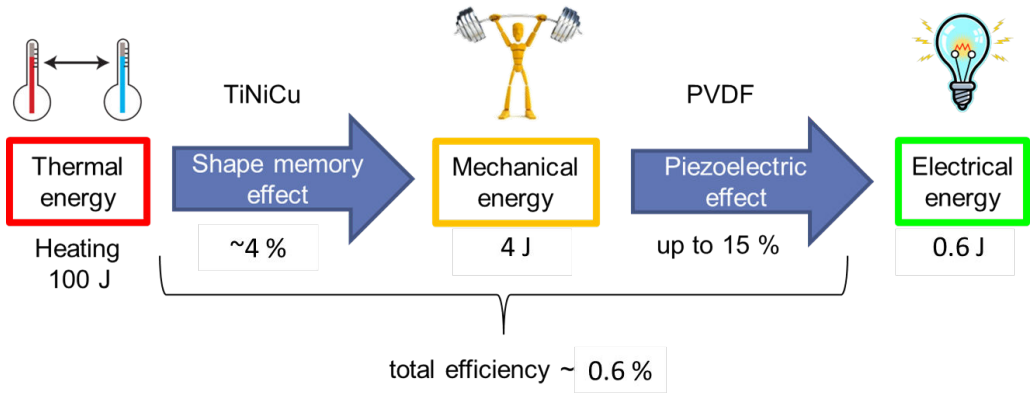

Figure 1.1: *Schematic estimation of thermal-to-electrical energy conversion using shape memory and piezoelectric effects.*

1.3 Organization of the manuscript

In the following paragraphs we will introduce to the reader the concepts of thermal energy harvesting, then we will briefly present the pyroelectic and piezoelectric theoretical models, and finally we will give an introduction to PVDF and NiTiCu materials before defining the main objectives of this work.

Since PVDF is subjected to heating and mechanical stress, it is important to assess how it behaves in such conditions, evaluate its pyroelectric behavior and study how its piezoelectric characteristics are affected. These aspects will be presented in chapter 2, where we will perform tensile and temperature measurements on commercial PVDF to measure its piezoelectric voltage coefficient and self-discharge dependence on temperature and strain.

Chapter 3 will be devoted to PVDF+SMA composites; fabrication methods, composite characterization and energy capabilities will be explored. We will also compare them with semi-flexible ceramic-based piezoelectric composites in terms of generated energy density.

Chapter 4 will deal with the circuitry involved in the power management of the energy harvested by our composites. Since the voltage generated by these harvesters can reach 400 V, a custom two-step buck converter was designed to lower the voltage to 1.5–2 V stable output, which was then used to power a wireless node transmitter.

1.4 Introduction to energy harvesting

Energy harvesting, in general terms, is the conversion of free environmental disregarded energy into a useful electrical energy is small scales, in contrast to large scale reliable renewable energies such as solar, hydroelectric or wind turbine production. The Institute of Physics defines energy harvesting as a process that captures small amounts of energy that would otherwise be lost[21]. The environmental energy can be present in many forms including light, vibration, temperature differentials, radio energy, magnetic energy and even biochemically produced energy[24]. The harvesting principle depends on the form of the available energy: it can be harvested by a piezoelectric element, a thermo-electric or pyroelectric generator, captured by an antenna etc. The principal difference of energy harvesting from conventional energy production is that it is free of charge, since it comes from energy which is otherwise wasted (as opposed to oil or coal production), and provides only a very small amount of power for low-energy electronics (as opposed to wind turbines or large solar panels). Energy harvesting usually targets disregarded energy sources, meaning sources that are not reliable and small. Main targets of energy harvesting applications include wireless ultra-low power devices, wearable electronics, wireless sensor networks, batteryless remote controls, car tire pressure sensors and alternatives to small batteries[21,25].

Table 1.1: *Typical maximal estimated data for various energy harvesting sources[22].*

	Conditions	Power density	Area or Volume	Energy per Day
Vibration	1 m/s^2	100 μW/cm^3	1 cm^3	8.64 J (assuming continuous vibration)
Solar	Outdoors	7500 μW/cm^2	1 cm^2	324 J (assuming light is available for 50% of time)
Solar	Indoors	100 μW/cm^2	1 cm^2	4.32 J (assuming light is available for 50% of time)
Thermal	ΔT=5°C	60 μW/cm^2	1 cm^2	2.59 J (assuming heat is available for 50% of time)

Any typical outdoor or indoor environment has a broad range of different energy sources. Among those already mentioned, solar, thermal and kinetic are three energies that are most typically used for harvesting energy from a typical outdoor environment[22]. It is difficult to generalize

these sources, since they are present in various conditions, they are not always available and their intensity can change in time. Therefore for each individual usage case, the most suitable source or combination of multiple sources must be considered, regarding the typical power levels that are available. Table 1.1 summarizes theoretical typical power levels for different energy sources. In terms of power density, solar energy in outdoor conditions provides far better results. However, if used indoors, it becomes comparable with other sources; in dirty environments where the cells can become obscured it is not suitable at all. Thus, the final choice of energy sources and methods of harvesting is largely determined by the applications. In the case of kinetic energy harvesting exploiting vibrations, the source vibration spectra will vary largely for different applications: for example, human movement is very different from machinery vibrations, therefore totally different approaches to the design of a generator are necessary. The same applies for thermal energy, which may be present as a spatial temperature gradient or as temporal temperature variations, and with a wide range of amplitudes.

Energy harvesting as it is known today appeared in the late 1990's. Among the first were researchers from MIT Media Laboratory who presented papers on power harvesting in shoes using PVDF and PZT insoles and a miniature magnetic rotor[26], and discussed the possibility of powering a computer using just human body power, such as heat, breath, or motions[27].

In 2000, Rabaey et al.[28] proposed an ultra-low power wireless network with an overall energy consumption decreased by a factor of 50. They also had a vision of self-contained and self-powered network nodes, by powering them with harvesting energy from vibrations.

Today, with growing global interest in the Internet of Things[29], and development of new wireless data transmission technologies and low-power devices, a number of academic and industrial groups are involved in the analysis and development of commercial energy harvesting technologies. Among them are big players such as Siemens with their spin-off company EnOcean GmbH supplying self-powered solutions for building automation[30], but also many smaller companies, such as Algra with pressure-driven piezoelectric generators[31], Pavegen with floor-tile generator from pedestrian footsteps[32], Micropelt with thermoelectric energy harvesting[2], Perpetuum Ltd with vibration harvesting[33], and others. In and around Grenoble area, partnership between INPG university and CEA have given birth to start-ups such Enerbee with motion based piezo-magnetic generators (fruit of collaborations of our team with CEA-Leti)[34], Hotblock with thermoelectric systems (CEA-Liten)[35], Arveni with mechanical energy harvesting[36]. The increased number of industries and academics working in the domain of energy harvesting clearly indicates the interest and the demand of such technologies for future everyday life. The interest becomes even more clear when we look at the financial side: the European Commission has reported that in 2009, the overall market for energy harvesters amounted to €463 million, with 67% being incorporated in consumer goods. In 2011, this number had grown to €530 million, with almost €11 million being spent on energy harvesters in wireless sensor applications. In 2011, most of the harvesters used in the market were solar cells, followed by electro dynamos, which together are among the most mature energy harvesting technologies. However, promising new technologies are starting to capture market share, enabling the powering of machines and equipment in areas where this was not possible before[23]. Market forecasts vary from $250 million in 2017 by Yole[37] to over $4 billion in 2021 by IDTechEx[38].

Since many different sources of energy are present and different energy harvesting strategies exist, it would take long to describe them all. Besides, many excellent reviews have been published recently, underlying state-of-the-art of energy harvesting technologies[24,39–42]. We will therefore

limit our discussion here to thermal energy harvesting alone, since this is the energy of interest in this work.

1.4.1 Typical power consumption of autonomous remote sensors

Before we proceed to technical details of thermal energy harvesting, let us estimate what energy levels are necessary to power a typical autonomous wireless sensor node. In general terms, its power consumption can be separated between the energy necessary for the sensor itself to perform physical measurements (e.g. temperature, pressure, pH, humidity, etc), and the energy necessary to send this information via a wireless protocol.

In a review by Dewan et al.[39] data for sensor consumption vary from 0.01 mW (temperature, pH, moisture measurements) to 85000 mW (ocean processes, underwater surveillance). For a conventional domestic sensor we can take value of 10 mW.

Modern wireless protocols have sub-watt power consumption, for example a Bluetooth transceiver consumes around 10 mW[43]. Recent Bluetooth Low Energy technology supports connection setup and data transfer as fast as 3 ms[44]. If we now calculate the energy needed for sensing and transmitting, we obtain:

$$E = P \cdot t = (10\ mW + 10\ mW) \cdot 3\ ms = 60\ \mu J$$

These numbers are approximate. It is difficult to give average energy values, since they are very different and depend on the system design. Moreover, many manufacturers voluntarily indicate little or no data on their products as it is very dependent on the applications, for example the number of data sent, the protocol used, board conception, etc. However, we can estimate that energy values in the order of magnitude of 100 μJ should be sufficient for a single event of sensing and wireless data transmission. From our own previous experience with ZigBee wireless protocol, energy of 100–150 μJ per emission is necessary.

1.4.2 Exploiting thermal energy

Thermal energy is present in many environments and in many forms, either as a spatial temperature gradient or as temporal temperature variations. Many attempts have been made in order to exploit this energy, which is otherwise usually wasted. Thermoelectric generators are typically used to exploit spatial temperature gradients as a continuous source. Pyroelectric materials are usually used for harvesting temporal temperature gradients. It is also possible to transform a temperature gradient into a temporal temperature variation, for example using a caloric fluid pumping between hot and cold sources[45], or using a mechanical system with a pyroelectric element oscillating between hot and cold sources[46–48]. Conversely, by maintaining a constant temperature at one end of the thermoelectric generator, it is possible to harvest temperature variations at the other end[49].

Market forecast for thermal energy harvesting goes to $100 million by 2016 and to over $950 million by 2024[50], and companies like EnOcean, Micropelt and HotBlock are already present in the market with their commercial products.

Within the next sections we will give a brief overview of the state of the art for thermal energy harvesting materials. We will try to compare which materials - thermoelectrics or pyroelectrics - are the most efficient under given conditions.

1.4.2.1 Thermoelectrics

The process of thermoelectric generation is described by the Seebeck effect. The devices usually consist of two materials: n-type and p-type semiconductors, which are connected electrically in series, but thermally in parallel. The two semiconductors produce electricity directly when their junctions are exposed to a temperature difference (figure 1.2).

Thermoelectric generators produce voltage in proportion to both the temperature difference between the hot and cold sides and to the difference between the Seebeck coefficients of the two materials, which is itself a function of temperature:

$$V = \int_{T_L}^{T^H} S_1(T) - S_2(T)\, dT \tag{1.1}$$

where T_L, T_H are the low and high temperatures, S_1, S_2 are the two materials Seebeck coefficients.

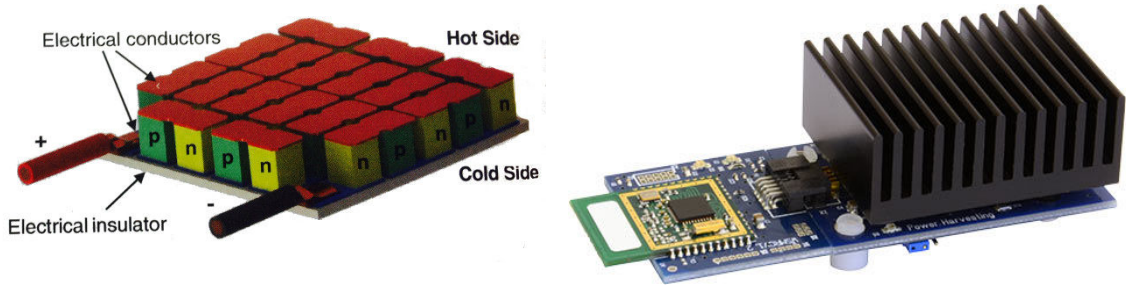

Figure 1.2: *Left: schematic of a thermoelectric module[1]; holes and electrons from p-type and n-type material respectively flow with the heat flow from hot to cold side. Right: thermoelectric generator with heat sink, from[2].*

The efficiency of thermoelectric generators is quite low because a material, to be effective, needs to be both a good electrical conductor and a good thermal insulator. Unfortunately most materials that are good electrical conductors are also good thermal conductors, and vice versa. To estimate thermoelectric property of a material, a figure of merit called ZT is used:

$$ZT = \frac{\sigma S^2}{\lambda}\left(\frac{T_H - T_L}{2}\right) \tag{1.2}$$

where σ is the electrical conductivity, λ is the thermal conductivity and S is the Seebeck coefficient.

Although theoretically unlimited, in practice the ZT values are close to 1. Figure 1.3 compares ZT values for the most commonly used thermoelectrics. As can be seen, the efficiency increases almost linearly with temperature.

Thermoelectrics have several advantages namely an absence of moving parts, silent operation, reliability and scalability. On the other hand, their efficiency is low, the price is quite high and a massive heat sink is often indispensable (figure 1.2). Nevertheless, there are many commercial products exploiting thermoelectrics such as 'Micropelt' generators[2], automotive applications[51,52], fuel cells[53,54] and watches[55].

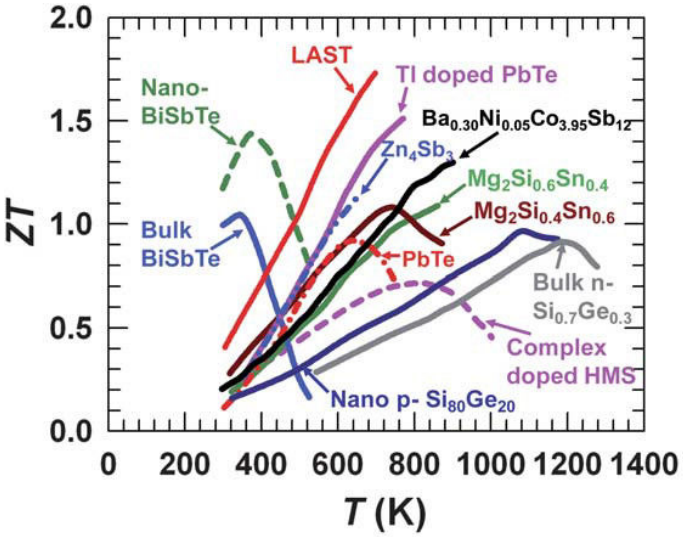

Figure 1.3: *State-of-the-art (2011) comparison of ZT from various materials*[3].

1.4.2.2 Pyroelectrics

Thermal energy can also be exploited using pyroelectric materials. As discussed by Sebald et al.[43], pyroelectric energy harvesting requires temperature variations in time, whereas thermoelectrics require spatial temperature gradients. In real life conditions the wasted heat energy, produced for example by working machines, usually creates spatial gradients, thus favoring thermoelectrics. However, the conversion rate can be much higher for pyroelectric energy generators, and theoretically it could reach the conversion rate of the Carnot cycle.

The pyroelectric effect is the property of some dielectric materials with polar point symmetry to have a spontaneous electrical polarization as a function of temperature. When a pyroelectric material experiences a temporal temperature change, it results in a flow of charges, called pyroelectric current, to or from the surfaces of the material. Assuming an homogeneous pyroelectric material throughout which the temperature T is uniform, the generated pyroelectric current is given by:

$$I = \frac{dQ}{dt} = S\lambda\frac{dT}{dt} \tag{1.3}$$

where Q is the induced charge, S is the electrode surface area and λ is the pyroelectric coefficient, given by:

$$\lambda = \frac{dP_s}{dT} \tag{1.4}$$

where P_s is the electrical polarization vector[56].

A simple illustration of a pyroelectric energy harvesting system is presented by Cha and Ju[4], from which we will provide some citations. Figure 1.4 illustrates an operation of the Ericsson cycle, which is the most commonly used cycle for thermal energy harvesting exploiting two sources of different temperatures. It consists of two constant-temperature and two constant field processes. As the temperature of the pyroelectric material is decreased [1→2], its polarization and surface bound charges increase. If the pyroelectric material is connected to an external circuit, the free charges on its electrodes will be redistributed to compensate for the change in the surface bound charges. Such charge redistribution results in a pyroelectric current flow in the circuit. More charges will accumulate as the external bias field is increased [2→3]. Next, as the pyroelectric

material is heated [3→4], the sign of pyroelectric current is reversed. The cycle is completed by reducing the external bias field back to its initial value [4→1]. The electrical work per cycle W corresponds to the area enclosed by the process lines 1-2-3-4, or simply $W = \oint EdD$.

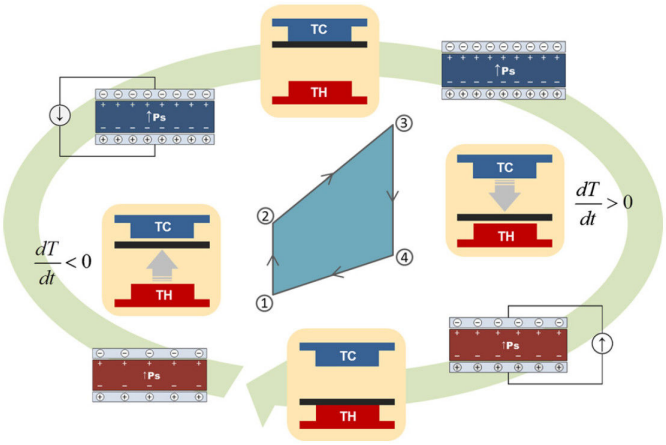

Figure 1.4: *Ericsson conversion cycle for pyroelectric energy harvesting. T_C is the cold source and T_H is the hot source. The graph in the middle represents the electric diplacement field D vs. electric field E. From[4].*

The phenomenon of spontaneous polarization at a temperature difference is called primary pyroelectricity. There is also a secondary pyroelectricity contribution, which is coming from the fact that all pyroelectrics are also piezoelectrics (although the converse is not true due to their polar crystal structure). This means that during heating the thermal expansion will change the polarization of the pyroelectric due to the piezoelectric effect. Assuming homogeneous heating, the total pyroelectric coefficient for the crystallographic direction m of the pyroelectric p_m can be written as[57]:

$$\rho_m = \rho_m^I + \sum_{i=1}^{6} e_{mi} \times \alpha_i \equiv \rho_m^I + \rho_m^{II} \tag{1.5}$$

where e_{mi} are anisotropic piezoelectric constants [C·m^{-2}], α_i are anisotropic thermal expansion coefficients [K^{-1}], and ρ_m^I and ρ_m^{II} are primary and secondary pyroelectric coefficients.

These pyroelectric coefficients can be presented in the form of pyroelectric charge coefficients ρ_Q [Coul·m^{-2}K^{-1}] or pyroelectric voltage coefficients ρ_V [V·K^{-1}]. The latter can be calculated with equation (1.6), as shown in[58]:

$$\rho_V = \frac{\rho_Q}{\varepsilon_r \times \varepsilon_0} \times h \tag{1.6}$$

where ε_r is the relative dielectric permittivity, ε_0 is the vacuum permittivity and h is the material thickness.

The pyroelectric voltage developed across the sample for a temperature change ΔT, is given by equation (1.7):

$$V = \frac{\rho_Q}{\varepsilon_r \times \varepsilon_0} \times h \times \Delta T \tag{1.7}$$

The main application of pyroelectric materials is passive infrared sensors, mostly used for motion detectors. Many companies share the market, with big industrial players present (Honeywell, Panasonic, Murata, etc.).

Now, as we have seen materials sensitive to temperature variations, we will go on and present material sensitive to mechanical stress. Theses materials are called piezoelectric.

1.5 Introduction to piezoelectricity: constitutive equations

Piezoelectric materials are a sub-class of dielectrics with a particular non-centrosymmetric crystallographic structure. The piezoelectric class contains 20 sub-classes, among which there are pyroelectric and ferroelectric materials. When a piezoelectric material is stressed by an external force, the lattices are strained and the barycenters of electric charges of unit cells are separated. This induces a polarization of the lattice as shown in figure 1.5, and it is called the direct piezoelectric effect.

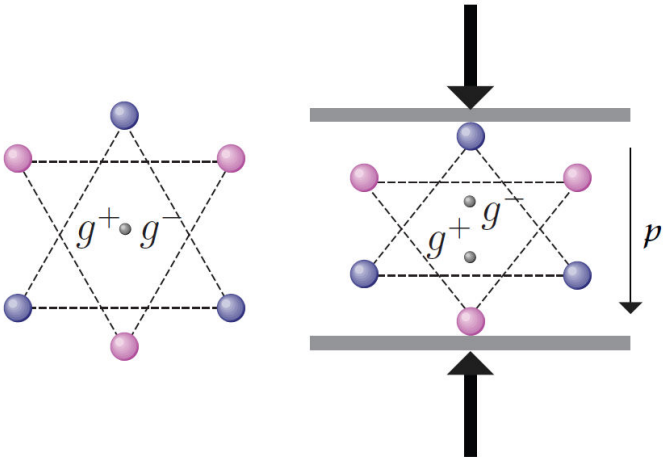

Figure 1.5: *Unit cell of a piezoelectric material without and with an applied external force. g^+ and g^- denote the centers of electric charges. From[5].*

Inversely, when a voltage is applied to a piezoelectric material, it is strained as shown in figure 1.6. This is called the reverse piezoelectric effect.

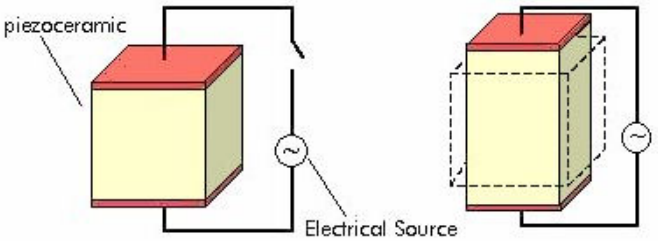

Figure 1.6: *Schematic drawing of the reverse piezoelectric effect. The material is strained upon application of electric field.*

1.5.1 Physical principle

Let us consider an isolated thermodynamic system with internal energy U, which is dependent on parameters such as stress T, strain S, electric field E, displacement field D, entropy σ and temperature Θ. Since the total energy of an isolated system is constant (first law of thermodynamics), the variations of energy dU may come from variations of its parameters. We can express dU in the following form:

$$dU = TdS + EdD + \Theta d\sigma \tag{1.8}$$

The entropy is usually considered constant therefore the last term is neglected, and we can simply write:

$$dU = TdS + EdD \tag{1.9}$$

In piezoelectric materials, a coupling between mechanical and electrical components is introduced, meaning that changing one will necessarily change the other. For example, the induced stress will be dependent not only on the applied strain, but also on the applied electric field. We can write for the stress:

$$\begin{aligned} T &= c^E \cdot S - e \cdot E \ \ (E = const) \\ T &= c^D \cdot S - h \cdot D \ \ (D = const) \end{aligned} \tag{1.10}$$

where c^E and c^D are stiffness coefficients under constant E and D, e and h are piezoelectric coefficients.

If we now perform the integration of equation (1.9) considering the electro-mechanical coupling we will obtain:

$$\Delta U = \frac{1}{2} c^E \cdot S^2 + \frac{1}{2} \varepsilon^S \cdot E^2 - e \cdot S \cdot E \tag{1.11}$$

Here the first term is the mechanical component, the second term is the electrical component and the third term is the electro-mechanical coupling component.

The greatest possible amount of available energy in the system is given by the Gibbs free energy G. It can be shown that a change in the Gibbs energy is given by ΔU:

$$\Delta G = \Delta U = \frac{1}{2} c^E \cdot S^2 + \frac{1}{2} \varepsilon^S \cdot E^2 - e \cdot S \cdot E \tag{1.12}$$

The partial differentials of ΔG will give us the system parameters. Depending on boundary conditions, four formalisms are possible. For example, under constant E and S we can write:

$$\begin{aligned} T &= \left. \frac{\partial \Delta G}{\partial S} \right|_{E=const} \\ D &= \left. \frac{\partial \Delta G}{\partial E} \right|_{S=const} \end{aligned} \tag{1.13}$$

Which will give us the following pair of equations:

$$\left. \begin{aligned} T &= c^E S - eE \\ D &= eS + \varepsilon^S E \end{aligned} \right|_{E,S=const} \tag{1.14}$$

For the other boundary conditions we can write three other pairs of equations:

$$\left. \begin{aligned} S &= s^D T + gD \\ E &= -gT + \beta^T D \end{aligned} \right|_{T,D=const} \tag{1.15}$$

$$\left. \begin{aligned} T &= c^D S - hD \\ E &= -hS + \beta^S D \end{aligned} \right|_{D,S=const} \tag{1.16}$$

$$\left. \begin{aligned} S &= s^E T + dE \\ D &= dT + \varepsilon^T E \end{aligned} \right|_{T,E=const} \tag{1.17}$$

Two mechanical constants (c - stiffness, s - compliance), two dielectric constants (ε - dielectric constant, β - permeability constant) and four piezoelectric constants ($e,\ g,\ h,\ d$) are used to

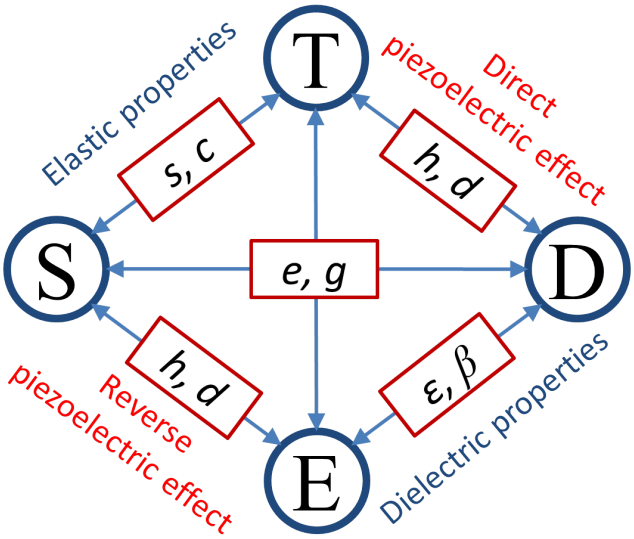

Figure 1.7: *Piezoelectric electo-mechanical coupling.*

describe the piezoelectric material. Using this constants we can describe the behavior of the material when one of the parameters has changed. Figure 1.7 schematically summarizes the electro-mechanical coupling.

All four piezoelectric formalisms are equivalent. This means that all of the piezoelectric coefficients are interconnected:

$$\begin{aligned} e &= c^E \cdot d \\ g &= \beta^T \cdot d \\ h &= \beta^S \cdot e \end{aligned} \tag{1.18}$$

As a quality factor, the coupling coefficient k^2 is introduced, which shows what proportion of an input mechanical energy is transformed into useful electric energy:

$$k^2 = \frac{Produced\ electric\ energy}{Input\ mechanical\ energy} \tag{1.19}$$

1.5.2 Piezoelectric modes

Due to their particular crystallographic structure, piezoelectric materials are highly anisotropic, meaning that the properties vary depending on the orientation of the crystal. In order to describe these orientations, 3 axes and 3 rotations are used as defined in figure 1.8. Usually, axis 3 is placed along the thickness of the sample, and axis 1 is placed in-plane along its longest side.

All the mechanical and electric parameters are tensors of different orders. To distinguish the piezoelectric and elastic coefficients measured along different axes, they are presented in matrix form and are denoted d_{ij}, where index i refers to the direction of generated voltage and index j refers to the direction of applied stress. To entirely determine the piezoelectric material behavior, 36 flexibility coefficients s, 18 piezoelectric coefficients d and 9 permittivity coefficients ε exist. To fully characterize the materials piezoelectric behavior, there are 63 coefficients to know, which is a large number. Nevertheless, even if piezoelectric materials are not centrosymmetric they have enough symmetry to reduce the number of coefficients. Taking into account this symmetry, the

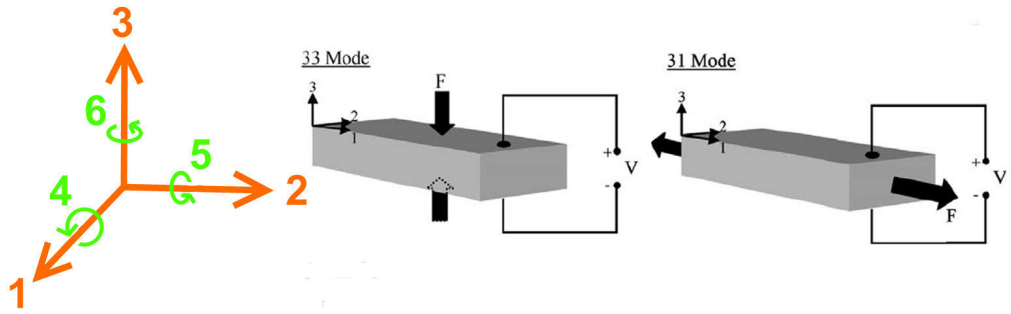

Figure 1.8: *Piezoelectric axes used to describe the orientation of a crystal and illustration of 3-3 and 3-1 modes.*

matrices for s, d and ε are shown in figure 1.9[59]. In practice, most of the time only 3 piezoelectric coefficients are used: d_{33}, d_{31} and d_{32}. We speak respectively of a "3-3 mode", "3-1 mode" or "3-2 mode" of operation.

$$s = \begin{bmatrix} s_{11} & s_{12} & s_{13} & 0 & 0 & 0 \\ s_{12} & s_{22} & s_{13} & 0 & 0 & 0 \\ s_{13} & s_{13} & s_{33} & 0 & 0 & 0 \\ 0 & 0 & 0 & s_{44} & 0 & 0 \\ 0 & 0 & 0 & 0 & s_{44} & 0 \\ 0 & 0 & 0 & 0 & 0 & 2(s_{11}-s_{12}) \end{bmatrix} \quad d = \begin{bmatrix} 0 & 0 & 0 & 0 & d_{15} & 0 \\ 0 & 0 & 0 & d_{15} & 0 & 0 \\ d_{31} & d_{32} & d_{33} & 0 & 0 & 0 \end{bmatrix}$$

$$\varepsilon = \begin{bmatrix} \varepsilon_{11} & 0 & 0 \\ 0 & \varepsilon_{22} & 0 \\ 0 & 0 & \varepsilon_{33} \end{bmatrix}$$

Figure 1.9: *Coefficient matrices for piezoelectric materials.*

The most commonly exploited piezoelectric materials are ceramic PZT ($Pb[Zr_xTi_{1-x}]O_3$, 0≤x≤1). Piezoelectricity is also found in natural materials such as quartz. Lead free materials are also developed, such as metallic AlN or $KNbO_3$. PVDF and its copolymers are naturally piezoelectric and belong to electro-active polymers. We will now give a short introduction to PVDF polymers, including their properties and applications.

1.6 Introduction to PVDF piezoelectric polymers

Polyvinylidene fluoride, polyvinylidene difluoride or simply PVDF is a chemically stable thermoplastic fluoropolymer synthesized by the polymerization of vinylidene difluoride. As early as 1969 Kawai[60] discovered the piezoelectric effect of PVDF and first measured its g_{31} and d_{31} coefficients, which were at least one order of magnitude greater than those of other polymers. Two years later, the pyroelectricity of PVDF was discovered by Bergman et al.[61]. Since then, PVDF and its copolymers have been studied for their use in pyroelectric and piezoelectric technologies. The process of manufacturing bi-oriented PVDF was developed later[62] and was shown to be advantageous for piezoelectic films[63]. Adaptation of this technological improvement by Piezotech company eliminated piezoelectric anisotropy and allowed for fabrication of higher performance PVDF films[64].

The semi-crystalline piezoelectric PVDF polymer shows a complex structure and can present

five distinct crystalline phases: α, β, γ, δ and ε. Different phases are related to different chain conformations: TTT (all trans) planar zigzag for the β-phase, TGTG' (trans-gauche-trans-gauche) for the α and δ phases and T_3GT_3G' for γ and ε phases[6]. Figure 1.10 shows the PVDF phases which are the most used for applications and investigated, namely α, β and γ phases.

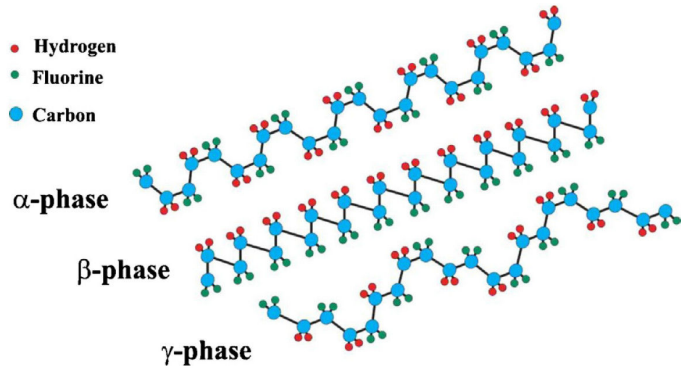

Figure 1.10: *Schematic representation of the chain conformation for the α, β and γ phases of PVDF. From[6]*

Many of the interesting properties of PVDF, in particular those related with its use as a sensor or actuator, are related to the strong electrical dipole moment of the PVDF monomer unit (5–$8{\cdot}10^{-30}$ C.m[65]) which is due to the electronegativity of fluorine atoms when compared to those of hydrogen and carbon atoms[66]. Thus, each chain possesses a dipole moment perpendicular to the polymer chain. If the polymer chains are packed in crystals to form parallel dipoles, the crystal possesses a net dipole moment as it is the case in polar β , γ and δ phases. In antiparallel chain dipoles, the net dipole moment vanishes as it is the case in non-polar α and ε phases[67]. The β-phase is the one with the highest dipolar moment per unit cell ($8{\cdot}10^{-30}$ C.m) when compared to the other phases[65], and it is the one that gives the PVDF its piezoelectric properties. Therefore, the polar β-phase has attracted much technological interest because of its ability for providing the highest pyro- and piezoelectric response[67]. As opposed to ceramic materials where the piezoelectric mechanism is governed by dipole reorientation, piezoelectricity in PVDF is believed to be dominated by volume electrostriction; as a consequence, the d_{33} and g_{33} piezoelectric coefficients are negative in PVDF[68].

Different strategies have been developed to obtain the electroactive phase of PVDF, mainly focusing on the development of specific processing procedures and the inclusion of specific fillers. As summarized by Martins et al.[6] the β-phase is most commonly obtained either by mechanical stretching of the α-phase, or from a melt under specific conditions such as high pressure, external electric field and ultra-fast cooling, or from solution crystallization at temperatures below 70°C or by the addition of nucleating fillers such as $BaTiO_3$, clay, hydrated ionic salt, PMMA, TiO_2 or nanoparticles such as ferrite, palladium or gold.

The stretching mechanism is of particular interest for us in this work, since the PVDF will experience stretching by the SMA. In this kind of β-phase formation, the applied stress results in the alignment of polymer chains into the crystals so that an all-trans planar zigzag (TTT) conformation is inducted. Such mechanism allows the dipoles to align normal to the direction of the applied stress[67]. The transformation process from α-phase to β-phase of PVDF by mechanical stretching as proposed by Li et al.[7] is summarized by the schematic drawing in figure 1.11. The alpha spherulite of PVDF with folded chains is readily obtained under conventional processing conditions. When a mechanical stretching is applied to the material, the transition region of crystalline structure starts from the middle of the spherulite, where the molecular chains are first

extended along the stretching direction. With the deformation of the material, regions of extended chains expand transversely along the middle of the spherulite. More and more extended chains are formed with the evolution of deformation of PVDF, until the entire spherulite of α-phase is transformed into the β-phase.

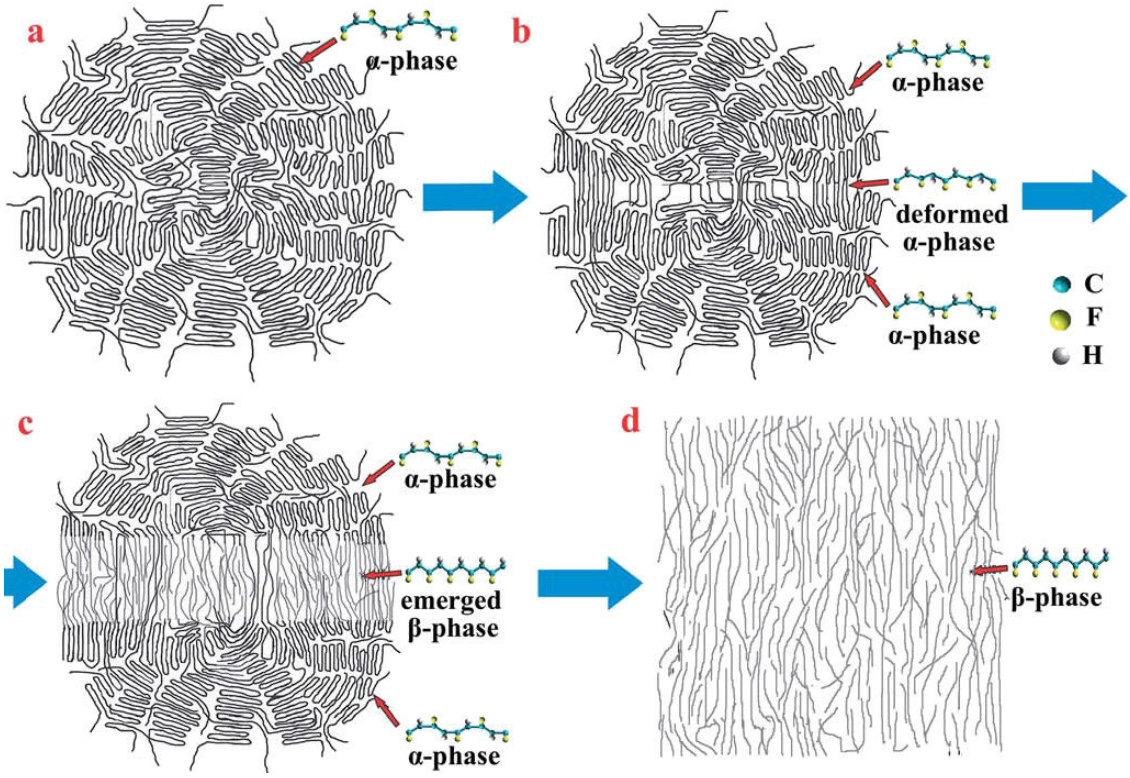

Figure 1.11: *Schematic drawing of the transformation process from α-phase to β-phase of PVDF by mechanical stretching. From*[7].

Yet another way to obtain PVDF in its electroactive phase is to use PVDF-based copolymers. They are developed and synthesized to improve material crystallinity, although the degree of polarization of the unit structure might be reduced[69]. One common PVDF copolymer is poly(vinylidenefluoride-co-trifluoroethylene) or simply P(VDF-TrFE), which has a piezoelectric coefficient of up to 38 pC/N[70] (up to twice us much as PVDF).

As reviewed by Qin et al.[69], PVDF is chemically inert, like many other fluorocarbon polymers. Its high resistance to hydrolysis, low degradation rate, and aging-independent material stiffness reveals the material biocompatibility[71] (U.S. Pharmacopeial class VI[72]). When PVDF comes into contact with human tissue, minimal cellular response without mineralization, intimal hyperplasia, or excessive fibrous tissue reaction has been detected[73]. Thus, PVDF can be used in biomedical applications, for example for active sensing structures in implantable pressure sensors[74,75].

The drawbacks of PVDF include poor adhesion to other materials due to its non-reactive properties, and its inability to form smooth films[76]. It has a relatively low thermal stability of ferroelectric properties (usually up to 80°C) due to its low glass transition temperature[77], and a large variation of relative dielectric constant (6–13) in the frequency range from 1 kHz to 1 MHz[78]. Finally, the production costs are still relatively high, especially for the P(VDF-TrFE) copolymers[69].

To add to the drawbacks, the PVDF material is known for its anisotropic properties of the piezoelectric effect[11,12,64,79]. The piezoelectric performance along direction 2 of uni-axially oriented films is lower than along direction 1, which comes from the anisotropic semicrystalline structure. This is attributed to processes occurring in the crystalline regions and in their interfaces with the amorphous surroundings[11]. However, in bi-axially oriented films (a technological process of Piezotech company) the anisotropic effects are eliminated[64,80]. Also, bi-oriented films have more uniform thickness and better long-term stability.

Its thermal, mechanical, electrical and piezoelectric characteristics (summarized in table 1.2) make PVDF a promising material for sensors[81–84] and energy harvesting applications[85–93]. Natural combination of dielectric and piezoelectric properties allowed the creation of self-charging power cells, where PVDF was used both as a separator and a piezo-element[94,95]. It has also been used for nonvolatile memories[96,97], transducers and actuators[98,99], and sensors[100–103]. Other numerous applications include insulation on electrical wires[104], binders and separators in lithium ion batteries[105], membranes[106] and even fishing lines[107].

Main industrial PVDF producers are American company Measurement Specialties and French group PiezoTech-Arkema. In this work we have used PVDF samples from these two manufacturers.

Table 1.2: *Thermal, mechanical, electrical and piezoelectric characteristics of PVDF, from[13,69,80].*

Mechanical properties	
Density	$\approx$ 1.78 g/cm^3
Tensile strength	20–50 MPa
Young's modulus	2000–4000 MPa
Moisture absorption	0.04–0.05 %
Thermal properties	
Glass transition temperature	> -35 °C
Melting point	$\approx$ 175 °C
Temperature stability	80–100 °C
Coefficient of thermal expansion	120–145 ppm/K
Electrical properties	
Dielectric constant	6–13 (at 1kHz–1MHz)
Loss tangent	0.02 at 1 kHz
DC breakdown field	80 V/μm at 25 °C
Piezoelectric properties	
Strain coefficient d_{33}	-15–33 pC/N
Strain coefficient d_{31}	6–23 pC/N
Voltage coefficient g_{33}	0.14–0.33 Vm/N
Voltage coefficient g_{31}	0.06–0.22 Vm/N
Pyroelectric coefficient ρ_Q	19–30 μC/m^{2}K
Coupling coefficient k_t	10–15 %

1.6.1 PVDF for thermal energy harvesting

PVDF has been used to harvest various mechanical energies, including vibrations[87,88], stretching[92], rain drop[86], air flow[90], handwriting[85] and magnetic[93] energies. Here we will however focus on harvesting thermal energies with PVDF and will present some recent results on this topic.

Table 1.3 compares the pyroelectric properties of the most common pyroelectric materials, including PVDF. As a result of its high $\frac{\rho_Q}{\varepsilon}$ ratio, the pyroelectric voltage coefficient of PVDF is about an order of magnitude larger than that of Lead Zirconate Titanate (PZT) and Barium Titanate ($BaTiO_3$). Considering this, PVDF and its co-polymers have attracted the attention of researchers, and many publications on pyroelectric energy harvesting have appeared just recently[4,8,9,108–113].

Table 1.3: *Comparison of pyroelectric materials, from[13].*

Material	TGS	$LiTaO_3$	$BaTiO_3$	PZT	$PbTiO_3$	PVDF	VF_2VF_3
ρ_Q	350	200	400	420	230	30	50
$\varepsilon/\varepsilon_o$	30	45	1000	1600	200	10.7	8.0
α	.16	1.31	1.00	.44	.67	.06	.06
L	225	646	564	374	461	138	138
P_v	1.32	.50	.05	.03	.10	.47	.71
M_l	.53	.16	.02	.01	.03	.20	.31
Pyroelectric Charge Coefficient				(ρ_Q)μCoul/[m^2•°K]			
Dielectric Constant				($\varepsilon/\varepsilon_o$),where ε_o=8.85pF/m			
Thermal Diffusivity				(α)m^2/sec •10^{-6}			
Thermal Diffusion Depth @ 1Hz				(L)μm			
Pyroelectric Voltage Coefficient				(P_V)ρ_Q/ε, V/[μm•°K]			
Figure of Merit				(M_l)ρ_Q/[C_V •ε], V •mm^2/J			

Cuadras et al.[108] reported in 2010 achieving up to 15 μJ of harvested energy with a PVDF thin film cell for temperature fluctuations from 300K to 360K in a time period of the order of 100 s. They have repeatedly heated commercial PVDF elements with a hair dryer, and used a full-wave rectifier circuit to charge a 1 μF load capacitor to 5.5 V. Based on the sizes provided (3×1.2 cm^2 and thickness 64 μm), we estimate the produced energy density to be around 65 $\mu J/cm^3$. Authors propose that, with a proper energy management circuit, this harvester could be useful for monitoring hot pipes, where the temporal temperature gradient is enough to power autonomous sensor nodes.

In 2013 Lee et al.[8] proposed to directly exploit the fact that the pyroelectric materials are also piezoelectrics, by fabricating what they have called a *Highly Stretchable Piezoelectric-Pyroelectric Hybrid Nanogenerator*. It consists of micro-patterned P(VDF-TrFE) with graphene electrodes, assembled on a micro-patterned polydimethylsiloxane (PDMS)-carbon nanotubes (CNTs) composite substrate. The result was a highly stretchable composite that could be stretched up to 30% and still produce a stable pyroelectric voltage. The maximum reported output voltage was 1.4 V upon simultaneous application of a different mode of strain (i.e. compress-release) and applied temperature of 20°C (thermal gradient of 120°C/s). Unfortunately the authors did not specify

the harvested energy. We can estimate it to be around 24 nJ (or 2 μJ/cm^3) based on the PVDF thickness (7 μm), its dielectric constant, and the size of the harvester (≈4×4 cm^2).

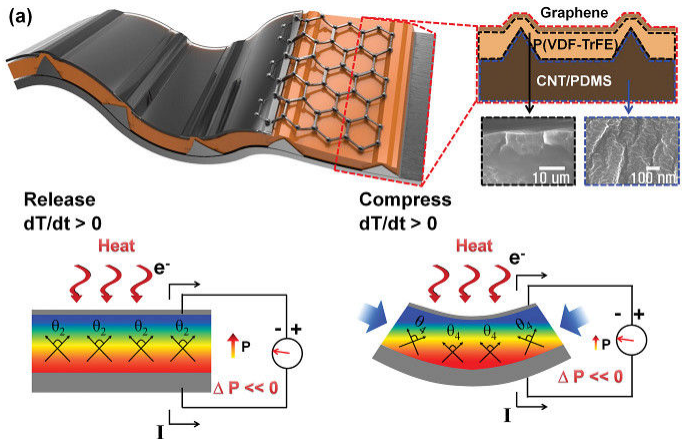

Figure 1.12: *Schematic illustration of the device and its functioning mechanism, with piezoelectric and pyroelectric output simaltaneously, from*[8].

Yang et al.[9] reported a flexible multimodal hybrid energy cell that is capable of simultaneously or individually harvesting thermal, mechanical, and solar energies. The multimodal harvester consisted of a PVDF layer, an array of ZnO nanowires and a poly(3-hexylthiophene) (P3HT) heterojunction solar cell. The PVDF part alone was able to produce 3.2 V with a temperature difference of 19 °C over 100 s. Based on the PVDF thickness (100 μm), its dielectric constant, and the size of the harvester estimated from figure 1.13 (≈5×3 cm^2), the corresponding energy density was around 0.5 μJ/cm^3. Multiple energy harvesting (i.e. thermal + piezo, thermal + solar) increased the overall output of the system.

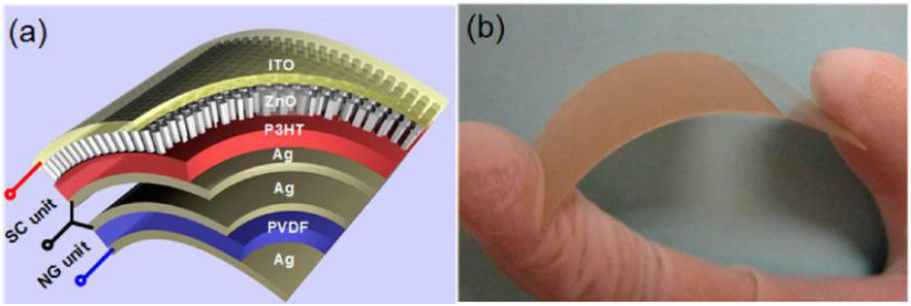

Figure 1.13: *(a) Schematic diagram and (b) photograph of the fabricated hybrid energy cell, from*[9].

Wu et al.[109] presented in 2014 a 2×2 cm^2 pyroelectric hetero-structure of lead zirconate titanate (PZT) particles embedded in P(VDF-TrFE) copolymer. Due to combined formability, low thermal conductivity and high pyroelectric coefficient, the authors proposed to use the composite as an infrared thermal sensor and were able to achieve high values of detectivity. In principle, the same heterostructure could be used for energy harvesting purposes, and it would most probably yield higher outputs compared to individual response of the components.

As an example, when Ericsson conversion cycle is applied higher energy densities are obtained, however application of very high electric field is necessary. Cha and Ju[4] have demonstrated the feasibility of using a liquid-based thermal interface between the pyroelectric P(VDF-TrFE) layer and a heat source/sink in order to increase the temporal temperature gradient. The use of glycerol as a dielectric liquid interface helped create a complete contact between two surfaces and eliminate

trapped gas layers. The evaluation of the harvester was done in this case by applying a bias electric field while monitoring the pyroelectric current. With a temperature difference of 60 °C between the heat sink and source, the device was able to harvest up to 550 mJ/cm^3 at applied electric fields of 750 kV/cm. For real life applications the authors however acknowledge that the harvester will not produce such a high energy since it will be not possible to apply such large bias fields.

As we can see from table 1.4, most of the pyroelectric thermal energy harvesters with PVDF or P(VDF-TrFE), tested in real life conditions, can produce from 0.5 to 65 μJ/cm^3 with temperature differences of 20–60°C.

Table 1.4: *Comparison of some state-of-the-art pyroelectric PVDF energy harvesters.*

Reference	ΔT	Voltage	Energy	Energy density	Remarks
Cuadras et al.[108]	30K	5.5 V	15 μJ*	65 μJ/cm^3*	<1 V per heating cycle
Lee et al.[8]	-	1.4 V	24 nJ*	2 μJ/cm^3*	T gradient not specified
Yang et al.[9]	19°C	3.2 V	0.8 μJ*	0.5 μJ/cm^3*	
Cha and Ju[4]	60°C	-	-	550 mJ/cm^3	bias field 750 kV/cm applied

* estimated based on data provided by authors.

To increase the efficiency of harvesters, research today looks into multimodal harvesting or enhanced materials. The way explored in this work is the fabrication of composite materials to enhance thermal energy harvesting. Composite energy harvesters can be realized either using materials of different families but same functionality (for example ceramics+polymers), or materials of different functionalities (for example pyroelectric+shape memory alloy), or combining a functional and a non-functional material. In the following section we will introduce shape memory alloys, which were used for fabrication of our composite harvesters. We will come back again to composite energy harvesting in chapter 3 where we will present our results on this matter.

1.7 Introduction to shape memory alloys

Shape Memory Alloys (SMA) belong to a family of materials which have the ability to return to a predetermined shape upon heating. The hot state of the SMA is called austenite; during cooling, the material undergoes a martensitic transformation which is a diffusion-less first order phase transition, resulting in shear-like deformation of the crystal lattice. The product of this transformation is called martensite. If the material is deformed when cold and then heated, the reverse change in crystal structure causes it to return to its original shape.

Not all alloys undergoing martensitic transformation present shape memory effect (e.g. martensitic steels), but only those where this transformation is thermoelastic, i.e. the coherence between two phases is conserved. Both direct and reverse transformations occur within some temperature interval and are characterized by start and finish temperatures. In addition, thermodynamically conditioned thermal hysteresis prevents these temperature intervals from coinciding.

Let us take a closer look at one-way shape memory effect, which is the most common effect of shape recovery, and is achieved only during heating. Schematic of a stress-strain-temperature curve is shown in figure 1.14. The first step in the loading sequence, when the strain is initially applied, induces linear stress in the martensitic structure with no macroscopic shape change. During the second stage, the mechanical stress in the martensitic phase induces reorientation of the

twin grains (so called detwinning) and results in large inelastic strain, which is not recovered upon unloading (blue curve). Next, the material is heated and the reverse martensitic transformation recovers the inelastic strain. Since martensite grains have been reoriented by stress, the return to austenite produces a large transformation strain having the same amplitude but the opposite direction to the inelastic strain, and the SMA returns to its original shape in its austenitic phase (red curve). Finally, the material is cooled down and the martinsitic phase is formed again; the process can now be repeated (green curve).

SMAs with two-way shape memory effect are different in the way that during cooling, the martensitic transformation is also accompanied by the induced strain. Thus, the material can remember both its hot and cold states.

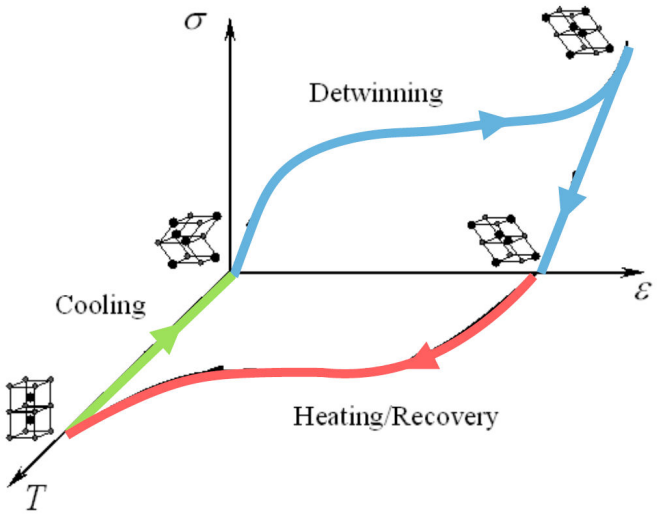

Figure 1.14: *Schematic the stress-strain-temperature curve of one-way shape memory effect. Adapted from[10].*

Martensitic transformation occurs within a certain thermodynamically-conditioned temperature interval, schematically shown in figure 1.15. During cooling, a direct transformation takes place within the temperature interval ΔT_M: starting at M_s and finishing at M_f. Similarly, during heating, a reverse transformation happens within the temperature interval ΔT_A: starting at A_s and finishing at A_f. The two transformations are shifted by ΔT_{hys} corresponding to the undercooling/overheating required to overpass the interface energy. Transformation interval ΔT_{transf}=A_f-M_f is the minimal amplitude of a thermal cycle required to complete both the direct and inverse transformations.

There are many families of materials that present the shape memory effect, including gold-cadmium, copper-zinc and iron-based metallic alloys, and polyether- or polyester-based polymers. Among those, the nickel-titanium alloy (or Nitinol, from Nickel Titanium Naval Ordnance Laboratory) discovered in 1959[114] has received a greater number of applications. Nitinol is less brittle and capable of high recoverable strains (twice that of the copper alloys)[115], and it can be produced in thin films[116] which is important for batch fabrication and MEMS technology. It also has very good electrical and mechanical properties, long fatigue life, and high corrosion resistance; its main electro-mechanical properties are summarized in table 1.5. Upon heating NiTi alloys can develop large stress and stains, up to 600 MPa and 10%, respectively. Generally, alloys with larger strain and stress have larger temperature intervals and hysteresis. This limits the energy that can be harvested from a given system. Moreover, all these characteristics are significantly dependent on the SMA composition, which means that the choice of an optimal alloy or the adjustment of its

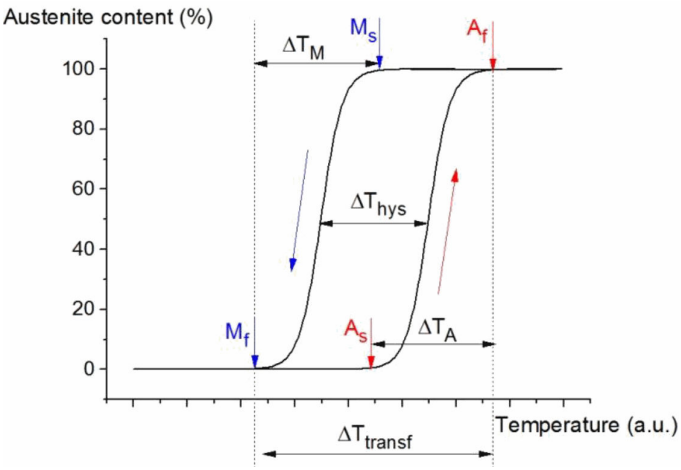

Figure 1.15: *Schematic of martensitic phase transformation in SMA.*

composition for specific energy harvesting applications are typically required.

To estimate the efficiency of heat conversion into mechanical energy by SMA, we can perform a series of simple calculations [49]. The input thermal energy required by the SMA body to perform mechanical work consists of the heat for increasing its temperature (typically by 20°C for NiTi) and of the latent heat of transformation ($\approx$ 20 J/g for NiTi [117,118]). Therefore the typical value of input energy is about 30 J/g. Specific mechanical work that can be produced by SMA can be calculated as a product of the mechanical stress generated ($\approx$ 500 MPa in average) and its relative deformation ($\approx$ 3% in average). In this way the useful work can be estimated as 15 J/cm^3 or 2.3 J/g (taking the density of NiTi as 6.5 g/cm^3 [117,119]). The efficiency, which is the ratio of work to input heat, can then be estimated as $2.3 \div 30 = 8\%$. While the published values vary within 3–30% [117,118], in the majority of theoretical and experimental publications the reported efficiency is < 10%.

Table 1.5: *Electro-mechanical properties of Nitinol alloy, summarized from [117–119]*

Density	6.5 g/cm^3
Resistivity (austenite)	82 μOhm.cm
Resistivity (martensite)	76 μOhm.cm
Latent Heat	20–25 J/g
Typical Elongation to Fracture	15.5 %
Typical Yield Strength (austenite)	560 MPa
Typical Yield Strength (martensite)	100 MPa
Elastic Modulus (austenite)	75 GPa
Elastic Modulus (martensite)	28 GPa
Poisson's Ratio	0.3
Energy Conversion Efficiency	3–30 %
Available Transformation Temperatures	-100–100°C

1.8 Specifications for autonomous thermal event sensor

Now that we have briefly introduced the physical principles and the materials used in this work, we can define the specifications of our energy harvesting device.

We want our device to be able to harvest random temperature variations, therefore to be frequency independent. This means that no matter if the event is often repeated or if it happens once in a while, the energy produced by the harvester should be the same.

Thermoelectric generators could not be used in such conditions, since they can work only with continuous temperature gradients. Single heating events are not sufficient for wireless transmission, and repeated events are needed to generate enough power.

Pyroelectric generators can, in principle, work with single heating events. However the generated power will still be frequency dependent, and the generated energy will be proportional to temperature gradient.

In contrast, composite energy harvesters can increase the generated energy density by utilizing two complementary effects: piezoelectric and pyroelectric. This multimodal harvesting approach will provide detection of random heating events in narrow temperature ranges, and generate enough energy for wireless communication. Moreover, use of SMA will add a sensing functionality to the device: in the ΔT_{transf} interval, detection of thermal events with predetermined threshold will be possible. Thus, the composite harvester will be able to sense and at the same time generate energy necessary to send the information about thermal event to a distant receiver.

The composite energy harvesting device will consist of PVDF films and NiTiCu ribbons, coupled together. The temperature induced strain of NiTiCu (2–3%) and increased temperature (up to 70°C) should be compatible with PVDF operational conditions. Finally, with heating from room temperature to 50–70°C, the harvester should generate output energy of around 100 μJ, enough to power a wireless transmitter.

Chapter 2

Characterization of PVDF for energy harvesting

The following chapter is devoted to a specific characterization of PVDF with regards to energy harvesting application. The material has been known since 1969, and many studies have been performed and published. We will briefly review the main characterization techniques used to study PVDF, with a focus on piezoelectric characterizations. Then we will present the experimental results aimed to characterize the performance of PVDF for thermal energy harvesting applications, in particular for the use in composite systems with shape memory alloys. We will therefore perform the characterization of the material in conditions similar to the targeted operational conditions.

The characterizations described further include the developed method of open-circuit voltage and energy measurements, g_{31} and g_{32} direct measurements at low strains and their nonlinearities at high strains, anisotropy investigations and self-discharge studies of PVDF under different conditions (i.e. temperature, strain, voltage).

2.1 Classical piezoelectric measurements of PVDF: state of the art

Usually piezoelectric coefficients of ceramic thin films are measured by optical interferometry analysis of the reverse piezoelectric effect[120–123], by frequency measurement methods[120,124] as well as with Berlincourt type piezometers[125,126]. Consequently the piezoelectric d_{33} or d_{31} charge coefficients are usually extracted from the measurement, from which the g_{33} or g_{31} voltage coefficients can be further recalculated.

Pizoelectric measurements of PVDF films have been reported using similar techniques. To name a few examples, Bune et al.[127] have measured the d_{33} coefficient in the frequency range of 1-100 kHz by laser interferometry. Roh et al.[79] used a low-frequency surface acoustic wave method to measure the complex wave number k_m from which the g_{ij} matrix was calculated using a numerical algorithm. Seminara et al.[128] have measured the dynamic behavior of a stand-alone PVDF film in pure bending. Finally, piezoresponse force microscopy (PFM) was also used to measure the d_{33} coefficient[129]. As in the case for ceramics, these methods are indirect, meaning that the g_{ij} coefficients are recalculated based on other measured constants. The coupling coefficient is usually recalculated from the impedance resonance frequencies[120], though it is known to be a troublesome method for PVDF due to its high mechanical losses[130]. Many experimental works on PVDF piezoelectric characterization use frequency measurements and study the dependence of piezoelectric coefficients on the measurement frequency in the high-frequency range[127,131]. It would be therefore interesting to measure the piezoelectric response in quasi-static conditions, similar to our applications of harvesting slow temperature fluctuations.

It has been shown by many research groups that the content of piezoelectric β-phase in PVDF depends on elongation[7,132,133], tensile strain rate[7,133,134] and heating[7,132,134]. It is agreed that the β-phase content strongly increases with elongation. It also increases with temperature from

room temperature to about 80°C, but decreases with further heating. Some works have shown a significant increase of β-phase with increased tensile strain rate, but other works have shown no effect at all or even a slight decrease[7,134]. Anyway, pronounced effects were only shown at high strain ranges of 100-550% and temperatures around 80°C. Little discussion was given to effects at smaller strains, and no direct effect of strain on the piezoelectric g_{31} voltage coefficient was measured. It would be therefore interesting to directly measure the g_{31} value and study its dependence on the applied stress and temperature, particularly in the range of envisaged applications i.e. a strain of about 2% and a temperature of up to 70°C.

There have been few experimental works on the behavior of piezoelectric properties of PVDF under applied low stress. One of the earliest works goes back to 1985 by Hahn[11]. He has studied the behavior of d_{31} and d_{32} under applied stress of up to 60 MPa in an uni-axially stretched PVDF. He noted the linear behavior of d_{31} and an unusual nonlinear decrease of d_{32} which he believed was due to intrinsic effects related to changes in dipole orientation. The large difference between the d_{31} and d_{32} values (d_{31} was measured to be about 20 times higher at room temperature) was explained by a particular arrangement of crystalline β-phase within an amorphous matrix (figure 2.1). The authors discussed that the piezoelectric response along direction 1 is mainly determined by a deformation of the amorphous regions, whereas direction 2 depends also on the deformation of the crystalline regions

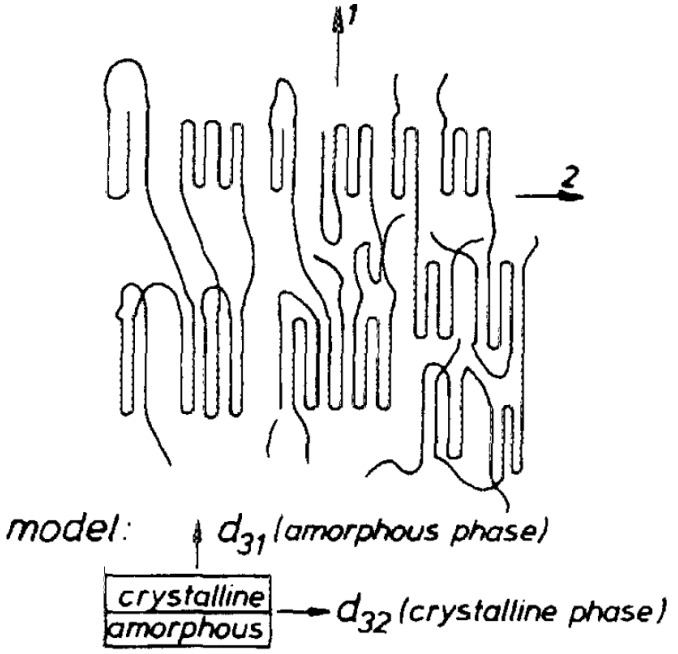

Figure 2.1: *Arrangement of crystalline structure of uniaxially-oriented PVDF and its representation by a simple mechanical model, as shown by Hahn[11].*

In 1993 Lynch[135] measured the piezoelectric e_{31} and e_{32} stress coefficients at small strains. He did not observe any significant strain dependency, and suggested that all of the non-linearities of the d_{ij} coefficients arise from the non-linearities of the elastic modulus.

In 2002 Lanceros-Mendez et al.[136] studied PVDF films during the deformation process by means of dielectric measurements and FTIR (Fourier Transform Infrared Spectroscopy) and later by SEM (Scanning Electron Microscope)[137]. The authors reported a reorientation of the β-phase chains from perpendicular to parallel to the stress orientation within the plastic region. Also a decrease in the degree of crystallinity due to the deformation was observed. Based on the results of this work one can expect the decrease of the piezoelectric properties within the plastic region of

the material due to the continuous reorientation of chains and decrease of crystallinity.

Sencadas et al.[12] in 2004 performed tensile tests on metallized 28 μm thick β PVDF films along direction 2. The generated electric response was measured in open-circuit under a constant strain rate at room temperature. The results (extract shown in figure 2.2) showed that the open-circuit voltage developed by the sample in a uniaxial deformation increased non-linearly with the applied strain in the pre-yielding zone and decreased in the post-yielding zone. The experimental idea is similar to our work, which is to determine the evolution of g_{ij} coefficients with the applied stress. Unfortunately, no precise values or information on how the g_{ij} coefficient was calculated are given, and only the g_{32} general behavior was interpreted.

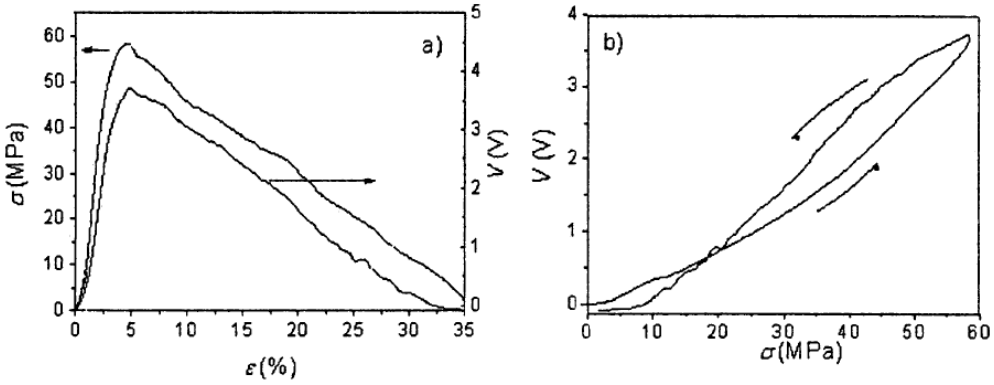

Figure 2.2: *Extract from[12]:(a) Stress and voltage versus strain, (b) voltage versus stress for β-PVDF for constant deformation experiments along direction 2.*

We can thus summarize that the g_{ij} piezoelectric coefficient is rarely being studied directly, although it is an important characteristic of the material for energy harvesting or generator applications. In view of this we have focused our efforts on directly measuring the g_{ij} coefficients, and perform the measurements in accordance to our targeted operational conditions, that is to say a quasi-static situation and high applied strain.

2.2 Output voltage and energy: theoretical estimations

To estimate the theoretical output voltage and generated energy density of a piezoelectric material used as a generator, we will describe the corresponding analytic equations and coupling matrix. Then, using known datasheet mechanical and piezoelectric constants we will calculate the maximum theoretical performance of PVDF and compare it with other common piezoelectrics.

2.2.1 Output voltage

We have previously seen that it is possible to describe the behavior of a piezoelectric material using the piezoelectric coupling matrix, which is given in its general form by equation (1.15). Depending on the way the material is used, and therefore the boundary conditions, the fundamental form can be rewritten accordingly. For the case of generators, the coupling matrix should be rewritten as to give the generated electric field under applied stress or strain. In the case of a free-standing composite coupled with SMA, PVDF experiences the applied strain while it remains mechanically free, which means that the stress T is constant. During the measurements, PVDF is

connected to an open electrical circuit, which means that there is no charge displacement and the electrical displacement field D is constant. If we consider this boundary conditions, the matrix from equation (1.15) can be rewritten in the following form:

$$\begin{cases} S = s^D T + g_{ij}^t D \\ E = -g_{ij} T + \beta^T D \end{cases} \tag{2.1}$$

where the s^D is the compliance under constant D, $\beta^T = (\varepsilon^T)^{-1}$ is the permeability constant under constant T and g^t is a transposed matrix of g.

Under the open circuit experimental conditions, D is equal to zero, so the matrix simplifies to:

$$\begin{cases} S = s^D T \\ E = -g_{ij} T \end{cases} \tag{2.2}$$

The subscript ^{D} indicates that the value was measured under constant D. However, these measurement conditions are not always possible or practical, and values are sometimes measured under constant E. For the case of flexibility s, the values measured under different conditions are connected by the following equation:

$$s^D = s^E + d^t \cdot \beta^T \cdot d \tag{2.3}$$

Depending on the material, the s^D and s^E can be very different, which leads to different elastic properties of the piezoelectric material, when measured under different experimental conditions, such as open-circuit or close-circuit measurements. For example, artifacts such as a saw-tooth outline of the thermal dilatation curve of PZT, have been reported to be caused by this phenomenon[138]. No such artifacts have been reported for PVDF to our knowledge.

To understand this impact of experimental conditions on mechanical properties of a piezoelectric, let us estimate the values of the first and second terms of the sum on equation 2.3 by using the standard material constants of PVDF, and compare it to PZT. To do so we need to take into account that s^E=YM^{-1} for 1-1 and 3-3 directions, $\beta^T = (\varepsilon^T)^{-1}$ and $d_{33}^t = d_{33}$. The main steps of calculations are shown in table 2.1.

Table 2.1: *Calculation of the terms contributing to s^D for PVDF and PZT. YM is the Young's modulus.*

	YM, GPa	ε_{rel}	d_{33}, pC/N	s^E, GPa^{-1}	$d_{33}^t \cdot \beta^T \cdot d_{33}$, GPa^{-1}	term1/term2
PVDF[13]	3	13	-30	3.33E-01	-7.82E-03	43
PZT[139]	60	1700	300	1.67E-02	5.98E-03	3

We can see that for PZT, the second term ($d^t \cdot \beta^T \cdot d$) is about 30% of the first term (s^E); therefore the s^D value is about 30% higher than the s^E value. On the other hand, for PVDF the second term is 43 times smaller than the first one and thus can be simply neglected; therefore the s^D and s^E values are nearly equivalent. This is one of important benefits of PVDF over PZT, since its mechanical compliance s does not depend on open-circuit or close-circuit conditions.

Let us now go further and extract the piezoelectric voltage from the second expression of equation (2.2). It can be expressed as a function of the material thickness t, its piezoelectric constant g_{ij} and the applied stress T:

$$V = -g_{ij} \cdot T \cdot t \tag{2.4}$$

From the point of view of sample geometry we can see that, when considering the same homogeneously applied stress, the output piezoelectric voltage should only be dependent on the material thickness and should be independent on the sample's length and width.

For practical use equation (2.4) can be then rewritten as a function of the strain S, applied to the material. However, this equation would only be valid in the elastic range of PVDF, where the strain and the stress are linearly proportional.

$$V = -g_{ij} \cdot S \cdot YM \cdot t \tag{2.5}$$

The graphical representation of the theoretical output voltage for a 30 μm thick PVDF in different working modes according to equation (2.5) is shown in figure 2.3. As expected from the corresponding piezo-coefficients, the 3-3 mode should yield a higher output voltage. However, as we will see further, this is not always the case, since experimentally, it is much more complicated to apply a homogeneous stress on thin flexible samples in pure 3-3 mode.

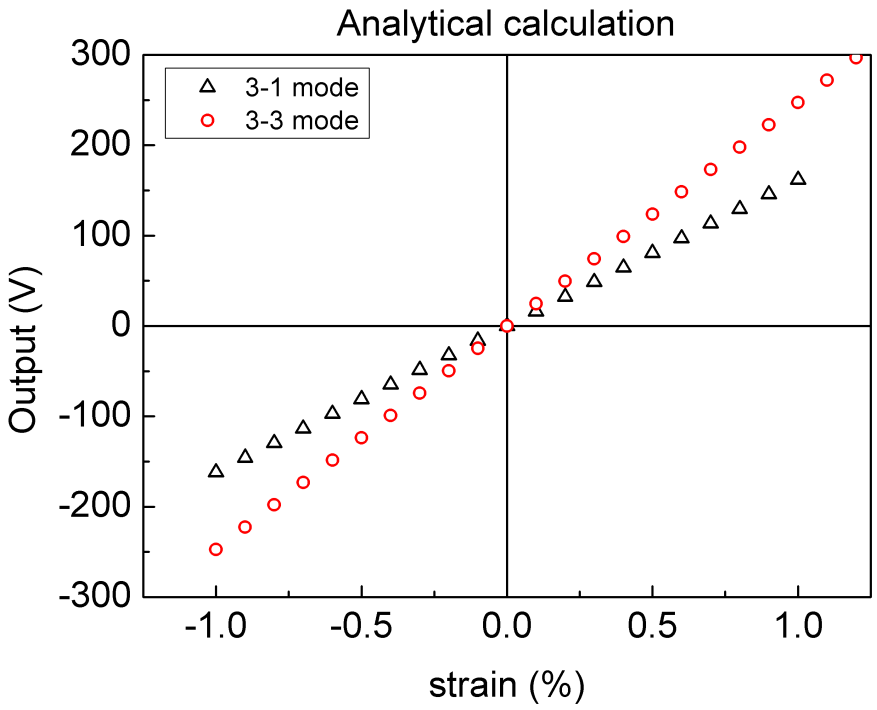

Figure 2.3: *Theoretical absolute voltage output of 30 μm PVDF for 3-3 and 3-1 modes. g_{31} and g_{33} are 0.216 and 0.33 Vm/N, respectively*[13].

2.2.2 Output energy

PVDF, because of its flexibility, is usually considered a high energy density material[140]. To estimate its electric output energy we have to make several assumptions: when the material is mechanically deformed by an external force, its mechanical energy can be characterized by the elastic energy density $U_{mechanical}$, given by:

$$U_{mechanical} = \frac{YM \cdot S^2}{2} \equiv \frac{T^2}{2 \cdot YM} \tag{2.6}$$

The conversion of mechanical energy into electrical energy is represented by the electromechanical coupling coefficient k expressed in %:

$$k = \sqrt{\frac{electrical\ energy\ stored}{mechanical\ energy\ applied}} = \sqrt{\frac{U_{electrical}}{U_{mechanical}}} \tag{2.7}$$

where $U_{electrical}$ is the output electrical energy density [J/cm^3].

Now, we can express the electrical energy density as a function of mechanical strain or stress:

$$U_{electrical} = k^2 \cdot \frac{YM \cdot S^2}{2} \equiv k^2 \cdot \frac{T^2}{2 \cdot YM} \tag{2.8}$$

Since PVDF and its copolymers are available by different suppliers and with different compositions, we have summarized some of the most popular commercial grades in table 2.2 to estimate their theoretical available energy density. We have calculated the energy density values using equation (2.8) at 2% strain, since it is our targeted strain value which is possible to achieve by using shape memory alloys. We have also added for comparison the data of non commercial state-of-the-art nanofibers, produced by PVDF electrospinning, and a conventional PZT material. For PZT, strain of 0.08% is taken for the calculations, since it is the average yield strain of the material (higher strains lead to failure of the material).

Table 2.2: *Calculation of theoretical output electrical energy density of different PVDF grades and comparison with PZT. For PVDF 2% strain is considered. For PZT the 0.08% strain is taken, considering its yield strain (ε_{yield}) and yield stress (σ_{yield}).*

Material	YM, GPa	σ_{yield}, MPa	ε_{yield}, %	k, %	$U_{electrical}$, mJ/cm^3
PVDF[13]	2-4	45-55	1.1-2.8$^{(a)}$	14	8-16
PVDF[80]	2.5	170	6.8$^{(a)}$	10-15	5-11
P(VDF-TrFE) 75/25[80]	0.95	90	9.5$^{(a)}$	10-15	2-4
P(VDF-TrFE) 70/30[80]	1	60	6$^{(a)}$	10-15	2-5
PVDF nanofibers[141]	3	60$^{(b)}$	2$^{(a)}$	12.5-21.8	9-29
PZT[142]	60	50$^{(c)}$	0.08	50	5

(a) value is calculated from YM and yield strength;
(b) average value for PVDF polymers is taken;
(c) average value for piezoelectric ceramics is taken[143].

From these simple calculations we can see that PVDF possesses a very high yield strain, which basically means that it can be deformed elastically to rather large deformations. It is a usual

characteristic property for polymers, but not common for all piezoelectric materials, where the elastic limit is usually lower than 0.1%, as it is the case for PZT.

In the best case, 2% strain, which could come from coupling an SMA with PVDF nanofibres from[141] possessing a high electro-mechanical coupling coefficient, we could theoretically harvest up to 30 mJ/cm^3, which is a very high and promising value. Practically however, it will be much lower, around 10 mJ/cm^3, because the electro-mechanical coupling coefficient of a common PVDF grade is lower, and there are always losses in the composite interfaces.

The aforementioned considerations will be useful for us for the measurement of piezoelectric coefficients. For example, from experimental results where the open-circuit voltage is measured as a function of applied stress, we can directly obtain the g_{ij} coefficient using equation (2.4). Similarly, from an energy vs. stress information we can calculate the k^2 coefficient using equation (2.8).

2.3 Output voltage and energy: experimental measurements

We have seen theoretical calculations for estimating the output voltage and energy of PVDF. Now, let us move forward to the practical side and see how voltage measurements are performed in this work. The measurement precision of the generated voltage has a direct impact on the final precision of the piezoelectric coefficients; it is therefore crucial. Conventional direct piezoelectric characterizations can be hampered by large electrical losses and uncontrolled charge leakage into the circuit during measurements, which may result in lower detected voltage and possible underestimation of the material properties. Taking into account the low permittivity (thus the capacitance) of piezoelectric polymers compared to ceramics, this problem becomes even more critical.

Usually, direct piezoelectric response measurements of polymers are made with a standard oscilloscope in a closed-circuit connection[86,144], or by using more sophisticated charge-amplifier circuits[88,145]. To minimize losses and leakages it is preferred to perform measurements at high frequencies, but even then the measured voltage usually remains low (it rarely exceeds 10 V).

In our work we focus on the harvesting of slow events in quasi-static conditions. Therefore a measurement technique is needed that would be able to give reliable measurements in such conditions. In the absence of a reliable existing technique, we have recently proposed a simple and accurate method for measuring the piezoelectric voltage of flexible organic films, working in real open-circuit conditions, and thus with virtually no charge leakage[146]. Open-circuit conditions are obtained by introducing a mechanical switch into the measurement circuit to separate the piezoelectric part (harvester) from the measuring part (collector). This allows for the accumulation of the produced charges without their immediate dissipation inside the measurement circuit; once accumulated, they are then dissipated in the collector when the acquisition of voltage is performed. The switch is kept in its open state during the mechanical deformation of the piezoelectric material while the produced charges accumulate on the electrodes. When the deformation is completed, the switch is closed and all the charges are transferred at once into the measurement circuit. A schematic representation of the described circuit is shown in figure 2.4.

To collect and measure the charges accumulated during deformation, we have proposed two possibilities using different equipment:

- Standard oscilloscope (Agilent DSO1014A).

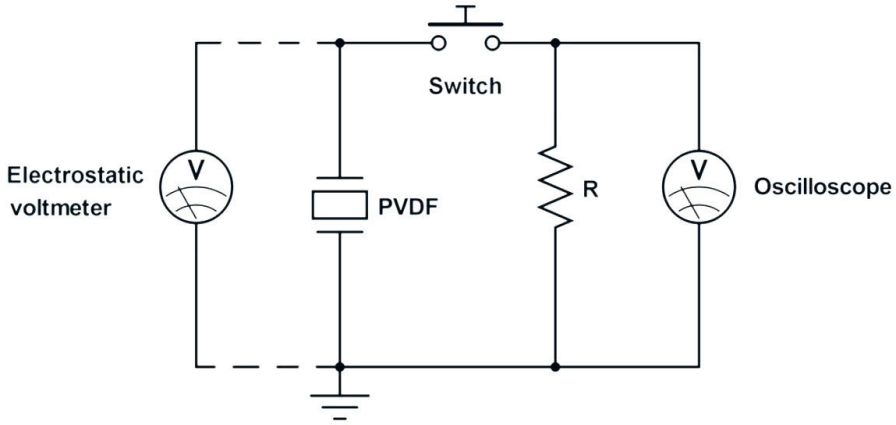

Figure 2.4: *Schematic presentation of the proposed measurement circuit with a switch, an oscilloscope and a contact-less electrostatic voltmeter.*

In this case, while the switch is open the oscilloscope detects no charges, so the voltage remains zero. Upon closing of the switch the piezoelectric sample is discharged into the known internal resistance, and the observed voltage rises instantaneously from zero to its maximum value. Then the switch remains closed and the charges dissipate in the measurement circuit, and the voltage decays back to zero.

- Non-contacting electrostatic voltmeter (TREK 370).

  This type of voltmeter measures electrostatic surface potential of the sample without physical contact, making the impedance of such system virtually infinite, and thus eliminating regular-oscilloscope charge leakages. In this work a TREK 370 voltmeter was used, which was connected in parallel to the sample and to an external resistance, separated by a switch. TREK 370 is capable of measuring in 0-3 kV range with 1 V resolution.

  The non-contact voltmeter set-up allows for real-time monitoring of the accumulating voltage during the application of the mechanical stress. The voltage behavior is different in this case: with the switch being open the voltage rises to its maximum value and stays at this value since there is no dissipation in the measurement circuit. Once the switch is closed, the discharge in the external resistance intervenes and the voltage drops to zero.

In figure 2.5 the output voltage curves obtained with both methods are shown. A conventional measurement with an oscilloscope in a closed-circuit is shown for comparison, from which we can see that the detected maximum voltage is 6 times lower than any of the proposed methods at 0.5% strain. The energy that was produced by the piezoelectric can be calculated as an equivalent to the energy dissipated in the external resistance. In general terms, from Joule first law, we can state that the power P dissipated from electrical energy to thermal energy equals to the voltage V drop across the element multiplied to the current I traveling through the resistor R[147]:

$$P = V \cdot I = \frac{V^2}{R} \tag{2.9}$$

Since the power is energy per unit time, the energy can be written in the following way:

$$E = \int P dt = \frac{V^2}{R} \cdot t \tag{2.10}$$

The discharge of the piezoelectric sample takes place over few tens of milliseconds during which several hundreds of measurement points are taken, therefore the integration is necessary to calculate the actual energy value:

$$E = \int_A^B \frac{V^2}{R}\, dt \tag{2.11}$$

Practically, the numerical integration is realized by the summation of all acquired measurement points with a constant Δt, which is characteristic of the measurement equipment:

$$E = \sum_A^B \frac{V^2}{R}\, \Delta t \tag{2.12}$$

The summation limits are fixed from the moment of the start of discharge (the switch is closed, point *A* in figure 2.5) to the moment when the discharge is completed (point *B*).

Since metallized PVDF can also be presented as a simple plate capacitor with a dielectric material, its energy can also be roughly estimated by the maximum energy that a capacitor with such capacitance can store (equation (2.13)).

$$E = \frac{1}{2} C V^2 \tag{2.13}$$

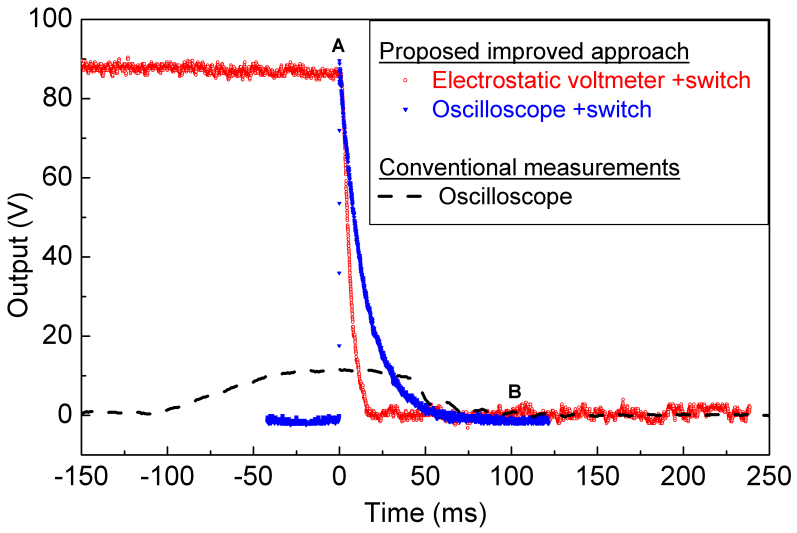

Figure 2.5: *Typical discharge curves for PVDF after 0.5% strain. When open-circuit, switch is closed at time zero. Open-circuit oscilloscope R=10 MΩ. Open-circuit electrostatic voltmeter R=1 MΩ. Conventional closed-circuit oscilloscope R=10 MΩ.*

Analyzing both the discharge behavior in figure 2.5 and the values in table 2.3, we can observe that the highest energy value can be obtained by integrating the voltage of the contact-less voltmeter and the oscilloscope in open-circuit conditions. This makes these methods the preferred measurement methods for our applications. The energy calculated by capacitance is slightly lower in both cases, which may come from underestimated capacitance value (the RCL-meter used for capacitance measurement is operated at 1 kHz frequency, while the quasi-static capacitance may

be higher). On the other hand, both voltage and energy values obtained by the conventional oscilloscope setup are much lower, which can be explained by continuous charge leakage in the system, which among others makes the voltage output dependent on strain application rate, i.e. when the sample is strained slowly the voltage will be lower than if the sample is strained rapidly.

Table 2.3: *Comparison of voltage and energy measurement methods. The values are calculated from the data in figure 2.5.*

	Oscilloscope	Oscilloscope with switch	Contact-less voltmeter
R, MΩ	10	10	1
Max voltage, V	11.6	89.6	90.8
Energy via integration, μJ	1.88	23	23.8
Energy via capacitance, μJ	0.36	22.4	23

Also, the duration of voltage discharge (time constant) in all cases depends greatly on material capacitance and on the collector circuit resistance. The latter effect is visible when comparing the curves from the electrostatic voltmeter and oscilloscope+switch in figure 2.5, where the discharge time increases with the increased resistance. On the other hand, physically speaking the generated energy value should only depend on the material capacitance and not on the circuit resistance. There is nevertheless an equipment measurement error that appears at low resistance values and leads to energy miscalculation. What happens is that at lower circuit resistances the time constant of the discharge is not governed by the PVDF capacitance anymore, but rather by the response speed of the voltmeter. This phenomenon is shown in figure 2.6 and comprises an increased energy value observed by electrostatic voltmeters and decreased energy observed by an oscilloscope at resistances < 10 kOhm.

This phenomenon is particularly pronounced for the electrostatic voltmeter. To highlight this, series of measurements were done using another brand of electrostatic voltmeter (244A Isoprobe electrostatic voltmeter from Monroe Electronics), which has a lower response speed than Trek, and which is able to give correct measurements only at resistances > 10 MOhm. For the Trek voltmeter and the Agilent oscilloscope the resistance could be as low as 10 kOhm with no considerable variations in energy. During this work most of the piezoelectric measurements were performed with resistance of 1–10 MOhm.

2.4 Direct piezoelectric characterization: controlled low strain

Now that we have seen how to accurately measure voltage, we need to know how to strain the PVDF in order to generate that voltage. That is, we need to find a way to mechanically deform the material in a precise, controllable and quasi-static manner. In this manuscript we propose and develop four approaches to apply the deformation to the PVDF samples. First, low strain was applied with mechanical press, four-point bending and tube bending. These methods are relatively fast to perform in laboratory scale, and allow simple experimental measurements of piezoelectric coefficients. Then, high strain was applied with tensile machine, which required more sophisticated set-up and automatization of experiment. Since PVDF may be subjected to rather high strains in composite structures with SMA, and little information is known about its

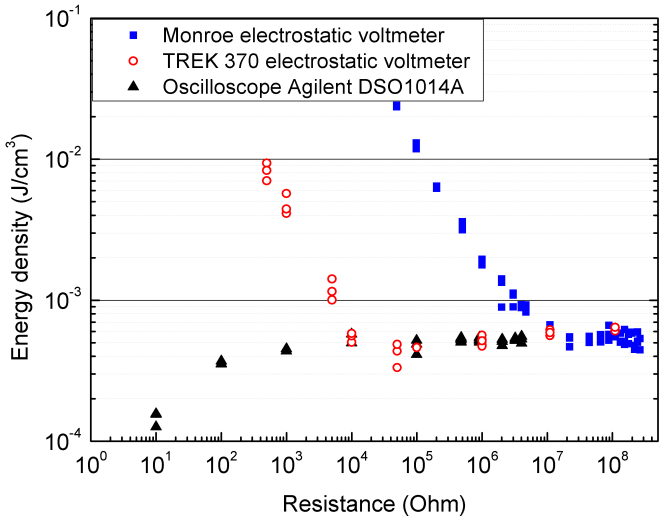

Figure 2.6: *Measured energy density deviations as a function of the circuit resistance. The correct energy values are above 10^7 Ohm and deviations take plase when the resistance is lowered. Measurements were performed with PVDF after 0.5% deformation.*

behavior in such conditions, we have for the first time studied directly its g_{31} coefficient under applied high strain.

All of these experimental approaches were adapted specially to soft flexible polymers, and allowed the application of controllable and quasi-static strain. Once the measurement methods were established, we have measured different commercial PVDF and P(VDF+TrFE) samples to get a direct evaluation of the voltage coefficients (g_{33} and g_{31}). Usually g_{ij} is calculated from d_{ij} coefficient by equation (1.18) and not measured directly. We have therefore compared our directly measured values with those of the supplier's datasheets. We have used 30 μm thick pre-assembled piezo-elements from Measurement Specialties (code-named LDT1 [148]) and metalized PVDF and P(VDF+TrFE) films of different thicknesses from PiezoTech [80]. The materials and their piezoelectric and mechanical properties are summarized in table 2.4.

Table 2.4: *Datasheet properties of commercial PVDF samples used to validate piezoelectric measurement methods (summarized from [13,80,148]).*

Name	Supplier	LxWxT, mm	d_{31}, pm/V	g_{31}, Vm/N	k_{31}, %	YM, GPa
LDT1	MeasSpec	30x12x0.028	23	0.216	12	2-4
PVDF	Piezotech	20x15x0.040	6 $\pm$10%	0.06 $\pm$20%	10-15	2.5 $\pm$20%
P(VDF-TrFE)	Piezotech	20x15x0.050	6 $\pm$20%	0.09 $\pm$20%	10-15	1 $\pm$20%

We will now describe the three methods of applying low strain and make a short comparison between them.

2.4.1 3-3 mode: compression

For this first method, a mechanical press was used, as shown in figure 2.7. It allows to compress a piezoelectric film along its thickness, exploiting the 3-3 mode. The sample was pressed between two flat metallic surfaces, with the applied weight being measured with a weight gauge. When pressure is applied to the sample, a mechanical deformation ε is induced. The values of ε can be calculated using a standard solid mechanics approach with the equation (2.14).

$$\varepsilon = \frac{W \cdot g}{A \cdot YM} \tag{2.14}$$

where W is the weight [kg], g is the free-fall acceleration [m^2/s], A is the area to which the weight is applied [m^2] and YM is the Young's modulus of the material [Pa].

(a) *Photo of the press with its weight gauge. The PVDF sample is visible inside the press with two electrodes hanging on the side*

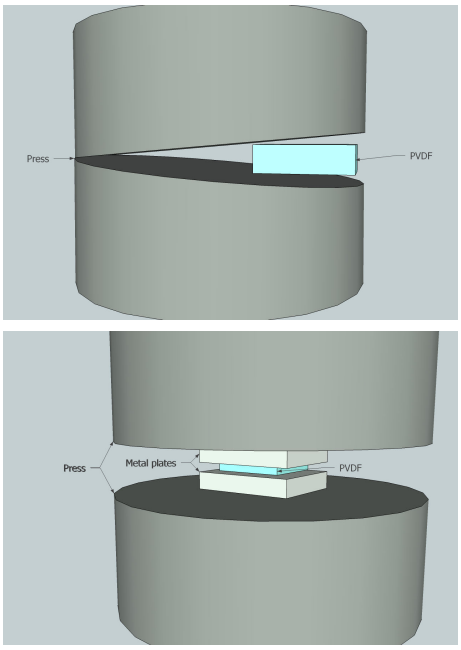

(b) *Exaggerated schematic drawing of a PVDF sample inside a press with and without small metal clamps to optimize pressure distribution*

Figure 2.7: *Mechanical press set-up.*

The corresponding output voltage V_{33} was measured simultaneously, and an example of V_{33} vs. load graph is presented in figure 2.8. After a certain load the output voltage drops dramatically, which suggests that mechanical breakdown of the sample has been reached.

In theory the press set-up is easy and the experiment itself is simple to perform. However, in practice this method has many disadvantages. First of all, the load gauge has a very large scale range and limited precision, making it difficult to detect and read the small changes in pressure. Also, the deformation mechanism of the sample is not clear, as large static-friction forces appear between the sample's surface and surrounding metallic disks, which do not allow the free flow of the material along its length direction. This has for consequence the fact that length and width of the sample stay virtually unchanged while its thickness is forced to decrease, which is not the case when the material is able to deform freely. Finally, the pressure applied to the press is not uniformly distributed to the sample, but instead it is applied to the surrounding metal disks. This leads to a situation where the force actually applied to the sample is much lower than the force measured by the gauge. This last issue can be partially solved by using small metal plates well adapted to the sample size (figure 2.7b).

The comparison between the experimental output voltage of LDT1 and the theoretical approximation for 3-3 mode according to equation (2.5) is presented in figure 2.9. A rather big offset between experimental and theoretical values is observed.

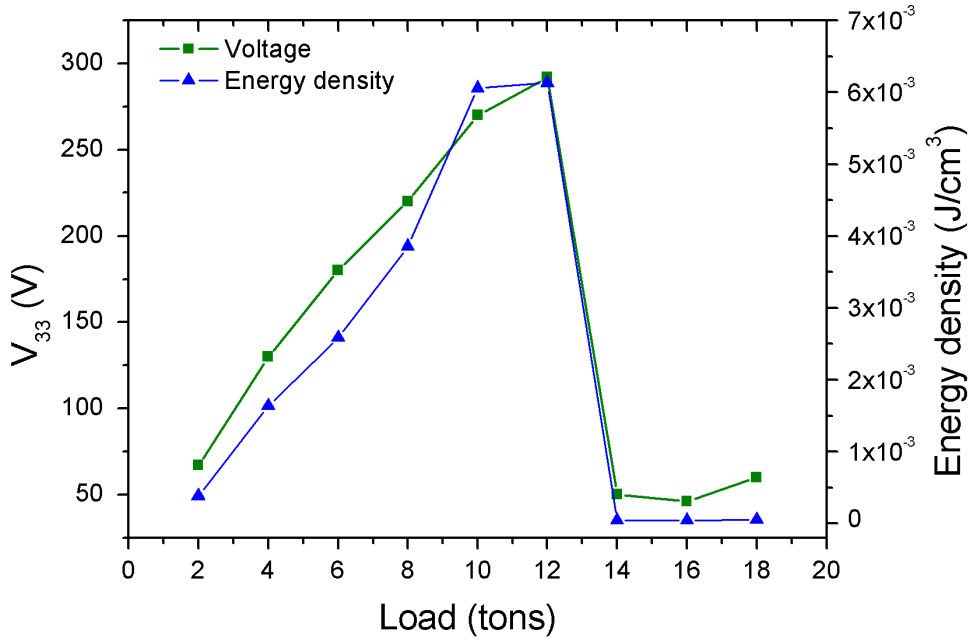

Figure 2.8: *Absolute voltage and energy density output vs. applied press load for 40 μm PVDF sample.*

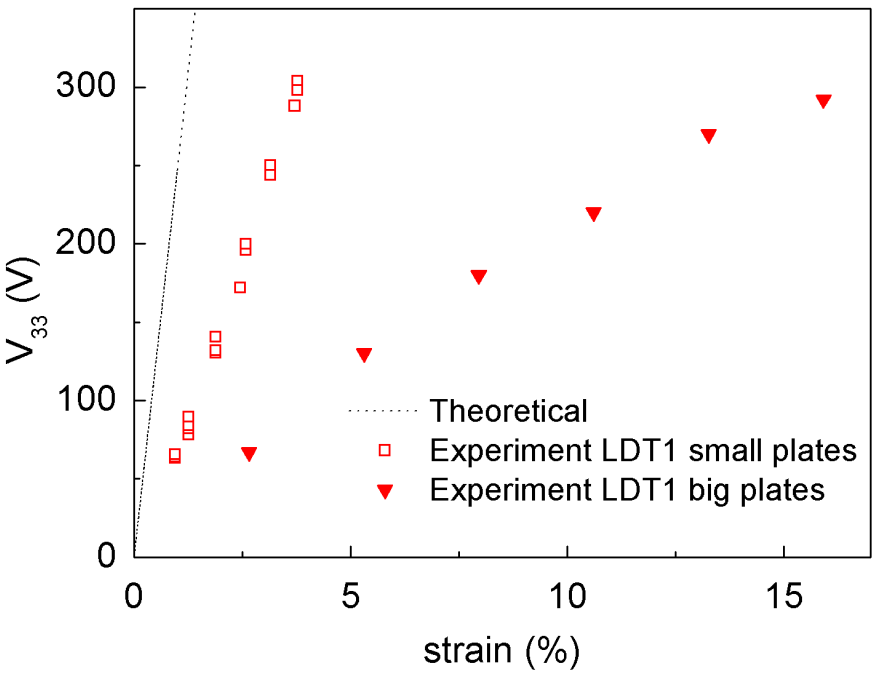

Figure 2.9: *Comparison of experimental and theoretical absolute voltage of LDT1 in 3-3 mode measured by press.*

In fact, the ratio between the sample surface area and the press surface area plays a critical role during the measurements. For example, if the press disks are too large compared to the sample they can touch on the sides, and then only a small part of the applied pressure will actually affect the sample, giving an overestimation of the sample strain according to equation (2.14). When the smaller intermediary disks are used, the applied pressure is distributed in a more homogeneous manner on the sample's surface, so the calculated strain values become closer to the actual values. But even in this case, as seen from figure 2.9, the experimental voltage curves are still below the theoretical curve; this leads to a gross underestimation of the g_{33} coefficient according to equation (2.15).

$$|g_{33}| = \frac{V_{33}}{t \cdot \varepsilon \cdot YM} \tag{2.15}$$

where V- generated voltage, t- sample thickness, YM - Young's modulus of PVDF.

2.4.2 3-1 mode: bending

Bending allows to strain the film along its length, making use of 3-1 mode. Four-point bending and tube bending were used to bend the samples.

2.4.2.1 Tube bending

In tube bending method, a metallized sample is glued to a flexible plastic substrate and is bent around a tube with known diameter. The sample is deformed along its length, making use of the 3-1 mode. The set-up of the experiment is shown in figure 2.10. When the sample is bent by itself, its neutral axis is situated in the middle of the sample, and the total strain is zero. When the sample is mounted on a much thicker substrate, the resulting effective neutral axis is completely shifted outside the sample and the strain calculation can be with certain hypothesis simplified to equation (2.16)[149].

$$\varepsilon = \frac{h/2}{r + h/2} \tag{2.16}$$

where h is the thickness of the substrate [m] and r is the radius of the tube [m].

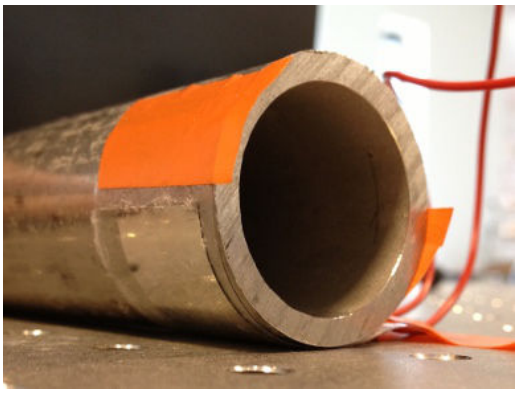

Figure 2.10: *Tube bending experiment.*

This method allows fast and easy measurements and a large range of deformations can be achieved simply by using tubes of different diameters. It is very repeatable, as confirmed by the

series of measurements done with one sample: voltage variation measured at fixed deformations was around $\pm 5\%$. During the experiment six different metal tubes of diameters ranging from 20 to 100 mm were used, giving PVDF sample deformations from 0.2% up to 0.7%. On each tube the sample was measured three times and average values of output voltage and energy were taken.

The comparison between the experimental output voltage of LDT1 and the theoretical approximation of 3-1 mode according to equation (2.5) is presented in figures 2.11. Positive strain values correspond to elongation of PVDF and negative values to compression, when sample with substrate was flipped over and bent in the opposite direction. Both theoretical and experimental values have a very good match, confirming the suitability of tube bending for direct piezoelectric characterization. In this case the g_{31} coefficient can be calculated by equation (2.17).

$$|g_{31}| = \frac{V_{31}}{t \cdot \varepsilon \cdot YM} \tag{2.17}$$

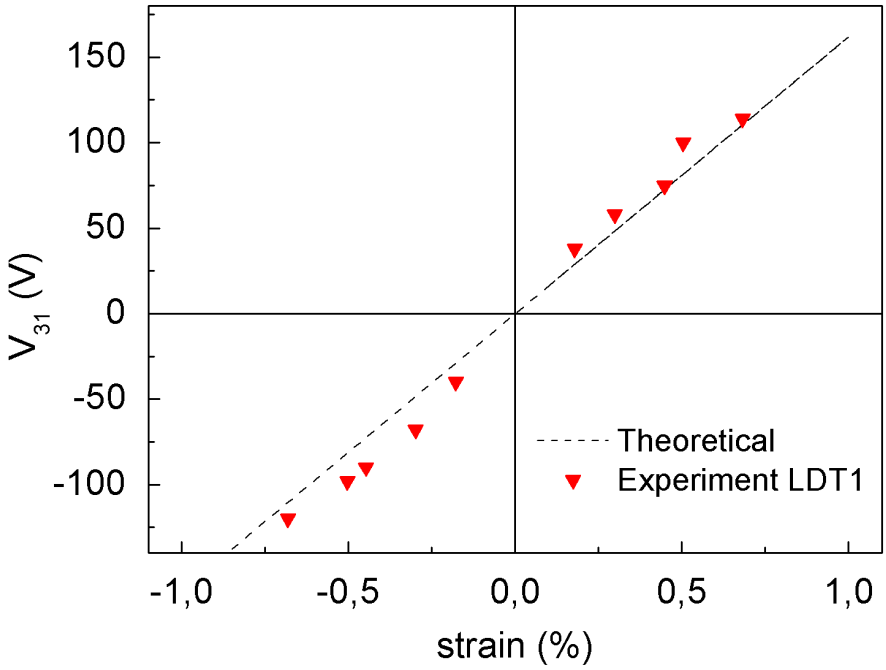

Figure 2.11: *Comparison of experimental and theoretical voltage of LDT1 in 3-1 mode measured by tube bending.*

Nevertheless, there are certain drawbacks of this method: the precise thickness of both the substrate and the glue layer are necessary to calculate the deformation; also, higher levels of strain are difficult to achieve, since either very thick substrate is necessary, which naturally limits its flexibility, or very small tube diameters should be used, which makes them difficult to manipulate.

2.4.2.2 Four-point bending

The schematic presentation of the four-point bending machine and a photo of the actual experimental set-up is shown in figure 2.12. To perform these experiments, a sample of metallized PVDF was glued to a plastic substrate having a thickness h by means of commercial epoxy glue. When

the geometry of the machine is known, the induced stress σ in the material can be calculated with the equation (2.18).

$$\sigma = \frac{3 \cdot F \cdot (l - b)}{2 \cdot w \cdot h^2} \tag{2.18}$$

where F is the load (force) [N], l is the span between the outer points [m], b is the span between the inner points [m], w is the width [m] and h is the thickness of the substrate [m].

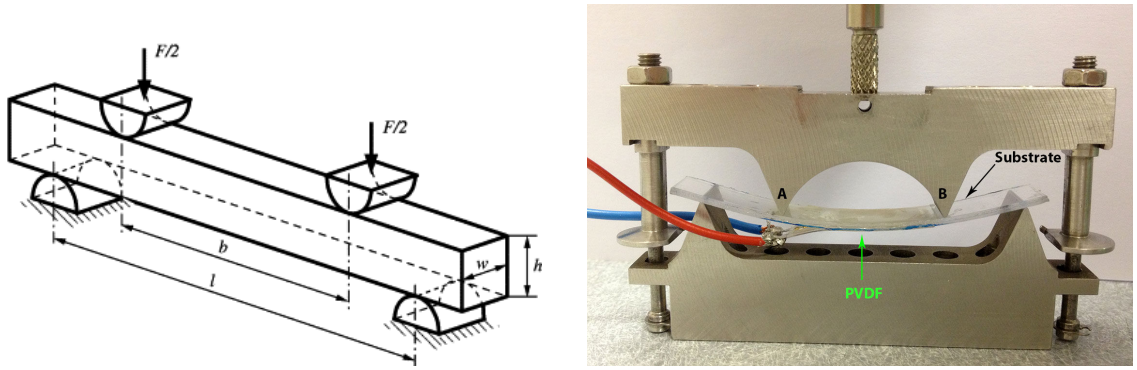

(a) *4-point bending schematic representation[150].* **(b)** *Photo of the sample during the measurement.*

Figure 2.12: *Four-point bending experiment.*

The load F is proportional to the vertical displacement of the machine, which is registered by an in-built displacement sensor. The output file of the machine after each bending experiment is provided as force vs. displacement, as shown in figure 2.13, from which the maximum F value is extracted.

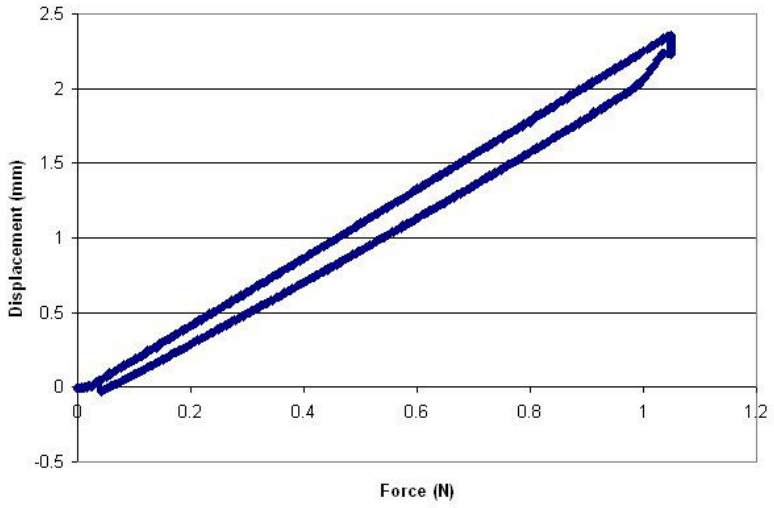

Figure 2.13: *Example of 4-point bending force vs. vertical displacement data file.*

Four-point bending is a mechanical test allowing precise calculations of stress. In our experimental conditions, stress is initially induced in the substrate, and the strain is transferred to PVDF. Therefore the nature of the substrate will impact the measurements (e.g. maximum strain and

stress) and the Young's modulus of the substrate is necessary to calculate the strain transferred to PVDF. In our case, the g_{31} coefficient was calculated by equation (2.19).

$$|g_{31}| = \frac{V_{31}}{t \cdot \sigma} \tag{2.19}$$

The experimental results of four-point bending experiments and tube bending experiments for an LDT1 sample are presented in figure 2.14. Both methods show excellent match, thus confirming the possibility of using either of them depending on availability and experimental conditions. Based on our experience the tube bending method is more convenient for measuring samples with larger surface areas, and it becomes quite difficult to manipulate and measure samples as their size decreases. In contrast, the four-point bending set-up is more adapted for small samples; the maximal size of the sample is limited to 2.75 cm^2 due to machine geometry.

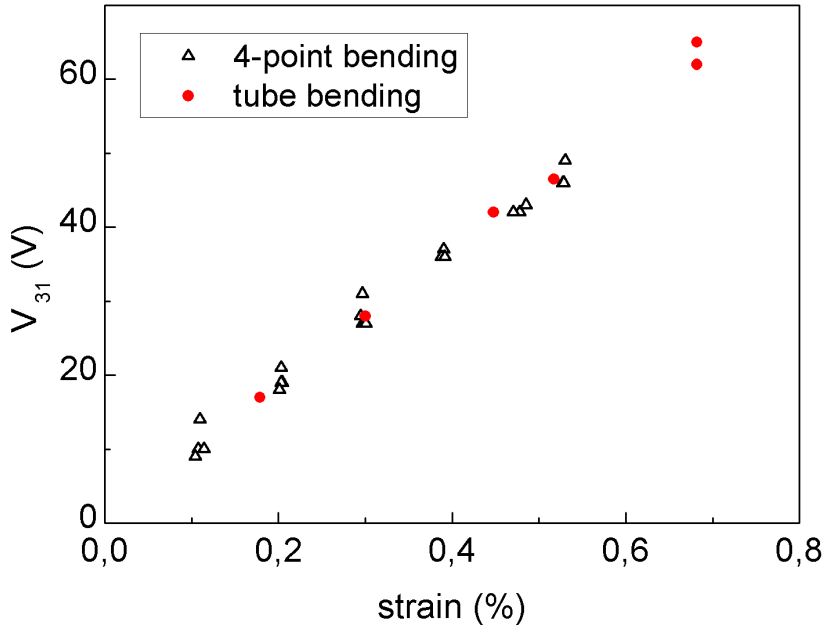

Figure 2.14: *Output voltage comparison of LDT1 PVDF sample, using four-point bending and tube bending methods.*

Output voltage and corresponding generated electric energy density as a function of applied strain for all samples are presented in figures 2.15 and 2.16 respectively. The classical linear voltage strain-dependence (as from equation (2.4)) is confirmed for all samples, with remarkable high voltage values up to 120 V. The slopes of the curves reflect at first order the differences in film thickness and also g_{31} coefficients. Thus, the samples with bigger thickness and/or higher g_{31} coefficient produce higher voltage for the same strain values.

Considering the electrical energy density, experimental results also agree with the expected parabolic strain dependence as predicted by equation (2.8). Since energy density is independent of the sample geometry, a direct correlation between values of g_{31} and steepness of parabolas is observed. Consistently, along with high voltages, we have observed remarkable high values of electrical energy density with about 0.5 to 1 mJ/cm^3 for strains of $\approx 1\%$. These values are of the same order of magnitude as the calculated theoretical values for 2% strain (shown in table 2.2), which confirms the good match between our proposed measurement and calculation techniques, their suitability and accuracy.

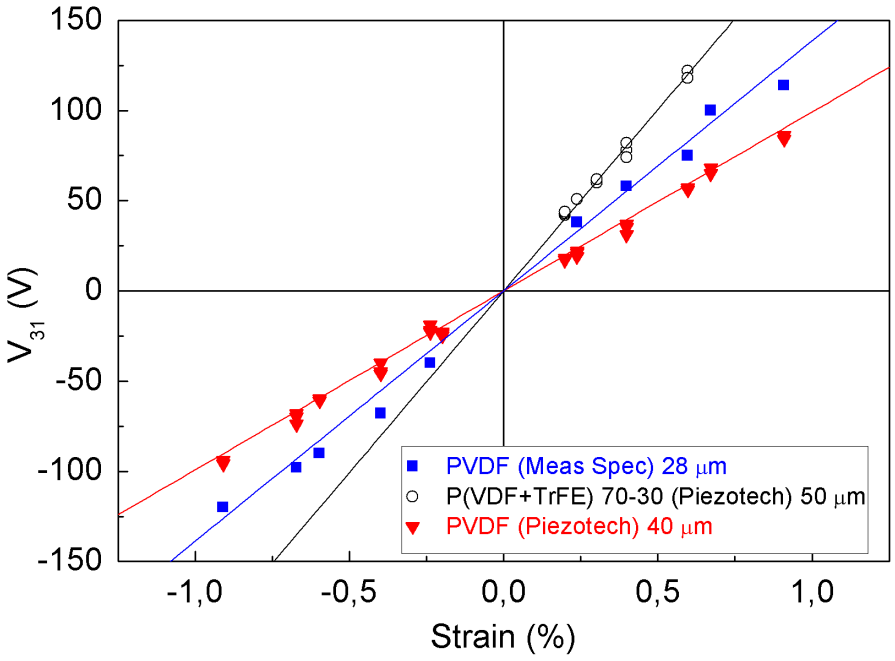

Figure 2.15: *Piezoelectric output voltage measured experimentally in 3-1 mode with the proposed techniques for three commercial PVDF samples under study.*

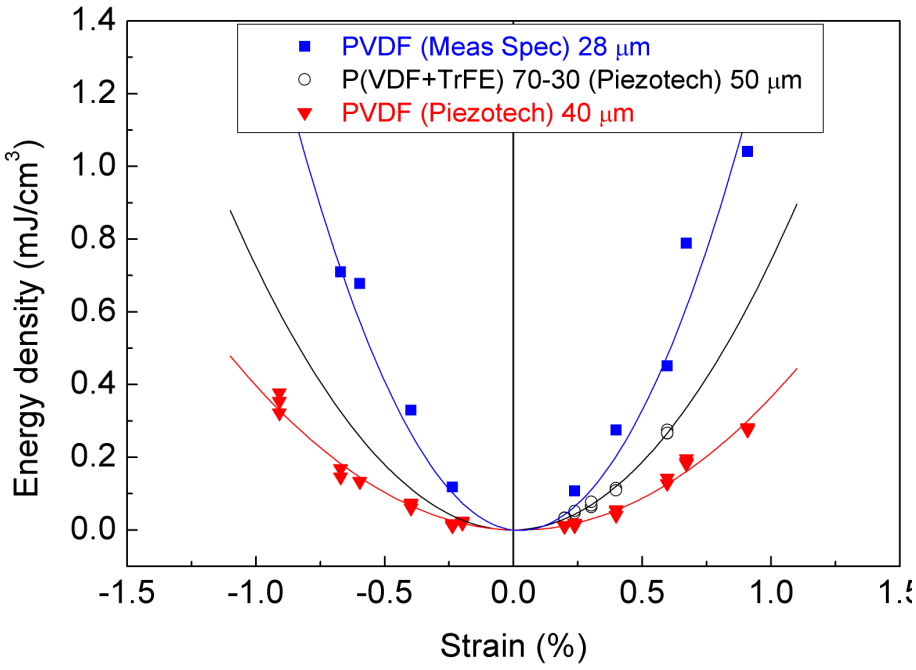

Figure 2.16: *Piezoelectric output energy density measured experimentally in 3-1 mode with the proposed techniques for three commercial PVDF samples under study.*

Finally, g_{31} voltage coefficient and k_{31} mechanical coupling factor were calculated from the resulting energy output curves with equation (2.8) as a ratio of input mechanical and generated electrical energies. The results of these calculations are shown in table 2.5 and compared with those of datasheets.

Table 2.5: *Comparison of piezoelectric coefficients between supplier datasheets and experimentally obtained values for the commercial PVDF samples under study.*

Name	Data-sheet values		Experimental values	
	g_{31}, Vm/N	k_{31}, %	g_{31}, Vm/N	k_{31}, %
LDT1 (28 μm) MeasSpec	0.216	12	0.22	13
PVDF (40 μm) Piezotech	0.06 $\pm$20%	10-15	0.09	5.5
P(VDF-TrFE) 70-30 (50 μm) Piezotech	0.09 $\pm$20%	10-15	0.4	12

It can be noted that the g_{31} coefficients are higher than those from datasheets, especially for the "Piezotech P(VDF-TrFE)" copolymer sample. When considering the k_{31} coupling factor, experimental values are in the range of the datasheet, except for the "Piezotech PVDF (40 μm)" sample. Such a low value may indicate an incorrect value of Young's modulus in this case. For example, when using value of 1.4 GPa instead of 2.5 GPa, which is still within the datasheet confidence interval, the calculated k_{31} is 10%, in agreement with the datasheet value.

To shortly conclude this section, we have proposed a method specially adapted for measuring direct piezoelectric voltage and energy of flexible polymers. Stress is applied with a high precision four-points bending system and voltage is measured with real open-circuit conditions using a mechanical switch. This technic allows exploring direct piezoelectric effect in quasi-static conditions, without use of high-precision equipment nor sophisticated measurement circuits. As a clear feature, we report unusual large strain-induced voltage and electric energy density for PVDF and copolymers. Remarkably high voltage and energy density values of up to 120 V and 1.2 mJ/cm^3 were obtained for 40 μm PVDF sample with 0.7% strain in 3-1 mode. We can conclude that the proposed method allows direct piezoelectric coefficient evaluations, which is adequate for generator or harvester considerations. The experimental results suggest that usual voltage coefficients of PVDF and P(VDF-TrFE) copolymers might be underestimated.

2.5 Direct piezoelectric characterization: controlled high strain

The four-point bending system allows direct measurement of the g_{31} coefficient of PVDF, but it relies on the supplier datasheet values of Young's modulus, which are often given with low precision (i.e. confidence interval of $\pm$20% for Piezotech films[80] and $\pm$30% for MeasSpec films[13]). Moreover, only small strain values are reachable with four-point bending (<1%, as can be seen from figure 2.15) due to the mechanical limitations of the machine. With tube bending, slightly bigger strains are possible with tubes of smaller diameters, but it eventually becomes unpractical to perform measurements on small tubes.

In order to improve the accuracy of the measurements, it is thus desirable to assess with higher confidence the Young's modulus of the samples prior to piezoelectric measurements. The use of

the tensile machine will let us a direct measurement of Young's modulus during the piezoelectric measurements, as well as direct control of the applied strain. This should greatly improve the precision of calculated piezoelectric coefficients and decrease the uncertainty due to analytic estimations made for strain and energy calculations on bending.

We have therefore decided to develop a method for in-situ measurement of voltage coefficients g_{31} as a function of tensile strain, performed under quasi-static and open-circuit conditions, independently from datasheet parameters, that would characterize PVDF as close as possible to the targeted operational conditions with high applied strains. For this, we have used a commercial tensile machine with custom fabricated clamps to strain PVDF, and directly studied for the first time the g_{31} coefficient under applied high strain.

The following sections will describe the working principle and the main results obtained with the proposed method. We will discuss the dependence of the g_{31} coefficient on the applied stress as well as the isotropy of piezoelectric properties when comparing g_{31} and g_{32} coefficients.

2.5.1 3-1 mode: tensile machine

Fixation design

A tensile machine from MTS was used to strain the films. It allowed loading speeds in the range of 0.1–10 mm/min, with a force sensor up to 125 N with around 0.001 N sensitivity. Such kind of machines are used for mechanical characterization of bulk materials (determination of Young's modulus, yield strength, etc). For thin films characterization there is an ISO standard[151] which suggests the geometrical parameters of the samples as well as their testing conditions. It is also necessary to pay special attention to the clamps which hold the sample in place during the measurements, as the thin films easily slip out of the clamps. Usually, pneumatic[152] or hydraulic[153] grips are recommended for use in these cases, but they are large and quite expensive. Therefore, we have decided to develop our own fixations, adapted for very thin films and allowing us to perform precise piezoelectric measurements.

For the design of our clamps we improved the original work of Thompson[154], who proposed to glue two small metal blocks directly onto the sample and then place them in the base of a specially shaped clamp with a small opening. The sample was thus firmly fixed in the clamps and no slipping was possible. The drawback of this approach was the amount of time required to carefully mount and glue each sample, and the parallel alignment of the metal end blocks which had to be very accurate to keep the film undistorted during stretching.

We have enhanced the design of Thompson, and made a fixation that would be easy to mount and that would naturally compensate for an imperfect alignment of the film in the clamps. Our clamp, as shown in figure 2.17, consists of three parts. Part 1 is a rectangular parallelepiped with an opening slit in the middle of one side where the PVDF film is inserted and glued with cyanoacrylate glue. Part 2 has a "C"-shape to which part 1 is connected by means of a cylindrical pin rod, which is part 3. Part 2 is then connected directly to the tensile machine by means of a screw. The design of the clamps allows for firm fixation of the thin PVDF samples with no slipping. The connection between parts 1 and 2 using a pin allows a free rotation of part 1, glued to the film, in part 2 around the axis perpendicular to the film surface. This allows for compensation of any eventual misalignment of the PVDF film inside the clamps. As a result, the tensile strength is applied homogeneously along the film cross-section and no shear forces appear, thus keeping the films undistorted during stretching. The drawback, however, is the amount of time required to

carefully mount, glue and connect the electrodes of each sample. Parts 1 and 2 were fabricated in a 3D printer from ABS plastic, and part 3 is a solid steel pin.

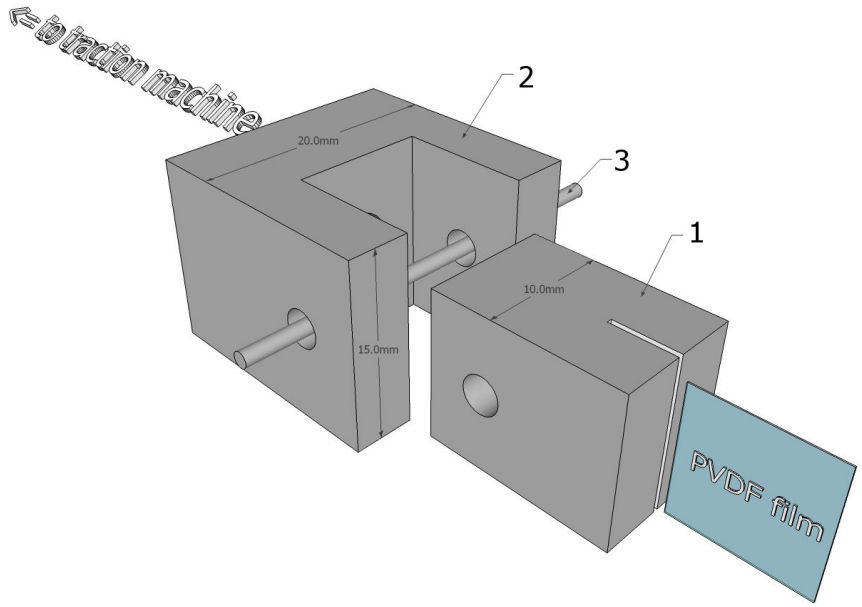

Figure 2.17: *Schematic drawing of the clamps used for PVDF thin film traction tests. The PVDF film is glued inside part 1, which is then fixed inside part 2 by means of a pin 3. Part 2 is directly screwed to a traction machine.*

The integrated force sensor in the tensile machine allows for direct calculation of the stress in the film. For a uniform force/stress distribution, the stress σ is given by the following equation[155]:

$$\sigma = \frac{F}{w \cdot t} \tag{2.20}$$

where σ is the stress [Pa], F is the force [N], w is the width [m] and t is the film thickness [m].

The film strain ϵ is calculated from the linear displacement sensor of the machine by:

$$\epsilon = \frac{\Delta l}{l} \tag{2.21}$$

where Δl is the linear displacement [m] and l is the film initial length [m].

A non-metalized PVDF sample mounted in clamps inside the tensile machine, and strained to plastic deformation is shown in figure 2.18.

Sample preparation

PVDF films from two suppliers were used: uni-axially oriented 110 μm thick films from Measurement Specialties having silver ink metallization, and bi-axially oriented 40 μm thick films from Piezotech with no metallization. The rectangular samples were cut manually from a large sheet of material using a cutter knife, in accordance with the ISO 527-3:1995 standard[151], which indicates sample geometry and testing conditions. Samples of rectangular shape with varying lengths from 20 to 40 mm and widths from 5 to 15 mm were prepared (see summary in table 2.6). They were then glued into the clamps with cyanoacrylate glue and were left to dry for at least 12 hours.

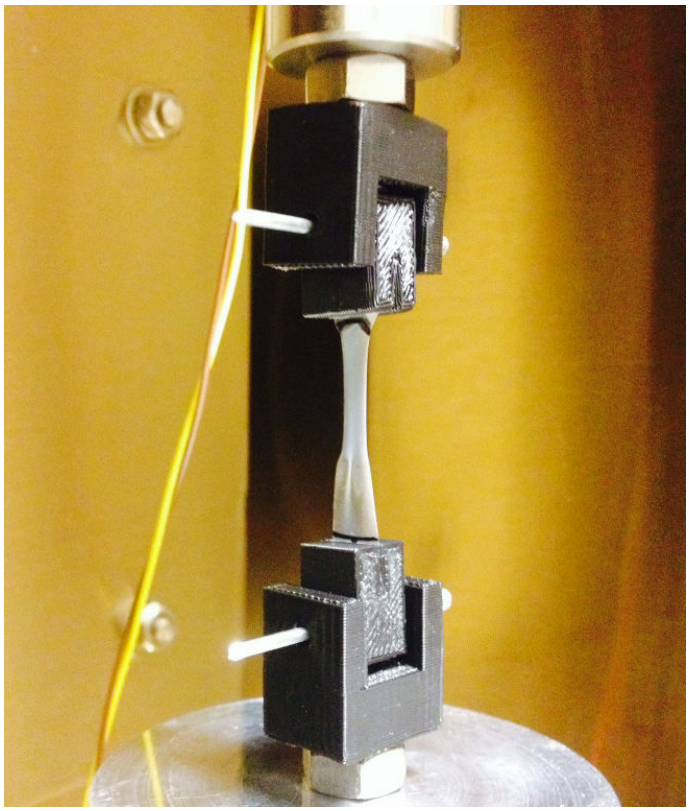

Figure 2.18: *PVDF sample mounted in clamps inside the tensile machine.*

To measure the generated voltage, a thin metal wire was glued with conductive epoxy to each surface of the sample, whether it is metallized or not. For not metallized samples, a thin layer of conductive silver grease (CircuitWorks CW7100) was applied. The use of conductive grease allowsto perform measurements up to 10% of strain without any degradation of the electrodes. Ready-to-measure samples in clamps with attached electrodes are shown in figure 2.19.

Measurement principle

The main idea for the measurement is quite simple: to apply a well-controlled and a well-measurable stress to the PVDF sample and to simultaneously obtain the generated open-circuit voltage. In practice it requires a good time synchronization between the applied stress/strain and the generated voltage capture, as well as a possibility to discharge the samples to bring the voltage back to zero level. For these reasons, the measurement procedure was automatized by a LabView script, which synchronized mechanical force and strain output of the tensile machine with voltage measurements and open/closed circuit states. Acquisition of force and strain data was done via a BNC port of the tensile machine by USB acquisition card (National Instruments USB-6009). The script collected and recalculated the data to obtain stress-strain and voltage-stress curves. Figure 2.20 shows the front panel of LabView during measurement.

The output voltage was measured by the contactless electrostatic voltmeter (Trek 370), directly connected to the sample. A mercury relay was used to switch the circuit onto a resistance load and to discharge the PVDF sample when necessary. The relay was closed and opened periodically, meaning that the observed voltage would repeatedly rise to a certain value and then drop to zero.

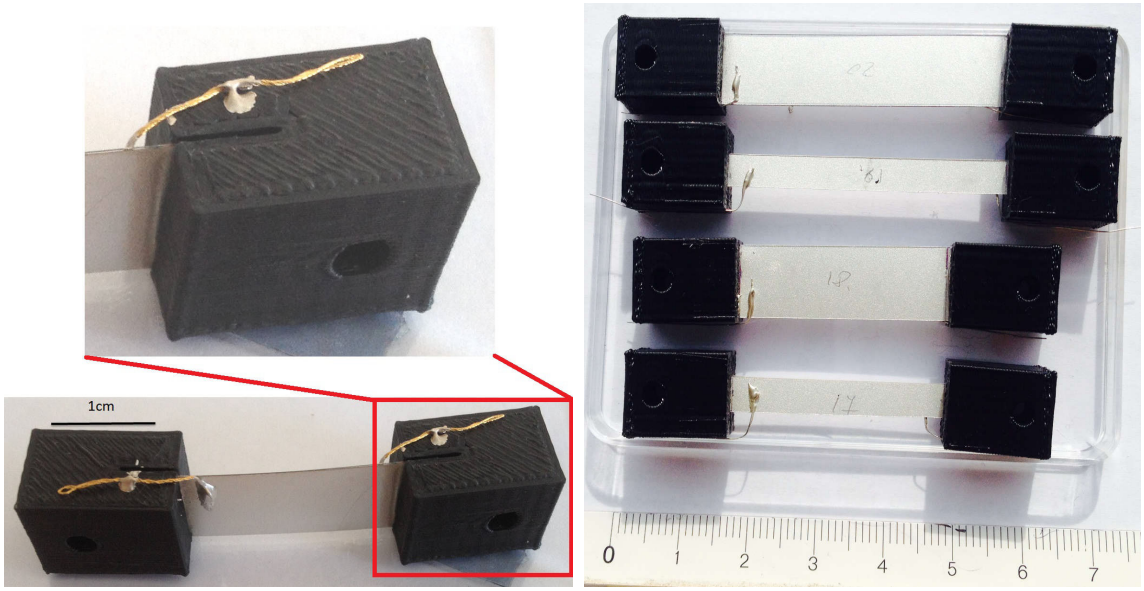

Figure 2.19: *Left: Metallized PVDF sample in clamps with attached electrodes ready for piezoelectric tensile measurements. Right: Different sample geometries.*

Table 2.6: *Geometrical sizes of prepared rectangular samples for the tensile experiment.*

Sample #	Length, mm	Width, mm	Ratio L:W
PVDF MeasSpec 110μm thickness, g_{31}=0.216 Vm/N			
M1.3	20	15	1.3
M2	20	10	2
M4	20	5	4
M6	30	5	6
M8	40	5	8
PVDF Piezotech 40μm thickness, g_{31}=0.056 Vm/N			
P1.3	20	15	1.3
P2	20	10	2
P3	30	10	3
P4	20	5	4
P6	30	5	6
P8	40	5	8

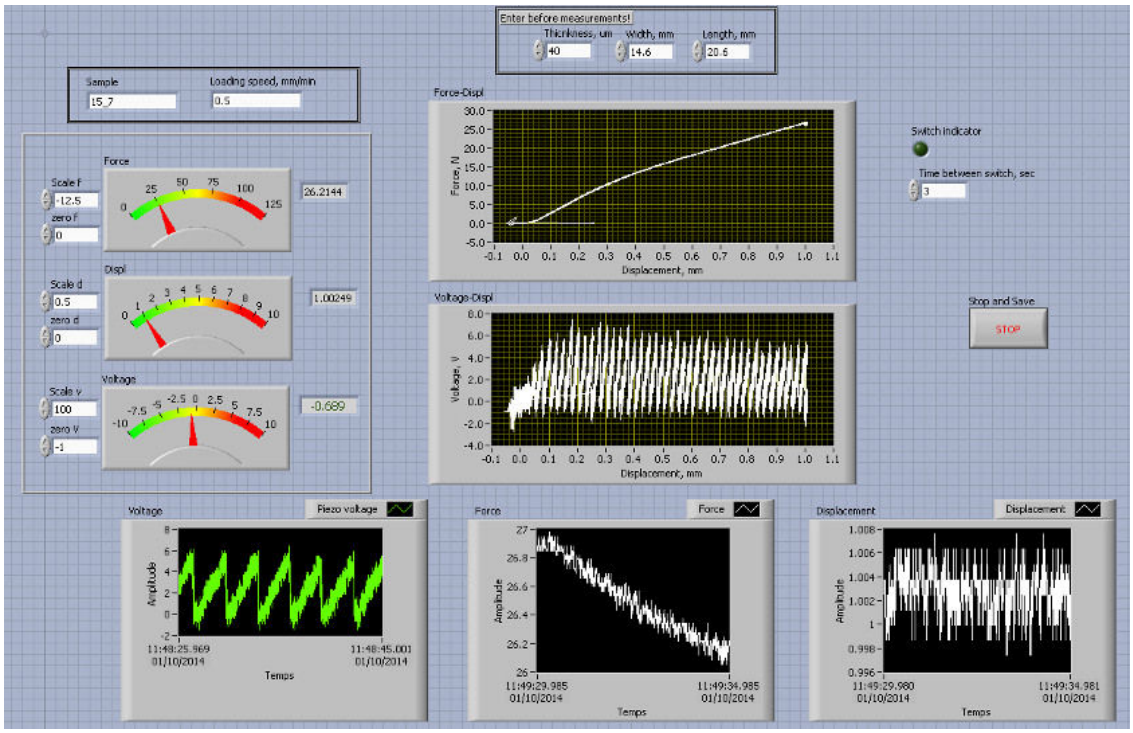

Figure 2.20: *LabView front panel during piezoelectric measurement.*

For most of the samples the switching period was set to 2 seconds, which was a compromise between piezoelectric voltage generation and voltage decay due to self-discharge [1].

The straining rate was kept constant during the measurement, and was set between 0.5 and 1.5 mm/min, depending on the sample length. Since some amorphous polymers are known to change their mechanical properties as a function of strain rate[156], we have measured PVDF Young's modulus with strain rates from 0.5 to 100 mm/min to verify if it is the case for PVDF (figure 2.21). We have not observed any variations of Young's modulus in the measured range, and can assume that for our experimental conditions the strain rate does not affect the PVDF mechanical properties.

A Matlab script was made to perform the calculations of voltage-stress slope each time the relay was in open state. The g_{31} was then calculated by equation (2.22) and plotted as a function of stress.

$$|g_{31}| = \frac{E}{T} = \frac{V_{31}}{t \cdot T} \tag{2.22}$$

where E-electric field, T-stress, V-voltage, t-PVDF thickness.

The measurements were performed at room temperature of 23°C and relative humidity of $\approx 46\%$. The thickness of samples was measured prior to voltage measurements and was assumed constant during stretching, as its variations due to Poisson ratio would be less than 2% in the measurement range.

Strictly speaking, in order to compare with literature values, the g_{ij} coefficient should only be calculated in the linear elastic region of the stress-strain curve. However, since our objective

[1] The voltage decay due to self-discharge phenomena will be discussed in details in Section 2.6

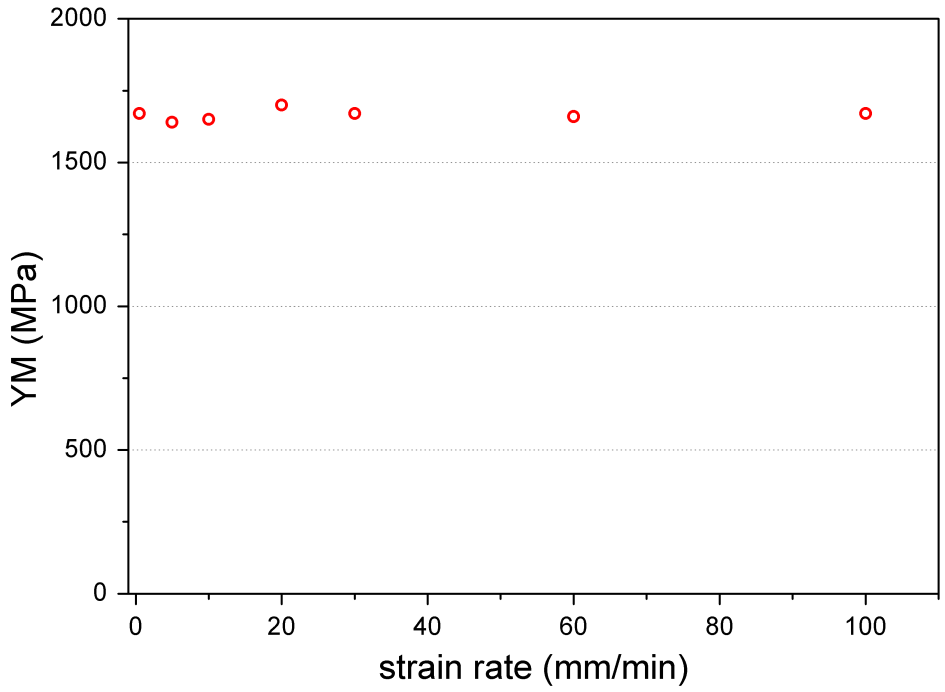

Figure 2.21: *Young's modulus as function of strain rate for 40µm PVDF Piezotech sample P2.*

here is to study PVDF behavior at high strain, we have explored values of strain which go beyond the linear elastic region. We will nonetheless still refer to the "g coefficient" as a coefficient of proportionality between the applied stress and the induced electric field, even beyond the elastic limit of the material.

2.5.2 Nonlinearities of piezoelectric coefficient

Typical measured voltage as a function of stress is shown in figure 2.22. The stress is increased continuously and so the voltage also rises continuously, which corresponds to the open relay state, shown in blue in the graph. Every 2 seconds approximately, the relay is closed for a short period of time shown red in the graph, during which the voltage drops to zero and stays around zero until the relay is opened again.

Results presented in figures 2.23 to 2.29 show both calculated g_{31} coefficient values as a function of applied stress on the left vertical axis, and the induced strain on the right vertical axis. In the following paragraphs we will compare samples of different geometries, from different suppliers and on different crystallographic orientations.

The results for Piezotech sample P6 are shown in figure 2.23. The value given by the supplier (g_{31}=0.056 Vm/N) is encircled on the left vertical axis and the confidence interval ($\pm$20%) is shaded. The calculated g_{31} values at low stress and strain are about 0.04 Vm/N which is below the datasheet value and out of the indicated confidence interval. With increasing stress, g_{31} increases until it reaches a maximum of 0.065 Vm/N and then gradually decreases to zero. Remarkably, the maximum value of g_{31} is situated in the middle of the elastic region, and the decrease corresponds to the change in the stress-strain slope, representing the beginning of the transition between elastic and plastic regions, in this case at 25-30 MPa and 1-1.5% strain. Within the strain

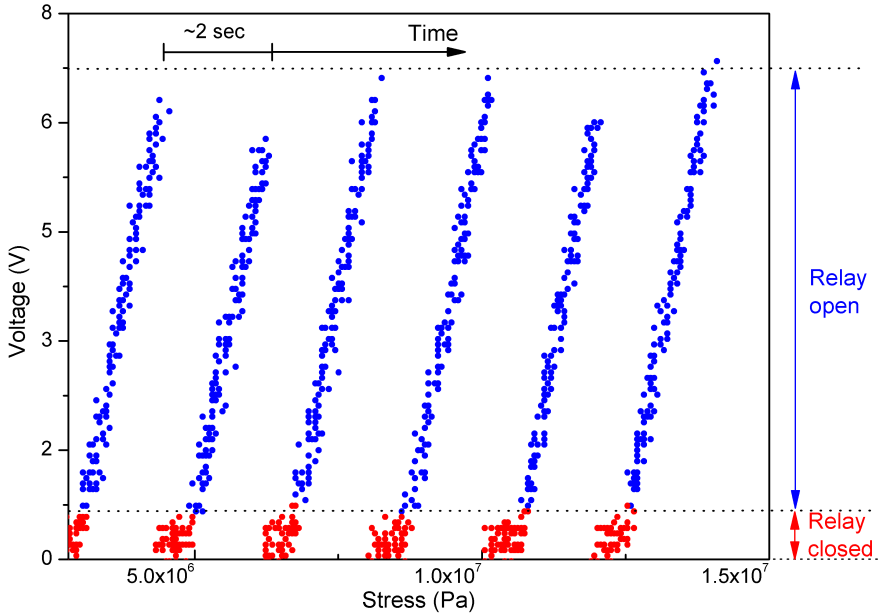

Figure 2.22: *Typical voltage measurement as a function of applied stress. The voltage drops to zero every time the realy closes, and stays nearly zero until the relay is opened.*

interval between 0.5 and 2% strain, the g_{31} values stay inside the datasheet confidence interval of 0.056 Vm/N $\pm$20%.

Figure 2.24 shows g_{31} coefficient vs. stress for three Piezotech samples P4, P6 and P8. Independently of the geometrical parameters, the main trend is visible for all the samples: at low stress and strain g_{31} is somewhat lower than the datasheet value, but it increases with stress until it reaches its maximum value of around 0.065 Vm/N and then gradually decreases. All three samples reach their maximum g_{31} value at around 25 MPa and 1.5% strain, which corresponds to the middle of the elastic deformation zone. The maximum is followed by a short plateau where the g_{31} value stays constant. The length of the plateau is visually independent on the sample L:W ratio. Once in the plastic region, the behavior of g_{31} coefficient is clearly impacted by the sample's geometrical parameters: the lower the L:W ratio, the slower the g_{31} coefficient decreases with stress. The stress-strain curves are also slightly different for samples of different geometries, however no significant change in the Young's modulus and the elastic limit value is observed.

The measured coefficient values are situated inside the confidence interval from strain of 0.5% to around 2%. At lower strains however, once more the measured values are lower than expected, which indicates that for practical applications it would be advisable to pre-strain the PVDF material to effectively exhibit its expected piezoelectric performance.

If we now compare the Piezotech samples with much lower L:W ratios, down to 1.3 (shown in figure 2.25) we can distinctly see the influence of the geometry on the g_{31} coefficient apparent values and behavior. Since wider samples with low L:W ratios (thus closer to a square than to a rectangle) no longer respect the geometry requirements in tensile experiments[151] for homogeneous stress distribution, some parts of the strained sample might experience higher stress than others, and equation (2.22) will lead to false and overestimated g_{31} values. Samples with low L:W ratios show g_{31} values starting from 0.06 Vm/N and going up to 0.14 Vm/N. Their stress-strain curves are significantly higher, meaning that for the same applied strain they undergo much lower

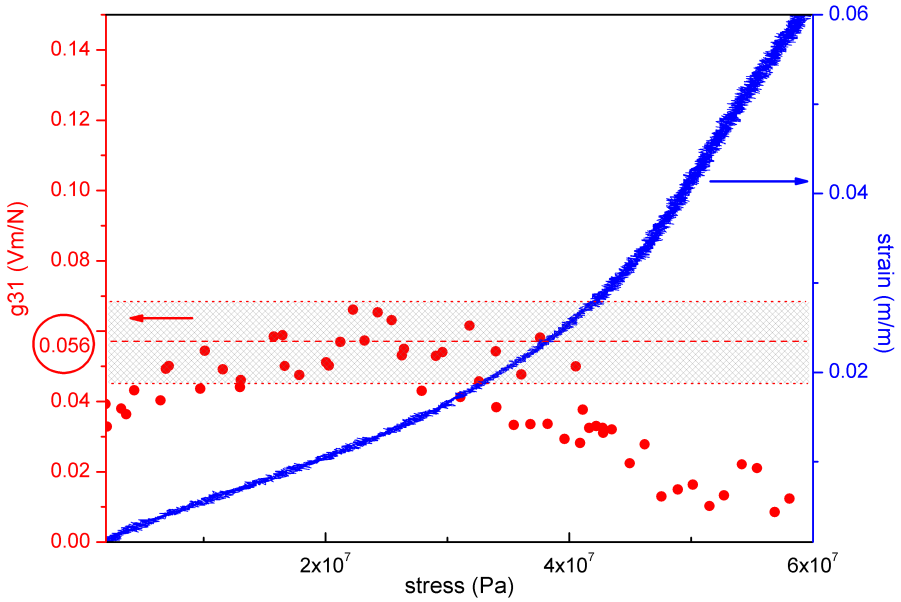

Figure 2.23: *Piezoelectric g_{31} voltage coefficient and strain as a function of applied stress for the Piezotech sample P6. The supplier datasheet value for g_{31} is 0.056±20% Vm/N. The confidence interval is shown by dotted lines.*

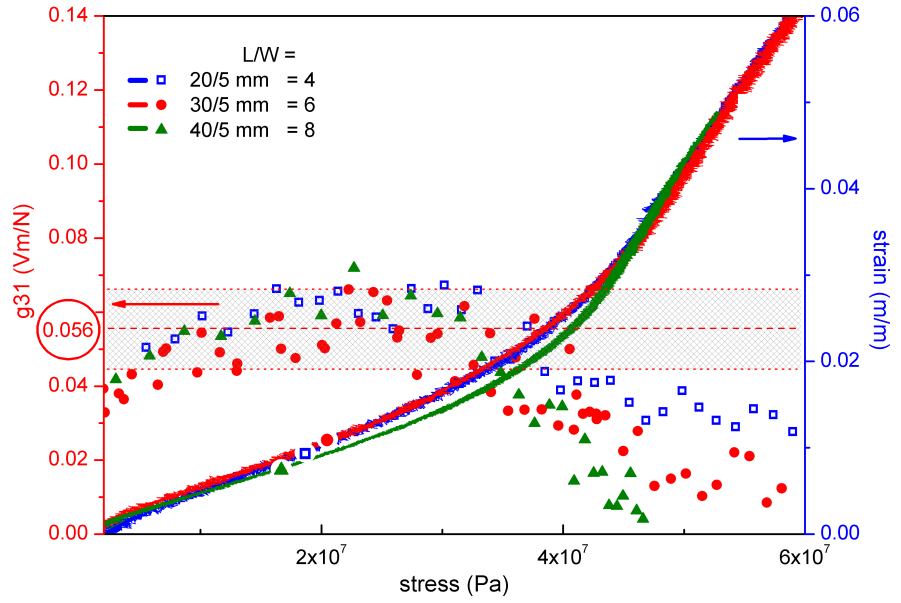

Figure 2.24: *Piezoelectric g_{31} voltage coefficient and strain as a function of applied stress for Piezotech samples P4, P6 and P8. Datasheet value of g_{31} is 0.056±20% Vm/N. The confidence interval is shown by dotted lines.*

stress than previous samples. At low L:W ratios, the Young's modulus decreases, and the transition between the elastic and plastic zones is much less noticeable.

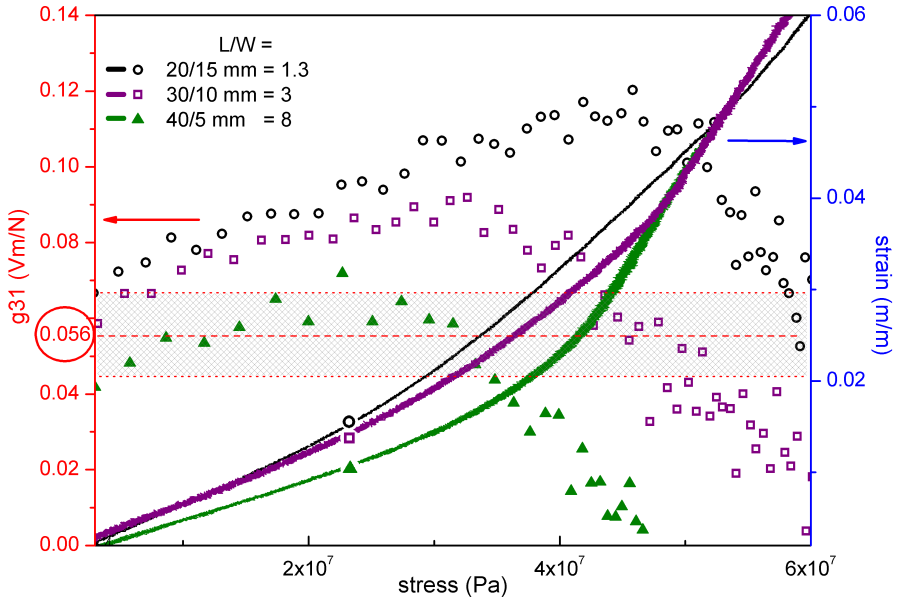

Figure 2.25: *Piezoelectric g_{31} coefficients as a function of applied stress for Piezotech samples P1.3, P3 and P8. Datasheet value of g_{31} is 0.056±20% Vm/N. The confidence interval is shown by dotted lines.*

In contrast, the 110 μm MeasSpec PVDF has an altogether different behavior (figure 2.26) with a more pronounced increase of the g_{31} value with stress. g_{31} increases with increasing stress and once again reaches its maximum around the beginning of transition between elastic and plastic regions at 60 MPa and 3% strain. The influence of the sample geometry is less visible than on the Piezotech samples: wide and narrow samples have similar g_{31} values and similar stress dependence. The maximum g_{31} values of samples M8 and M6 are near the datasheet value. The wide sample M1.3 has higher g_{31} values for the same reasons as proposed before, namely for non-homogeneous stress distribution. Since the confidence interval for g_{31} is not provided by the supplier, we cannot affirm until what stress the measured values are reasonable.

In contrast with the Piezotech samples, the g_{31} values at low stress for MeasSpec samples are significantly lower than the datasheet value and they stay low until relatively high strain is applied. In other words, to reach the declared datasheet value of the piezoelectric coefficient, the sample has to be pre-strained to about 3%, which approaches the limit of the linear elastic region.

Table 2.7 summarizes the measured g_{31} coefficients and Young's moduli for different samples, and figure 2.27 graphically illustrates it. As a general trend, long and narrow samples with higher L:W ratio are closer to the datasheet values than the shorter and wider samples. If we consider the g_{31} coefficients, MeasSpec samples with geometries of L:W of 2 and higher have more or less similar values, which are close to the datasheet. Piezotech samples need to have L:W of 4 and higher to be in the datasheet confidence interval. Considering the Young's modulus, Piezotech samples from L:W of 3 and higher, but only one measured MeasSpec sample with L:W of 8 does fall into the confidence interval. These results shows the importance of an appropriate choice of sample geometry for the testing procedures as well as for the future prototype fabrication, to ensure that the working hypotheses, in this case homogeneous stress distribution in the samples, are valid.

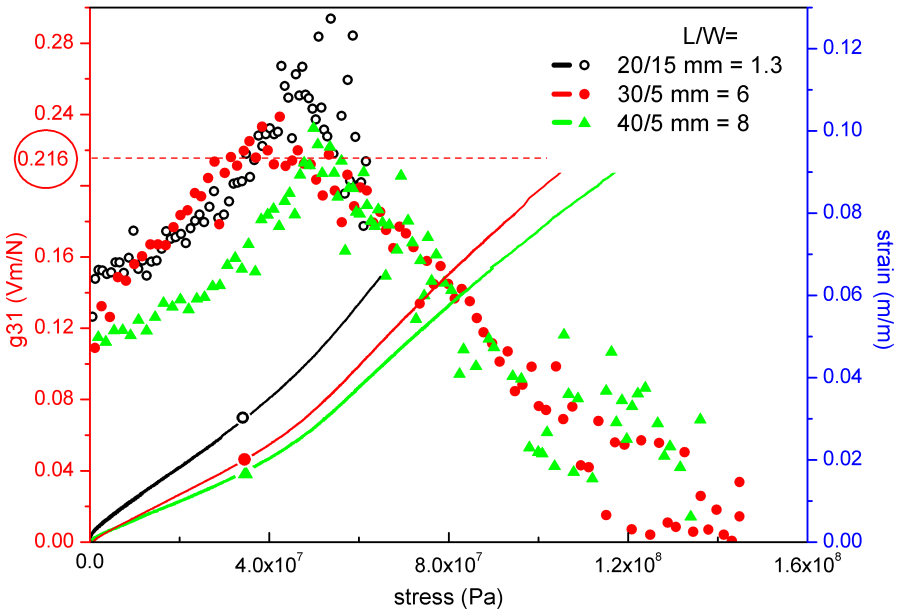

Figure 2.26: *Piezoelectric g_{31} as a function of applied stress for MeasSpec samples M1.3, M6 and M8. Datasheet value of g_{31} is 0.216 Vm/N.*

Table 2.7: *Experimentally measured g_{31} piezoelectric coefficients and Young's moduli for samples with different Length:Width ratios. Supplier datasheet values are shown for reference.*

Size, mm	Ratio L:W	Max g_{31}, Vm/N	YM, MPa
PVDF MeasSpec 110μm			
20×15	1.3	0.29	1300
20×10	2	0.24	1600
20×5	4	0.24	1900
30×5	6	0.24	1900
40×5	8	0.23	2100
	datasheet[13]	0.216	3000±30%
PVDF Piezotech 40μm			
20×15	1.3	0.12	1800
20×10	2	0.1	1650
30×10	3	0.09	2200
20× 5	4	0.067	2300
30×5	6	0.065	2150
40×5	8	0.07	2400
	datasheet[80]	0.056±20%	2500±20%

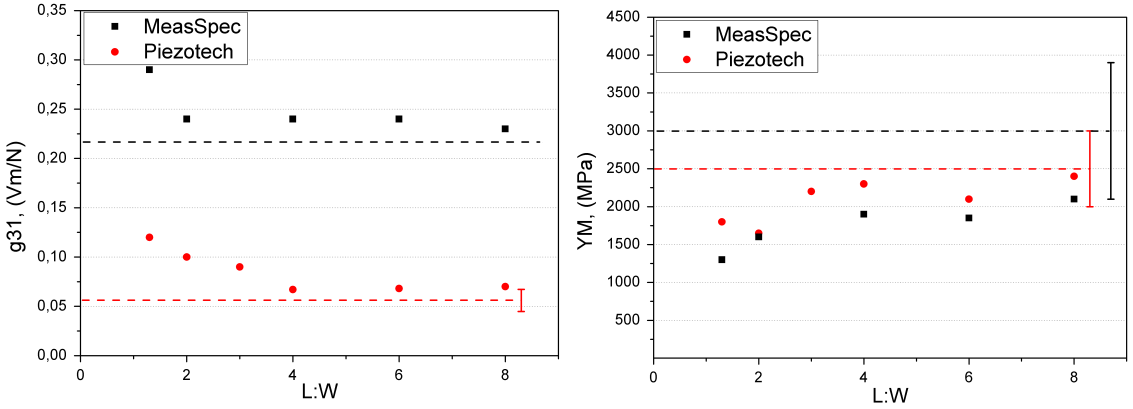

Figure 2.27: *Experimentally measured g_{31} piezoelectric coefficients and Young's moduli for samples with different L:W ratios. Datasheet values and confidence intervals are shown dotted lines and error bars.*

The presented experimental results of in-situ direct measurements of the piezoelectric g_{31} voltage coefficient of PVDF commercial films indicate for the first time a strong dependence of the apparent g_{31} coefficient on the applied strain and sample geometry. Bi-axially oriented PVDF showed a maximum value of g_{31} coefficient in the middle of the elastic region of the material. Uni-axially oriented PVDF showed a maximum g_{31} value near the transition from elastic to plastic deformation regions. The length:width ratio of the rectangular samples influenced significantly the measured g_{31} voltage coefficient, which was apparently higher for the wider and shorter samples (smaller L:W ratio). The importance of an appropriate choice of material geometry for direct piezoelectric measurements is also demonstrated.

The obtained results indicate that the datasheet values of the piezoelectric voltage coefficients, provided by the material manufacturers, might be overestimated at low stress. This may be connected to the difference between the measurement methods used here and by the manufacturers. When strained, the g_{31} is increased, suggesting pre-strain is an important parameter for applications. Both commercial grades of PVDF from Piezotech and MeasSpec had to be strained from 0.5 up to 3% in order to observe the announced data-sheet values.

Without additional micro-structural studies it is difficult to argue on the origins of the observed phenomena of the decreased g_{31} in the plastic region. Reorientation of the β-phase chains from perpendicular to parallel to the stress orientation within the plastic region and a decrease in the degree of crystallinity [136,137] may contribute to the overall decrease of the piezoelectric properties. Also non-linearities of the elastic modulus during stretching may lead to non-linearities of the piezoelectric coefficients [135]. This is however an important experimental result, since highlights the benefits of pre-straining the PVDF to obtain higher voltage output. Since in our composites the strain delivered by the SMA is expected to be in order of 2%, this creates an almost ideal working condition to maximize the PVDF output.

Anisotropy study

As we have already discussed earlier, the PVDF material is known for its anisotropic piezoelectric properties [11,12,64,79]. The piezoelectric performance along direction 2 of uni-axially oriented films is lower than along direction 1, which comes from the anisotropic semicrystalline structure

of PVDF. This is attributed to processes occurring in the crystalline regions and in their interfaces with the amorphous surrounding[11]. In bi-axially oriented films the anisotropic effects are eliminated[64,80].

To study the directional anisotropy of the piezoelectric effect, additional samples were cut from the same PVDF sheets in two perpendicular directions. This allows extracting the g_{32} coefficient in addition to previously measured g_{31}. Figures 2.28 and 2.29 show g_{31} and g_{32} coefficients as a function of stress for Piezotech and MeasSpec samples respectively.

The Piezotech samples are bi-axially stretched by the manufacturer, which is specifically mentioned in the datasheet[80], meaning that the intrinsic anisotropy should be less pronounced or not visible at all. Indeed, the performed measurements present no anisotropy, with the g_{31} and the g_{32} coefficient being practically identical along the full measurement range.

Meanwhile, MeasSpec does not give information about sample fabrication conditions. We therefore assume that they have been stretched only uni-axially and that anisotropy should occur. Indeed, the results show a high level of anisotropy in these samples, with g_{32} being up to 10 times lower than g_{31}. The behavior of g_{32} is completely different, since it does not have a maximum value, but instead decreases to zero quickly with stress, and then even changes it sign. This behavior can be explained by mechanically induced reversible depolarization[11]. Zero and negative g_{32} values will be obtained as soon as overall polarization is reduced with increased mechanical stress. Two different mechanisms can account for this phenomena:

- overall sample size effect due to changes in mechanical properties,
- intrinsic effect related to changes in dipole orientation.

The anisotropy characteristic of the material is closely connected with its g_{31} geometry sensitivity. When stretched in one direction, the material is compressed in perpendicular directions due to Poisson effect. For a piezoelectric material this means that the observed g_{31} coefficient is always a sum of g_{31}, g_{32} and g_{33} coefficients. The MeasSpec PVDF has much lower g_{32}, which makes it less sensitive to geometry form-factor of samples. In contrast, the Piezotech PVDF has equivalent values of g_{31} and g_{32}, which makes it highly sensitive to sample geometry.

To summarize, the bi-axially oriented PVDF from Piezotech has shown fully isotropic behavior, with g_{31} and g_{32} being identical in the measurement range. The uni-axially oriented PVDF from MeasSpec has shown strong piezoelectric anisotropy, with g_{32} at low strain being 5 times lower than the measured g_{31}, and 10 times lower than the datasheet g_{31} value.

2.6 Self discharge study

The equivalent circuit of a PVDF film comprises a voltage source in series with a capacitance. Dielectric imperfections in PVDF would lead to the appearance of a leakage current, which depends on the input voltage according to Ohm's Law[157]. The presence of leakage currents leads to phenomena of self-discharge, meaning that the PVDF generated piezo- or pyro-electric charges will partly dissipate before they are harvested. This will have an impact on the final harvested energy, especially for our targeted operational conditions, where the PVDF is kept in open-circuit conditions and the charges are harvested at once, some time after they are generated.

For typical PVDF leakage current measurements, the samples are subjected to a DC bias voltage and the steady-state current through the PVDF is measured with a multimeter[157–159]. The results are thus presented in terms of picoAmperes (pA). In our case, and given our operational

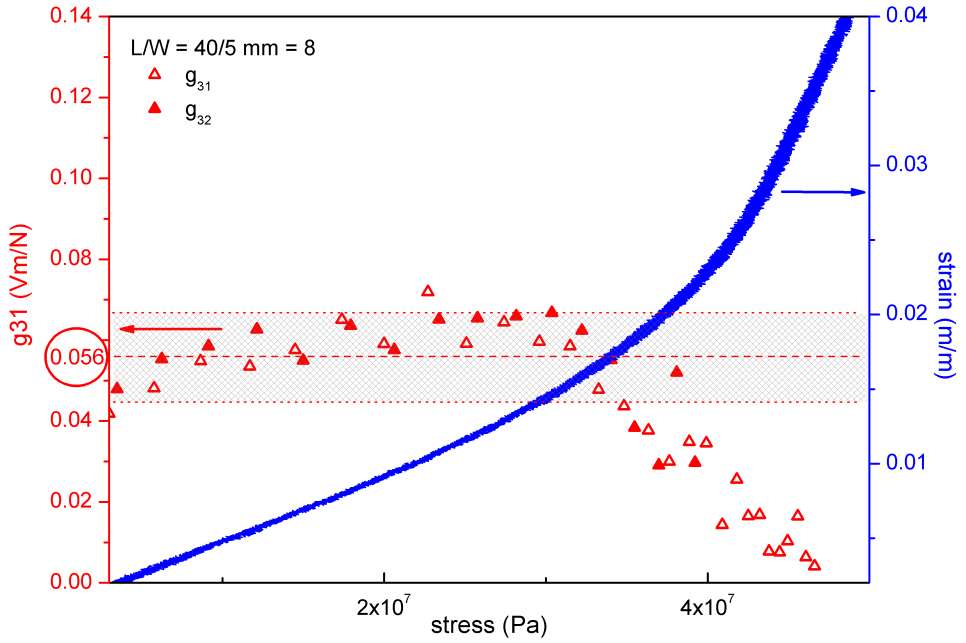

Figure 2.28: *Anisotropy study of Piezotech samples. Comparison of g_{31} and g_{32} vs. applied stress. Datasheet value of g_{31} is 0.056 Vm/N.*

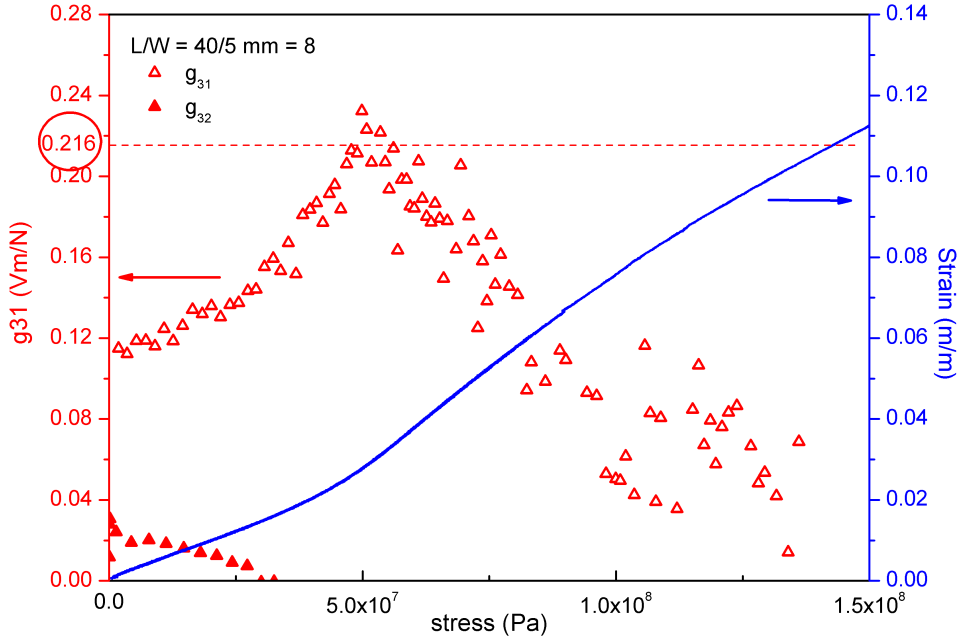

Figure 2.29: *Anisotropy study of MeasSpec samples. Comparison of g_{31} and g_{32} vs. applied stress. Datasheet value of g_{31} is 0.216 Vm/N.*

conditions, a more relevant way of characterizing losses due to leakage current would give a "feel" of how long the material can keep its charges. This is the reason why we have decided to study PVDF self-discharge phenomena by means of voltage decay over time. The samples were charged to high voltages with a power source and the variations were then observed with a contactless voltmeter. The samples were isolated and kept in open-circuit condition during measurements, therefore any discharge must be connected to leakages inside the material. Samples were tested under different voltage, temperatures, strains and vacuum conditions. Time of half-discharge (i.e. time lapse until voltage drops to half of the initial value) and time constant (i.e. time lapse until voltage drops to $1 - 1/e \approx 63.2\%$ of the initial value) were extracted from the self-discharge curves. The results of PVDF are compared with a bulk ceramic PZT material and a flexible PZT-fiber-based MFC composite[160]. The measurements (except temperature study) were performed at a room temperature of $\approx 23°C$ and relative humidity of $\approx 50\%$.

2.6.1 Effect of voltage

First, the effect of voltage is presented. Figure 2.30 shows measurements of time of half-discharge and time constant as a function of both voltage magnitude and corresponding electric field for PVDF, bulk PZT and MFC. The thicknesses of materials were 28 μm, 200 μm and 430 μm respectively.

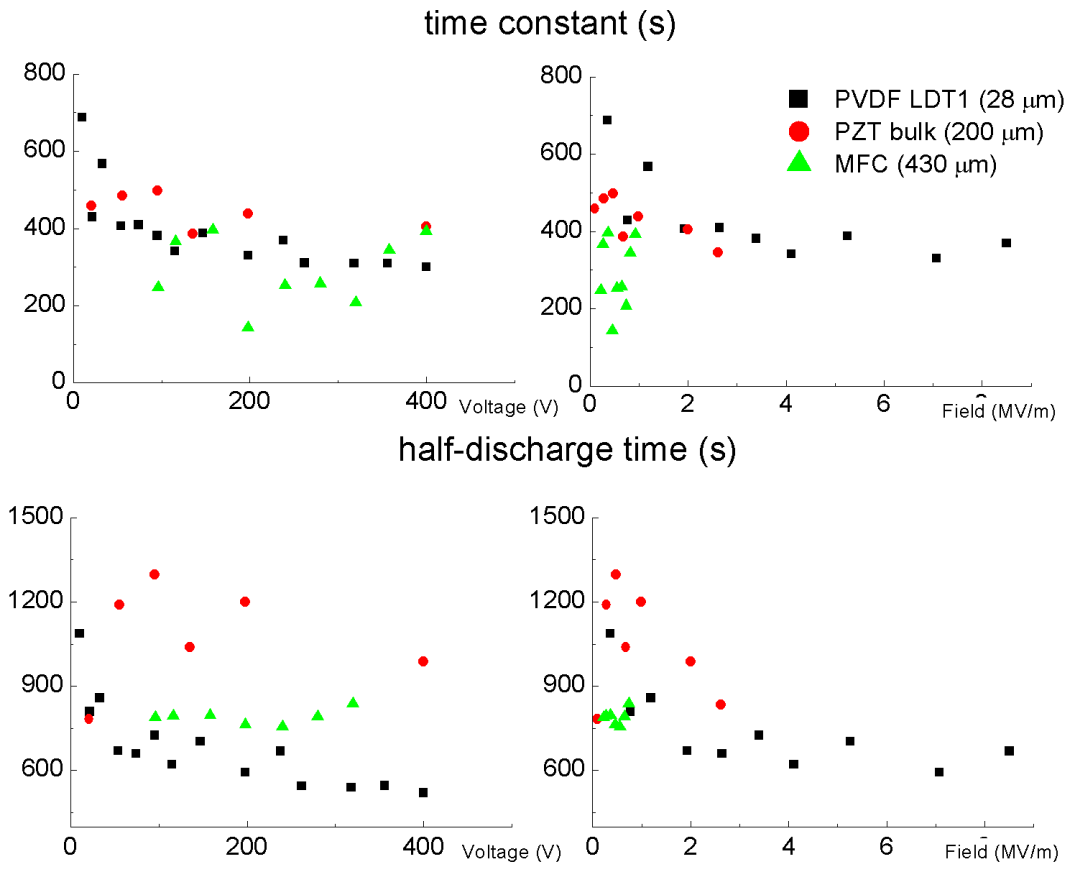

Figure 2.30: *Self-discharge characteristics: time constant and half-discharge time as a function of applied voltage for PVDF, PZT and MFC materials. Thicknesses of materials are 28 μm, 200 μm and 430 μm respectively.*

PVDF and bulk PZT show similar behaviors, with consistent decrease of discharge times, meaning faster discharge, with increased voltage/field magnitude. Based on the time constant values, PVDF is more stable than PZT at low field values. The half-discharge time is higher for bulk PZT, which means that when comparing the two materials, PVDF is more stable at the beginning of the discharge but discharges faster afterwards. This will be important information for the further power management circuit design, as the acquisition of voltage will take place only a given time after the generation, and more charges available at that moment will translate to higher energy harvested in the end.

At higher field values, PVDF seems to have slightly more leakage than bulk PZT. This is an important issue since, as we will see further our composite will generate up to 400 V. In practice this issue can be solved by increasing the thickness of PVDF, thus proportionally reducing the field.

For the case of MFC, tested voltage values correspond to rather low fields of <1 MV/m. No clear trends can be deduced from the discharge curves for this material under these experimental conditions: higher voltage values are therefore necessary to correctly compare MFC with the other materials.

Figure 2.31 shows half-discharge times as a function of voltage and corresponding fields for different PVDF grades.

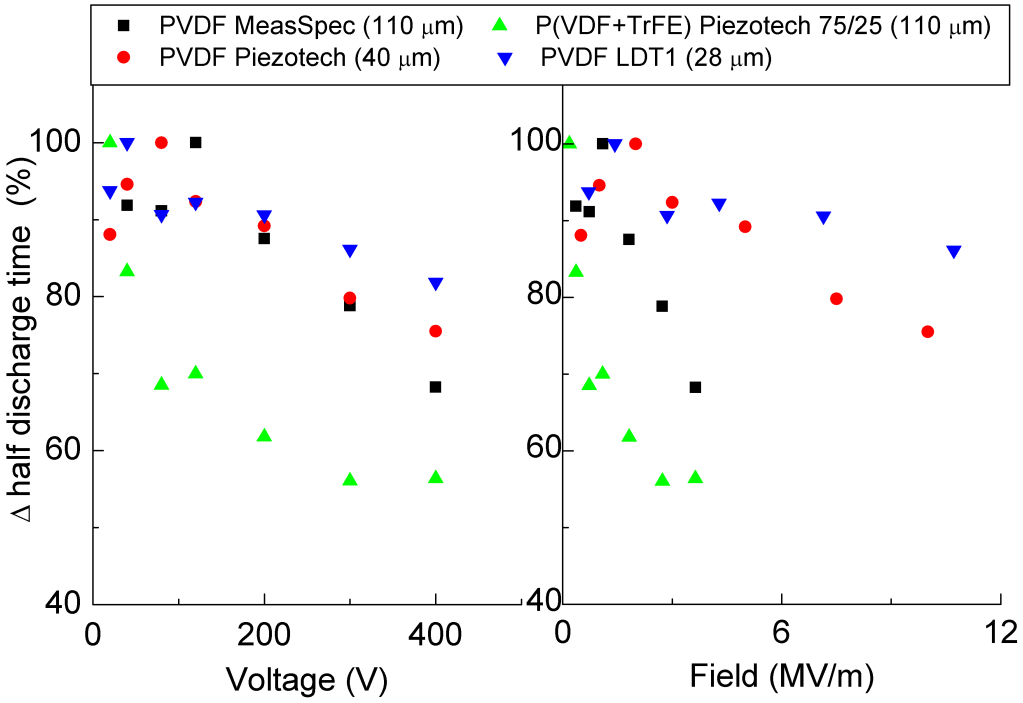

Figure 2.31: *Self-discharge characteristics: normalized half-discharge time as a function of applied voltage (left) and field (right) for different PVDF grades.*

In this case, the half-discharge time of each sample has been normalized with respect to its highest value. We can observe that at lower fields (<1 MV/m) there is no significant difference between samples, but at higher fields samples behave quite differently. The discharge time for P(VDF+TrFE) sample decreases fast with increasing field, making it the least stable of all the tested samples. The LDT1 sample seems to be the most stable, with the highest discharge time

and the smallest variation with applied field. It is not straightforward what parameters affect the self-discharge time and why is it different for different PVDF samples. Many factors may be involved, including the thickness of the material, metallization, form factor, packaging, etc. For example, the LDT1 sample is laminated with a thin protective coating, which may well account for its higher stability.

2.6.2 Effect of temperature

To study the effect of temperature on self-discharge, samples were placed in a furnace at a given temperature, stabilized for 5 minutes, and then discharged to remove the generated pyroelectric charges. Samples were then charged with a 100 V potential and the self-discharge was observed with a contactless voltmeter. The effect of temperature on the half-discharge time is shown on the left side of figure 2.32. We can observe that temperature has a significant impact on the discharge behavior of PVDF: all the tested grades demonstrate an exponential decay of half-discharge time with increased temperature. At 60°C the samples self-discharge 10 times faster than at room temperature. According to manufacturers, after 90°C the polarization of PVDF is no longer thermodynamically stable[13,80].

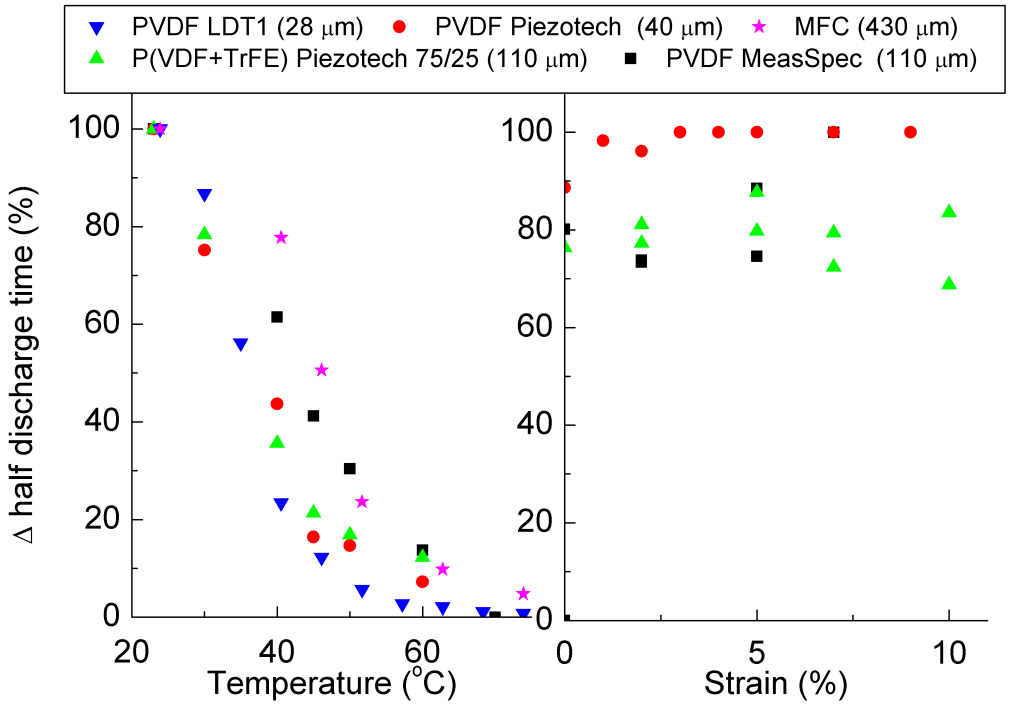

Figure 2.32: *Self-discharge characteristics: normalized half-discharge time as a function of temperature (left) and applied strain (right) for different PVDF grades. Comparison with MFC is shown only for temperature graph.*

The MFC sample has shown similar behavior, increasing strongly its self-discharge with temperature. In average, however, it is slightly more stable than the PVDF samples.

In practice, this means that energy harvester performance will be greatly affected by the increased temperature. With higher temperatures, generated charges will need to be harvested faster than they can disappear due to self-discharge.

2.6.3 Effect of strain

The effect of applied strain on the half-discharge time is shown on the right side of figure 2.32. Samples were strained with the tensile machine, then discharged to remove the piezoelectric charges, then charged with a 100 V potential. The obtained results indicate that there are no significant variations of the discharge time when pre-straining the material, up to 10% strain.

2.6.4 Other effects

Additional measurements were performed under vacuum conditions ($\approx 10^{-5}$ bar) to examine if the humidity level impacts the measurements. No difference in the discharge time was observed for all tested PVDF samples, therefore we conclude that the humidity level is not critical for self-discharge phenomena of PVDF. This is an important benefit compared to ceramic piezoelectrics such as PZT, which is very sensitive to humidity[161] and can degrade quite quickly in humid environments. Therefore PVDF would need less packaging for working in real life conditions.

2.7 Temperature dependence of piezoelectric coefficients

Since, in most cases, the harvesting of thermal energy necessarily implies the heating of PVDF, it is important to see how the piezoelectric properties are affected by temperature. Previous works show that the d_{31} coefficient is gradually increased with temperature in the range of -70 to +70°C[13,154,162] whereas the d_{33} coefficient has a slight decrease[162]. Taking into account the nonlinear behavior of the PVDF dielectric constant, the g_{31} was reported to increase with temperature as well[13]. This results are in agreement with the increase of the β-phase content with temperature, as discussed earlier. Some authors, however, report no change in the g_{31} behavior up to 80°C[163]. We have therefore decided to measure on our own the evolution of the g_{31} coefficient with temperature.

Figure 2.33 shows the measured output voltage for LDT-0 and Piezotech 40 μm samples in the temperature range of 20 to 80°C. The corresponding g_{31} values are shown in figure 2.34. The measurements were performed by the four-point bending method inside a furnace, the open-circuit voltage was acquired with an oscilloscope and a switch.

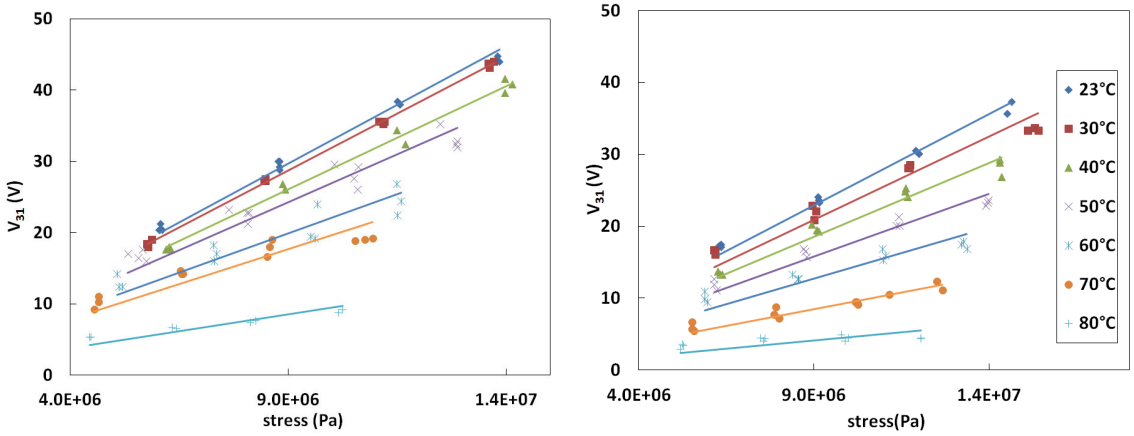

Figure 2.33: *Open-circuit generated voltage in 3-1 mode vs stress for different temperatures for LDT-0 (left) and Piezotech 40 μm (right) samples.*

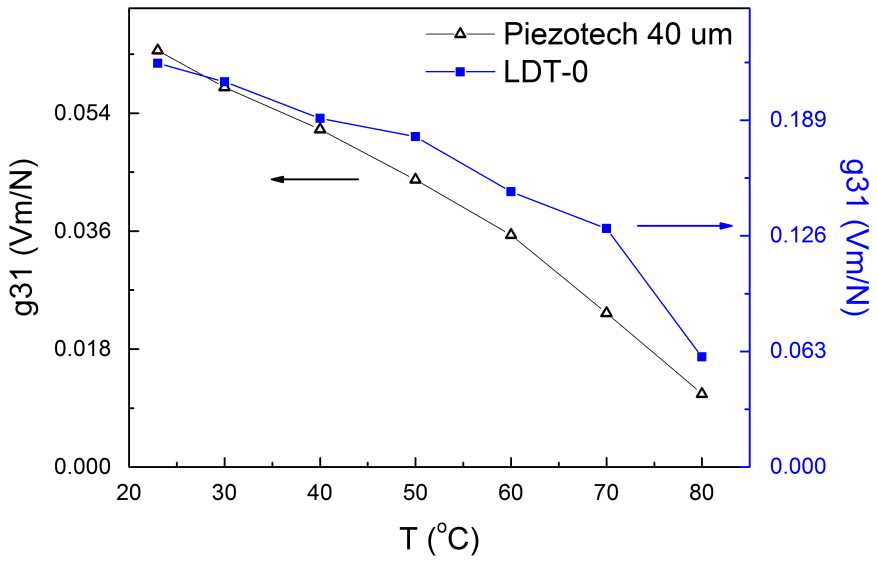

Figure 2.34: *Temperature dependence of g_{31} for LDT-0 and Piezotech 40 μm samples.*

From the graphs we can observe that for a given applied stress, PVDF generates less voltage with increased temperature, which leads to a decreased g_{31}. This is however in contradiction with literature results. Since the calculation of stress during four-point bending does not take into account material Young's modulus (see equation (2.18)), the temperature variation of the latter cannot explain these results. However, the decreased Young's modulus of the substrate may lower the stress/strain transferred to the sample and hence the generated voltage. One of the other possible explanations for the obtained results is the self-discharge, which as we have just seen increases proportionally with temperature. This would lead to a continuous charge leakage and voltage decrease during voltage generation and before acquisition. Since the stress is applied quite slowly with the four-point bending machine, the total loss of charges might be rather significant. Additional measurements are necessary to obtain further explanations of the observed phenomena, however we can preliminary conclude that increased temperature may inhibit the observed piezoelectric output.

2.8 Conclusions

In this chapter we have proposed and studied several measurement methods which enable us to obtain reproducible measurements of PVDF polymer film piezoelectric coefficients in quasi-static and real open-circuit conditions. The benefits of the proposed methods are:

- Stress was applied with high precision (except for the press method) and the piezoelectric voltage was measured with open-circuit conditions using a mechanical switch;
- Technique allows exploring direct piezoelectric effect in quasi-static conditions, without sophisticated measurement circuits;
- Technique is advantageous for piezoelectric measurements of polymers since higher voltage values can be observed in comparison with conventional closed-circuit measurements;
- Non-contact electrostatic voltmeter allows for the measurement with virtually no leakage into the circuit;
- Actual produced electric energy per elementary act of strain can be directly calculated by integration of the discharge curves into an external resistance;
- Neasured voltage and energy values are independent of the strain application rate, and depend only on the final strain value;

In terms of measurement accuracy, the main limit of the proposed method is set mostly by the measurement equipment. For instance, the TREK 370 voltmeter is capable of measuring in 0-3 kV range with 1 V resolution: outside of those limits high measurement errors will appear.

The proposed methods are particularly suitable for generator or harvester applications working with slow natural gradients, and we will use them to characterize our energy harvester composites.

The study of PVDF under external factors allowed us to estimate its behavior in a composite system coupled to an SMA. For the envisaged working conditions of 50-60°C with 1-3% strain we can summarize that:

- Piezoelectric output i.e. g_{31} coefficient is increased with applied strain, especially for uni-axially oriented PVDF. When the material is deformed beyond its plastic region, the piezoelectric output is decreased. For bi-axially oriented Piezotech PVDF the g_{31} increased from 0.04 Vm/N to 0.065 Vm/N with 1% strain and then gradually decreased. For uni-axially MeasSpec PVDF the g_{31} increased from 0.12 Vm/N to 0.28 Vm/N with 3% strain and then decreased;
- Self-discharge time constant in PVDF is higher than that in MFC and bulk PZT, suggesting slower discharge. Among PVDF samples, encapsulated LDT1 seems to be the most stable, with the highest discharge time and the smallest variations with applied field;
- Self-discharge phenomenon is much higher at higher temperatures: at 60°C PVDF self-discharge 10 times faster than at room temperature. Ceramic MFC has similar behavior, but is slightly more stable than the PVDF samples. In practice the generated charges need to be harvested fast enough to minimize losses;

- Self-discharge is not affected by the applied strain, at least at the operational range of our applications;
- Humidity seem not to affect the self-discharge, as opposed to ceramic piezoelectrics which are highly sensitive to it;
- Literature data suggests that g_{31} is increased with temperature. Our measurements however show that it is steadily decreased. Additional tests on this subject are necessary;

Based on these results, PVDF is a well adapted material for our application. The main problem seems to be the increased temperature self-discharge, but this can be prevented by proper encapsulation and packaging of the PVDF. Also, lower working temperatures will naturally be beneficial.

Chapter 3

Composites for thermal energy harvesting

In this chapter we will present the results of our composite thermal energy harvesting prototypes. Two different sorts of prototypes will be discussed: one using PZT-based semi-flexible MFC piezoelectric as piezoelectric material, and second using PVDF piezoelectric polymer, both coupled with a shape memory alloy. The PVDF composite is shown here for the first time, therefore a thorough discussion will be given concerning the fabrication and measurement process, as well as the obtained results. The MFC composite concept was previously presented by our group (PhD manuscript by Dr Zakharov[49] and in several articles[16,18]). Here we will present some recent important improvements of this composite, notably concerning the matching of surface areas of MFC and SMA and improving the connection layer, as well as a change in the measurement technique. These results will also serve as a baseline for comparison.

3.1 State of the art

Before presenting the experimental results, we will give a brief overview of the state-of-the-art of the existing thermal energy harvesting technologies with composite systems. We have already seen examples of "conventional" thermal harvesting, making use the pyroelectric effect alone. Now we will show composite systems, which can potentially increase the efficiency of the harvesting and therefore the generated energy. We will give examples of composite thermal energy harvesters making use of bimorphs and shape memory alloys.

3.1.1 Pyroelectric bimorphs

The secondary pyroelectricity originates from the piezoelectric properties of pyroelectric materials. It is therefore possible to increase the total pyroelectric response of a material by enhancing its piezoelectric strain. This can be done by directly coupling a pyroelectric material with an elastic material, which by heating or cooling will create a difference in thermal expansion between the two layers, thus generating the strain in the pyro/piezoelectric layer.

First considerations of such effects were proposed by Newnham et al.[164] and later by Dunn[165]. They confirmed the possibility of improving the pyroelectric effect by piezoelectricity.

Later, the first experimental demonstration of the pyroelectric effect enhancement by using laminated composites was presented by Chang and Huang[14] in 2010, preceded by a mathematical model[166] in 2008. First, the authors fabricated laminated Steel/PZT/Steel structures that showed more than 100% enhancement in pyroelectric coefficient, by increasing the contribution of the secondary pyroelectric effect. Similar composites made with PVDF showed that even with a thin coating of steel can improve the electrical energy output. A slight improvement of $\approx 15\%$ in power density was shown, however no numerical value of pyroelectric coefficient was given.

To our knowledge, Chang and Huang[14] were the only authors to experimentally demonstrate an enhancement of the pyroelectric coefficient in laminated composites. Unfortunately, the details of their experimental procedure for pyroelectric coefficient measurements are unclear, and little information is given on PVDF composites. In general, we conclude that up to date there is a lack of experimental studies on this subject.

3.1.2 Shape memory alloy composites

Now, let us see examples of systems making use of SMA. First, the simplest system design of a heat engine utilizing an SMA has been proposed by Wang et al.[167] (schematic drawing in figure 3.1). It consists of a single TiNi cantilever which is heated through contact with a hot source. When heated, the cantilever bends thus losing the contact with the hot source. The spring connected to the free end of the cantilever brings it back to the hot source, and the process repeats.

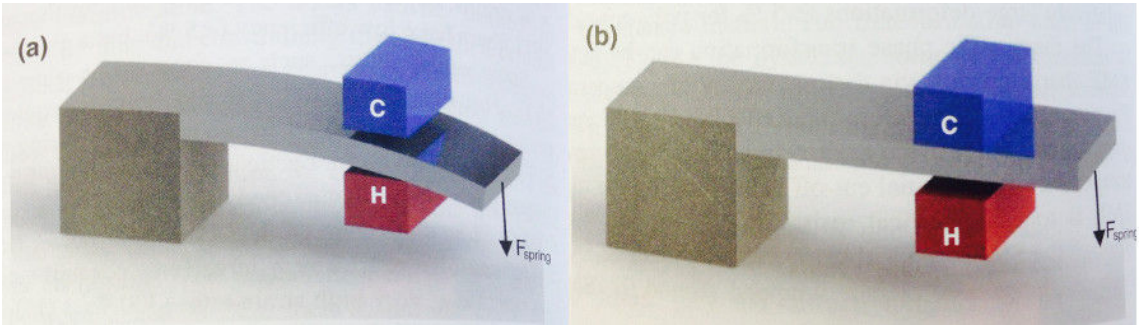

Figure 3.1: *Simple TiNi SMA MEMS heat engine design. SMA is in its (a) hot and (b) cold states. Drawing from[1]*

In[14] the authors used one-way SMA springs to act as a kind of heat pump transferring heat from hot to cold surfaces. The steel springs were returning SMA springs into their original shape, as shown in figure 3.2. The introduction of springs in this structure *'should maximize the surface contact between the pyroelectric element and the temperature surfaces, aiding thermal conduction'*. However, no clear experimental evidence of the benefits from using SMA was shown.

In 1992 Chen et al.[168] proposed for the first time the hybridization of an SMA and a piezoelectric, fabricating a thin laminated composite which demonstrated combined shape memory and ferroelectric properties. The authors called them "SMARTIES", an acronym for Shape Memory Actuators and Regulating Transducers for Intelligent Electronic Systems. The authors fabricated a 2 layer laminated composite in which sol-gel films of PZT or PLZT were deposited on commercial 100 μm thick TiNi shape memory alloy ribbons. To measure ferroelectric properties of PLZT, the TiNi layer was used as one of the electrodes, while the second one was sputter-deposited. The composites showed two-way shape memory effect of 0.4% (transition temperature $\approx$82 °C) without any electrical of mechanical degradation of PLZT. However, at 0.5% strain the PLZT layer cracked. Unfortunately, the piezoelectric property measurements were reported to be in progress and were not shown, and no further publications about SMARTIES appeared.

Sato[169] experimentally presented a functional NiTi wire covered by a PZT thin film, and demonstrated the self-sensing capabilities of the composite. By combining shape memory, piezoelectric and pyroelectric effects, the multifunctional device could be used as a self-sensing actuator,

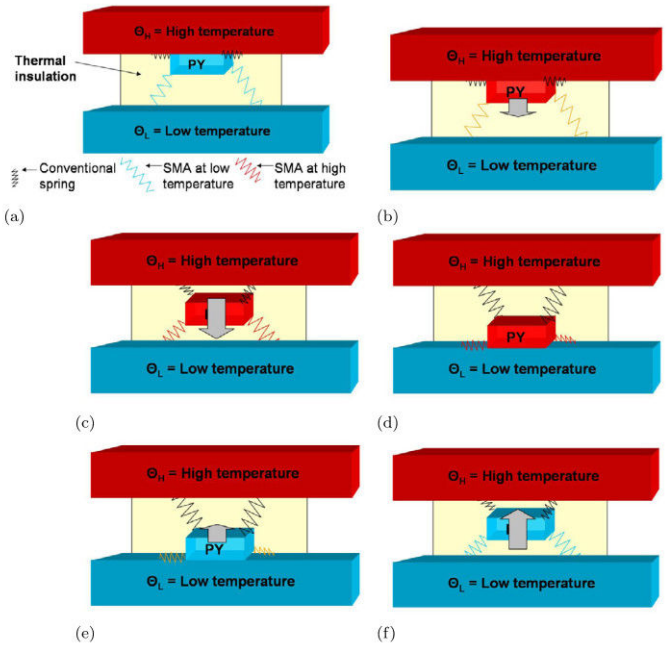

Figure 3.2: *Schematic of a pyroelectric energy harvesting device with SMA springs. From[14].*

where the SMA transformation is detected by the piezoelectric or the pyroelectric effect; the shape memory effect is used for rough actuation, and the piezoelectric effect performs precise actuations.

Several groups have published modeling results on piezoelectric+SMA composites[170–174]. For example, Jiang and Batra[172] analytically studied a 3-phase composite consisting of a polymer matrix with SMA and PZT inclusions. Later, Namli et al.[173] showed an analytic model of a hybrid composite comprised of SMA fibers with piezoelectric ceramic; generated power of the piezo-SMA composite was calculated to be linearly proportional to the cross-sectional area of the composite, thickness of the piezo phase and frequency of thermal fluctuations.

For the first time, an SMA/piezoelectric composite for thermal energy harvesting was experimentally demonstrated in 2011 by our group by Dr. Lebedev[175]). A free-standing, free-deforming bimorph laminated composite of NiTiCu+MFC was proposed (figure 3.3a) and the harvested energy density of 30 mJ/cm^3 per heating/cooling cycle was reported. This value was remeasured more accurately in later work[18], taking into consideration the actual active volume of the composite, and was found to be 750 μJ/cm^3 with a single temperature variation of 60°C.

The same year Namli and Taya[176] presented experimental results of their analytic model[173] on Piezo-SMA coupling. Unlike our composite, their composite consisted of two bulk pieces of NiTi and PZT, rigidly clamped mechanically inside a testing machine. The group has reported to obtain up to 8.6 μW, however since neither the dimensions of the harvester nor the energy per cycle were reported, it is impossible to compare the two composites.

Later in 2012 our group reported an original NiTiCu/PZT "machine" harvester[18] (figure 3.3b). A harvested energy density value of 450 μJ/cm^3 over a temperature increase of 35°C was reported. The specific geometry of the "machine" allowed to separate the pyroelectric response of the PZT from its piezoelectric response (for the sake of research). Thus, the measured composite energy output was coming only from the piezoelectric effect, and naturally its value was lower than that of the laminated NiTiCu+MFC composite, which exploited both effects.

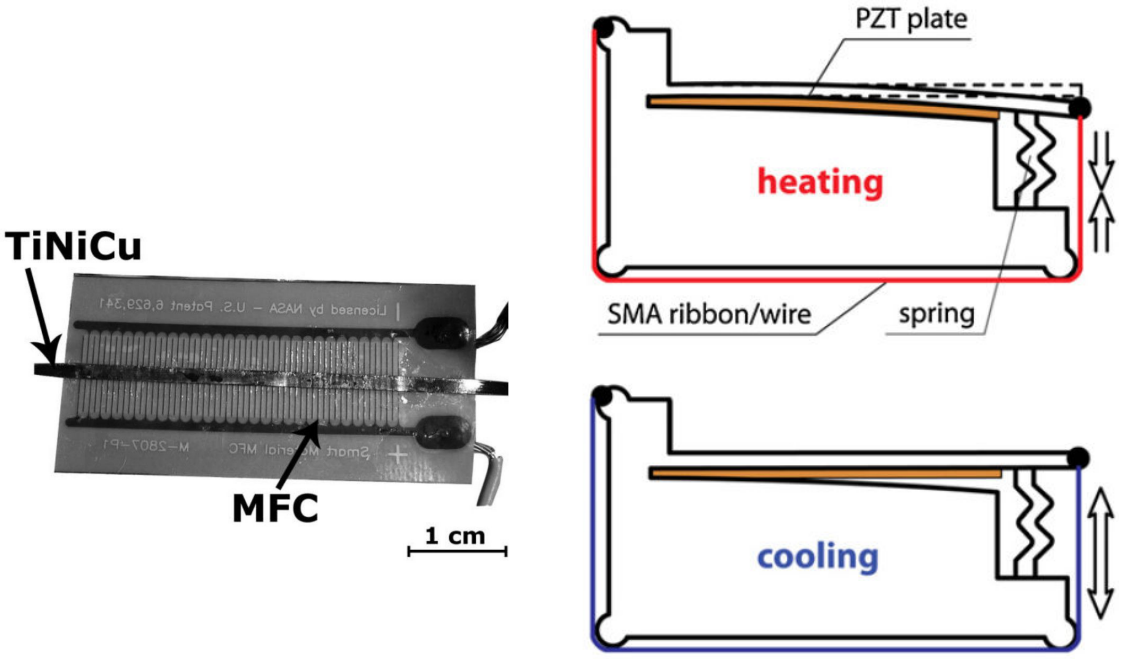

(a) *First SMA/piezo energy harvester*[175].

(b) *Schematic view of the NiTi/PZT "machine" harvester*[18].

Figure 3.3: *SMA+piezoelectric thermal energy harvesters proposed by our group.*

In 2013 Avirovik et al.[15] presented a similar device which consisted of a piezoelectric bimorph and an SMA wire, heated remotely by laser (figure 3.4). As in the case of our "machine" the pyroelectric and the piezoelectric responses were separated. The composite was able to produce useful voltage of 1.5 V with a single heating by ≈70°C. A maximum power of 0.05 μW was achieved.

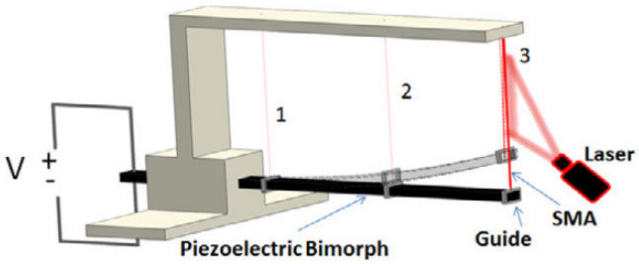

Figure 3.4: *Shape memory alloy-piezoelectric hybrid transducer from*[15]

3.1.3 Pyroelectric effect enhancement by shape memory alloy

Since the SMAs are capable of producing strain while heating or cooling, they can potentially be combined with a pyroelectric material in order to increase the secondary pyroelectric effect (second term of equation (1.5)). We have seen earlier that the pyroelectric coefficient of a pyroelectric composite can be higher than that of a pyroelectric alone; however, an SMA was never considered for such use.

Our group proposed for the first time in 2013 to use the enhanced shape memory composite scheme for pyroelectric materials[16]. To understand the interest of using an SMA, we have to consider what is the maximum "induced piezoelectricity" in non-SMA bimorph composites.

Usually a difference in coefficients of linear thermal expansion (CLTE) of the two layers is exploited to affect the secondary pyroelectric coefficient. For example let us take the extreme case of polypropylene, which has one of the highest thermal expansion coefficients (130 ppm/K[177]). Assuming a coupling with a non-expanding pyroelectric ceramic, the difference in CLTE for 30 K would give just 0.4% strain. Taking the case of a steel/PZT composite, the effect would give only 0.04% strain. For the PVDF/polypropylene coupling we would have no effect at all since CLTEs of both materials are roughly the same.

On the other hand, an SMA can provide strains of the order of 4%, even for small temperature variations of 1–30 K, independent of the temperature variation rate. These strains are much higher, and moreover the temperature range in which they take place can be adjusted by changing the SMA composition, depending on the targeted applications. The principle is illustrated in figure 3.5: (a) the pyroelectric material alone is shown, where the pyroelectric effect is characterized by the sum of primary and secondary pyroelectric coefficients; (b) when a SMA/pyro-piezoelectric bimorph is deformed in its hot state, an additional term is produced by the thermally-induced strain of the SMA, increasing the total output.

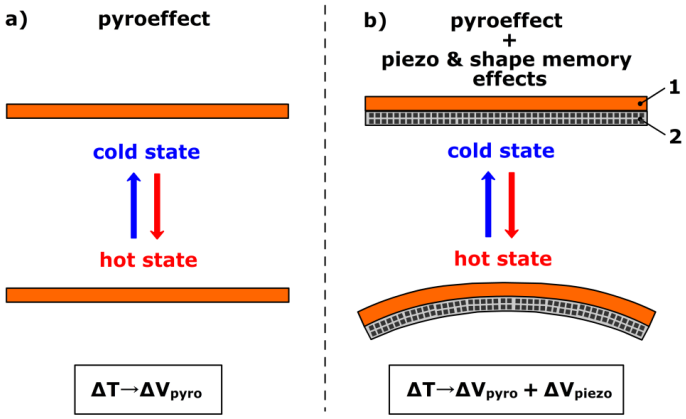

Figure 3.5: *Principle of our proposed pyroelectric enhancement. 1 - pyro/piezo-electric layer, 2 - SMA layer, ΔT - temperature change, ΔV_{pyro} - generated pyroelectric voltage, ΔV_{piezo} - generated pyroelectric voltage due to SMA. From[16]*

This scheme could theoretically be used to create artificial pyroelectrics by coupling piezoelectrics which do not show a pyroelectric response, with an SMA layer. This would be particularly interesting if a certain piezoelectric-only material had a very high piezo constant, higher than those piezoelectrics which intrinsically have pyroelectric properties. Such material is however yet to be found.

An inherent drawback of SMAs is that the shape memory effect is generally only a one-way effect. This means that SMA memorizes only its hot shape and thereby needs a bias element to recover its initial cold shape. In the bimorph composite, the second elastic layer acts as a bias spring on the SMA on cooling and returns it to its initial shape. Since in the case of NiTi the pseudoplastic strain is typically around 4%, a highly flexible material is needed for the bimorph. Metals and ceramics may not be convenient, since their elastic limit is less than 1%. Thereby soft flexible structures or polymers may be the optimal choice for the elastic layer.

3.2 MFC + SMA composite

The first approach to thermal energy harvesting presented here, is the composite bimorph consisting of semi-flexible Macro Fiber Composite (MFC) piezoelectric and NiTiCu SMA. Materials

were assembled together into a compact composite structure using epoxy glue. MFC is intrinsically pyroelectric and piezoelectric, therefore its electric thermal response can be enhanced by coupling with a shape memory material.

3.2.1 Materials and methods

Micro Fiber Composites (MFC)

MFC is a composite piezoelectric material produced by Smart Materials Inc.[178]. It consists of rectangular ≈ 140 μm thick PZT fibres, aligned between top and bottom electrodes, and embedded within a polymer insulating Kapton matrix. The MFC can be acquired in many different types and shapes. The type used in this work was M-8503-P1, which exploits g_{33} piezoelectric effect of PZT by using inter-digitated electrodes. When being elongated or shortened along their length, the PZT fibres generate electrical charges which are collected at the bonding pads.

NiTiCu Shape memory alloy

The SMA materials used in the work were 40 μm thick ribbons of $Ti_{50}Ni_{25}Cu_{25}$ (atomic %), kindly provided by Dr. A. Shelyakov (NRNU "MEPhI", Moscow, Russia). They were prepared by a melt spinning technique, as described in[179]. As shown in previous work on bimorph laminated composites with NiTiCu[17], a thermal annealing at 500°C for 5 min is necessary to obtain a suitable micro-crystalline structure. In these conditions, the SMA/steel composites showed the maximum deformation in the region 51–66°C with rather small hysteresis (figure 3.6). In the current work, similar thermoelastic behaviour was assumed for the SMA/piezoelectric composites.

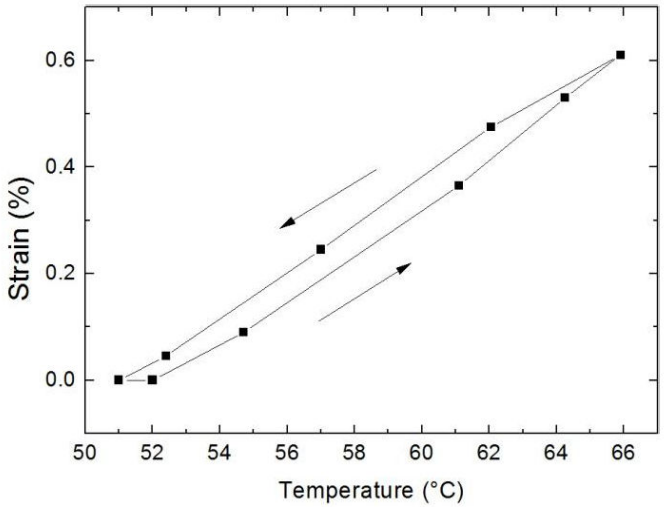

Figure 3.6: *Temperature dependence of the flexural strain of a laminated composite of NiTiCu/steel ribbons[17].*

Composite fabrication

The composites were fabricated by gluing 85 mm long NiTiCu ribbons on MFC with a non-conducting epoxy glue (3M Scotch-Weld DP 460). Prior to gluing, both MFC and ribbons were wiped clean with acetone and isopropanol. Then the glue was applied on both surfaces, followed by pressing the surfaces together with a hand press. In order to dry the glue completely, the composite was kept inside the press for at least 20 hours at room temperature. The final composite

is shown in figure 3.7. Composites with either one ribbon on one side of the MFC, or with two ribbons (one on each side of the MFC) were fabricated.

In our previous works[16,18] a cyanoacrylate glue ("Super Glue") was used to assemble the composites. However, practice showed that it could not sustain the repeated large deformations of the SMA at high temperature. To improve this point, high shear strength epoxy glue was used, showing much better properties in terms of adhesion, thermal and strain stability.

It is worth noting that as the strain of SMA is much larger than the maximal operational strain for the MFC (0.5%), the mechanical assembly remains critical. Imperfections of the glue connection might decrease the strain transmitted from SMA to MFC; in the present case this allowed us not to destroy the piezoelectric layer during operation, but on the other hand, part of the mechanical work generated by the SMA is lost, and the efficiency of the energy harvesting is thus decreased.

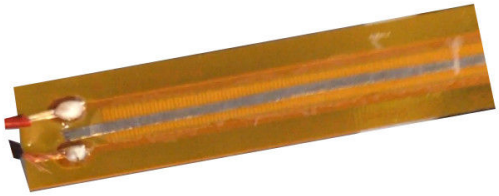

Figure 3.7: *The MFC + NiTiCu composite.*

Table 3.1 summarizes the geometrical parameters of the fabricated composite. The active volume of the composite was estimated by equation (3.1) to approximately 39 mm^3 for composites with one SMA ribbon, and 46 mm^3 for composites with two SMA ribbons. The surface ratio of SMA/active MFC was equal to 66%.

$$2 \cdot w_{SMA} \cdot l_{SMA} \cdot t_{SMA} + w_{MFCactive} \cdot l_{MFCactive} \cdot t_{MFCactive} \tag{3.1}$$

where *w* is the width, *l* is the length and *t* is the thickness. Subscript SMA relates to SMA ribbons and $MFCactive$ to active area of MFC. Factor two takes into account the two SMA ribbons.

Table 3.1: *Geometrical parameters of MFC and NiTiCu ribbons. For MFC the overall size and the active area size (where the PZT wires are present) are specified.*

size	MFC overall	MFC active	NiTiCu
length, mm	110	85	85
width, mm	14	3	2
thickness, μm	300	127	40
capacitance, nF	0.68	-	-

3.2.2 Experimental procedure: controlled heating

To evaluate the prepared composites and observe the impact of the SMA layer during its heat-induced deformation, it was necessary to heat the samples to temperatures higher than A_s, in a well controlled and measurable manner. As proposed by Huang[180], several methods exist to heat an SMA wire. We have tested the following methods:

- Electric current heating
- Water bath heating
- Oil thermostated bath heating

Each method has its own disadvantages and benefits, and may be used depending on the working conditions and composite configuration. We will discuss briefly each method and its experimental implication during this work.

Electric current heating

Since the NiTiCu is intrinsically a good electricity conductor, the ribbon can be heated by applying an electrical current; this method was used in our previous works[18,175]. According to Joule's first law the amount of heat released in a conductor is proportional to the square of the current: $Q \propto I^2 * R$. Therefore, to heat the SMA ribbon and induce the deformation due to the phase change, a direct electric current can be applied to the ribbon. In our case the resistance of the ribbon was ≈2 Ω, and 1 A current was usually sufficient to heat from room temperature to ≈80°C in less than 1 min. Then the ribbon was naturally cooled down in air.

The temperature was measured using a commercial infrared thermal camera SC500 (FLIR Systems) with 0.1°C thermal resolution. An additional magnifying lens allowed a spatial resolution of 0.1 mm. An example of a measurement is shown in figure 3.8, where the ribbon is glued to the middle of a MFC. Since the ribbon was glued onto the MFC, the MFC participated in the thermal exchange. It is visible that the ends of the ribbon are hotter than the central part since they are not glued to the MFC and there is no thermal conduction into the MFC in these areas. This naturally brings errors to temperature measurements and ribbon deformations, as it may happen that only part of the ribbon is transformed. Moreover, the temperature control of the ribbon is not straightforward. Considering these disadvantages, despite its ease of implementation, this method was abandoned in the current work and other methods were proposed.

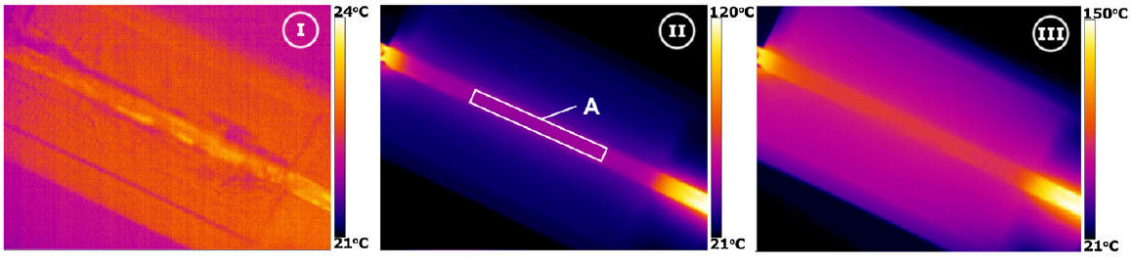

Figure 3.8: *Infrared images of the NiTiCu/MFC composite at different heating temperatures, from[18].*

Water bath heating

Since Joule heating resulted in a non-homogeneous heating of the composite, the idea of using a homogeneous thermostat came naturally. This measurement method allows careful comparison of the electric response of the MFC alone with that of the composite. As a first test, a water bath was used. It consisted of a double-walled 250 cl plastic cup filled with hot water. To measure the samples, they were first immersed in a bath with hot water and then in a bath with room-temperature water. The measurements were done from hot to cold temperatures, since the temperature change

could be obtained by simply letting the hot water bath to naturally cool down by several degrees. Since the natural cooling of the bath was slow and the measurement time was much faster, we could assume that the temperature was constant during one given measurement. The temperature was monitored by a thermocouple immersed in the water.

This rather simple system allowed for an easy set-up and very quick experiments. However, since water is a good electric conductor, some unwanted short-cuts took place sometimes, thus disturbing the measurements. Also, the thermal stability of such a system was not exceptional, as the lack of feedback temperature regulation meant that temperature could not be kept at a constant level for a long period. Additionally, PZT fibers in MFC are sensitive to humidity[161] and their properties can degrade quite quickly in water despite encapsulation. It is because of these reasons this method was finally abandoned and heating in an oil thermostat was introduced.

Oil thermostated bath heating

The improved heating system was composed of a commercial regulated thermostat (P-Selecta Univeba) with heated dielectric oil. The temperature was set manually via the potentiometer, and its evolution was controlled by an infrared thermal camera and an external thermocouple. The overview of the set-up with all the principal elements is shown in figure 3.9a. This set-up solved both problems of non-homogeneous heating when using current, and shortcuts due to electrical conductivity of water.

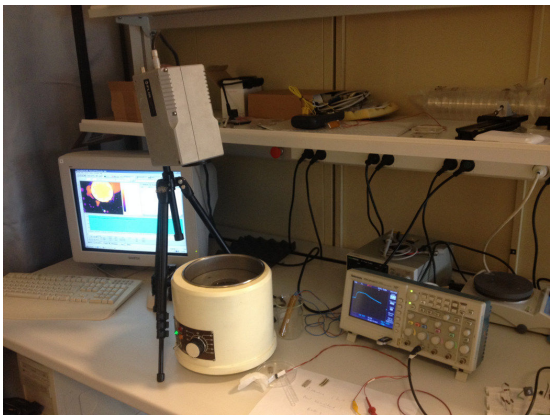

(a) *Oil thermostat set-up along with IR camera and oscilloscope.*

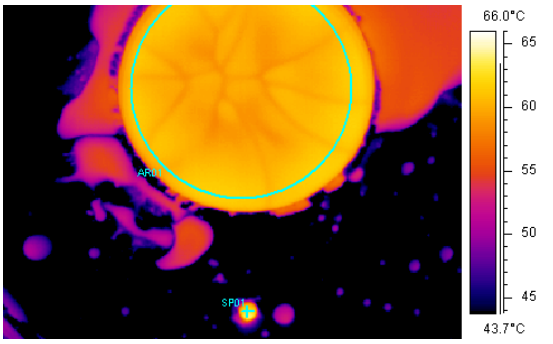

(b) *Infra-red image of the heated thermostat from above. The area marked AR01 is the oil, the cross marked SP01 is the heating element, both seen through an opening of the lid.*

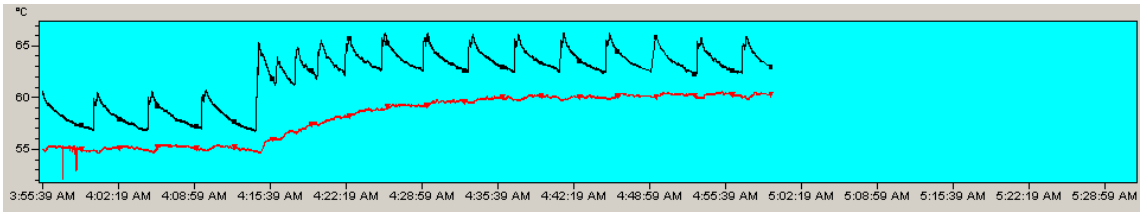

(c) *Evolution of thermostat temperature. Bottom red line is oil temperature, top black line is heating element temperature.*

Figure 3.9: *Oil thermostat set-up.*

Prior to the measurements, the thermostat was stabilized at a given temperature for 30 minutes. The oil temperature evolution measured by FLIR camera is shown in figure 3.9c with the red bottom line representing the temperature of the oil, and the black top line representing the tem-

perature of the thermostat heating element. The oil temperature stabilizes after approximately 15 minutes, while the heating element turns on and off repeatedly to keep the oil at a constant value throughout time. In figure 3.9b the heat distribution in the oil is shown from above. The circle area marked "AR01" corresponds to the oil reservoir. As we can see from the figure, the heat is very homogeneous with minor fluctuations due to surface cooling. Prior to each measurement, the oil was manually stirred to homogenize the temperature.

Considering the superior thermal homogeneity and the ability to control temperature, this method was used for all the measurements presented in the following sections.

3.2.3 Results: composite output

The devices presented here and their study are an evolution of previous composites made by our group[16,18], and as such several improvements were made. First, as shown in the previous section, an improved experimental procedure for heating has been set-up, ensuring precise and homogeneous temperatures. Second, a better match between the active area of the MFC and that of the SMA (same as the one used here) has been ensured. Indeed, with previously used MFC's (M-2814), only 28% of the active area of the MFC was covered by the SMA, whereas in the present device this ratio is increased to 66%.

To measure the output voltage of the composite, a contact-less electrostatic voltmeter connected to an oscilloscope was used.

Two geometries of composites were tested. First, with one SMA ribbon glued only on one side of the MFC, and second with two SMA ribbons, one glued on each side of the MFC. For both geometries, the shortening of the SMA ribbon during heating is transferred to the MFC, and this deformation is then transformed into piezoelectric voltage. There is however an important difference between the two geometries: on the first case the shrinkage of a single ribbon results in bending of the composite, which acts as a bimorph actuator. This bending results in either tensile or compressive stress on the PZT fibers (depending on the side of the MFC), which produces an electric voltage of either positive or negative sign. In the case of the second geometry with SMA on both sides of the MFC, there is no bending of the composite, but instead a pure linear contraction, which is better from the mechanical point of view. Also, since there is twice as much of the SMA material acting on the MFC, we can expect higher forces and strains on the PZT fibers, which will result in higher produced piezoelectric voltage.

The composites were evaluated in the range of temperatures from 30 to 75°C. The two different composite geometries as well as a blank MFC sample were tested. Five measurements of each sample were performed at each temperature, and for each measurement the maximum output voltage was recorded. Measurements were performed by immersing samples in the heated oil thermostated bath. Figure 3.10 shows the maximum voltage of each sample as a function of temperature.

Since the composite, upon heating, will generate voltage due to both pyroelectric effect and SMA-induced piezoelectric effects, it is necessary to measure the individual contribution of each effect to the overall voltage output. In order to do so, the pure pyroelectric output was measured separately on a blank MFC sample, containing no SMA. Then, the composites were measured and their output was compared to the standalone MFC output. The difference was directly linked to the piezoelectric contribution of the SMA.

The pyroelectric output of blank MFC was measured first, it is shown in black in figure 3.10. It

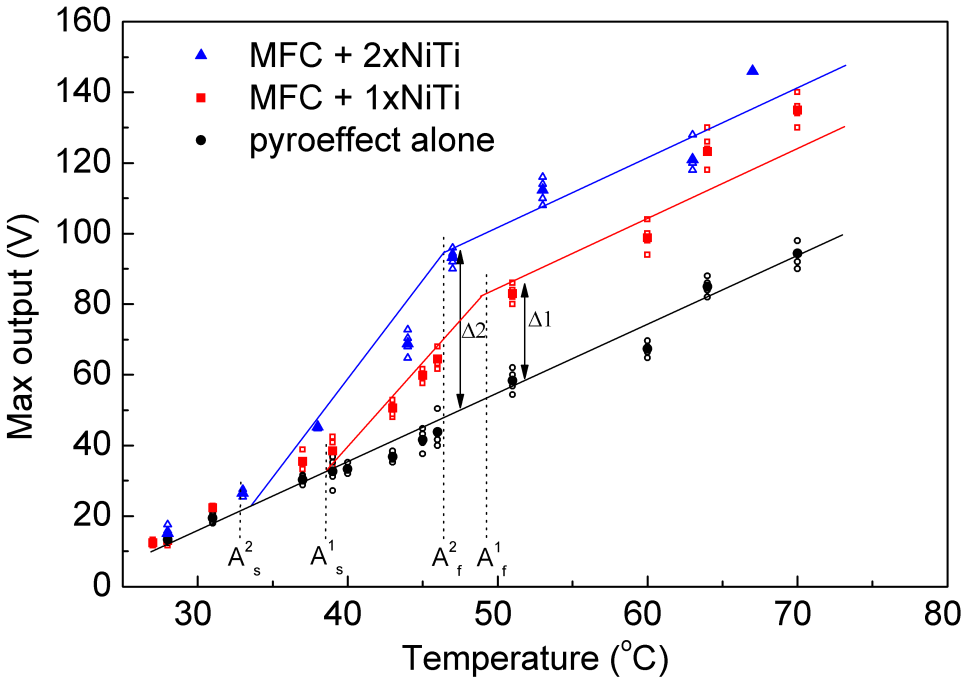

Figure 3.10: *Maximum voltage output of MFC+SMA composites and MFC alone at different temperatures. The empty symbols represent the actual measured values, and the filled symbols show the averaged values for each measurement. The corresponding trend lines are drawn manually.*

increased linearly with temperature, in accordance with theory (see equation (1.7)). The behavior of composites of both geometries was significantly different from the pure pyroelectric output: at low temperatures their output coincides with the pyroeffect, but starting from a certain temperature, their voltage increases considerably. This temperature corresponds roughly to A_s, which is the start temperature of austenitic transition in the SMA ribbon. When the SMA is heated above this temperature, it starts contracting and acting on the MFC, thus producing an additional piezoelectric voltage and changing the slope of the voltage output. When the temperature reaches A_f, which is the finish temperature of austenitic transition in the SMA ribbon, there is no more additional strain caused by the deformation, and the slopes of the voltage output should be equivalent to the pure pyroeffect slope.

From figure 3.10 we can draw multiple conclusions. The first and most important one, is that both composites strongly increase the produced voltage. The difference $\Delta 1$ between the pyroeffect and the composite with one SMA ribbon is 30 V, and $\Delta 2$ between the pyroeffect and the composite with two SMA ribbons equals to 50 V, which correspond to 50% and 100% increase of the voltage output respectively at A_f point (around 47°C). The generated composite energy is proportional to the voltage squared, therefore increase of the voltage by a factor of two yields in increase of the energy by a factor of four. The composite with two SMA ribbons is clearly more advantageous for two reasons: it yields higher voltage (and consequently higher energy) values, and mechanically it presents linear contraction instead of bending.

Another conclusion that can be made is that the actual A_s and A_f temperatures of the composites are higher than the A_s and A_f temperatures of a free standing SMA ribbon. The expected measured A_s for the free-standing SMA is 30°C, whereas the value extracted from figure 3.10 is

around 33°C for composite with 2 ribbons and around 37°C for composite with 1 ribbon. Similarly for A_f, which are extracted to be around 46°C and 49°C for two composites, instead of 33°C for free standing SMA ribbon. This fact suggests that the transition temperature range of the ribbons changes if external mechanical constrains are applied. Measurement of electrical resistance[1] of NiTiCu ribbons glued to 100 μm polypropylene substrate showed a shift of both A_s and A_f towards higher temperatures (figure 3.11). We can thus confirm the impact of the substrate on transition temperatures. This might be very important for the future applications, as a careful design and evaluation of the composite system would be needed in order to asses its working temperature ranges.

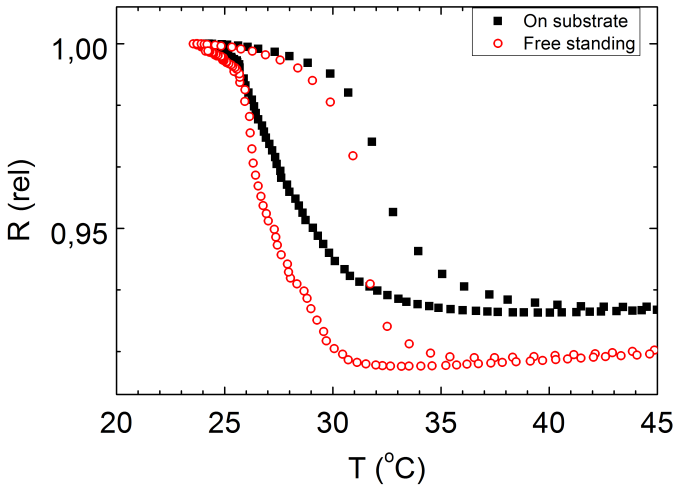

Figure 3.11: *Relative electrical resistance vs. temperature of a NiTiCu ribbon glued to a substrate, and of a free-standing one.*

The summary of output voltage, energy and energy densities of the composites is given in table 3.2. Relative increase in energy values compared to MFC alone reached 320% for the composite with two SMA at A_f (≈46°C).

It is also necessary to note the difference on the behavior of the composites above the A_f temperature: the 2xNiTi composite has a pronounced point after A_f where the voltage slope changes and becomes equivalent to the pyroeffect slope. The 1xNiTi composite has a less apparent change point and moreover its A_s temperature is more shifted towards hot temperatures. The probable reason for this comes from different mechanical behavior of the composites, however further experiments need to be performed to understand the phenomenon and precisely ascertain the impact of mechanical constraints.

Moreover, as we have already seen in chapter 2, MFC and bulk PZT piezoceramics are known for suffering from leakage phenomena[161,181]. Even under open-circuit conditions during the charge generation phase, not all charges stay on the electrodes, but some dissipate inside the material. This self-discharge can be rather quick: as observed by Lafont et al.[181], at room temperature the voltage on the MFC measured by a non-contact voltmeter decreased from 300–400 V (3–4 kV/mm) by 25–30% in the first 3 seconds, but then stayed rather stable. Lipscomb et al.[161] observed that leakage in bulk PZT increases with increasing temperature, humidity and electric field. In particular, he measured a decrease by 1 order of magnitude of the PZT resistance when increasing temperature from 45 to 85°C.

For more reading on the results of the original MFC composite previously presented by our group, the reader is referred to the thesis of Dr. Zakharov[49], where various phenomena are

[1] Electrical resistance is representative of austenite/martensite transformation, since the resistances of the two phases are distinctly different.

Table 3.2: *Summary of output voltage, energy and energy density for standalone MFC and the two MFC+SMA composites. Each value is an average of 5 measurements. ΔV and ΔE values are calculated as a relative increase to the MFC alone at the same temperature.*

	MFC alone	MFC + 1xNiTi	MFC alone	MFC + 2xNiTi
V at A_s [V]	31	38	22	26
V at A_f [V]	56	86	46	94
E at A_f [μJ]	1.1	2.5	0.7	3.0
E_d at A_f [μJ/cm^3]	33.3	64.5	22.5	65.3
V at 70°C [V]	94	123	94	142
E at 70°C [μJ]	3.00	5.14	3.00	6.86
E_d at 70°C [μJ/cm^3]	93.9	131.9	93.9	149.0
ΔV at A_f [V (%)]	-	30 (54)	-	48 (104)
ΔE at A_f [μJ (%)]	-	1.5 (136)	-	2.3 (318)
ΔV at 70°C [V (%)]	-	29 (31)	-	48 (51)
ΔE at 70°C [μJ (%)]	-	2.1 (71)	-	3.9 (128)

presented and discussed.

3.2.4 Summary

To summarize the results of this section, an optimized version of the original hybrid NiTiCu/MFC composite for thermal energy harvesting was fabricated and tested; a series of improvements were made, including the optimization and matching of the surface areas of NiTiCu ribbons and MFC, improving the mechanical bonding of the two materials, and changing the heating and measurement methods.

At A_f temperature of 47°C (temperature variation of ≈25 °C) the composite consisting of two NiTiCu ribbons, one on each side of MFC, harvested 65 μJ/cm^3. Therefore with further optimization the system can meet the requirement for wireless data transmission and can be potentially used for such applications.

Hybridization of an SMA and a pyro/piezoelectric ceramic material was shown to be effective: when compared to the MFC alone, the output voltage was increased by 104% and the output energy by 318% with the composite consisting of two NiTiCu ribbons at the A_f temperature of 47°C.

3.3 PVDF + SMA composite

The first prototypes combining a piezoelectric with a shape memory material being successful, we decided to go further and change the piezoelectric material. In fact, using MFC piezoelectrics might not be the optimal choice, as it withstands less than 0.45% strain according to its data sheet[178], whereas the SMA used in this work can provide up to 3% of strain[182]. In comparison, PVDF can withstand much larger strains and is also much more flexible than the ceramic piezoelectric composites, which can be more advantageous for an energy harvesting composite coupled with SMA. That is why we have decided to replace the MFC by PVDF, and to compare the two

composites in terms of energy density and energy increase ratio coming from the shape memory alloy compared to the pure pyroelectric response.

3.3.1 Materials and methods

PVDF

For the fabrication of the composites and pyroelectric measurements, the following samples of PVDF from Measurement Specialties were used:

- Commercial piezoelectric elements LDT-0, which comprise a 28 μm thick PVDF polymer film with screen-printed Ag-ink electrodes, laminated to a 0.125 mm Mylar substrate, and fitted with two crimped contacts. Technical and geometrical details of the components are shown in figure 3.12a and table 3.3;
- Commercial piezoelectric elements LDT-1. Their main differences from LDT-0 are the increased length and width and the pre-soldered wire connections for ease manipulation. Technical and geometrical details of the components are shown in figure 3.12b and table 3.3;
- Plain prepolarized sheet of 110 μm thick PVDF. For the composite fabrication, the sheet was cut to small pieces of convenient size. The metallization was done by applying conductive epoxy glue.

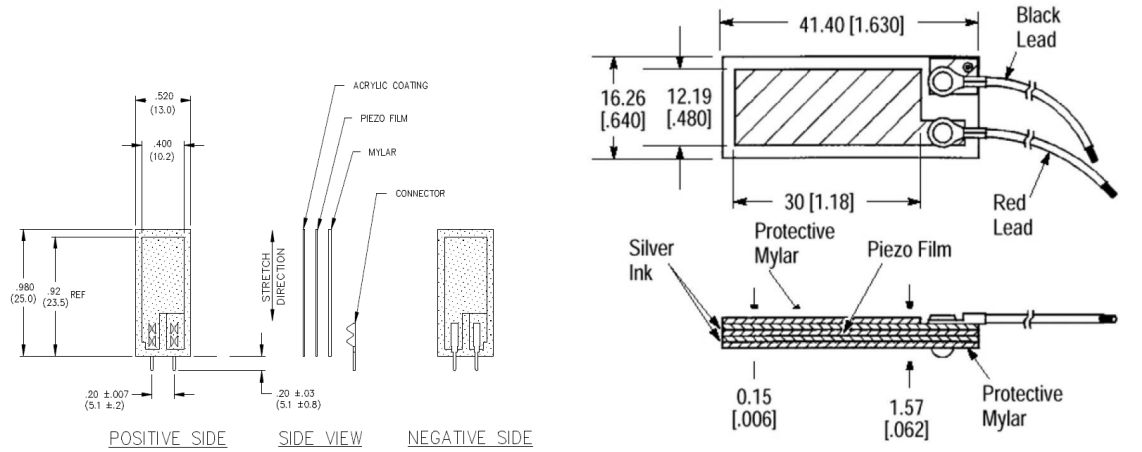

(a) *Schematic drawing of LDT-0. Dimensions in inches (mm).*

(b) *Schematic drawing of LDT-1. Dimensions in mm (inches).*

Figure 3.12: *Geometrical characteristics of LDT-0 and LDT-1 PVDF laminated components from Measurement Specialties[19].*

NiTiCu Shape memory alloy

For the fabrication of PVDF composites we used the same kind of NiTiCu ribbons as for the MFC composites. Width of the ribbons was 2 mm and thickness was 40 μm. However here we used two alloys with different phase transformation temperatures: A_s of ≈40°C and 30°C, depending on availability.

Table 3.3: *Geometric and operational parameters of LDT-0 and LDT-1 PVDF[19].*

Element	LDT-0	LDT-1
PVDF thickness, μm	28	28
Active length, mm	15	30
Active width, mm	10	12
Capacitance, nF	0.5	1.38
Operating temperature, °C	0–85	0–70
Electrodes	screen-printed Ag	screen-printed Ag

We have also tested $Ni_{55}Ti_{45}$ wires from Nimesis Technology[183] (commercial reference NTSM01). Wires of 100 μm diameter, having A_s of ≈45°C, were used to make flat stent-like structures assembled to the PVDF.

Composite fabrication

To evaluate the performance of PVDF + SMA composites, various geometries and materials were tested. To connect the SMA ribbons to the PVDF, either non-conductive commercial epoxy (3M Scotch-Weld DP 460) or silver-filled conductive epoxy (CircuitWorks CW2400) glues were used. Prior to gluing, both PVDF and ribbons were cleaned with isopropanol. Then, a thin layer of glue was spread on PVDF, the ribbons were placed and the assembly was pressed together with a hand press. In order to dry the glue and ensure the connection, the components were kept inside the hand press for at least 20 hours at room temperature.

The first set of composites, shown in figure 3.13, were made to study the effect of the SMA position on the PVDF on the composite output. The NiTiCu ribbons were approximately 20 mm long and 2 mm wide, and they were glued to the LDT-0 elements using non-conductive epoxy, followed by 24 hours drying. The ribbons with A_s of 40°C were used for these composites. The samples on the left and on the right in figure 3.13 have NiTiCu ribbons glued on the Mylar side of LDT-0, and the sample in the middle has NiTiCu glued on the PVDF side.

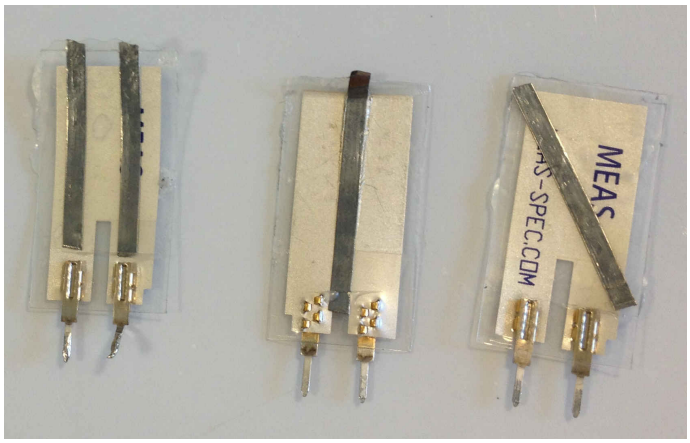

Figure 3.13: *Different geometries of NiTiCu ribbons glued onto LDT-0 components.*

The second set of composites was designed to maximize the strain of PVDF and make it more homogeneous. For that two ribbons of NiTiCu were glued parallel to each other on both sides of a PVDF element. In this case the plain PVDF sheet of 110 μm, and ribbons with A_s of 30 °C

were used. To connect the elements together, conductive epoxy was used, which served at the same time as both bonding layer and as electrodes to collect charges from the PVDF surface. To hold and perform the electrical measurements, the composites were inserted into a custom holder, which consisted of two Plexiglas plastic plates with patterned copper scotch lines glued to them. When the holder was assembled, the copper lines were in contact with the conductive epoxy on both sides of PVDF, thus serving as extension wires to ease the measurements. Figure 3.14 shows the final assembled composite and its schematic drawing.

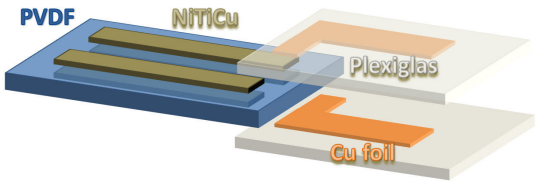

(a) *Schematic drawing of the composite inside sample holder. The NiTiCu ribbons are on both sides of PVDF.*

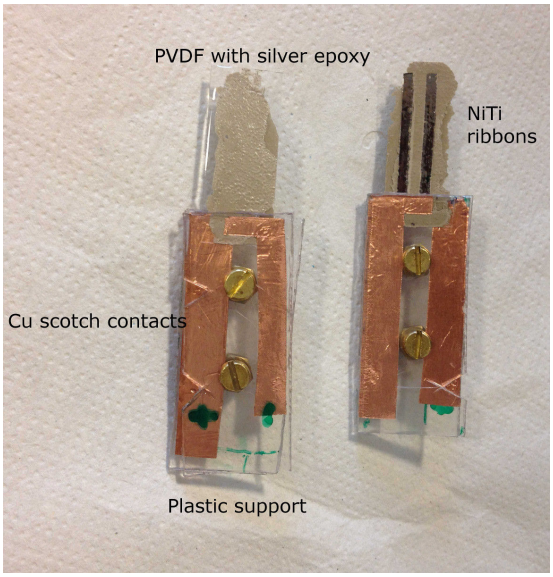

(b) *Left: reference sample of PVDF alone, covered with conductive epoxy. Right: PVDF + NiTiCu composite.*

Figure 3.14: *Composite of 110 µm-thick PVDF + two 40 µm-thick NiTiCu ribbons on each side, assembled in sample holder.*

Table 3.4 summarizes the geometric parameters of the fabricated composite. Since there are four NiTiCu ribbons on the composite, its active volume can be estimated by:

$$4 \cdot w_{SMA} \cdot l_{SMA} \cdot t_{SMA} + \cdot w_{elec} \cdot l_{elec} \cdot t_{PVDF} \tag{3.2}$$

where w represents width, l length and t thickness. Subscript SMA relates to SMA ribbons, $elec$ to electrodes and $PVDF$ to piezoelectric film. Factor 4 takes into account the four SMA ribbons.

Using this estimation, the active volume of this composite is equal to 27.6 mm^3, which makes it almost twice less than that of the MFC composite. In these prototypes 50% of the active area of PVDF is covered with SMA.

Experimental procedure

All the composites were evaluated in a range of temperatures going from 30 to 70°C. The heating was done by immersing the samples in the oil thermostat, as explained in section 3.2.2. Five measurements of each sample were performed at each temperature, and for each measurement the maximum output voltage was recorded with the electrostatic contact-less voltmeter. The generated energy was then calculated by either equation (2.12) or (2.13).

Table 3.4: *Geometrical parameters of PVDF and NiTiCu ribbons for the second set of composites (fig. 3.14).*

size	PVDF	Electrode	NiTiCu
length, mm	25	23	23
width, mm	10	8	2
thickness, μm	110	-	40
capacitance, nF	0.25	-	-

3.3.2 Results: composite output

3.3.2.1 Comparison with pyroelectric harvesters

Many extensive works on thermal energy harvesting using the pyroelectric properties of PVDF have been published. This includes works on Olsen and Ericsson cycles[110,112,113], composite systems[14,109], infrared harvesting[111], chemical methods of increasing the pyroelectric coefficient[111,184] and many others[4,8,108]. Many authors present their results in terms of power [W] or power density [W/cm^3 or W/g] as the amount of produced energy over time, because they work with continuous temporal temperature variations. In this work, since the goal is to harvest random, long and quasi-static temperature events, we present the composite results in terms of energy [J] and energy density [J/cm^3], which makes it sometimes difficult to compare the performance with other systems. Additionally, the intention of this work is not to compete with the state-of-the-art pyroelectric generators in terms of output energy or power, but rather to experimentally demonstrate the possibility to increase the pyroelectric response of PVDF by coupling it with a shape memory alloy, more specifically, in the case of discrete thermal events.

3.3.2.2 Pyroelectric output of PVDF

PVDF material in itself has high pyroelectric response. To correctly estimate the performance of our composite systems, it is important to first measure the pure pyroelectric performance of the material. As explained previously in section 1.4.2.2, the performance of a pyroelectric material can be characterized by its pyroelectric charge coefficient ρ_Q or voltage coefficient ρ_V, which shows what charge/voltage output is produced by the system when it is heated by 1 degree Celsius, and is given by equation (1.6).

Using the following data-sheet values for PVDF: ρ_Q = 30·10$^{-6}C/m^2K^{-1}$, ε_r = 12.5[13] and taking h = 28 μm (as the thickness of LDT elements), we obtain a theoretical value of ρ_V = 7.6 V/°C. In comparison, for the MFC with ρ_Q = 238·10$^{-6}C/m^2K^{-1}$[185], ε_r = 1800[142] and h = 127 μm[186], one obtains ρ_V = 1.9 V/°C. This comparison shows that even thinner PVDF samples are able to produce higher voltage than PZT, with the same temperature difference.

To determine the experimental value of the pyroelectric charge and voltage coefficients, a series of measurements was performed on the first set of composites. An LDT-1 sample alone (without SMA) was placed consequently in hot oil and room-temperature oil, and its voltage output was observed with a contact-less voltmeter. Then the hot oil temperature was raised and the measurement was repeated. In figure 3.15 we can see the evolution of voltage vs. time when heating from 21 to 45°C and cooling back. On both curves the voltage first increases due to

pyroelectricity and then decreases due to self-discharge phenomena. The voltage decay of the heating curve is much faster, which is explained by higher self-discharge at elevated temperatures, as was shown in section 2.6.2. Self-discharge is an important phenomenon which strongly affects the performance of piezoelectric materials, and it needs to be taken in account for the system design.

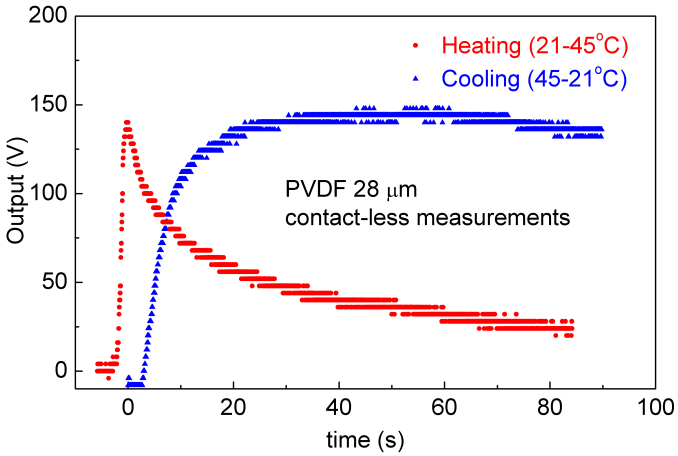

Figure 3.15: *Voltage output of an standalone LDT sample when heated (red) and cooled (blue). The absolute voltage is shown for ease of comparison.*

Both values of voltage on heating and on cooling were measured in a temperature range going from 40 to 70°C. Three measurements were done for each temperature. The experimental points together with theoretical values are shown in figure 3.16. The calculated pyroelectric charge coefficient is $27{\cdot}10^{-6}C/m^2K^{-1}$ for the heating curve and $29{\cdot}10^{-6}C/m^2K^{-1}$ for the cooling curve, which is in good agreement with the theoretical value ($30{\cdot}10^{-6}C/m^2K^{-1}$). Uncertainty of temperature measurements may account for the small discrepancy of values. Also, increased self-discharge impacts the heating curve: we can see that the red curve in figure 3.16 starts to change its slope after around 55°C. In fact, if we calculate the pyroelectric charge coefficient only from data points between 30 and 50°C, we will obtain value of $28{\cdot}10^{-6}C/m^2K^{-1}$, which is closer to the theoretical value. Finally, since the measured and the theoretical pyroelectric coefficients match quite well, we can conclude that the experimental conditions are set correctly and the PVDF sample is heated homogeneously at a known temperature, thus we can further proceed with temperature measurements of the composite systems.

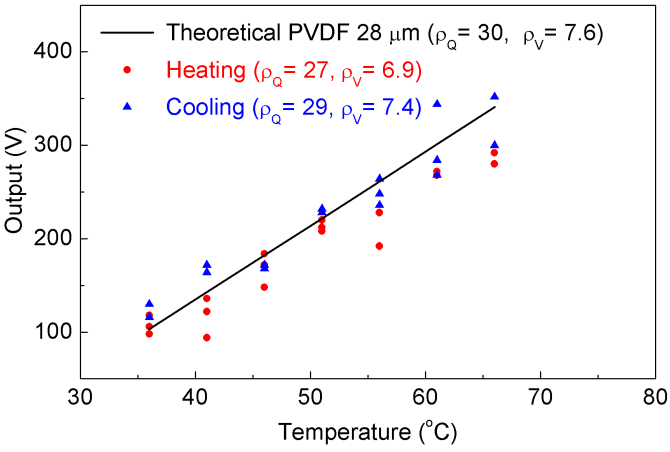

Figure 3.16: *Output voltage of a standalone LDT-1 sample as a function of temperature.* $[\rho_Q]$=$10^{-6}Cm^{-2}K^{-1}$, $[\rho_V]$=V/K.

3.3.2.3 Different composite geometries

The samples on the left and on the right in figure 3.13 have NiTiCu ribbons glued on the Mylar side of LDT-0, and the sample in the middle has NiTiCu glued on the PVDF side. During the measurements, the sample in the middle was damaged and deformed because the strain developed in the NiTiCu ribbon unglued the PVDF film from the Mylar substrate, therefore such configuration was considered to be weak and was not used in the further experiments. Table 3.5 summarizes the composites parameters and their output voltage and energy.

Table 3.5: *Maximum voltage and energy output of the prepared PVDF+SMA composites.*

Geometry	Max Voltage, V	Max Energy, μJ
pyro alone	128	4.1
diagonally	160	6.4
parallel	152	5.8

Figure 3.17 presents the output voltage and energy as a function of temperature for the first set of composites with different geometries as well as LDT-0 sample alone. At low temperatures the output of the composites is similar to the blank LDT-0. When the temperature is raised up to 45°C, above the A_s phase transition temperature of the used SMA ribbons, additional piezoelectric voltage due to the SMA contractions sums up to the pyroelectric voltage, and the difference in the output voltage starts appearing. At 50°C (the A_f temperature) the average output voltage of the composites is 20 V higher than that of pure PVDF, and at 70°C the difference goes up to 40 V. This corresponds to approximately 40% of the voltage increase for both temperatures. The output energy presented has an increase of more than 80% at 50°C compared to that of PVDF alone.

If we now compare the composites with different geometries of SMA between them, we will see that there is no significant variation. The diagonal geometry seems to produce a slight, but not significant higher output. Moreover, the practice showed that mechanically it is more favorable to have composites with parallel arrangements of SMA, as it yields a more predictable and repeatable output due to better homogeneity of SMA strain distribution on the PVDF. Therefore this configuration was retained for the fabrication of second set of composites with 110 μm-thick PVDF.

Wires composite geometries

Wires of NiTi were used to make flat mesh and stent-like structures on PVDF, as proposed by Nimesis Technology (figure 3.18). The wires were first weaved then glued directly to PVDF. However, preliminary tests showed little impact of wires on composite output. We suppose that due to their geometry while providing relatively high strain, the generated stress of bent structures is low and not sufficient for PVDF. Other woven structures should be further tested in order to generate higher strains. Also, during fabrication, sharp edges of NiTi wires sometimes pushed too hard into PVDF and damaged it. To solve this, the wires could be first embedded in a soft matrix (e.g. epoxy glue) and then glued to PVDF; this will not hinder the wires strain but will protect the PVDF from their edges.

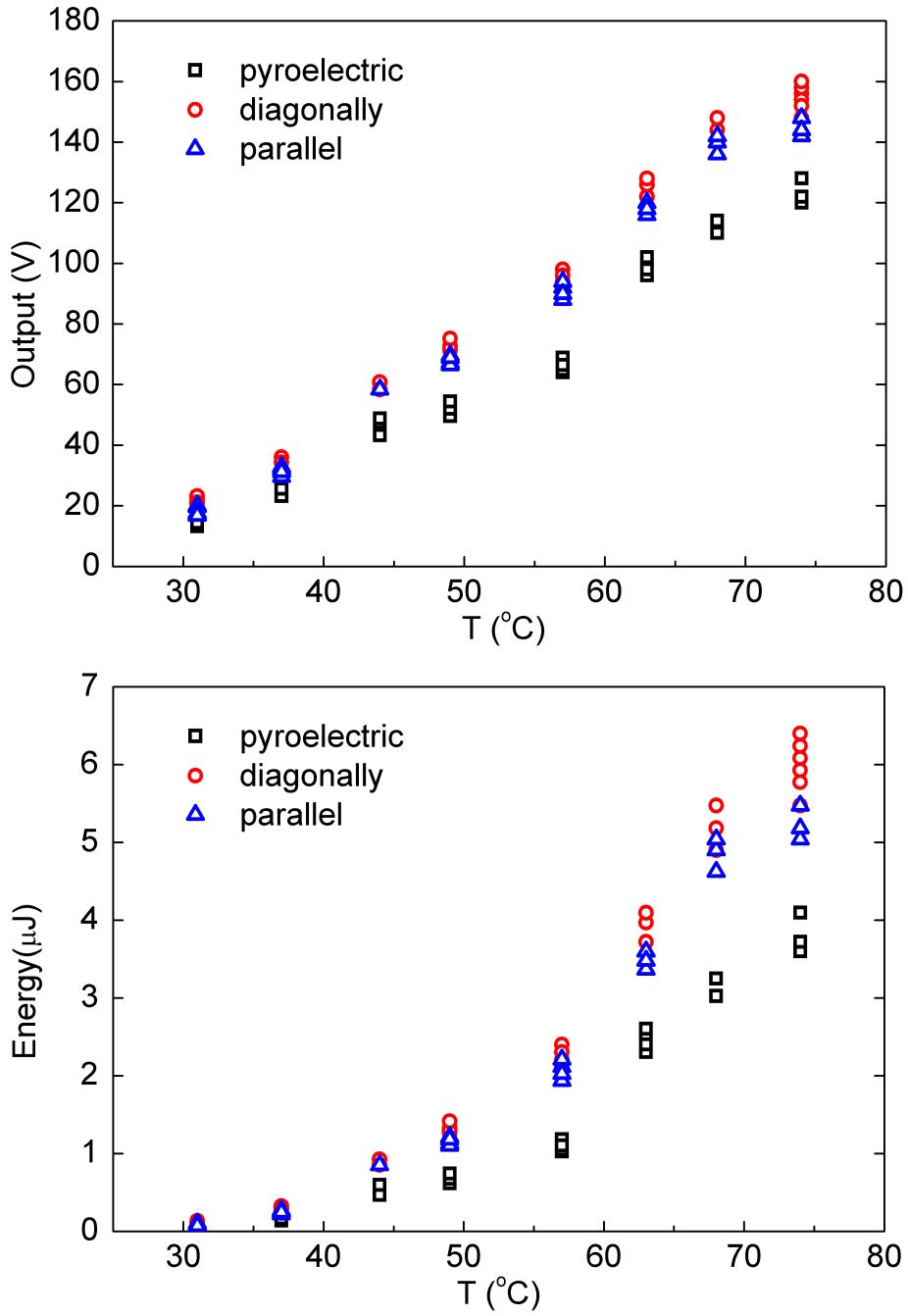

Figure 3.17: *First set of composites output voltage and energy with different geometries and comparison with pure pyroelectric response of LDT-0 samples. SMA A_s phase transition temperature is $\approx 40°C$.*

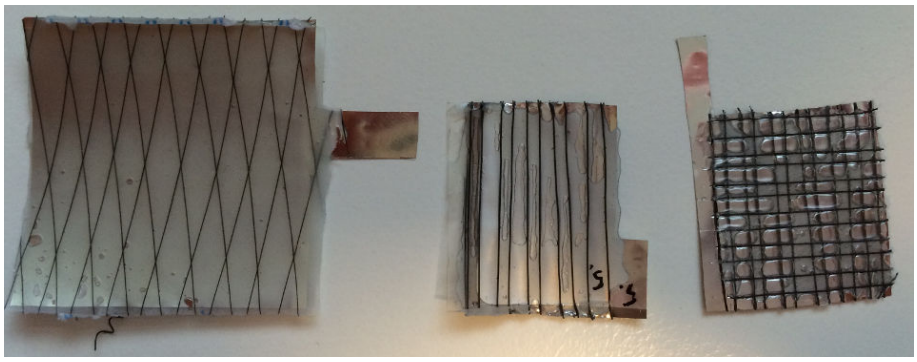

Figure 3.18: *Mesh and stent-like structures with NiTi wires on PVDF as proposed by Nimesis Technology.*

3.3.2.4 Composite with optimal geometry

The results of the second set of composites from figure 3.14b, are shown in figure 3.19. The output voltage behavior of the PVDF composites is similar to that of the MFC composites. The pyroelectric effect linearly increases with temperature, and at low temperatures there is no difference between composite output and pure pyroelectric output. When the A_s temperature is reached, the SMA starts contracting the PVDF, thus producing an additional piezoelectric voltage and changing the slope of composite output voltage. After the A_f temperature is reached, there is no more additional strain caused by the deformation, and the slope of the output voltage is once more equivalent to the pure PVDF pyroeffect slope.

The produced composite output voltage, coming both from pyroelectricity and SMA-induced piezoelectricity, is increased strongly when compared to the pure pyroelectric response of PVDF. The difference between pure PVDF and the composite at 40°C, which is the apparent A_f point of the composite, is equal to 133 V, which corresponds to a 77% voltage increase compared to pure pyroelectric output and a 210% energy increase compared to pure pyroelectric energy.

Harvested energy density as a function of temperature is an important characteristic of the harvester, since it allows comparison with MFC composites as well as other systems. It is presented in figure 3.19. The PVDF composite energy density goes as high as 2.7 mJ/cm^3 at 70°C. At 40°C, just above the A_f temperature, the energy density is around 427 μJ/cm^3.

The energy density of 427 μJ/cm^3 corresponds to a harvested energy of 11.8 μJ. This energy is not enough for wireless data transmission, and needs to be increased to at least 100 μJ for one burst. Considering the same composite performance, the same materials (implying the same SMA thickness and width, and same PVDF thickness) and the same geometries (SMA on each side of PVDF with 50% surface coverage), we would have to increase the total active volume of the composite up to 234.2 mm^3 to obtain 100 μJ. This volume depends on parameters such as the active length of the composite L, the active width of the composite W and the number of SMA ribbons n on each side of PVDF. With other parameters being constants of the material (PVDF thickness = 0.11 mm, SMA width = 2 mm, SMA thickness = 0.04 mm) we can write a system of equations:

$$\begin{cases} \text{Active volume} = L \cdot W \cdot 0.11 + 2 \cdot n \cdot (L \cdot 2 \cdot 0.04) = 234.2\ mm^3 \\ \dfrac{\text{SMA surface}}{\text{PVDF surface}} = \dfrac{L \cdot 2 \cdot n}{L \cdot W} = 0.5 \end{cases} \tag{3.3}$$

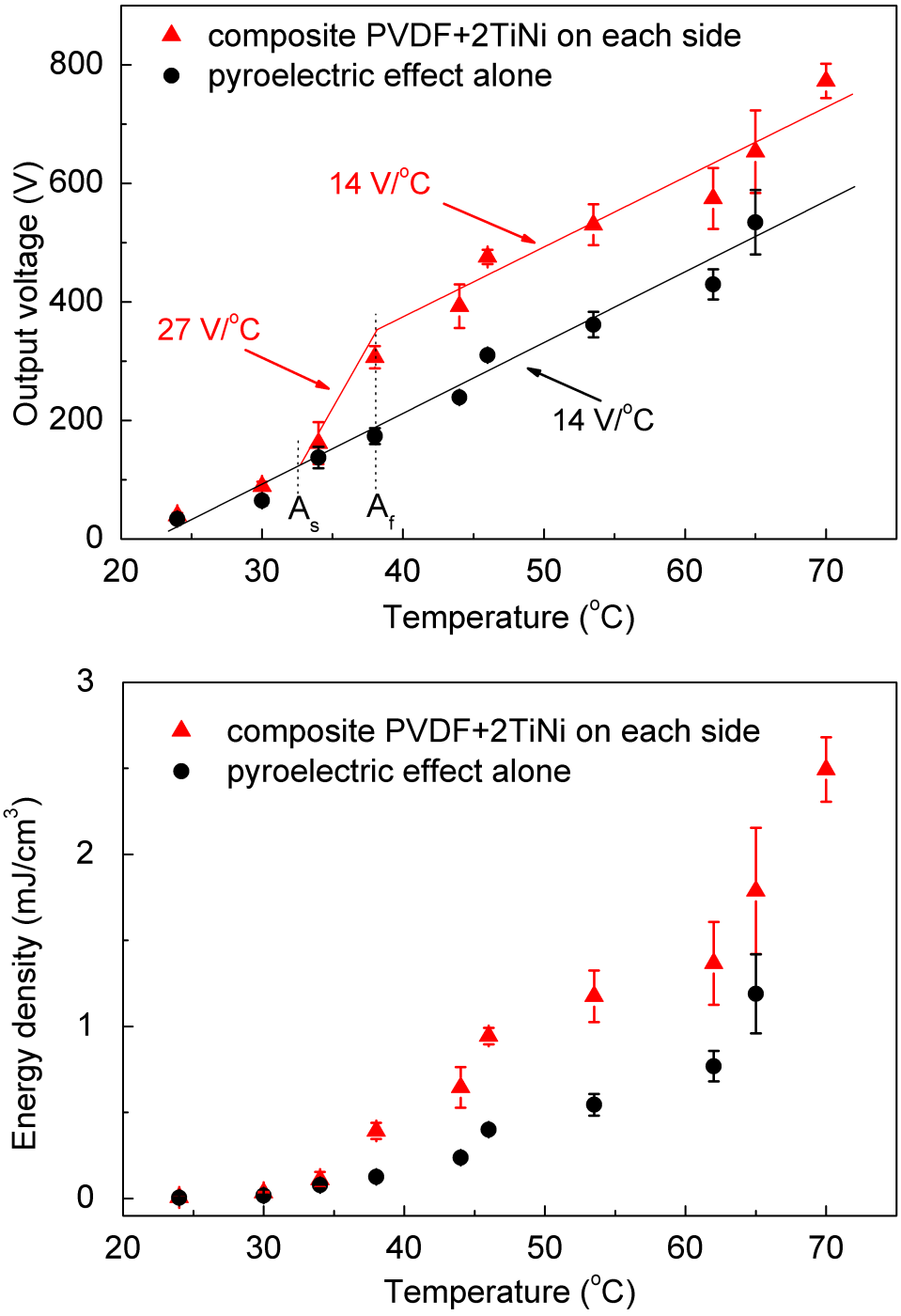

Figure 3.19: *Composite output voltage and energy and comparison with pure pyroelectric response of 110 µm PVDF at different temperatures. Empty symbols represent the actual measured values, and filled symbols show the average value for each temperature. The corresponding trend lines are drawn manually.*

By solving these equations we find that $L \cdot n = 390$ and $W = 4n$. If we now fix the number of SMA ribbons to 10, we will obtain values of W=40 mm and L=39 mm. This means that PVDF composite with active area of around 4×4 cm^2 and SMA/PVDF ratio of 50%, at 40°C will be able to produce 100 μJ energy, which is sufficiently for wireless data transmission.

As can be seen from figure 3.19, energy has a non-linear dependency on temperature, and in order to harvest small temperature variations, it is critical to increase the electric response of the composite within this small ΔT. For this, the use of an SMA with a sharp phase transition is required. It is worth noting however that generally the SMA with sharp transitions produces less mechanical work, so less strain will be transferred to the piezoelectric layer. A compromise should be found depending on the application, temperature range and temperature variations.

The summary of output voltage, energy and energy densities for the second set of composites is given in table 3.6.

Table 3.6: *Summary of voltage, energy and energy density outputs for pure PVDF and PVDF+SMA composites from the second set. Each value is an average of 5 measurements. ΔV and ΔE values are calculated as a relative increase to the value of PVDF alone at the same temperature.*

	PVDF alone	PVDF+4NiTi
V at A_s [V]	64.8	88.9
V at A_f [V]	173	306
E at A_f [μJ]	3.8	11.8
E_d at A_f [μJ/cm^3]	186	427
V at 70°C [V]	699	773
E at 70°C [μJ]	61.1	74.8
E_d at 70°C [μJ/cm^3]	2213	2710
ΔV at A_f [V (%)]	-	133 (77)
ΔE at A_f [μJ (%)]	-	8 (210)
ΔV at 70°C [V (%)]	-	74 (10)
ΔE at 70°C [μJ (%)]	-	13.7 (22)

As an experimental observation, we can note that at temperatures higher than A_s, the composite was visibly shrinking when placed into the oil. It also took longer time for the voltage signal to rise to its maximum value, as there is an effect of latent heating and transformation of SMA which takes some time. Starting from approximately 65°C, the SMA started to unglue from the PVDF on one side. Above 70°C, the composite could not flatten completely on cooling, indicating that the strength of PVDF was not enough to pull the SMA ribbons back to their initial position. Beyond 75°C the SMA was unglued from both sides of PVDF and no further measurements were possible. Therefore, the application temperature range is limited mostly by the bonding layer, which becomes weak at higher temperatures, as well as the elastic properties of PVDF, which may not be sufficiently stiff at high temperatures, to recover the SMA to its initial cold shape on cooling.

As it was the case for MFC composites, the apparent A_s and A_f temperatures of PVDF composites are higher than the corresponding temperatures of a stand-alone NiTiCu SMA ribbon. The expected A_s temperature is 29°C, whereas the value depicted from figure 3.19 is around 32°C.

The expected A_f is 32°C, whereas the depicted value is around 40°C. This shift observed in the composites is however larger than the shift observed during R(T) measurements of ribbon on substrate (figure 3.11); moreover, the shift seems to be more pronounced for the MFC composite than for the PVDF one.

Since the direct strain vs. temperature characteristic response of the actual NiTiCu ribbons was not measured, we cannot be sure of the exact temperature when the deformation takes place, and the exact impact of the substrate nature (material, rigidity) on the transformation temperature. Of course, the piezoelectric layer is a natural strain sensor itself, but this method is indirect, and additional experiments should be made to directly observe the composite deformation in order to confirm at what temperatures the NiTiCu strain is transferred to the piezoelectric layer. For example, laser interferometry in combination with micro-mirrors placed on the composite can be used for calculation of the actual developed strain on heating[187].

3.3.2.5 Sign of the piezo/pyroelectric effects

As mentioned in[49], in order to be effective, the composite must be designed in such way as to provide the same output voltage sign of pyroelectric and piezoelectric effects. Therefore, the sign of the SMA layer strain (tension or compression) must be chosen with respect to the sign of the exploited piezoelectric constants .

In our NiTiCu/PVDF composite energy harvester, the effects are of the same sign, resulting in an increased generated voltage and energy. Since the g_{31} piezoelectric voltage coefficient is positive for the PVDF[13], its compression will yield in voltage of positive sign. The same reasoning is also valid for the pyroelectric coefficient, which is positive, meaning that on heating the voltage sign will be positive. Therefore, in our experimental conditions the pyroelectric effect at heating has the same sign as the piezoelectric effect at longitudinal contraction due to SMA shortening. In general, for such types of composites, mechanical engineering must be considered with respect to the signs of piezo- and pyro-electric coefficients for every application case.

3.3.3 Summary

Original hybrid laminated composites composed of a fully flexible piezoelectric polymer and a shape memory alloy were fabricated and tested. Their ability to harvest energy from temperature variations was experimentally shown.

At 40°C (i.e. temperature variation of ≈20°C) the composite comprising PVDF with four NiTiCu ribbons and having an active volume of 27.6 mm^3, harvested 11.8 μJ of energy, which corresponds to an energy density of 0.43 mJ/cm^3. This energy density is sufficient to meet the requirement for wireless data transmission and can be potentially used for such applications by simply increasing the active area of composite while keeping a reasonable size (4x4 cm^2).

Hybridization of an SMA with a pyro/piezoelectric polymer increases remarkably the output of the pyroelectric polymer alone: the output voltage was increased by 77% and the output energy was increased by 210% at the A_f temperature of composite.

The measurements should be done in an open-circuit configuration during deformation for effective energy harvesting: the generated charges must accumulate to their maximum value before being harvested.

Since the PVDF charge leakage is considerably high at elevated temperatures, arrangements should be made to work around this issue: either charge acquisition should be done very shortly after heating to loose the minimum of charges, or lower application temperatures should be targeted.

3.4 Comparison of composites

Since two different piezoelectric materials were used for the fabrication of the same functional type of composite, it is interesting to compare the outputs of both devices. The active volume of MFC composite (46 mm^3) was almost twice bigger than that of PVDF composite (27.6 mm^3). The ratio of SMA/piezoelectric active surfaces was 66% for SMA and 50% for PVDF composite. Despite these differences, the energy density values can be used for comparison, since they are representative of the composite performance independently of the volume. Table 3.7 summarizes the produced voltages and energy densities for the two composites: PVDF with four NiTiCu ribbons, and MFC with two NiTiCu ribbons. At the A_f temperature, the PVDF-based composite produces over 220% higher voltage and over 560% higher energy density than the MFC composite, and this despite a lower SMA/piezo surface ratio. Along with superior flexibility and lower price of the PVDF, this result makes it a very interesting and promising candidate for flexible thermal energy harvesting.

Fairness of the comparison of the two composites, however, can be argued. Their parameters, i.e. capacitance, piezoelectric and pyroelectric charge coefficients, Young's modulus and geometries are different. For these differences, purely physical comparison of the composites is probably not possible. But what is important for the practical applications, is the amount of voltage and energy which a thermal harvesting device with a certain size, at a certain temperature difference can deliver to the consumer device. And based on this judgments, the PVDF composite outperforms greatly its MFC-based predecessor.

Table 3.7: *Voltage and energy density values for MFC and PVDF composites. The apparent A_f is ≈47°C for the MFC and ≈40°C for the PVDF composite.*

	volume [mm^3]	SMA/piezo surface [%]	V@A_f [V]	E_d@A_f [$\mu J/cm^3$]	V@70°C [V]	E_d@70°C [$\mu J/cm^3$]
MFC+2NiTi	46	66	94	65.3	142	149
PVDF+4NiTi	27.6	50	306	427	773	2710

3.5 Conclusions and perspectives

In this chapter we have validated the concept of coupling a shape memory alloy with a fully flexible pyro/piezoelectric material for thermal energy harvesting. It was experimentally shown that the harvested energy is increased compared to pyroelectric material alone in the temperature range corresponding to the phase transformation in the SMA.

The original hybrid MFC+NiTiCu laminated composite was optimized compared to previous work. An MFC of different type was used, with a surface area closer to SMA ribbons, and SMA/MFC surface ratio of 66%. The bonding quality was improved by stronger epoxy glue. Finally, a new measurement procedure was implemented, allowing for better homogeneity of heating and stress transformation, and therefore a more precise evaluation of the composite output.

A novel hybrid PVDF+NiTiCu laminated composite was made. Its performance in terms of output voltage and energy density was measured and found to be superior to the MFC-based composite. At 40°C the composite comprising PVDF with four NiTiCu ribbons and having active volume of 27.6 mm^3, harvested 11.8 μJ of energy, which corresponds to an energy density of 0.43 mJ/cm^3. Since PVDF has a lower Young's modulus than MFC, even higher deformations (hence higher voltages and energies) are possible with further proper optimization. Combination of high flexibility, relatively low price and bio-compatibility makes PVDF a perfect candidate for such types of flexible thermal energy harvesting devices with sensing capabilities. Coupling PVDF with SMA will further allow temperature threshold sensing capabilities.

However there are a number of possible improvements to be made to the composite. Work still needs to be done in order to increase the efficiency of harvesting with small temperature variations. For example, an SMA with sharper phase transition could be used, which could be obtained by adjusting NiTiCu composition. Alternatively, a different shape memory alloy, e.g. CuZnAl or CuAlNi, could be used. Also, arrangements should be made to directly measure the strain transferred from SMA to piezoelectric layer, to understand the impact of the bonding layer on overall performance. Finally, advanced geometries such as stent structures should be further studied for composite improvement.

The energy densities produced by the PVDF composite are appropriate for modern wireless protocols for simple data transmission with reasonable scaling-up of the composite area. However, the generated voltages are too high to be used directly in the consumer electronics. Therefore a custom power management is necessary to lower the voltage with minimum loss of energy.

Chapter 4

Energy harvesting prototype

Disregarded alternative power sources often depend on uncontrolled environmental conditions, and as such often operate in discontinuous, even random, mode. Since they usually provide low energies, which are rarely produced in a form that is readily usable as a power source, a power management scheme is necessary to operate such systems. The ideal power management will control the energy harvesting operation, store the energy in a storage medium such as a capacitor or a rechargeable battery, provide the required voltage and current to the sensor, and intelligently control the power distribution to the sensor and the subsystems[39].

A thermal energy harvesting device is expected to be able, at a given temperature variation, to power a low consumption electronic system with a stable DC voltage of around 1.5–5 V. The dimensions of the device should generally be discreet: small, thin or flexible depending on application. The credit card format (8×5 cm) with a thickness of a few millimeters would be compulsory for certain applications, such as payment display cards with integrated dynamic security[188].

This chapter is dedicated to the design and construction of a complete energy harvester prototype. The core of the prototype is the PVDF generator, producing useful charges upon heating and cooling. In order to harvest these charges, several elements are needed, as schematically illustrated in figure 4.1. First, a thermal switch is necessary, which would control the transfer of charges from PVDF to management circuit in a suitable way. Second, the management circuit needs to rectify and lower the generated high voltages. In order to ensure high efficiency of the conversion and small size of the device, a custom surface mounted circuit is desired. Finally, a housing is essential, that would hold together all the components, and let the thermal energy pass in and out freely.

A working prototype was built, comprising all the necessary elements, and able to power a wireless emission card. We will now explain in detail the materials and methods used for the fabrication of the prototype, and will present its performances.

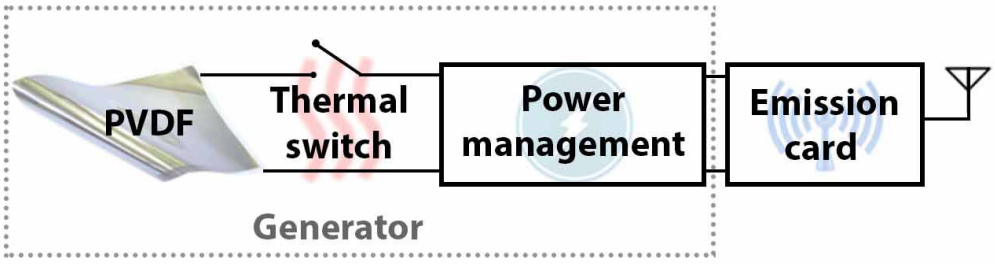

Figure 4.1: *Schema of energy harvesting prototype.*

For simplicity of fabrication and demonstration purpose we have first built a prototype with PVDF alone, exploiting only its pyroelectric effect. Once the prototype is optimized with PVDF alone, we will replace it by an SMA composite to increase the produced energy, and add temperature threshold sensing functionality for the final energy harvesting device.

4.1 Thermal switch

As discussed in chapter 2, section 2.3, in order to maximize the harvested energy, the harvester should operate in open circuit conditions during the charge generation, and charges should be collected at the end of this generation stage. Thus, a switch is necessary to transfer the charges from PVDF to the management circuit. This transfer should be done upon both heating and cooling, when the desired temperatures are reached. Between these temperatures, the switch needs to be in its open-state to allow charge accumulation in the PVDF. Also, in order to increase the overall conversion efficiency, ideally the switch should not consume nor dissipate any energy; in other words, it should at least not be an active component.

4.1.1 Bimetallic switch

Commercial thermal switches, consisting of bimetallic elements and triggering at a certain temperature, are readily available. We have tested several models, with a triggering temperature of 50°C. We initially chose Airpax 6700 series (inset in figure 4.2) due to its compact size and low contact resistance (50 mΩ).

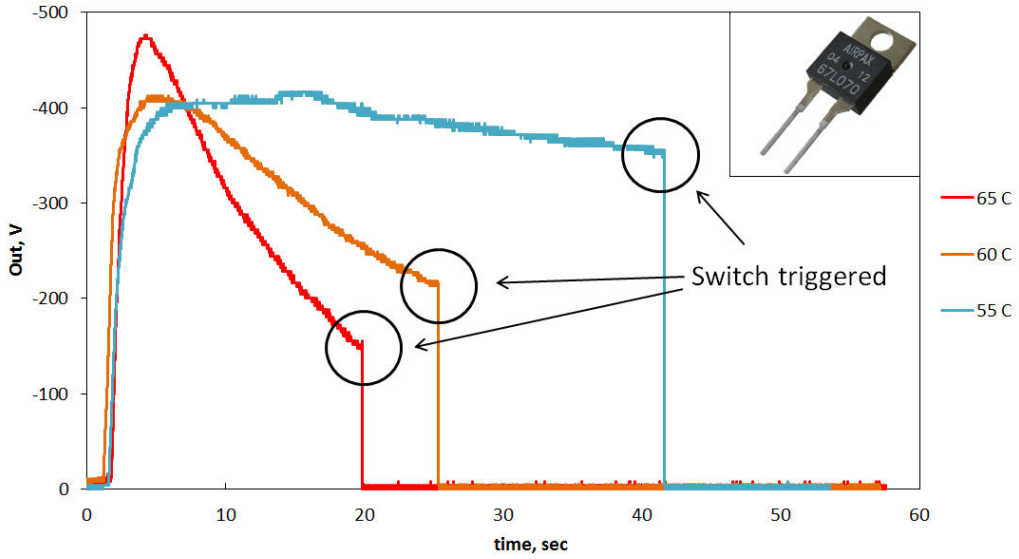

Figure 4.2: *PVDF self-discharge with 50°C bimetallic switch heated in oil thermostat. Voltage is measured with contact-less voltmeter. Inset: Airpax 6700 bimetallic thermal switch.*

The tests were performed by plugging the switch to the PVDF generator and heating both at the same time either in an oil thermostat or in an oven. The voltage generated by PVDF was measured with a contact-less voltmeter, and the voltage drop down to zero corresponded to the switch trigger moment.

Heating in oil thermostat was done with temperatures varying between 50 and 65°C. It took the switch from 20 to 40 seconds to trigger when heated to 65 and 55°C, respectively. However, after 20 seconds at 65°C, only 30% of PVDF charges were left, the rest dissipated due to self-discharge. At lower temperatures it takes longer for the switch to trigger, but the self-discharge is also slower; as a result the harvested voltage is higher for lower temperatures (figure 4.2). It would seem that the operation at 55°C could be useful, since the self-discharge is relatively weak.

Therefore tests in conditions closer to real use, with heating in an oven, i.e. in air rather that an oil bath, were performed.

When the switch was tested in an oven, the results were not satisfying: the switch took too long to trigger. While the PVDF takes only a few of seconds to reach its maximum voltage, the switch took up to 10 minutes to trigger. During this time the PVDF would have already lost most of its generated charges due to self-discharge. Such a long triggering time may be explained by a relatively thick plastic packaging of the switch, that slows down the heat exchange. Therefore, despite their immediate availability and simplicity of use, these bimetallic switches were considered not suitable for our application.

4.1.2 SMA switch

We have therefore decided to design our own thermal switch. The idea of making a mechanical switch consisting of an SMA wire, with same transformation temperatures as those used in the energy harvesting composite came naturally. In this way, the switch would trigger roughly at the same temperature where the harvester reaches its maximum energy.

The principle of our SMA switch is simple: an SMA wire is connected to a bendable steel rod, which acts as both a bias force spring and an electrode at the same time. Two electrodes are fixed on either side of the rod (figure 4.3). At room temperature, the rod is in contact with the cold electrode. When the assembly is heated, the SMA wire pulls the rod, which bends and goes first into an intermediary position before contacting with the hot electrode. When the rod is in an intermediary position, it does not touch any electrode, keeping the circuit in open-state. The transition zone corresponds to the temperature range between A_s and A_f, and can be additionally adjusted by changing either distances between the rod and the electrodes, or the tension of the SMA wire. PVDF charges during this transition zone.

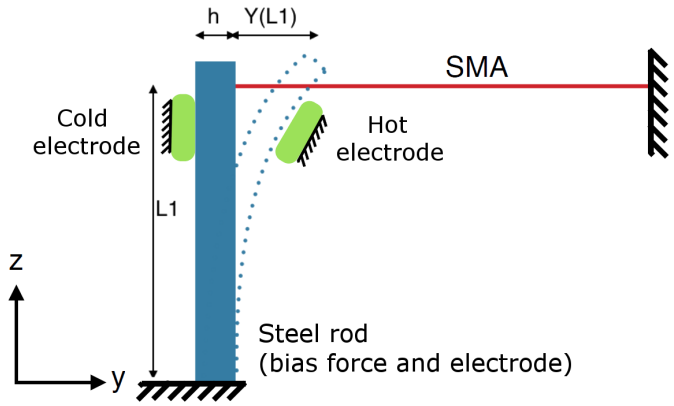

Figure 4.3: *Schematic drawing of the functioning principle of SMA switch.*

Let us now calculate the deflection of the steel rod $y(L_1)$. We suppose that the deformation ε_0 of the free-standing SMA wire is known. The length of SMA wire in martensite phase (cold state) is equal to L_m. Then, when the wire is connected to the rod, the deformation of the wire is given by:

$$\varepsilon_{sma} = \varepsilon_0 - \frac{y(L_1)}{L_m} \tag{4.1}$$

Now we can estimate the force applied by the wire on the rod (knowing the radius R of the wire and its Young's modulus YM_{sma}):

$$F = \pi R^2 \cdot \varepsilon_{sma} \cdot YM_{sma} \tag{4.2}$$

This force will bend the rod:

$$\frac{\partial^2 y}{\partial z^2} = \frac{1}{\rho} = \frac{M}{YM_{rod} \cdot I_{Gx}} \tag{4.3}$$

where ρ is the curvature radius, M the moment of force, I_{Gx} the second moment of area, which can be expressed as:

$$|M| = (L - z)F \tag{4.4}$$

$$I_{Gx} = \frac{\pi}{4} r^4 \tag{4.5}$$

So by combining the two equations, we have:

$$\frac{\partial y}{\partial z} = \frac{L_1 F}{YM_{rod} \cdot I_{Gx}} z - \frac{F}{2 \cdot YM_{rod} \cdot I_{Gx}} z^2 \tag{4.6}$$

Finally, we obtain the equations of the linear deformation and the rod deflection:

$$y(z) = \frac{L_1 F}{2 \cdot YM_{rod} \cdot I_{Gx}} z^2 - \frac{F}{6 \cdot YM_{rod} \cdot I_{Gx}} z^3 \tag{4.7}$$

$$y(L_1) = \frac{L_1^3 F}{3 \cdot YM_{rod} \cdot I_{Gx}} \tag{4.8}$$

Combining now with equations (4.1) and (4.2), we obtain the final equation of the rod deflection:

$$y(L_1) = \left(\frac{L_1^3 \pi R^2 \cdot YM_{sma}}{3 \cdot YM_{rod} \cdot I_{Gx}} \varepsilon_0 \right) \left(1 + \frac{1}{L_m} \frac{L_1^3 \pi R^2 \cdot YM_{sma}}{3 \cdot YM_{rod} \cdot I_{Gx}} \right)^{-1} \tag{4.9}$$

The deflection represents the distance between the electrodes in the switch, and it should be sufficiently large to make adjustments possible, but not too large to ensure that the triggering time is short and reliable. Using equation (4.9) we adjust the deflection by changing the geometry of the switch (L_1, L_m) and the diameter of the rod (I_{Gx}). This allows the proper sizing of the switch, to make sure that the steel rod stays in its elastic region during its deformation.

The first prototype was realized with a steel plate instead of a rod. The NiTi wire was connected at one end to the plate, and at the other end to a micrometer adjustment screw for the precise tuning of the NiTi wire length and the steel plate deflection. At first, a switch with only a hot electrode was realized; the cold electrode was added later (figure 4.4). The gap between the hot and cold electrodes was adjustable by means of two smaller screws.

In order to maximize charge recovery while minimizing losses, and considering the working temperatures studied for PVDF, the triggering time of the switch at a given temperature should be less than a minute. This time can be adjusted by changing the gap between the electrodes: smaller

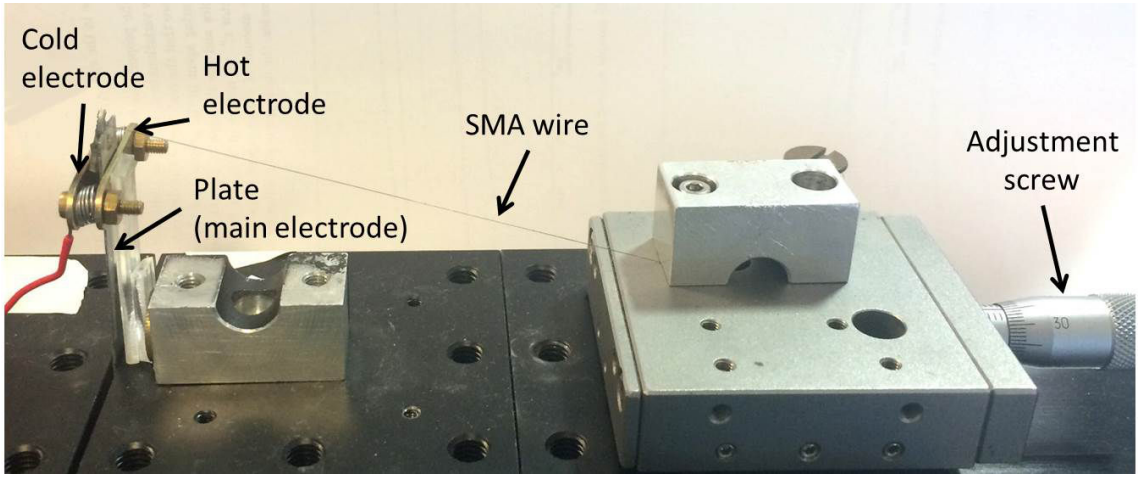

Figure 4.4: *First prototype of SMA-based switch with hot and cold electrodes.*

gap means faster triggering and bigger gap means longer triggering. However, if the gap is too small, the reliability of the switch is decreased, since very precise adjustments of the steel plate would be necessary. Conversely, if it is too large, the switch will not be triggered at all.

Figure 4.5 shows closing time of the switch with just the hot electrode, as a function of temperature and plate-electrode gap. We can see that both parameters have a great impact on the closing time: for example at 55°C, changing the gap from 0.12 to 0.20 mm increases the time by a factor 10.

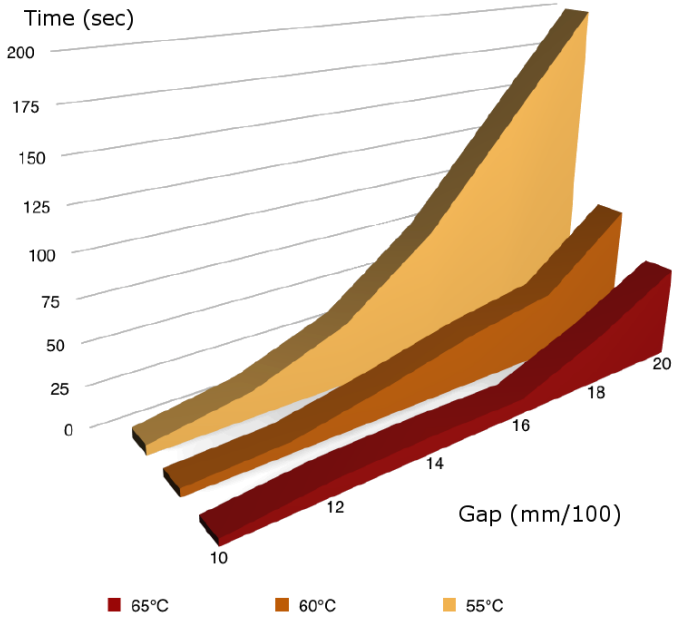

Figure 4.5: *SMA-based switch closing time as a function of temperature and plate-electrode gap (for the switch with only the hot electrode).*

The results for the switch with both hot and cold electrodes are similar. The difference in use is that now we must take into account both the time it takes to open from the cold electrode and then time to close into the hot electrode. From our tests on PVDF we know that optimized settings are a couple of seconds for opening, and 40 to 60 seconds for closing. These settings allowed to obtain a good response time of the switch, necessary for the efficient functioning of the energy harvesting. However, there were two major drawbacks to this first switch prototype: poor

quality of the contact electrodes (made of copper tape), which sometimes caused rebounds during triggering, and the size of the switch itself, which was quite bulky.

The second prototype was much more compact (credit card area format) and had improved contact quality. It was assembled directly inside a 7×5 cm box, which then served as a housing for the rest of the harvester components. The switch setup had a maximum thickness of 5 mm at the bottom of the box, shown in figure 4.6 (NB: thickness of 5 mm is due to the standard screws used, for ease of manipulation, and can be reduced with smaller screws). The previous theoretical calculations seen previously become important to achieve a functional switch of such compact geometry.

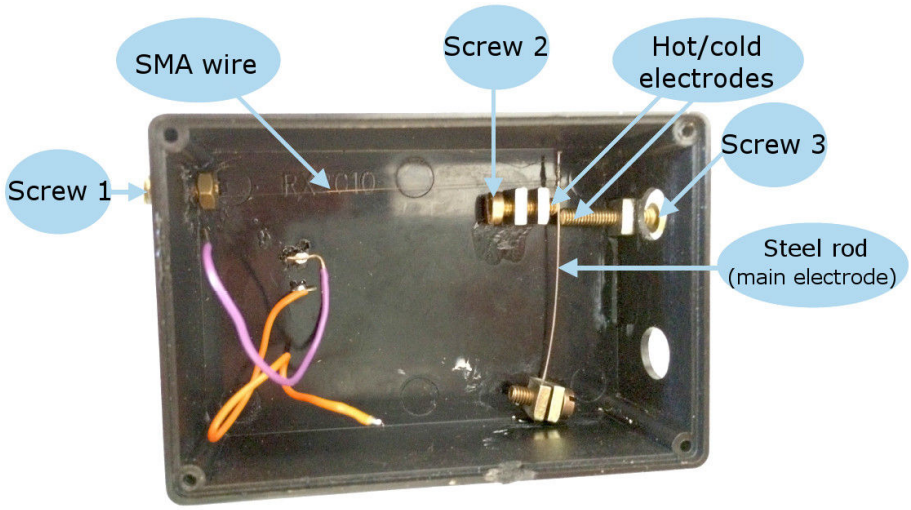

Figure 4.6: *Second prototype of SMA-based adjustable switch with hot and cold electrodes*

Figure 4.6 shows the main elements of the switch, including the steel rod, NiTi wire, cold and hot electrodes, and three adjusting screws. Two of the adjustment screws (2 and 3) also act as hot and cold electrodes respectively, and the steel rod also served as the main electrode. The role of each screw is the following:

- Screw 1: Preload adjustment of the force applied on the rod in the cold state;
- Screw 2: Adjustment of the distance between the rod and the hot electrode;
- Screw 3: Adjustment of the distance between the rod and the cold electrode. This adjustment is done when the assembly is in hot state and the SMA wire is contracted, otherwise the rod is in contact with the cold electrode.

The ends of screws 2 and 3, serving as hot and cold electrodes respectively, as well as the section of the steel rod making contact, were rounded and polished, to ensure good electrical contact. A close-up observation of the contact area is shown in figure 4.7. Measurements confirm the the good contact between the electrodes.

The NiTi wire used for the switch had an A_s temperature of 45°C. When heated to 60–70°C, the switch has shown good operational characteristics. At its initial state, the steel rod is in contact with the cold electrode, and the switch is in closed state (figure 4.8). When placed in a preheated

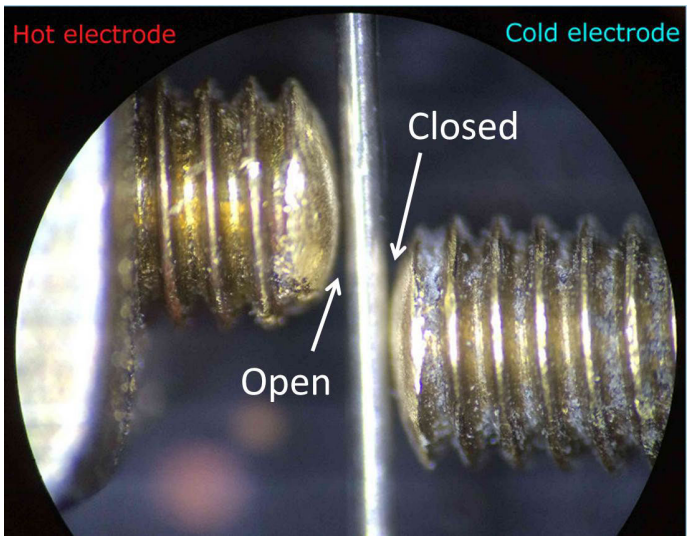

Figure 4.7: *Close-up photo of the contact zone between hot and cold electrodes, and the rod. In this case cold is in contact.*

oven, the switch opens after just a few seconds, as the rod bends and loses contact with the cold electrode. After about 40 seconds, the switch closes, as the rod comes in contact with the hot electrode. In the present conditions, the duration during which the switch is opened (≈40 s) is optimal for the PVDF to generate maximum charges and not lose them due to self-discharge. During cooling, the switch performs a reverse cycle, with however a longer opening period: it stays open for slightly more than a minute. This increased time is explained by slower cooling due to natural convection. Nevertheless, this will not lead to an increase in charge leakage, since at low temperatures the self-discharge is much slower, as shown in chapter 2, section 2.6.

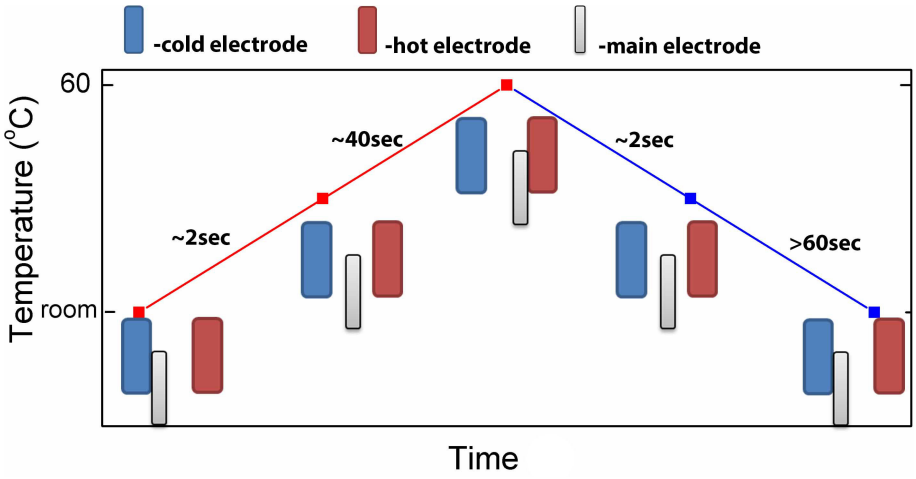

Figure 4.8: *Schematic of switching time between cold and hot electrodes. Time axis is not to scale.*

4.2 Power management circuit

The role of the power management circuit is to convert the voltage, generated by the PVDF and transferred via the switch (around 400 V), into a "usable" voltage of 1–5 V. Since the ratio of input to output voltage is very high, one-step conversion would result in high losses. As shown by Lafont[187], the simplest solution is to lower the voltage using a sufficiently big capacitor connected

directly in parallel; however, with our voltage values the conversion efficiency will not exceed 50%. We therefore decided to make a two-step conversion circuit: first step to lower the voltage to 10–15 V, and second step to lower it further to a stable 1–5 V. The first step lowers the voltage to a value which fluctuates according to the input voltage and energy; this is not convenient, since it may exceed the requirements of the consumer device and damage it. The second step provides a stabilized and regulated voltage, independent on the input voltage and energy.

A schematic of the conversion circuit is shown in figure 4.9. The first step consists of a custom-made DC-DC buck converter, and the second step is a commercial buck converter (TI TPS62122). We will now focus on each step separately and explain the conversion principle.

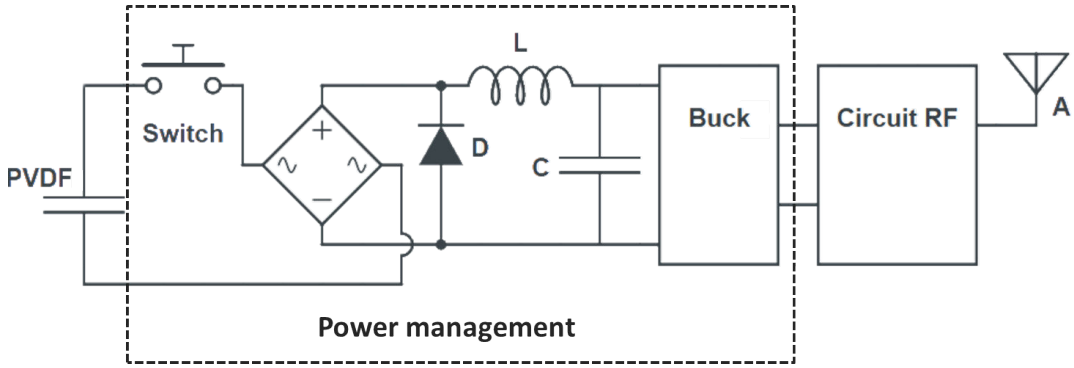

Figure 4.9: *Complete conversion power management circuit. The input (PVDF element) is on the left side, and the output is on the right, supplying RF transmitter with antenna.*

4.2.1 First step voltage conversion

The first step is a DC-DC converter, which lowers the voltage through the ratio between the input and output capacitors. The input energy is stored in the PVDF capacitance C_{in}. It is then rectified through a diode bridge, and transferred via an inductor L to the output capacitance C_{out}, with efficiency η. From the law of energy conservation, we can write:

$$\frac{C_{out}V_{out}^2}{2} = \eta \cdot \frac{C_{in}V_{in}^2}{2} \tag{4.10}$$

From there we can extract the output voltage V_{out}:

$$V_{out} = \sqrt{\frac{\eta \cdot C_{in}}{C_{out}}} V_{in} \tag{4.11}$$

The output capacitance is associated with an inductor and a flyback diode (marked L and D in figure 4.9). When the switch is open, the electrical current in the circuit is zero. Once the switch is closed, the current rises in the inductor due to the voltage at its terminals. The voltage and current are linked by:

$$U = -L\frac{di}{dt} \tag{4.12}$$

where L is the inductance, di/dt is the current variation over time.

The voltage across the input capacitor is then reduced. With time, variation of voltage across the inductance decreases, thus decreasing its current. When the switch is opened again, the current

becomes zero and the voltage across the inductor flows towards the output. The inductor discharges all its energy, stored in the form of a magnetic field, into the output capacitor.

The flyback diode is used to eliminate the voltage spike across the inductor, when it sees a sudden decrease of current. As previously shown, the diode efficiency in such configuration increases with increased output voltage[187], hence the interest of two-step conversion with relatively big intermediary voltage.

Another advantage of this type of energy transfer is that it is independent of time: the PVDF is discharged into the inductance, which first transforms the energy into the magnetic form, and then transfers it to the output capacitor. Thus the first-step voltage conversion depends only on the ratio of input and output capacitances. This structure has no active components, therefore no energy is lost to power the components. However, some losses are inevitable (Joule heating, imperfections of the components) and the efficiency η will never be 100%. Here, with proper optimization described further, we were able to obtain up to 70-75% efficiency conversion.

4.2.1.1 Component optimization

Diodes

Since the input voltage delivered by the PVDF can be as high as 400 V, the use of high breakdown voltage diodes is necessary. This usually implies very resistive diode, with significant conduction losses and high threshold voltage. This also justifies the choice of a conversion in two steps. After a series of tests (figure 4.10), MURS140 type diodes were chosen to be the most effective. These diodes can withstand up to 400 V continuous reverse voltage before breaking down, and have a fast recovery time of 50 ns[189].

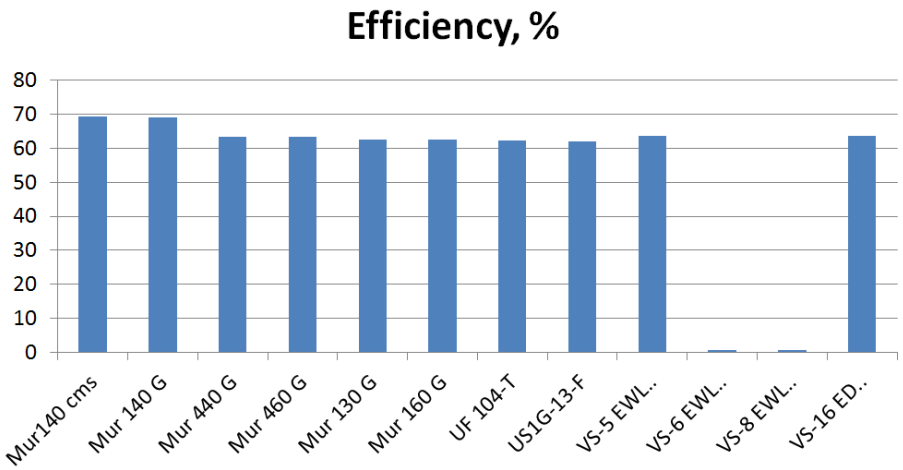

Figure 4.10: *Conversion efficiency of different diodes. Input conditions: inductance L=1.2 mH, R=2.7 Ohm; V_{in}= 296 V; C_{in}=4.6 nF; C_{out}=2.14 μF.*

Inductors

The inductor is a key element of the conversion. It is also one of the most bulky ones, that takes the most physical space. It must be capable of storing all the energy generated by the system, which generally means high inductance value. At the same time, higher inductance means bigger volume,

which should be kept at minimum. Therefore, a compromise between performance and volume is necessary. Similarly, its series resistance should be low, and its saturation current needs to be high (at least higher than the current generated by the PVDF). After testing various commercial inductors (figure 4.11), a compromise was found for an inductor CoilCraft 105D, of dimensions 10mm x 10mm x 4.2mm, inductance L = 1 mH and series resistance R = 1,7Ω.

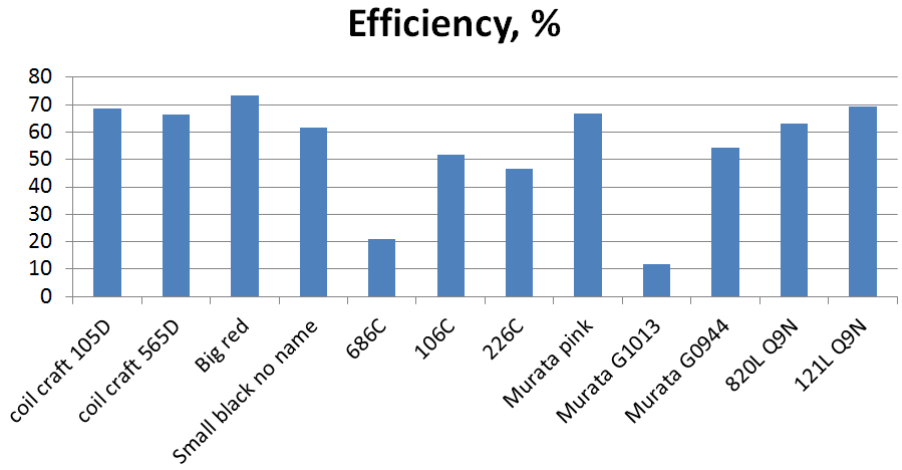

Figure 4.11: *Conversion efficiency of different inductors. Input conditions: diode MURS 140; V_{in}= 312 V; C_{in}=4.6 nF; C_{out}=2.14 µF.*

Capacitances

In order to optimize the values of input and output capacitances, a simulation in LTspice circuit simulator was performed (figure 4.12). The input voltage was fixed to 300 V, and the output voltage, energy and efficiency were calculated as a function of various C_{in} and C_{out} values.

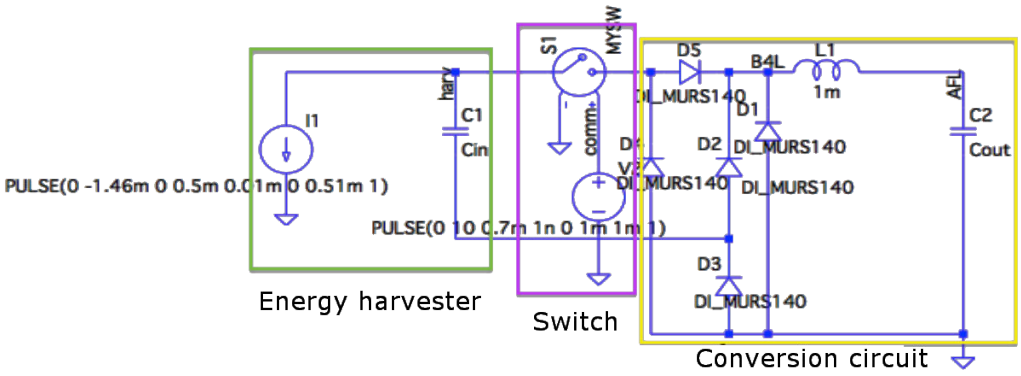

Figure 4.12: *Simulation in LTspice of the first step converter, including diode bridge, inductor and flyback diode.*

Simulation results are shown in figure 4.13. The output voltage behavior is well in accordance with equation (4.11): it increases with increasing C_{in}, and decreases with decreasing $\frac{C_{in}}{C_{out}}$ ratio. The output energy and efficiency follow the same trend. It is therefore desirable to increase C_{in} and decrease C_{out}. The input capacitance depends on the geometry of the PVDF: reducing the thickness or increasing the surface area will increase the capacitance. The choice of the output

capacitor is up to us, nevertheless its value should not be too small, since the output voltage should not exceed 15 V (maximum voltage supported by the second-step buck converter).

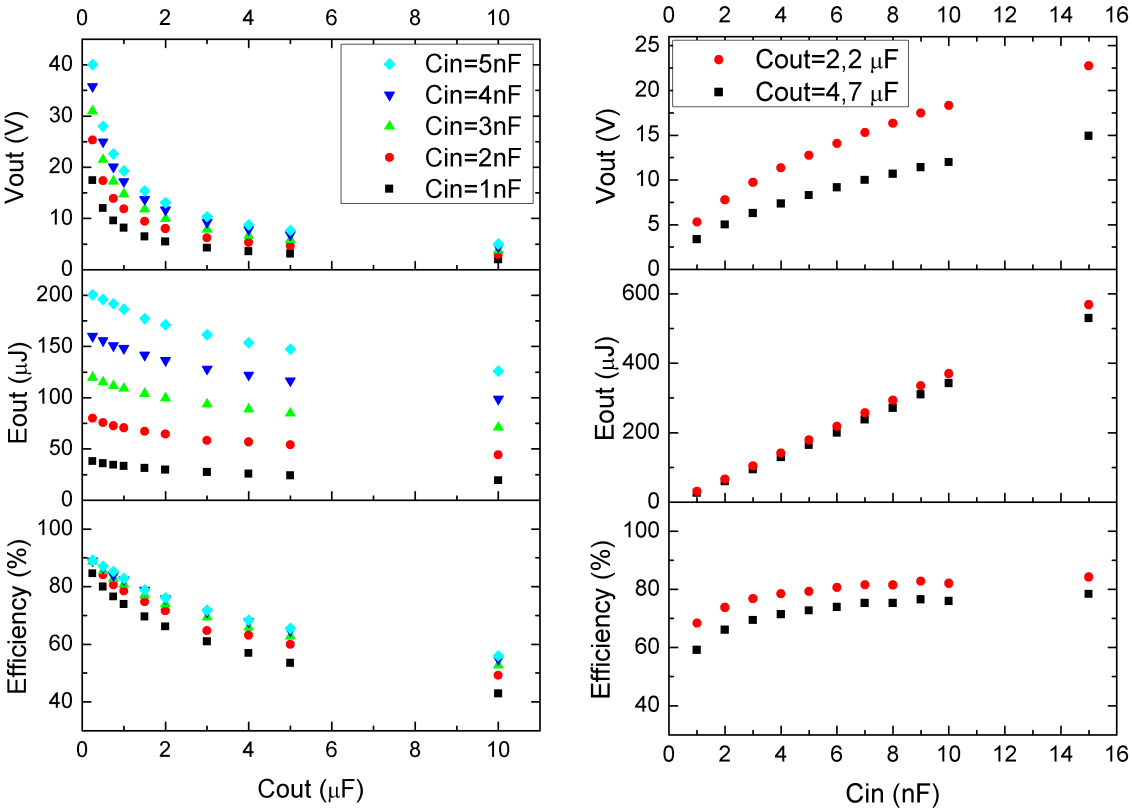

Figure 4.13: *Output voltage (V_{out}), output energy (E_{out}) and efficiency (η) as a function of output capacitance (C_{out}) and input capacitance (C_{in}).*

It is specified in the datasheet of the second-step buck converter[190] that the preferable input capacitance (i.e. the output capacitance of the first-step converter) should be a tantalum capacitor of 4,7 or 2,2 μF. So the simulation was run for these two fixed C_{out} values, varying the C_{in} values. The results are shown in figure 4.13.

The optimal input voltage for the second-step buck converter is ≈8 V. If achieve this voltage at the output of the first-step converter, we can expect the highest overall conversion efficiency. From figure 4.13, with the input voltage of 300 V, we have 8 V with following parameters:

- C_{out} = 4.7 μF : C_{in} = 4.8 nF, E_{out} = 155 μJ , η = 71.5 %
- C_{out} = 2.2 μF : C_{in} = 2.5 nF, E_{out} = 85 μJ , η = 75 %

Using C_{out} of 4.7 μF yields in slightly lower efficiency, than with 2.2 μF. However, the absolute value of output energy is almost twice as high and it meets the requirements of 100 μJ necessary for wireless transmission, therefore this capacitance value should be preferred.

Test circuit

Once all the components were provisionally determined, a testing circuit was built with manual switch, and experimental measurements were carried out and compared with simulation results. In

order to obtain repeatable input voltage values, the PVDF was substituted by a capacitor of 4.8 nF, charged to the desirable voltage by a voltage generator.

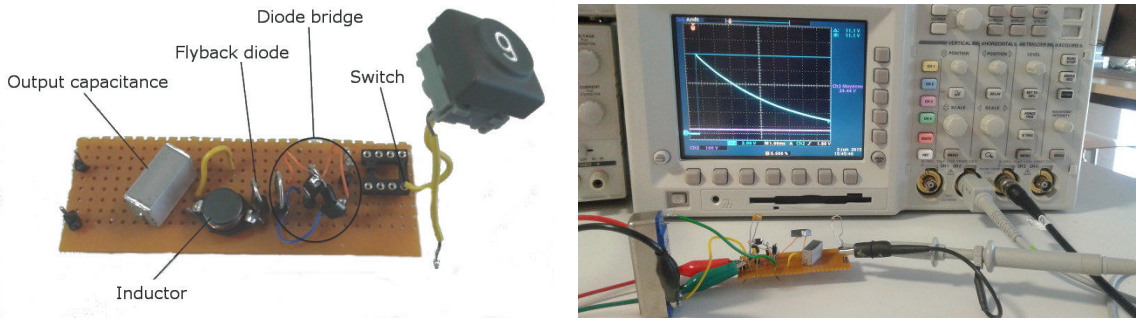

Figure 4.14: *Left: test circuit of the first-step converter. Right: typical measurement of the circuit output voltage.*

The measurement circuit is shown in figure 4.14. Comparison between experimental and simulation values of output energy, voltage and efficiency, performed for C_{in} of 4.8 nF and C_{out} of 4.7 μF, are shown in figure 4.15.

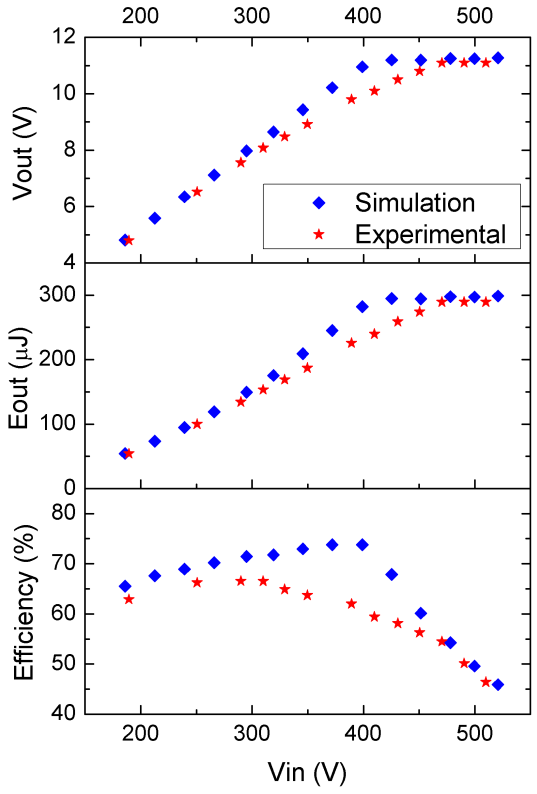

Figure 4.15: *Comparison of experimental and theoretical output energy, voltage and efficiency as a function of input voltage, for C_{in} = 4.8 nF and C_{out} = 4.7 μF.*

The first conclusion is that the experimental results fit quite well with the simulations. The measurements confirmed that with an input capacitance C_{in} of 4.8 nF and an output capacitance C_{out} of 4.7 μF, the output voltage is around 8 V for the input voltage of 300 V. In addition, the output voltage does not exceed 12 V, even for input voltages above 400 V. Therefore there is no risk of damaging the second-step buck converter, which cannot support voltages higher than 15 V.

Theoretically, the conversion efficiency increases with input voltage, until it reaches a maximum of 73% at 400 V. After 400 V, which is the breaking down voltage of MURS140 diodes, the efficiency drops quickly, due to the fact that the diodes become conductive in the reverse direction. Moreover, experimentally the efficiency already starts decreasing from about 310 V. We believe this is due either to saturation of the inductor, or to long exposure time of the diode to elevated temperatures of up to 75°C. In fact, the circuit that have spent longer time in the heated oven, have shown lower efficiency than the new diodes. For these reasons, in the final prototype the circuit should be isolated from overheating. Also it would be preferable to work at input voltages around 300 V or slightly lower.

4.2.2 Second step conversion

A commercial step-down buck converter from Texas Instruments (TPS62122) was used for the second-step conversion. The advantage of this converter is that it can convert input voltage of 2–15 V to stable voltages of 1.5–5 V, regulated by two resistances R_1 and R_2 (figure 4.16). As we pass from first-step to second-step converter, the output voltage and capacitance of the first stage become the input voltage and capacitance of the second. The output voltage and capacitance of the second stage are the final output values of the converter, which will be used to power the consumer device (in our case - a wireless emission card).

The converter was regulated to provide output voltage of 1.8 V, necessary for the emission card. To do so, the following components were used: R_1=300 kΩ and R_2=240 kΩ, C_{ff}=22 pF, L=22 μH and C_{out}=4.7 μF. Here, the choice of components was simpler than for the first-step converter, since most of them are given in the datasheet[190]. Only the appropriate $\frac{R_1}{R_2}$ ratio had to be chosen to set the desired output voltage.

The converter was also tested experimentally with various input capacitances, charged to different voltages. The output was observed with an oscilloscope, and presented a plateau of DC voltage, followed by a capacitance discharge decay (figure 4.16). The time length of the plateau depends on the input energy: higher energy means longer plateau.

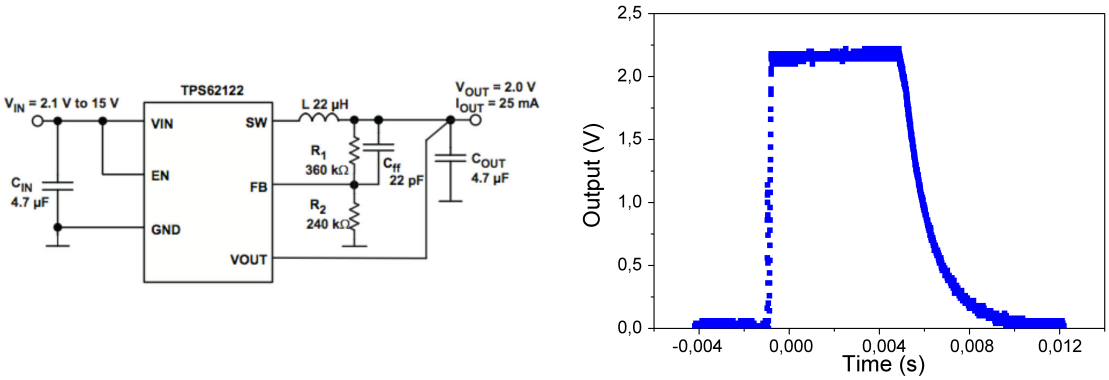

Figure 4.16: *Electric diagram and typical output of the TPS62122 buck converter. In this case the output voltage was set to 2.2 V.*

The output voltage of the commercial buck is 1.8 V when the input voltage is 3 V or greater. In these conditions, the efficiency increases with increased input voltage from 40% at 2 V reaching 85% at 6 V. From 6 V on, it gradually decreases, as seen in figure 4.17.

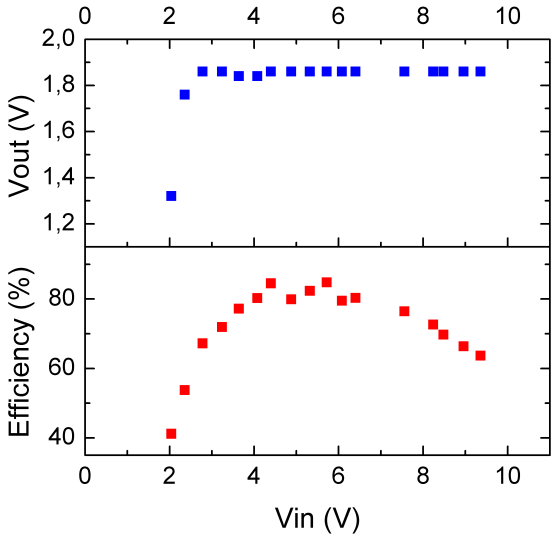

Figure 4.17: *Output voltage and efficiency of the TPS62122 buck converter, as a function of input voltage.*

As for the first-step converter, a compromise between efficiency and energy should be found, since a minimum energy is needed for applications. Here, the slightly decreased efficiency with increased input voltage may be compensated by an increase in output energy. We must therefore look at overall output of the converter, by combining the two steps together, to find their combined optimal functioning condition.

4.2.3 Final converter

The output energy of the final converter, combining first- and second-step conversions, was measured as a function of input energy, which corresponds to different temperature conditions of the harvester (figure 4.18).

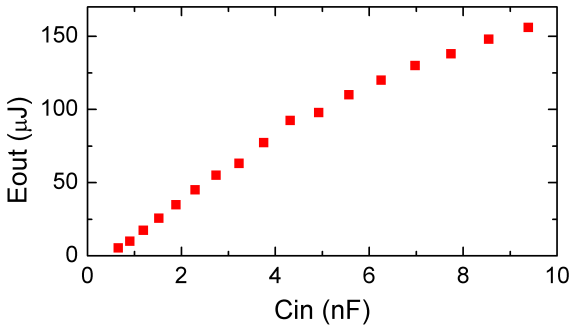

Figure 4.18: *Final output energy as a function of input capacitance (V_{in}=300 V).*

As previously, the harvester at this stage was "simulated" by a charged capacitor: various capacitances from 0.5 to 10 nF, charged to 300 V, represented different input energies. The output energy showed almost a linear increase with the input capacitance, i.e. input energy. Output energy of 100 μJ was obtained with input capacitance of 4.8 nF. However the practical capacitance of PVDF is limited by its size and thickness: with the credit card format of 110 μm thick PVDF, by stacking four PVDF sheets, we obtained up to 6.2 nF. Further increasing the capacitance is possible, but is troublesome.

When the input capacitance was fixed to 4.8 nF and the input voltage was varied, we have observed a linear increase of the output energy proportional to input voltage (figure 4.19). The overall efficiency varied from ≈36 to 47% at different voltages. The maximum efficiency of ≈47% was obtained for an input voltage of 300 V. Theoretically, we could obtain up to 62% efficiency: 73% at first-step and 85% at second-step. Practically it is lower possibly due to composite imperfections and variations. Nevertheless, in these conditions the output energy was ≈100 μJ, which is sufficient to power our wireless emission card. Therefore we have proceeded to mounting all the components together for the final prototype.

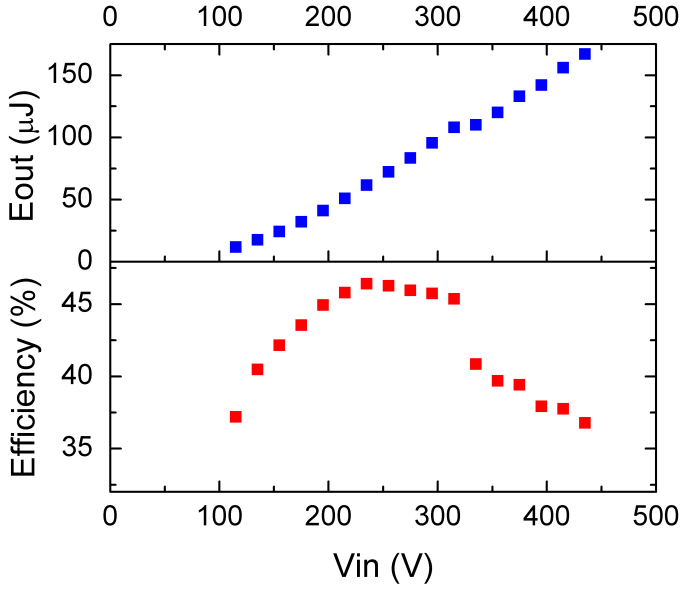

Figure 4.19: *Final converter output energy and efficiency as a function of input voltage (C_{in}=4.8 nF).*

For the fabrication of the final two-step converter, surface-mount technology was chosen in order to limit the bulk of the power conversion stage. The circuit design was realized with KiCad software and then printed on a PCB card in G2Elab. The components were mounted in CEDMS university facility. Consecutive steps of fabrication are shown in figure 4.20.

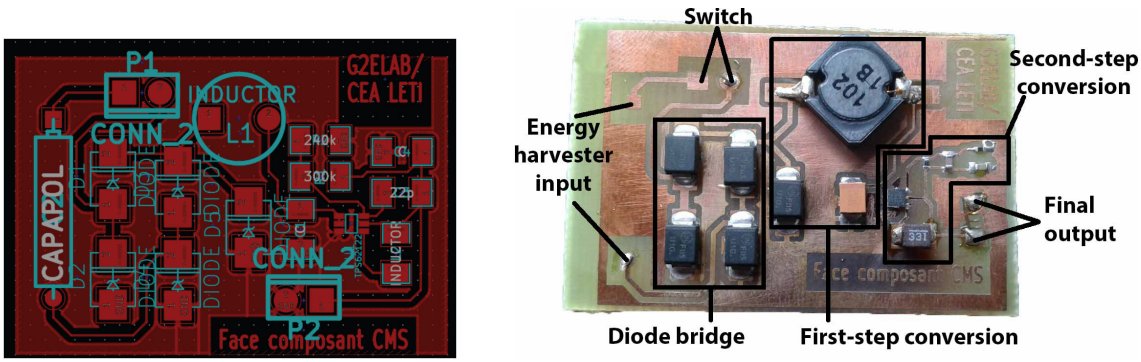

Figure 4.20: *Design of the converter in KiCad, and final printed PCB card with mounted components.*

4.3 Intermediary prototype: pyroeffect only

For this first intermediary prototype we used plain 110μm thick PVDF from MeasSpec, cut to 3 cm×4.8 cm sheets, without SMA. To increase the capacitance of the harvester, without increasing the produced voltage, we have connected four sheets of PVDF in a parallel stack. The overall capacity of the stack was 6.2 nF.

The components of the energy harvester were mounted together inside the 7×5 cm box. To ensure good heat convection inside the box, it was drilled with small holes on every side. The switch was mounted first at the very bottom, followed by PVDF and then the power management circuit. Figure 4.21 shows different assembly steps and the completer energy harvesting prototype.

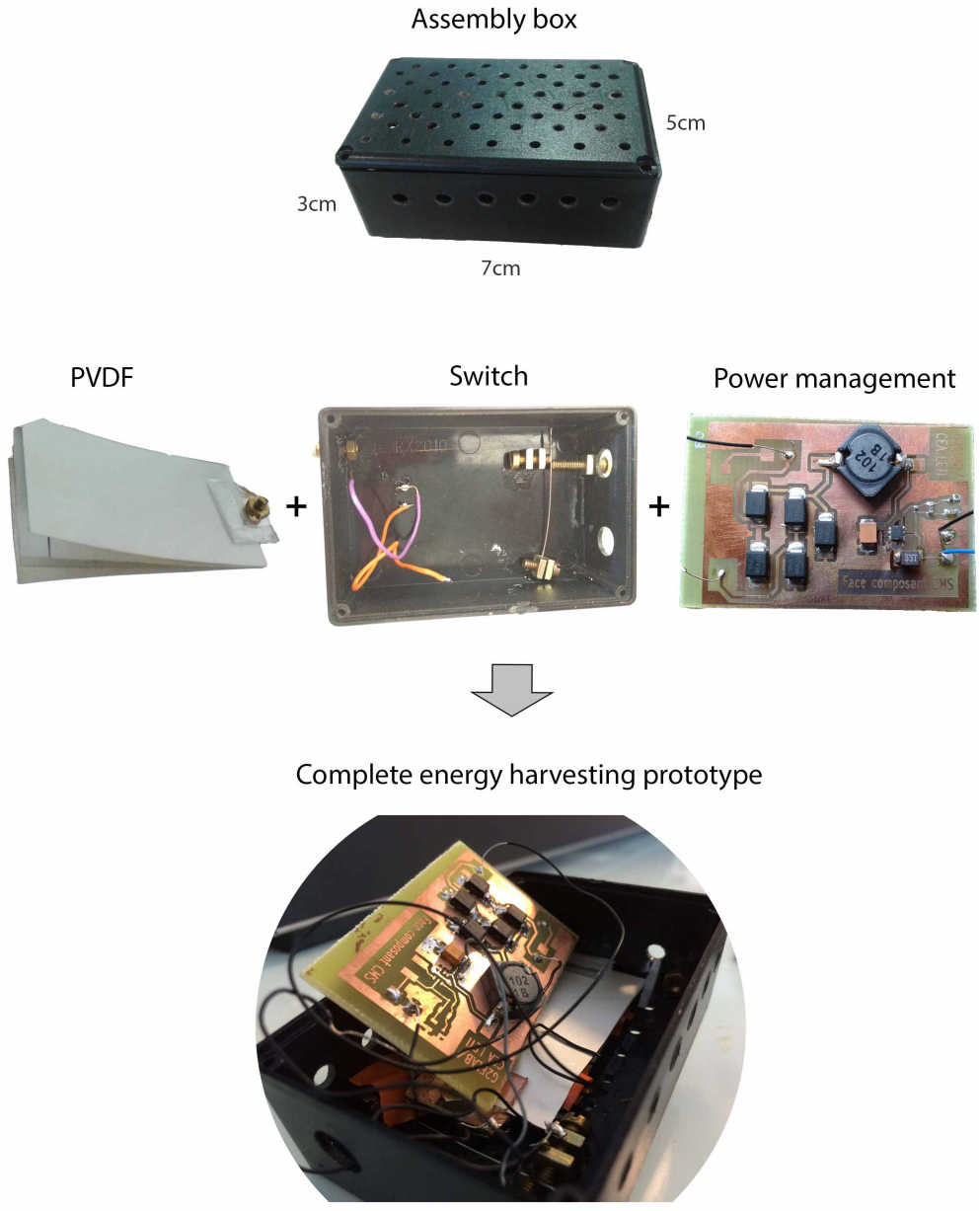

Figure 4.21: *Complete energy harvesting prototype mounted together inside the 7×5 cm box.*

When the energy harvester was heated to 70°C in an oven, it produced 1,86 V and ≈100 μJ at the output. On cooling, when the harvester was taken out of the oven, the same output was produced, which confirms that the switch and the conversion circuit function together correctly and in a predictable manner. We can now connect the harvester to the wireless transmission card, and test the functioning of the complete system.

4.3.1 Wireless transmission card

Since the available energy is limited, many researchers focus on minimizing energy usage by applying smart power management strategies. Duty cycling, data reduction, and mobility are used for reducing power consumption at the sensor level and consuming only as much energy as is harvested[39,191].

We have used a custom low-energy consumption wireless transmission node, developed with the CEA Showroom. The node consisted of an emission card and a reception card (figure 4.22). To power the emission card, pulses of at least 60 μJ are necessary. This energy was supplied by the energy harvester. The reception card was powered by external source of 3.5 V.

The emission card was composed of a Texas Instrument RF chip (CC110L) with a Texas Instruments micro-controller. The functionalities and extra components were kept to a minimum in order to minimize the energy consumption.

The important point is the embedded code on the micro-controller that handles the energy consumption. When the micro-controller is supplied with energy and wakes up, the code limits the energy consumption to program the RF chip, which then sends two signals of one byte each. Then the system goes back to sleep until the next energy input.

The RF is programmed to emit at a frequency of 868 MHz, with a rate of 250 kBits/s. The energy consumption of the system per cycle (wake up + programming + sending) is about 60 μJ. This allows to transmit the signal to a distance up to 40 meters, which is reasonably far for most wireless sensor applications.

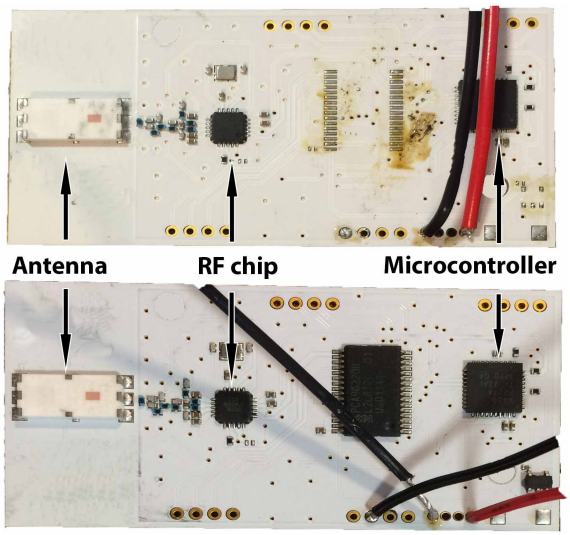

Figure 4.22: *Emission (top) and reception (bottom) wireless cards (CEA showroom).*

4.3.2 Signal transmission test

Finally, when the emission card was connected to the energy harvester, it was able to transmit a signal each time the device was heated in the oven to 70°C and each time it was cooled to the ambient temperature. The successful transmission of the signal was confirmed by a blinking LED on the reception card. Figure 4.23 shows consequent steps of harvester functioning: (1) harvester is connected to the emission card; (2) harvester is placed in the oven and the oven is closed; (3) emission card, powered by the harvester, sends signal to the reception card that flashes with a LED on the moment of signal reception.

The use of metallic oven however blocked wireless transmission, since it acted as Faraday cage, so the emission card had to be kept outside the oven. To test the prototype assembly together at heating and cooling, we have therefore built a simple wooden furnace heated with a hair dryer. A wooden furnace allowed the transmission, and approached tests to real-life conditions where the heat distribution is less homogeneous than in a conventional oven.

The furnace was a rectangular wooden box with an opening on one short side to insert the prototype, and a hole in the second short side where a hair dryer was inserted. A perforated plate, placed right after the hair dryer, cut the flow of air and spread it throughout the box. Temperature inside the box was measured with a thermocouple. Depending on the position of the box (horizontal or vertical), position of the thermocouple (in the corner or in the center), ventilation speed of the hair dryer (normal or maximal) and the position of the prototype inside the box, the thermal profile changed.

After a week of fine adjustments, the energy harvesting prototype was able to detect temperature variations in the furnace and reliably generate 100 μJ energy. The wireless transmission was confirmed by a LED blink each time the device was heated in the furnace and each time it was cooled to the ambient air out of the furnace. In this functioning mode, the energy harvester can detect a single heating/cooling event, and the same time use the generated energy in the event to transmit information about it, wirelessly. Thus, we can say that an operational energy harvesting prototype has been built, adapted for autonomous functioning and wireless communication.

4.4 Optimization

At this stage, there are a number of considerations to take into account for further optimization of the harvester. One of the most important is distribution of heat in the system. The box used for the housing limits the temperature that reaches the PVDF and the SMA in the switch. This explains the fact why the switch is triggered only at 70°C, while the wire A_s temperature is actually around 50°C. At the triggering moment at 70°C, the temperature of the PVDF surface is only 60°C, as measured by a thermocouple. Therefore, the housing box not only increases the time it takes for PVDF to "sense" the external temperature variation, but it also decreases the temperature seen by PVDF and the voltage that is generated.

The switch geometry needs to be further optimized, mainly to facilitate tuning and to shorten adjustment time. Also, problems such as electric sparking between electrodes due to air breakdown need to be studied.

At the circuit level, performance needs to be studied after repeated use at elevated temperatures (60–70°C) and high voltages (300–400 V). Degradation of components or soldering connections may lead to decreased overall performance. Also the inductor must be carefully chosen in order to avoid saturation at high input voltages.

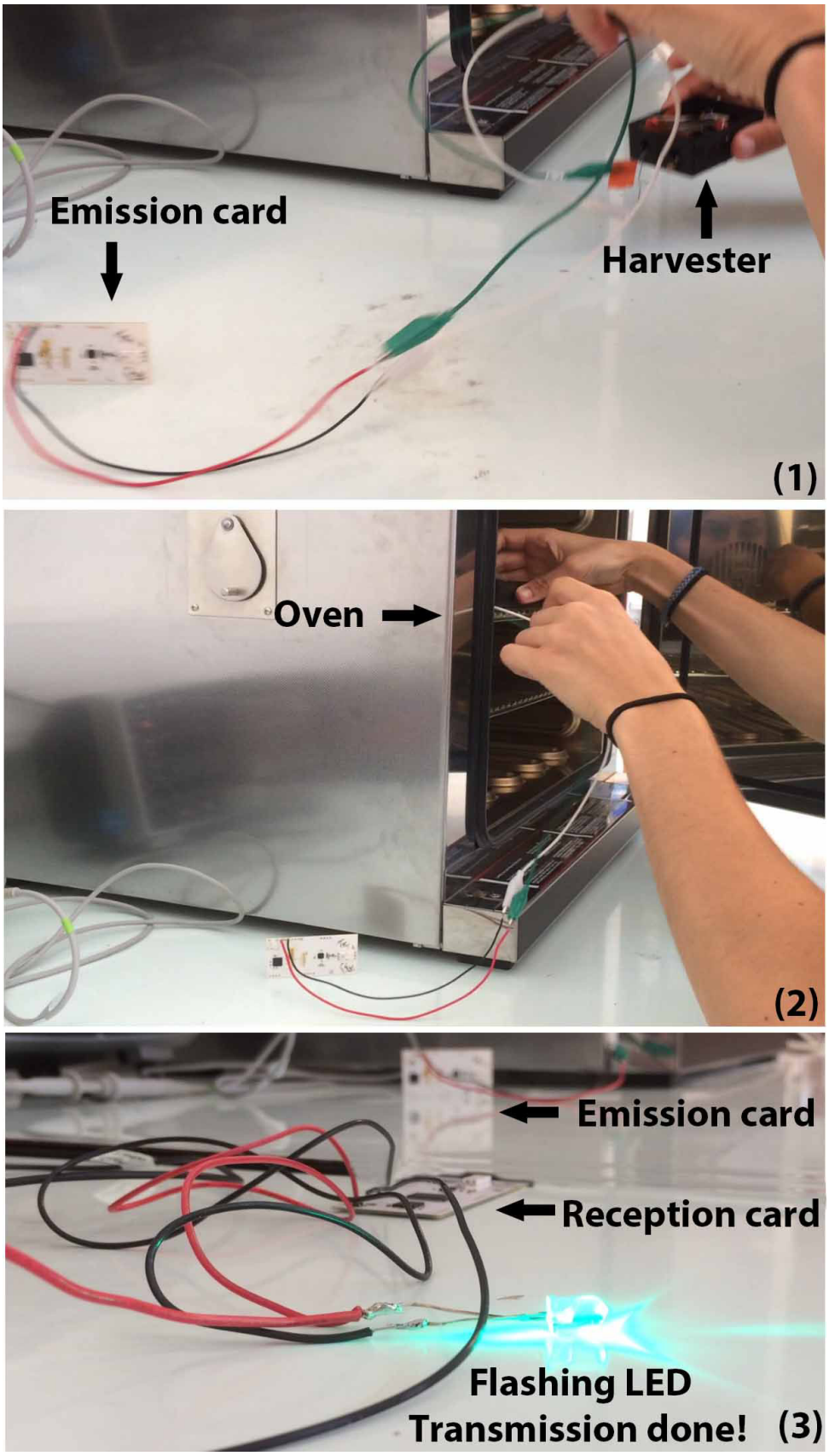

Figure 4.23: *Still frames from experimental video. The reception card flashes an LED as it recieves a signal from the emission card. Emission is powered by the energy harvester.*

4.5 Final prototype: SMA composite

So far, energy harvesting prototype was built utilizing only the pyroelectric effect of PVDF. Coupling PVDF with SMA is the next step. It will increase the sensitivity of the harvester in a particular temperature range, defined by SMA, and add the temperature threshold sensing capabilities. We will therefore have a autonomous self-powered temperature-threshold sensing device.

Coupling with SMA can also double the generated energy. This will allow us to either supply power to more sophisticated electronic circuit with additional functionalities, or to lower the operational temperature to obtain the same output energy at smaller ΔT.

All building blocks, necessary for the harvester are ready and operational: PVDF + SMA composite, thermal switch, power management and transmission cards. Unfortunately, for the lack of time, experimental results of this final prototype are not included in this manuscript. Final assembly is done (figure 4.24), and the tests are currently in progress.

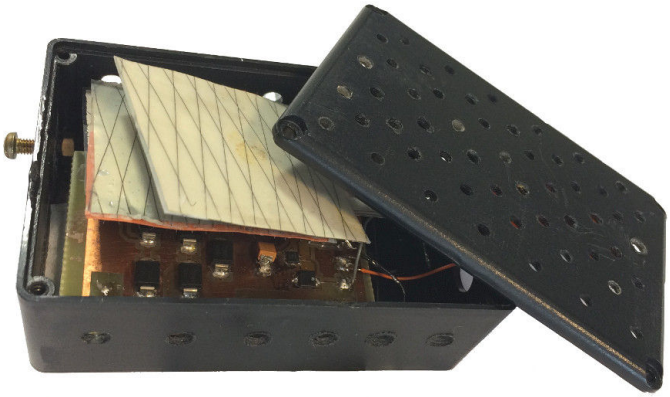

Figure 4.24: *Final energy harvesting prototype, containing PVDF + SMA composite.*

4.6 Conclusions and perspectives

An intermediate complete functional energy harvesting prototype, based on pyroelectric effect only, was realized and tested. It contains several key components, each necessary for the overall efficient functioning of the harvester:

- A customized thermal switch was designed and built. It consisted in a passive mechanical switch based on SMA wire. The switch was tuned to trigger and close the circuit both upon heating to 70°C, and cooling to room temperature. In the intermediary temperature the switch kept the circuit open for optimum charge collection;
- For demonstration, a stack of four PVDF sheets was used to generate voltage on heating and cooling. When heated in an oven at 70°C, PVDF was able to generate ≈300 V voltage, corresponding to ≈200 μJ energy. The sheets of PVDF were electrically connected in parallel, which allowed the increase of overall capacitance and energy without increasing the voltage.
- A dedicated power management circuit, comprising an original two-step DC-DC converter, was designed and realized on a PCB card. Series of simulations allowed optimizing the electronic components for the working prototype. The circuit was able to convert input voltage peaks of 300 V into a stable output of 1.86 V with nearly 50% efficiency. Further optimization can increase the efficiency;

With all components assembled together, the energy harvester was able to generate 100 μJ energy per thermal event. This energy was sufficient to power a wireless transmission card, sending a signal to a receiver, indicating the detection of the thermal event.

A number of improvements were proposed in order to increase the output energy and improve the conversion efficiency of the harvester:

- First of all, the PVDF should be coupled with SMA elements. Here, only the pyroelectric effect of PVDF was used for simplicity of demonstration. Coupling with SMA can double the produced energy. Coupling will also increase the sensitivity of the harvester in a particular temperature range, defined by the SMA, and improve the temperature threshold sensing capabilities. This allows us to either supply power to more sophisticated electronic circuit, or address lower temperatures while keeping the same output energy;
- Another packaging for the harvester should be imagined, in order to have more efficient heat exchange with the external environment. Heat exchange on both heating and cooling is an important factor which strongly affects the final output energy of the harvester;
- If we want to address higher temperatures, i.e. higher produced voltage, different adapted electronic components should be used. The current circuit design gradually lose their performance after continuous exposure to 400 V and 75°C. Ageing tests on these conditions should be performed for both the components and wiring in order to evaluate performance evolution with time;
- Additional tests should be performed in order to determine the impact of heating frequency and heating rate on the composite performances.

Chapter 5

General conclusion and outlook

The main objective of this thesis was to design, fabricate and evaluate a new thermal device for energy harvesting. We conclude this work with a functional energy harvesting prototype, able to harvest thermal energy in forms of quasi-static temporal temperature gradients. The energy harvesting prototype produced 100 μJ useful output energy upon both heating and cooling from room temperature to 70°C. This energy was used to power a wireless transmission card, sending a signal to a receiver on each thermal event. Thus, a concept of harvesting and detection of single heating or cooling events was validated, including the transmission of the information wirelessly. Pyroelectric effect alone was used for this first demonstration, and all the building blocks are ready for fabrication of an SMA-assisted PVDF harvester, that would act as a self-powered thermal-threshold sensor.

In chapter 4, key components were designed and realized, leading to an overall efficient energy harvester. First, a stack of four PVDF sheets was assembled to generate adequate energy on heating and cooling. When heated at 70°C in an oven, we were able to produce around 300 V and 200 μJ raw energy. Second, a custom power management circuit, comprising a two-step DC-DC buck converter, was designed and realized on a PCB card. A series of simulations allowed optimizing the electronic components for the actual practical use. The circuit was able to convert input voltage peaks of 300 V into a stable output voltage of 1.86 V with nearly 50% efficiency. Then, a passive mechanical switch based on shape memory alloy wire was made and tuned in order to trigger and close the circuit both upon heating to 70°C and cooling to room temperature. The key point was keeping the circuit open for optimum charge collection in the intermediate temperatures.

This realization (first proof of concept) was possible with advanced characterization and understanding of PVDF functioning principles. Chapter 2 was dedicated to evaluate PVDF performances for thermal energy harvesting and also to obtain reproducible measurements of piezoelectric coefficients in quasi-static and real open-circuit conditions. We have described several custom measurement methods, adapted specially for flexible polymer films. For piezoelectric measurements, the stress was applied with high precision by a four-point bending system or by tube bending. The generated voltage was measured in open-circuit conditions with a non-contact electrostatic voltmeter. Energy was measured by discharging this voltage into a resistance by means of a mechanical switch. The contactless method allowed for the measurement with virtually no leakage into the circuit. This measurement technique was clearly advantageous for piezoelectric measurements of flexible polymers since higher voltage values and energies have been observed in comparison with conventional closed-circuit measurements. Outstanding voltages up to 120 V and energy densities up to 1.1 mJ/cm^3 were obtained with 1% of applied strain. The measured piezoelectric g_{31} coefficients of commercial PVDF films were determined with precision and revealed slightly higher values than datasheet. Additionally, the g_{31} coefficient was found to increase with applied strain within the PVDF elastic region. When the material was deformed beyond its plastic region, the piezoelectric output decreased. For bi-axially oriented Piezotech PVDF, the g_{31} increased from 0.04 Vm/N to 0.065 Vm/N up to 1% strain and then gradually decreased. For

uni-axial MeasSpec PVDF, the g_{31} increased from 0.12 Vm/N to 0.28 Vm/N up to 3% strain and then decreased. We conclude that bi-axially oriented PVDF is more convenient for SMA-assisted harvesting applications: it should be easier to design such a device due to smaller variations of g_{31} and no piezoelectric anisotropy, even though this material has reduced g_{31} value compared to uni-axial PVDF.

Also, in chapter 2 we investigated self-discharge. The self-discharge phenomenon in PVDF was found to increase strongly with increased temperature. At 80°C, which is the depolarization limit, material was discharged almost instantly. As a consequence, since the operating conditions of our harvester are at elevated temperatures, harvesting must be faster than self-discharge to ensure little losses. Lower working temperatures will naturally be beneficial. The self-discharge was not affected by the applied strain, at least up to 10%. It was neither affected by relative humidity in air, as opposed to commonly used PZT ceramic piezoelectrics, which is a major advantage for applications with PVDF.

To increase the energy output of PVDF upon heating, we have proposed coupling the PVDF with a thermal shape memory alloy (NiTiCu), which was detailed in chapter 3. When heating or cooling, in addition to pyroelectric voltage, the SMA strain induced a piezoelectric voltage in PVDF, which added to the total voltage. The total harvested energy was experimentally shown to increase by up to 210% when compared to PVDF alone in the temperature range corresponding to the SMA phase transformation. The properties of PVDF+NiTiCu laminated composites were detailed. It was measured to be superior to the previously demonstrated semi-flexible MFC-based composites. At 40°C the composite, comprising PVDF with four NiTiCu ribbons, and having an active volume of 27.6 mm^3, was able to harvest 12 μJ, which corresponds to an energy density of 0.43 mJ/cm^3. Since PVDF is more flexible than MFC, higher voltages and energies are possible with further proper optimization. Work needs still to be done in order to increase the efficiency for small temperature variations. For example, SMA with sharper phase transitions could be used, which could be obtained by adjusting the NiTiCu composition. Alternatively, a different shape memory alloy could be used. Also, arrangements should be made to directly measure the strain transferred from the SMA to the piezoelectric layer, in order to understand the impact of bonding layer on overall performance.

Beyond these conclusions, there are number of important perspectives. The first optimization step is to integrate the PVDF+SMA composite to the complete energy harvesting prototype. Hybridization will increase the sensitivity of the harvester in a particular temperature range, defined by the SMA. Coupling will also increase the produced energy, meaning that we will be able either to supply power to a more sophisticated electronic circuit, or lower the operation temperature to have the same output energy at smaller ΔT. The second step would be to perform additional tests in order to determine the impact of heating frequency and heating rate on the composite performance. Finally, aging tests should be performed for all the components in order to evaluate performance evolution with time. If necessary, different adapted electronic components should be used, that would withstand repeated exposures to high voltages and temperatures.

In conclusion, this work can be an important milestone towards flexible, low profile thermal energy harvesters and autonomous sensors. We are convinced that unconventional power sources, which were disregarded up to now, will become exploitable in the near future based on hybrid and composite structures. This is actually one of the fast growing technological markets, as the success of ventures, such as EnerBee, attests.

Bibliography

[1] Steven Percy, Chris Knight, Scott McGarry, Alex Post, Tim Moore, and Kate Cavanagh. *Thermal to Electrical Energy Converters*. SpringerBriefs in Electrical and Computer Engineering. Springer New York, 2014. ISBN 978-1-4614-9214-6. doi:10.1007/978-1-4614-9215-3.

[2] Micropelt. Thermoelectric energy harvesting, 2015. URL http://micropelt.com.

[3] Jeannine R. Szczech, Jeremy M. Higgins, and Song Jin. Enhancement of the thermoelectric properties in nanoscale and nanostructured materials. *J. Mater. Chem.*, 21:4037–4055, 2011. doi:10.1039/C0JM02755C.

[4] Gilhwan Cha and Y. Sungtaek Ju. Pyroelectric energy harvesting using liquid-based switchable thermal interfaces. *Sensors and Actuators A: Physical*, 189:100–107, Jan 2013. ISSN 0924-4247. doi:10.1016/j.sna.2012.09.019.

[5] Nicolas Galopin. *Modelling and characterisation of smart materials for the design of magneto-electric devices*. Theses, Université Paris Sud - Paris XI, December 2007. URL https://tel.archives-ouvertes.fr/tel-00274483.

[6] P. Martins, A.C. Lopes, and S. Lanceros-Mendez. Electroactive phases of poly(vinylidene fluoride): Determination, processing and applications. *Progress in Polymer Science*, 39(4): 683 – 706, 2014. ISSN 0079-6700. doi:10.1016/j.progpolymsci.2013.07.006. Topical issue on Electroactive Polymers.

[7] Li Li, Mingqiu Zhang, Minzhi Rong, and Wenhong Ruan. Studies on the transformation process of PVDF from α to β phase by stretching. *RSC Adv.*, 4:3938–3943, 2014. doi:10.1039/C3RA45134H.

[8] Ju-Hyuck Lee, Keun Young Lee, Manoj Kumar Gupta, Tae Yun Kim, Dae-Yeong Lee, Junho Oh, Changkook Ryu, Won Jong Yoo, Chong-Yun Kang, Seok-Jin Yoon, and et al. Highly stretchable piezoelectric-pyroelectric hybrid nanogenerator. *Advanced Materials*, 26(5):765–769, Feb 2013. ISSN 0935-9648. doi:10.1002/adma.201303570.

[9] Ya Yang, Hulin Zhang, Guang Zhu, Sangmin Lee, Zong-Hong Lin, and Zhong Lin Wang. Flexible hybrid energy cell for simultaneously harvesting thermal, mechanical, and solar energies. *ACS Nano*, 7(1):785–790, 2013. doi:10.1021/nn305247x.

[10] SmartLab Texas A&M. Detailed introduction to shape memory alloys, 2015. URL http://smart.tamu.edu/overview/smaintro/detailed/detailed.html.

[11] Bernd R. Hahn. Studies on the nonlinear piezoelectric response of polyvinylidene fluoride. *Journal of Applied Physics*, 57(4):1294–1298, 1985. doi:10.1063/1.334528.

[12] V. Sencadas, V. Moreira, J. F. Mano, and S. Lanceros-mendez. Electrical response of β-PVDF in a constant uniaxial strain rate deformation. *Ferroelectrics*, 304(1):43–46, 2004. doi:10.1080/00150190490454459.

[13] Inc. Measurement Specialties. *Piezo Technical Manual*, 2015. URL http://www.meas-spec.com/news/Position/TechnicalManual.aspx?menu_id=546&tax_id=128.

[14] H. H. S. Chang and Z. Huang. Laminate composites with enhanced pyroelectric effects for energy harvesting. *Smart Materials and Structures*, 19(6):065018, 2010. doi:10.1088/0964-1726/19/6/065018.

[15] Dragan Avirovik, Ashok Kumar, Robert J Bodnar, and Shashank Priya. Remote light energy harvesting and actuation using shape memory alloy - piezoelectric hybrid transducer. *Smart Materials and Structures*, 22(5):052001, 2013. doi:10.1088/0964-1726/22/5/052001.

[16] D Zakharov, B Gusarov, E Gusarova, B Viala, O Cugat, J Delamare, and L Gimeno. Combined pyroelectric, piezoelectric and shape memory effects for thermal energy harvesting. In *Proc. PowerMEMS*, volume 476, page 012021, 2013. doi:10.1088/1742-6596/476/1/012021.

[17] D. Zakharov, G. Lebedev, V. Koledov, P. Lega, D. Kuchin, A. Irzhak, V. Afonina, E. Perov, A. Shelyakov, V. Pushin, and V. Shavrov. An enhanced composite scheme of shape memory actuator for smart systems. *Physics Procedia*, 10(0):58 – 64, 2010. ISSN 1875-3892. doi:10.1016/j.phpro.2010.11.075. 3rd International Symposium on Shape Memory Materials for Smart Systems/E-MRS 2010 Spring Meeting.

[18] Dmitry Zakharov, Gor Lebedev, Orphee Cugat, Jerome Delamare, Bernard Viala, Thomas Lafont, Leticia Gimeno, and Alexander Shelyakov. Thermal energy conversion by coupled shape memory and piezoelectric effects. *Journal of Micromechanics and Microengineering*, 22(9):094005, 2012. doi:10.1088/0960-1317/22/9/094005.

[19] *LDT with Crimps Vibration Sensor/Switch Leaflet*, 2015. URL http://www.meas-spec.com/downloads/LDT_Series.pdf.

[20] BP. Statistical review of world energy, 2014. URL https://www.bp.com/content/dam/bp/pdf/Energy-economics/statistical-review-2014/BP-statistical-review-of-world-energy-2014-full-report.pdf.

[21] IOP Institute of Physics. What is energy harvesting?, 2015. URL http://www.iop.org/resources/energy/.

[22] S. Beeby and N.M. White. *Energy Harvesting for Autonomous Systems*. Artech House Series Smart Materials, Structures, and Systems. Artech House, Incorporated, 2014. ISBN 9781596937192. URL https://books.google.fr/books?id=7H9xdFd4sikC.

[23] European Commission Business Innovation Observatory. Clean technologies - energy harvesting, 2014. URL http://ec.europa.eu/enterprise/policies/innovation/policy/business-innovation-observatory/files/case-studies/32-clt-energy-harvesting.pdf.

[24] Adnan Harb. Energy harvesting: State-of-the-art. *Renewable Energy*, 36(10):2641 – 2654, 2011. ISSN 0960-1481. doi:10.1016/j.renene.2010.06.014.

[25] IOP Institute of Physics. Types of energy harvesting materials, 2015. URL http://www.iop.org/resources/energy/materials/page_50300.html.

[26] J. Kymissis, C. Kendall, J. Paradiso, and N. Gershenfeld. Parasitic power harvesting in shoes. In *Wearable Computers, 1998. Digest of Papers. Second International Symposium on*, pages 132–139, Oct 1998. doi:10.1109/ISWC.1998.729539.

[27] T. Starner. Human-powered wearable computing. *IBM Systems Journal*, 35(3.4):618–629, 1996. ISSN 0018-8670. doi:10.1147/sj.353.0618.

[28] J.M. Rabaey, M.J. Ammer, Jr. da Silva, J.L., D. Patel, and S. Roundy. Picoradio supports ad hoc ultra-low power wireless networking. *Computer*, 33(7):42–48, Jul 2000. ISSN 0018-9162. doi:10.1109/2.869369.

[29] Internet of things global standards initiative, 2015. URL http://www.itu.int/en/itu-T/gsi/iot/Pages/default.aspx.

[30] EnOcean. Energy harvesting wireless solutions and networks, 2015. URL http://www.enocean.com/.

[31] Algra. World's first piezo key w.o displacement - no battery, no cable, 2015. URL http://www.algra.ch/content.php?MAIN_RUB_ID=126&subcatid=154&content=cms.

[32] Pavegen. Harvesting kinetic energy from every footstep., 2015. URL http://www.pavegen.com.

[33] Perpetuum. The world leader in vibration harvester powered wireless sensing systems, 2015. URL http://www.perpetuum.com/.

[34] Enerbee. Energy harvesting technology- revolutionizing energy autonomy, 2015. URL http://www.enerbee.fr/.

[35] HotBlock OnBoard. Thermoelectric energy and sensing systems. URL http://www.hotblock.fr/.

[36] Arveni. URL http://www.arveni.fr/.

[37] Antoine Bonnabel and Yann de Charentenay. Energy harvesting market will approach USD 250M in five years, 2012. URL http://www.yole.fr/iso_upload/Mag/ACMEMStrendsOct%202013.pdf.

[38] IDTechEx. Energy harvesting and storage for electronic devices 2011-2021, 2011. URL http://www.idtechex.com/research/reports/energy-harvesting-and-storage-for-electronic-devices-2011-2021-000270.asp.

[39] Alim Dewan, Suat U. Ay, M. Nazmul Karim, and Haluk Beyenal. Alternative power sources for remote sensors: A review. *Journal of Power Sources*, 245:129 – 143, 2014. ISSN 0378-7753. doi:10.1016/j.jpowsour.2013.06.081.

[40] Zhong Lin Wang, Guang Zhu, Ya Yang, Sihong Wang, and Caofeng Pan. Progress in nanogenerators for portable electronics. *Materials Today*, 15(12):532 – 543, 2012. ISSN 1369-7021. doi:10.1016/S1369-7021(13)70011-7.

[41] Shashank Priya and Daniel J. Inman, editors. *Energy Harvesting Technologies*. Springer US, 2009. ISBN 978-0-387-76463-4. doi:10.1007/978-0-387-76464-1.

[42] Steven R Anton and Henry A Sodano. A review of power harvesting using piezoelectric materials (2003-2006). *Smart Materials and Structures*, 16(3):R1, 2007. doi:10.1088/0964-1726/16/3/R01.

[43] G. Sebald, E. Lefeuvre, and D. Guyomar. Pyroelectric energy conversion: Optimization principles. *Ultrasonics, Ferroelectrics and Frequency Control, IEEE Transactions on*, 55 (3):538–551, March 2008. ISSN 0885-3010. doi:10.1109/TUFFC.2008.680.

[44] Bluetooth. Low energy technology. URL http://www.bluetooth.com/Pages/low-energy-tech-info.aspx.

[45] Gael Sebald, Daniel Guyomar, and Amen Agbossou. On thermoelectric and pyroelectric energy harvesting. *Smart Materials and Structures*, 18(12):125006, 2009. doi:10.1088/0964-1726/18/12/125006.

[46] A Arnaud, S Boisseau, S Monfray, O Puscasu, G Despesse, J Boughaleb, Y Sanchez, F Battegay, M Fourel, S Audran, F Boeuf, J Delamare, G Delepierre, G Pitone, and T Skotnicki. Piezoelectric and electrostatic bimetal-based thermal energy harvesters. *Journal of Physics: Conference Series*, 476(1):012062, 2013. doi:10.1088/1742-6596/476/1/012062.

[47] Shankar Karanilam Thundiparambu Ravindran, Michael Kroener, and Peter Woias. A bimetallic micro heat engine for pyroelectric energy conversion. *Procedia Engineering*, 47(0):33 – 36, 2012. ISSN 1877-7058. doi:10.1016/j.proeng.2012.09.077. 26th European Conference on Solid-State Transducers, {EUROSENSOR} 2012.

[48] Scott R. Hunter, Nickolay V. Lavrik, Thirumalesh Bannuru, Salwa Mostafa, Slo Rajic, and Panos G. Datskos. Development of mems based pyroelectric thermal energy harvesters. In *Proc. SPIE 8035, Energy Harvesting and Storage: Materials, Devices, and Applications II*, volume 8035, pages 80350V–80350V–12, 2011. doi:10.1117/12.882125.

[49] Dmitry Zakharov. *Composite materials on the basis of a shape memory alloy & a pyro/piezoelectric material for thermal energy harvesting*. Theses, Université de Grenoble, Feb 2014. URL https://tel.archives-ouvertes.fr/tel-01060158.

[50] IDTechEx. Thermoelectric energy harvesting 2014-2024: Devices, applications, opportunities, 2015. URL http://www.idtechex.com/research/reports/thermoelectric-energy-harvesting-2014-2024-devices-applications-opportunities-000392.asp.

[51] MIT Technology Review. Powering your car with waste heat, 2011. URL http://www.technologyreview.com/news/424092/powering-your-car-with-waste-heat/.

[52] International Thermoelectric Society. Thermoelectric power for automobiles arrives in europe, 2009. URL http://www.its.org/node/5670.

[53] Xiaohang Chen, Yuan Wang, Ling Cai, and Yinghui Zhou. Maximum power output and load matching of a phosphoric acid fuel cell-thermoelectric generator hybrid system. *Journal of Power Sources*, 294:430 – 436, 2015. ISSN 0378-7753. doi:10.1016/j.jpowsour.2015.06.085.

[54] Mingzhou Zhao, Houcheng Zhang, Ziyang Hu, Zhufeng Zhang, and Jinjie Zhang. Performance characteristics of a direct carbon fuel cell/thermoelectric generator hybrid system. *Energy Conversion and Management*, 89:683 – 689, 2015. ISSN 0196-8904. doi:10.1016/j.enconman.2014.10.035.

[55] G. Jeffrey Snyder. Small thermoelectric generators. *The Electrochemical Society*, 2008. URL http://www.electrochem.org/dl/interface/fal/fal08/fal08_p54-56.pdf.

[56] Y. Xu. *Ferroelectric Materials and Their Applications*. North-Holland, 1991. ISBN 9780444883544. URL http://books.google.fr/books?id=FixRAAAAMAAJ.

[57] Cady Walter Guyton. *Piezoelectricity*. New York/London: McGraw-Hill Book Company, 1946. URL https://archive.org/details/piezoelectricity031514mbp.

[58] L. Pintilie and I. Pintilie. Temperature dependence of the pyroelectric voltage in a 2-2 connectivity pyroelectric bimorph. *Ferroelectrics*, 200(1):219–235, 1997. doi:10.1080/00150199708008608.

[59] Ieee standard on piezoelectricity. *ANSI/IEEE Std 176-1987*, 1988. doi:10.1109/IEEESTD.1988.79638.

[60] Heiji Kawai. The piezoelectricity of poly (vinylidene fluoride). *Japanese Journal of Applied Physics*, 8(7):975, 1969. doi:10.1143/JJAP.8.975.

[61] J. G. Bergman, J. H. McFee, and G. R. Crane. Pyroelectricity and optical second harmonic generation in polyvinylidene fluoride films. *Applied Physics Letters*, 18(5):203–205, 1971. doi:10.1063/1.1653624.

[62] T. Mizuno, M. Ohta, and M. Segawa. Doubly oriented film of polyvinylidene fluoride, Nov 1981. URL http://www.google.com.au/patents/US4298719.

[63] R. Betz. The advantages of bioriented piezo-electric film. *Ferroelectrics*, 75(1):397–404, 1987. doi:10.1080/00150198708008992.

[64] Pierre Ueberschlag. PVDF piezoelectric polymer. *Sensor Review*, 21(2):118–126, 2001. doi:10.1108/02602280110388315.

[65] Helena M.G. Correia and Marta M.D. Ramos. Quantum modelling of poly(vinylidene fluoride). *Computational Materials Science*, 33(1-3):224 – 229, 2005. ISSN 0927-0256. doi:10.1016/j.commatsci.2004.12.040. Proceedings of the E-MRS 2004 Spring Meeting;

Symposium H: Atomic Materials Design: Modelling and Characterization E-MRS 2004 Spring Meeting, Symposium H.

[66] Enzo Giannetti. Semi-crystalline fluorinated polymers. *Polymer International*, 50(1):10–26, 2001. ISSN 1097-0126. doi:10.1002/1097-0126(200101)50:1<10::AID-PI614>3.0.CO;2-W.

[67] A. Salimi and A.A. Yousefi. Analysis method: FTIR studies of β-phase crystal formation in stretched PVDF films. *Polymer Testing*, 22(6):699 – 704, 2003. ISSN 0142-9418. doi:10.1016/S0142-9418(03)00003-5.

[68] Ilias Katsouras, Kamal Asadi, Mengyuan Li, Tim B. van Driel, Kasper S. Kjaer, Dong Zhao, Thomas Lenz, Yun Gu, Paul W. M. Blom, Dragan Damjanovic, Martin M. Nielsen, and Dago M. de Leeuw. The negative piezoelectric effect of the ferroelectric polymer poly(vinylidene fluoride). *Nature Materials*, Oct 2015. doi:10.1038/nmat4423.

[69] Yiheng Qin, Matiar M.R. Howlader, M. Jamal Deen, Yaser M. Haddara, and P. Ravi Selvaganapathy. Polymer integration for packaging of implantable sensors. *Sensors and Actuators B: Chemical*, 202(0):758 – 778, 2014. ISSN 0925-4005. doi:10.1016/j.snb.2014.05.063.

[70] Kenji Omote, Hiroji Ohigashi, and Keiko Koga. Temperature dependence of elastic, dielectric, and piezoelectric properties of a single crystalline films of vinylidene fluoride trifluoroethylene copolymer. *Journal of Applied Physics*, 81(6):2760–2769, 1997. doi:10.1063/1.364300.

[71] Elisabeth Urban, Martin W. King, Robert Guidoin, Gaetan Laroche, Yves Marois, Louisette Martin, Alain Cardou, and Yvan Douville. Why make monofilament sutures out of polyvinylidene fluoride. *ASAIO Journal*, April/June 1994. URL http://journals.lww.com/asaiojournal/Abstract/1994/04000/Why_Make_Monofilament_Sutures_Out_of.6.aspx.

[72] Arkema inc. kynar and kynar flex PVDF performance characteristics & data brochure, 2015. URL http://asia.kynar.com/export/sites/kynar-asia/.content/medias/downloads/literature/kynar-kynar-flex-pvdf-performance-chracteristics.pdf.

[73] Gaetan Laroche, Yves Marois, Robert Guidoin, Martin W. King, Louisette Martin, Thien How, and Yvan Douville. Polyvinylidene fluoride (PVDF) as a biomaterial: From polymeric raw material to monofilament vascular suture. *Journal of Biomedical Materials Research*, 29(12):1525–1536, 1995. ISSN 1097-4636. doi:10.1002/jbm.820291209.

[74] Sang-Soo Je, T. Sharma, Youngkyu Lee, B. Gill, and J.X. Zhang. A thin-film piezoelectric PVDF-TrFE based implantable pressure sensor using lithographic patterning. In *In Proc. IEEE 24th International Conference on Micro Electro Mechanical Systems (MEMS)*, pages 644–647, Jan 2011. doi:10.1109/MEMSYS.2011.5734507.

[75] Tran Quang Trung, Nguyen Thanh Tien, Young Gug Seol, and Nae-Eung Lee. Transparent and flexible organic field-effect transistor for multi-modal sensing. *Organic Electronics*, 13 (4):533 – 540, 2012. ISSN 1566-1199. doi:10.1016/j.orgel.2011.12.015.

[76] J. Scheirs, S. Burks, and A Locaspi. Developments in fluoropolymer coatings (review). *Trends in Polymer Science*, 3(3):74–82, March 1995. URL http://www.scopus.com/record/display.url?eid=2-s2.0-0002391929&origin=inward&txGid=D5F4D2245FF92E4B2B895ECCFA21AA7D.N5T5nM1aaTEF8rE6yKCR3A%3a2#.

[77] Oscar Bryan Wilson. *Introduction to theory and design of sonar transducers*. Peninsula Pub, 1988.

[78] J.E. Mark. *The Polymer Data Handbook*. Oxford University Press, Incorporated, 2009. ISBN 9780195181012. URL http://books.google.fr/books?id=ZCYCPwAACAAJ. ISBN 0195181018, 9780195181012.

[79] Yongrae Roh, V.V. Varadan, and Vijay K. Varadan. Characterization of all the elastic, dielectric, and piezoelectric constants of uniaxially oriented poled PVDF films. *Ultrasonics, Ferroelectrics, and Frequency Control, IEEE Transactions on*, 49(6):836–847, June 2002. ISSN 0885-3010. doi:10.1109/TUFFC.2002.1009344.

[80] S.A.S. Piezotech. *Piezotech Piezoelectric Films Leaflet*, 2015. URL http://www.piezotech.fr/image/documents/22-31-32-33-piezotech-piezoelectric-films-leaflet.pdf.

[81] Yongang Jiang, Hiroyuki Hamada, Syohei Shiono, Kensuke Kanda, Takayuki Fujita, Kohei Higuchi, and Kazusuke Maenaka. A PVDF-based flexible cardiorespiratory sensor with independently optimized sensitivity to heartbeat and respiration. *Procedia Engineering*, 5 (0):1466 – 1469, 2010. ISSN 1877-7058. doi:10.1016/j.proeng.2010.09.393. Eurosensor XXIV Conference.

[82] Zhiyong Sun, Lina Hao, Shuai Li, and Jiawei Shen. A PVDF micro-force sensor based on inverse-model algorithm and its applications. In *In Proc. IEEE International Conference on Information and Automation (ICIA)*, pages 801–806, June 2011. doi:10.1109/ICINFA.2011.5949104.

[83] Junfeng Cai, Xiaozhong Fu, and Hongbo Liu. Design of PVDF stress sensor and its application in the stress test of foam plastic. In *In Proc. Measurement, Information and Control (MIC), 2012 International Conference on*, volume 2, pages 821–824, May 2012. doi:10.1109/MIC.2012.6273415.

[84] M. Kurata, X. Li, K. Fujita, L. He, and M. Yamaguchi. PVDF piezo film as dynamic strain sensor for local damage detection of steel frame buildings. In *Proc. SPIE*, volume 8692, pages 86920F–86920F–10, 2013. doi:10.1117/12.2009554.

[85] E.S. Nour, M.O. Sandberg, M. Willander, and O. Nur. Handwriting enabled harvested piezoelectric power using zno nanowires/polymer composite on paper substrate. *Nano Energy*, 9:221 – 228, 2014. ISSN 2211-2855. doi:10.1016/j.nanoen.2014.07.014.

[86] Romain Guigon, Jean-Jacques Chaillout, Thomas Jager, and Ghislain Despesse. Harvesting raindrop energy experimental study. *Smart Mater. Struct.*, 17:015039, 2008. doi:10.1088/0964-1726/17/01/015039.

[87] S. Takamatsu, T. Kobayashi, T. Imai, T. Yamashita, and T. Itoh. All polymer piezoelectric film for the application to low resonance frequency energy harvester. *Procedia Engineering*, 25:203 – 206, 2011. ISSN 1877-7058. doi:10.1016/j.proeng.2011.12.050. EurosensorsXXV.

[88] Yonggang Jiang, Syohei Shiono, Hiroyuki Hamada, Takayuki Fujita, Kohei Higuchi, and Kazusuke Maenaka. Low-frequency energy harvesting using a laminated PVDF cantilever with a magnetic mass. In *Proc. PowerMEMS*, 2010. URL http://cap.ee.ic.ac.uk/~pdm97/powermems/2010/poster-pdfs/375_Jiang_111.pdf.

[89] Shun di Hu, Kuo-Chih Chuang, and Horn sen Tzou. PVDF energy harvester on flexible rings. In *In Proc. Symposium on Piezoelectricity, Acoustic Waves and Device Applications (SPAWDA)*, pages 100–105, Dec 2010. doi:10.1109/SPAWDA.2010.5744283.

[90] Chengliang Sun, Jian Shi, Dylan J. Bayerl, and Xudong Wang. PVDF microbelts for harvesting energy from respiration. *Energy Environ. Sci.*, 4:4508–4512, 2011. doi:10.1039/C1EE02241E.

[91] S. Dey, M. Purahmad, S.S. Ray, A.L. Yarin, and M. Dutta. Investigation of PVDF-TrFE nanofibers for energy harvesting. In *In Proc. Nanotechnology Materials and Devices Conference (NMDC), IEEE*, pages 21–24, Oct 2012. doi:10.1109/NMDC.2012.6527581.

[92] Jiyoung Chang, Michael Dommer, Chieh Chang, and Liwei Lin. Piezoelectric nanofibers for energy scavenging applications. *Nano Energy*, 1(3):356 – 371, 2012. ISSN 2211-2855. doi:10.1016/j.nanoen.2012.02.003.

[93] Michael Cleveland and Hong Liang. Magnetocaloric piezoelectric composites for energy harvesting. *Smart Materials and Structures*, 21(4):047002, 2012. doi:10.1088/0964-1726/21/4/047002.

[94] Xinyu Xue, Sihong Wang, Wenxi Guo, Yan Zhang, and Zhong Lin Wang. Hybridizing energy conversion and storage in a mechanical-to-electrochemical process for self-charging power cell. *Nano Letters*, 12(9):5048–5054, 2012. doi:10.1021/nl302879t. URL http://dx.doi.org/10.1021/nl302879t.

[95] Lili Xing, Yuxin Nie, Xinyu Xue, and Yan Zhang. PVDF mesoporous nanostructures as the piezo-separator for a self-charging power cell. *Nano Energy*, 10:44 – 52, 2014. ISSN 2211-2855. doi:10.1016/j.nanoen.2014.09.004.

[96] Seok Ju Kang, Youn Jung Park, Insung Bae, Kap Jin Kim, Ho-Cheol Kim, Siegfried Bauer, Edwin L. Thomas, and Cheolmin Park. Printable ferroelectric PVDF/PMMA blend films with ultralow roughness for low voltage non-volatile polymer memory. *Advanced Functional Materials*, 19(17):2812–2818, 2009. ISSN 1616-3028. doi:10.1002/adfm.200900589.

[97] Wei Jin Hu, Deng-Ming Juo, Lu You, Junling Wang, Yi-Chun Chen, Ying-Hao Chu, and Tom Wu. Universal ferroelectric switching dynamics of vinylidene fluoride-trifluoroethylene copolymer films. *Scientific Reports*, 4(4772), April 2013. doi:10.1038/srep04772.

[98] Presicon Acoustics. PVDF transducers, 2015. URL http://acoustics.co.uk/products/ultrasonic-transducers/pvdf-transducers/.

[99] Oliver Pabst, Stefan Holzer, Erik Beckert, Jolke Perelaer, Ulrich S. Schubert, Ramona Eberhardt, and Andreas Tunnermann. Inkjet printed micropump actuator based on piezoelectric polymers: Device performance and morphology studies. *Organic Electronics*, 15(11):3306 – 3315, 2014. ISSN 1566-1199. doi:10.1016/j.orgel.2014.09.007.

[100] Yiin-Kuen Fuh, Po-Chou Chen, Zih-Ming Huang, and Hsi-Chun Ho. Self-powered sensing elements based on direct-write, highly flexible piezoelectric polymeric nano/microfibers. *Nano Energy*, 11:671 – 677, 2015. ISSN 2211-2855. doi:10.1016/j.nanoen.2014.10.038.

[101] Myoung-Soo Kim, Hye-Rin Ahn, Seok Lee, Chulki Kim, and Yong-Jun Kim. A dome-shaped piezoelectric tactile sensor arrays fabricated by an air inflation technique. *Sensors and Actuators A: Physical*, 212:151 – 158, 2014. ISSN 0924-4247. doi:10.1016/j.sna.2014.02.023.

[102] Y R Wang, J M Zheng, G Y Ren, P H Zhang, and C Xu. A flexible piezoelectric force sensor based on PVDF fabrics. *Smart Materials and Structures*, 20(4):045009, 2011. doi:10.1088/0964-1726/20/4/045009.

[103] Jingjing Zhao and Zheng You. A shoe-embedded piezoelectric energy harvester for wearable sensors. *Sensors*, 14(7):12497, 2014. ISSN 1424-8220. doi:10.3390/s140712497.

[104] Arkema. Excellent performance for wire and cable applications, 2015. URL http://americas.kynar.com/en/markets-applications/energy-and-electrical/wire-and-cable/index.html.

[105] Arkema. Kynar PVDF resins for battery binders and separators, 2015. URL http://americas.kynar.com/en/markets-applications/energy-and-electrical/battery/index.html.

[106] Arkema. Membrane processing applications, 2015. URL http://americas.kynar.com/en/markets-applications/industrial-applications/membranes/index.html.

[107] Seaguar. Fishing lines, 2015. URL http://www.seaguar.com/about-seaguar/.

[108] A. Cuadras, M. Gasulla, and V. Ferrari. Thermal energy harvesting through pyroelectricity. *Sensors and Actuators A: Physical*, 158(1):132 – 139, 2010. ISSN 0924-4247. doi:10.1016/j.sna.2009.12.018.

[109] C.G. Wu, P. Li, G.Q. Cai, W.B. Luo, X.Y. Sun, Q.X. Peng, and W.L. Zhang. Quick response pzt/p(vdf-trfe) composite film pyroelectric infrared sensor with patterned polyimide thermal isolation layer. *Infrared Physics & Technology*, 2014. ISSN 1350-4495. doi:10.1016/j.infrared.2014.05.010.

[110] Lia Kouchachvili and Michio Ikura. Pyroelectric conversion - effects of P(VDF-TrFE) preconditioning on power conversion. *Journal of Electrostatics*, 65(3):182 – 188, 2007. ISSN 0304-3886. doi:10.1016/j.elstat.2006.07.014.

[111] A Navid, C S Lynch, and L Pilon. Purified and porous poly(vinylidene fluoride-trifluoroethylene) thin films for pyroelectric infrared sensing and energy harvesting. *Smart Materials and Structures*, 19(5):055006, 2010. doi:10.1088/0964-1726/19/5/055006.

[112] Ashcon Navid and Laurent Pilon. Pyroelectric energy harvesting using olsen cycles in purified and porous poly(vinylidene fluoride-trifluoroethylene) [P(VDF-TrFE)] thin films. *Smart Materials and Structures*, 20(2):025012, 2011. doi:10.1088/0964-1726/20/2/025012.

[113] Randall B. Olsen, David A. Bruno, Joseph M. Briscoe, and Everett W. Jacobs. Pyroelectric conversion cycle of vinylidene fluoride-trifluoroethylene copolymer. *Journal of Applied Physics*, 57(11):5036–5042, 1985. doi:10.1063/1.335280.

[114] George B. Kauffman and Isaac Mayo. The story of nitinol: The serendipitous discovery of the memory metal and its applications. *The Chemical Educator*, 2(2):1–21, 1997. doi:10.1007/s00897970111a.

[115] H Kahn, M A Huff, and A H Heuer. The tini shape-memory alloy and its applications for mems. *Journal of Micromechanics and Microengineering*, 8(3):213, 1998. doi:10.1088/0960-1317/8/3/007. URL http://stacks.iop.org/0960-1317/8/i=3/a=007.

[116] S. Miyazaki, Y.Q. Fu, and W.M. Huang. *Thin Film Shape Memory Alloys: Fundamentals and Device Applications*. Cambridge University Press, 2009. ISBN 9780521885768. URL http://www.cambridge.org/9780521885768.

[117] TiNi Alloy Company. Shape Memory Alloy Microdevices, 2015. URL http://www.tinialloy.com/.

[118] Yong Liu. The work production of shape memory alloy. *Smart Materials and Structures*, 13(3):552, 2004. doi:10.1088/0964-1726/13/3/014.

[119] C.M. Jackson, H.J. Wagner, R.J. Wasilewski, United States. National Aeronautics, and Space Administration. *55-Nitinol–the alloy with a memory: its physical metallurgy, properties, and applications: a report*. NASA SP. Technology Utilization Office, National Aeronautics and Space Administration, 1972. URL http://ntrs.nasa.gov/archive/nasa/casi.ntrs.nasa.gov/19720022818.pdf.

[120] J. Fialka and P. Benes. Comparison of methods of piezoelectric coefficient measurement. In *Instrumentation and Measurement Technology Conference (I2MTC), 2012 IEEE International*, pages 37–42, May 2012. doi:10.1109/I2MTC.2012.6229293.

[121] J.-M. Liu, B. Pan, H.L.W. Chan, S.N. Zhu, Y.Y. Zhu, and Z.G. Liu. Piezoelectric coefficient measurement of piezoelectric thin films: an overview. *Materials Chemistry and Physics*, 75 (1-3):12 – 18, 2002. ISSN 0254-0584. doi:10.1016/S0254-0584(02)00023-8.

[122] Glenn J T Leighton and Zhaorong Huang. Accurate measurement of the piezoelectric coefficient of thin films by eliminating the substrate bending effect using spatial scanning laser vibrometry. *Smart Materials and Structures*, 19(6):065011, 2010. doi:10.1088/0964-1726/19/6/065011.

[123] C.M Lueng, H.L.W Chan, C Surya, W.K Fong, C.L Choy, P Chow, and M Rosamond. Piezoelectric coefficient of GaN measured by laser interferometry. *Journal of Non-Crystalline Solids*, 254(1-3):123 – 127, 1999. ISSN 0022-3093. doi:10.1016/S0022-3093(99)00383-X.

[124] J.D.N. Cheeke, Y. Zhang, Z. Wang, M. Lukacs, and M. Sayer. Characterization for piezoelectric films using composite resonators. In *Ultrasonics Symposium, 1998. Proceedings., 1998 IEEE*, volume 2, pages 1125–1128 vol.2, 1998. doi:10.1109/ULTSYM.1998.765036.

[125] Americanpiezo. Wide-range d33 meter. URL https://www.americanpiezo.com/standard-products/d33-meter.html.

[126] Piezotest. d33 piezometer systems. URL http://www.piezotest.com/d33piezometer.php.

[127] A. V. Bune, Chuanxing Zhu, Stephen Ducharme, L. M. Blinov, V. M. Fridkin, S. P. Palto, N. G. Petukhova, and S. G. Yudin. Piezoelectric and pyroelectric properties of ferroelectric langmuir-blodgett polymer films. *Journal of Applied Physics*, 85(11):7869–7873, 1999. doi:10.1063/1.370598.

[128] L. Seminara, M. Valle, and M. Capurro. Bending response of PVDF piezoelectric sensors. In *Sensors, 2012 IEEE*, pages 1–4, Oct 2012. doi:10.1109/ICSENS.2012.6411405.

[129] Valentina Cauda, Bruno Torre, Andrea Falqui, Giancarlo Canavese, Stefano Stassi, Thomas Bein, and Marco Pizzi. Confinement in oriented mesopores induces piezoelectric behavior of polymeric nanowires. *Chemistry of Materials*, 24(21):4215–4221, 2012. doi:10.1021/cm302594s.

[130] D.H. Turnbull, M.D. Sherar, and F.S. Foster. Determination of electromechanical coupling coefficients in transducer materials with high mechanical losses. In *Ultrasonics Symposium, 1988. Proceedings., IEEE 1988*, pages 631–634 vol.2, Oct 1988. doi:10.1109/ULTSYM.1988.49454.

[131] Lucia Seminara, Marco Capurro, Paolo Cirillo, Giorgio Cannata, and Maurizio Valle. Electromechanical characterization of piezoelectric PVDF polymer films for tactile sensors in robotics applications. *Sensors and Actuators A: Physical*, 169(1):49 – 58, 2011. ISSN 0924-4247. doi:10.1016/j.sna.2011.05.004.

[132] V. Sencadas, R. Gregorio, and S. Lanceros-Mendez. α to β phase transformation and microstructural changes of PVDF films induced by uniaxial stretch. *Journal of Macromolecular Science, Part B*, 48(3):514–525, 2009. doi:10.1080/00222340902837527.

[133] Behzad Mohammadi, Ali Akbar Yousefi, and Samad Moemen Bellah. Effect of tensile strain rate and elongation on crystalline structure and piezoelectric properties of PVDF thin films. *Polymer Testing*, 26(1):42 – 50, 2007. ISSN 0142-9418. doi:10.1016/j.polymertesting.2006.08.003.

[134] P. Sajkiewicz, A. Wasiak, and Z. Gocłowski. Phase transitions during stretching of poly(vinylidene fluoride). *European Polymer Journal*, 35(3):423 – 429, 1999. ISSN 0014-3057. doi:10.1016/S0014-3057(98)00136-0.

[135] Christopher S. Lynch. Polyvinylidene fluoride (PVDF) elastic, piezoelectric, pyroelectric, and dielectric coefficients and their non-linearities. *Ferroelectrics*, 150(1):331–342, 1993. doi:10.1080/00150199308211451. URL http://dx.doi.org/10.1080/00150199308211451.

[136] S. Lanceros-Mendez, M. V. Moreira, J. F. Mano, V. H. Schmidt, and G. Bohannan. Dielectric behavior in an oriented β-PVDF film and chain reorientation upon transverse mechanical deformation. *Ferroelectrics*, 273(1):15–20, 2002. doi:10.1080/00150190211756.

[137] R. Barbosa, J. A. Mendes, V. Sencadas, J. F. Mano, and S. Lanceros-Mendez. Chain reorientation in β-PVDF films upon transverse mechanical deformation studied by SEM and dielectric relaxation. *Ferroelectrics*, 294(1):73–83, 2003. doi:10.1080/00150190390238630.

[138] A. M. Simpson and W. Wolfs. Thermal expansion and piezoelectric response of PZT channel 5800 for use in low-temperature scanning tunneling microscope designs. *Review of Scientific Instruments*, 58(11):2193–2195, 1987. doi:10.1063/1.1139486.

[139] Material: Lead zirconate titanate (PZT), 2015. URL https://www.memsnet.org/material/leadzirconatetitanatepzt/.

[140] Hyunuk Kim, Yonas Tadesse, and Shashank Priya. Piezoelectric energy harvesting. In Shashank Priya and Daniel J. Inman, editors, *Energy Harvesting Technologies*, pages 3–39. Springer US, 2009. ISBN 978-0-387-76463-4. doi:10.1007/978-0-387-76464-1_1.

[141] Chieh Chang, Van H. Tran, Junbo Wang, Yiin-Kuen Fuh, and Liwei Lin. Direct-write piezoelectric polymeric nanogenerator with high energy conversion efficiency. *Nano Letters*, 10 (2):726–731, 2010. doi:10.1021/nl9040719. PMID: 20099876.

[142] Morgan Advanced Materials. *Typical Properties of Piezo-Ceramics*, 2015. URL http://www.morganelectroceramics.com/resources/piezo-ceramic-tutorials/typical-properties/.

[143] T. Fett, D. Munz, and G. Thun. Tensile and bending strength of piezoelectric ceramics. *Journal of Materials Science Letters*, 18(23):1899–1902, 1999. ISSN 0261-8028. doi:10.1023/A:1006698724548.

[144] D Vatansever, R L Hadimani, T Shah, and E Siores. An investigation of energy harvesting from renewable sources with PVDF and PZT. *Smart Mater. Struct.*, 20:055019, 2011. doi:10.1088/0964-1726/20/5/055019.

[145] G Canavese, S Stassi, V Cauda, A Verna, P Motto, A Chiodoni, S Marasso, and D Demarchi. Different scale confinements of PVDF-TrFE and as functional material of piezoelectric devices. In *Sensors, IEEE*, pages 1–4, 2012. doi:10.1109/ICSENS.2012.6411330.

[146] E Gusarova, B Gusarov, D Zakharov, M Bousquet, B Viala, O Cugat, J Delamare, and L Gimeno. An improved method for piezoelectric characterization of polymers for energy harvesting applications. *Journal of Physics: Conference Series*, 476(1):012061, 2013. doi:10.1088/1742-6596/476/1/012061.

[147] Alexandra von Meier. *Electric Power Systems: A Conceptual Introduction*. Wiley survival guides in engineering and science. Wiley, 2006. ISBN 9780470036402. URL http://books.google.fr/books?id=qI2fNj2voe8C.

[148] Inc. Measurement Specialties. *Piezo Sensor - LDT Series*, 2015. URL http://www.meas-spec.com/product/t_product.aspx?id=5435.

[149] Federal Aviation Administration. Calculation of bend radii from tensile elongation data, September 2003. URL https://www.faa.gov/aircraft/air_cert/design_approvals/csta/publications/media/calc_bend_radii_tensile_elong_data.pdf.

[150] Stephan Schoenfelder, Matthias Ebert, Christof Landesberger, Karlheinz Bock, and Jorg Bagdahn. Investigations of the influence of dicing techniques on the strength properties of thin silicon. *Microelectronics Reliability*, 47(2-3):168 – 178, 2007. ISSN 0026-2714. doi:10.1016/j.microrel.2006.09.002.

[151] Plastics - determination of tensile properties - part 3: Test conditions for films and sheets. *BS EN ISO 527-3:1996*, 1966. URL http://www.iso.org/iso/iso_catalogue/catalogue_tc/catalogue_detail.htm?csnumber=4594.

[152] Pneumatic vice grips, 2015. URL http://www.testresources.net/grips-fixtures/by-product-type/pneumatic-vice-grips/.

[153] Hydraulic vice grips, 2015. URL http://www.testresources.net/accessories/tensile-grips/tensile-hydraulic-grip-g135-180/.

[154] Mitchell L. Thompson. *On the Material Properties and Constitutive Equations of Piezoelectric Poly Vinylidene Fluoride (PVDF)*. PhD thesis, Drexel University, April 2002. URL http://dspace.library.drexel.edu/bitstream/handle/1860/86/thompson_thesis.pdf;jsessionid=5B95195C6D5CC6A278C8B039AEFA4A7D?sequence=14.

[155] Standard test method for tensile properties of plastics. *ASTM D638 - 10*, 2010. URL http://www.astm.org/Standards/D638.htm.

[156] J. Richeton, S. Ahzi, K.S. Vecchio, F.C. Jiang, and R.R. Adharapurapu. Influence of temperature and strain rate on the mechanical behavior of three amorphous polymers: Characterization and modeling of the compressive yield stress. *International Journal of Solids and Structures*, 43(7-8):2318 – 2335, 2006. ISSN 0020-7683. doi:10.1016/j.ijsolstr.2005.06.040.

[157] Wen Yang Chang, Cheng Hung Hsu, and Chih Ping Tsai. Leakage and fatigue characteristics of polyvinylidene fluoride film. *Applied Mechanics and Materials*, 284-287(Cha): 158–162, January 2013. doi:10.4028/www.scientific.net/AMM.284-287.158.

[158] M. Y. Chung and D. C. Lee. Electrical properties of polyvinylidene fluoride films prepared by the high electric field applying method. *Journal of the Korean Physical Society*, 38(2): 117–122, February 2001. doi:10.3938/jkps.38.117.

[159] Aleksandra M. Vinogradov, V. Hugo Schmidt, George F. Tuthill, and Gary W. Bohannan. Damping and electromechanical energy losses in the piezoelectric polymer {PVDF}. *Mechanics of Materials*, 36(10):1007 – 1016, 2004. doi:10.1016/j.mechmat.2003.04.002.

[160] Macro fiber composite (MFC) - smart material, 2015. URL http://www.smart-material.com/MFC-product-main.html.

[161] I.P. Lipscomb, P.M. Weaver, J. Swingler, and J.W. McBride. The effect of relative humidity, temperature and electrical field on leakage currents in piezo-ceramic actuators under

dc bias. *Sensors and Actuators A: Physical*, 151(2):179 – 186, 2009. ISSN 0924-4247. doi:10.1016/j.sna.2009.01.017.

[162] Gary D. Jones, Roger Alan Assink, Tim Richard Dargaville, Pavel Mikhail Chaplya, Roger Lee Clough, Julie M. Elliott, Jeffrey W. Martin, Daniel Michael Mowery, and Mathew Christopher Celina. *Characterization, performance and optimization of PVDF as a piezoelectric film for advanced space mirror concepts.* Nov 2005. doi:10.2172/876343.

[163] Aleksandra Vinogradov and Frank Holloway. Electro-mechanical properties of the piezoelectric polymer PVDF. *Ferroelectrics*, 226(1):169–181, 1999. doi:10.1080/00150199908230298.

[164] R.E. Newnham, D.P. Skinner, and L.E. Cross. Connectivity and piezoelectric-pyroelectric composites. *Materials Research Bulletin*, 13(5):525 – 536, 1978. ISSN 0025-5408. doi:10.1016/0025-5408(78)90161-7.

[165] Martin L. Dunn. Micromechanics of coupled electroelastic composites: Effective thermal expansion and pyroelectric coefficients. *Journal of Applied Physics*, 73(10):5131–5140, 1993. doi:10.1063/1.353787.

[166] H. H. S. Chang and Z. Huang. Substantial pyroelectric effect enhancement in laminated composites. *Applied Physics Letters*, 92(15):152903, 2008. doi:10.1063/1.2907701.

[167] Z. Wang, S.R. Kirkpatrick, T. Adams, and A. Siahmakoun. TiNi MEMS heat engine. In *Proc. SEM X international congress & exposition*, page 4, 2006. URL http://sem-proceedings.com/04s/sem.org-SEM-X-Int-Cong-s058p01-TiNi-MEMS-Heat-Engine.pdf.

[168] Jayu Chen, Qi Chang Xu, Michael Blaszkiewicz, Richard Meyer, and Robert E. Newnham. Lead zirconate titanate films on nickel-titanium shape memory alloys: Smarties. *Journal of the American Ceramic Society*, 75(10):2891–2892, 1992. ISSN 1551-2916. doi:10.1111/j.1151-2916.1992.tb05526.x.

[169] Hiroshi Sato. Development of multifunctional wire that combines shape-memory alloy to piezo electric material. In *Proc. SPIE 6929, Behavior and Mechanics of Multifunctional and Composite Materials*, volume 6929, pages 69291I–69291I–7, 2008. doi:10.1117/12.779754.

[170] D C Lagoudas and Zhonghe Bo. The cylindrical bending of composite plates with piezoelectric and sma layers. *Smart Materials and Structures*, 3(3):309, 1994. doi:10.1088/0964-1726/3/3/007.

[171] S.B. Choia, Y.K. Park, and T. Fukuda. A proof-of-concept investigation on active vibration control of hybrid smart structures. *Mechatronics*, 8(6):673 – 689, 1998. ISSN 0957-4158. doi:10.1016/S0957-4158(98)00029-4.

[172] B. Jiang and R. C. Batra. Micromechanical modeling of a composite containing piezoelectric and shape memory alloy inclusions. *Journal of Intelligent Material Systems and Structures*, 12(3):165–182, 2001. doi:10.1106/MW7X-YEJK-17XD-GD2N.

[173] Onur Cem Namli, Jae-Kon Lee, and Minoru Taya. Modeling of piezo-sma composites for thermal energy harvester. In *Proc. SPIE 6526, Behavior and Mechanics of Multifunctional and Composite Materials*, volume 6526, pages 65261L–65261L–12, 2007. doi:10.1117/12.715786.

[174] H Alicia Kim, David Betts, Aki I T Salo, and Christopher Bowen. Shape memory alloy-piezoelectric active structures for reversible actuation of bistable composites. *AIAA Journal*, 48(6):1265–1268, June 2010. doi:10.2514/1.J050100.

[175] G. A. Lebedev, B. V. Gusarov, B. Viala, J. Delamare, O. Cugat, T. Lafont, and D. I. Zakharov. Thermal energy harvesting using shape memory/piezoelectric composites. In *Proc. Solid-State Sensors, Actuators and Microsystems Conference (TRANSDUCERS), 2011 16th International*, pages 669–670, June 2011. doi:10.1109/TRANSDUCERS.2011.5969842.

[176] Onur Cem Namli and Minoru Taya. Design of piezo-SMA composite for thermal energy harvester under fluctuating temperature. *Journal of Applied Mechanics*, 78(3):031001, February 2011. doi:10.1115/1.4002592.

[177] H. Karian. *Handbook of Polypropylene and Polypropylene Composites, Revised and Expanded*. Plastics Engineering. Taylor & Francis, 2003. ISBN 9780824748265. URL http://books.google.fr/books?id=4gjpmpVu8IsC.

[178] *Macro Fiber Composite (MFC) brochure*, 2015. URL http://www.smart-material.com/media/Datasheet/MFC-V2.1-2013-web.pdf.

[179] A.V. Shelyakov, N.N. Sitnikov, V.V. Koledov, D.S. Kuchin, A.I. Irzhak, and N.Yu. Tabachkova. Melt-spun thin ribbons of shape memory tinicu alloy for micromechanical applications. *International Journal of Smart and Nano Materials*, 2(2):68–77, 2011. doi:10.1080/19475411.2011.567305.

[180] W. Huang. On the selection of shape memory alloys for actuators. *Materials & Design*, 23 (1):11 – 19, 2002. ISSN 0261-3069. doi:10.1016/S0261-3069(01)00039-5.

[181] Thomas Lafont, L Gimeno, J Delamare, G A Lebedev, D I Zakharov, B Viala, O Cugat, N Galopin, L Garbuio, and O Geoffroy. Magnetostrictive-piezoelectric composite structures for energy harvesting. *Journal of Micromechanics and Microengineering*, 22(9):094009, 2012. doi:10.1088/0960-1317/22/9/094009.

[182] A.V. Irzhak, D.I. Zakharov, V.S. Kalashnikov, V.V. Koledov, D.S. Kuchin, G.A. Lebedev, P.V. Lega, E.P. Perov, N.A. Pikhtin, V.G. Pushin, I.S. Tarasov, V.V. Khovailo, V.G. Shavrov, and A.V. Shelyakov. Actuators based on composite material with shape-memory effect. *Journal of Communications Technology and Electronics*, 55(7):818–830, 2010. ISSN 1064-2269. doi:10.1134/S1064226910070120.

[183] Nimesis Technology. Shape memory materials, 2015. URL http://www.nimesis.com/domaine/nimesis-advanced-devices/produits-et-solutions/materiaux-memoire-de-forme/.

[184] Lia Kouchachvili and Michio Ikura. Improving the efficiency of pyroelectric conversion. *International Journal of Energy Research*, 32(4):328–335, 2008. ISSN 1099-114X. doi:10.1002/er.1361.

[185] J. Xie, X.P. Mane, C.W. Green, K.M. Mossi, and Kam K. Leang. Performance of thin piezoelectric materials for pyroelectric energy harvesting. *Journal of Intelligent Material Systems and Structures*, 21(3):243–249, 2010. doi:10.1177/1045389X09352818.

[186] R. Brett Williams, Daniel J. Inman, and W. Keats Wilkie. Temperature-dependent thermoelastic properties for macro fiber composite actuators. *Journal of Thermal Stresses*, 27(10): 903–915, 2004. doi:10.1080/01495730490498386.

[187] Thomas Lafont. *Recuperation d'energie par couplage piezoelectrique et magnetostrictif et electronique de gestion adaptee*. Theses, Université de Grenoble, Jul 2014. URL http://www.theses.fr/s126142.

[188] nagraID. The world leader in display card manufacturing, 2015. URL http://www.nidsecurity.com/products/.

[189] Diodes Inc. MURS140 - MURS160 surface mount super-fast rectifiers, 2015. URL http://www.diodes.com/datasheets/ds30130.pdf.

[190] Texas Instruments. TPS62122 step-down converter, 2015. URL http://www.ti.com/product/tps62122.

[191] Giuseppe Anastasi, Marco Conti, Mario Di Francesco, and Andrea Passarella. Energy conservation in wireless sensor networks: A survey. *Ad Hoc Networks*, 7(3):537 – 568, 2009. ISSN 1570-8705. doi:10.1016/j.adhoc.2008.06.003.

Publications and conferences

Publications

B. Gusarov, E. Gusarova, B. Viala, L. Gimeno, O. Cugat, ***PVDF piezoelectric voltage coefficient in-situ measurements as a function of applied stress***, Journal of Applied Polymer Science (2015).

B. Gusarov, E. Gusarova, B. Viala, L. Gimeno, S. Boisseau, O. Cugat, E. Vandelle, B. Louison, ***Thermal energy harvesting by piezoelectric PVDF polymer coupled with shape memory alloy***, Sensors & Actuators: A. Physical, submitted (2015).

E. Gusarova, B. Gusarov, D. Zakharov, M. Bousquet, B. Viala, O. Cugat, J. Delamare and L. Gimeno, ***An improved method for piezoelectric characterization of polymers for energy harvesting applications***, in Proc. PowerMEMS London, Journal of Physics: Conference Series, 476, 012061 (2013), doi:10.1088/1742-6596/476/1/012061.

D. Zakharov, B. Gusarov, E. Gusarova, B. Viala, O. Cugat, J. Delamare, and L. Gimeno, ***Combined pyroelectric, piezoelectric and shape memory effects for thermal energy harvesting***, in Proc. PowerMEMS London, Journal of Physics: Conference Series, vol. 476, p. 012021 (2013), doi:10.1088/1742-6596/476/1/012021.

G. Lebedev, B. Gusarov, B. Viala, J. Delamare, O. Cugat, T. Lafont, and D. Zakharov, ***Thermal energy harvesting using shape memory/piezoelectric composites***, in Proc. IEEE Transducers Beijin, China, pp 669 (2011) doi:10.1109/TRANSDUCERS.2011.5969842.

Conferences

B. Gusarov, L. Gimeno, E. Gusarova, B. Viala, S. Boisseau, and O. Cugat, ***Flexible composite thermal energy harvester using piezoelectric PVDF polymer and shape memory alloy***, Transducers'15, Anchorage, USA, oral presentation (2015).

E. Gusarova, B. Viala, A. Plihon, B. Gusarov L. Gimeno, and O. Cugat, ***Flexible screen-printed piezoelectric P(VDF-TrFE) copolymer microgenerators for energy harvesting***, Transducers'15, Anchorage, USA, poster (2015).

B. Gusarov, D. Zakharov, E. Gusarova, B. Viala, O. Cugat, J. Delamare and L. Gimeno, ***Thermal energy harvesting by combined pyroelectric, piezoelectric and shape memory effects***, SENSO 2014, Aix-en-Provence, France, oral presentation (2015).

Résumé français

Cette thèse présente un travail expérimental dédié à la récolte de l'énergie thermique. Ce travail porte sur un très petit aspect d'un problème beaucoup plus vaste: le monde industriel moderne fait face à un problème croissant de l'énergie; les combustibles fossiles sont limitées et coûteuses de l'environnement, et les sources d'énergie alternatives ne peuvent pas encore remplacer entièrement. La consommation mondiale d'énergie augmente progressivement chaque année, et les principales sources d'énergie étant consommés sont non-renouvelables charbon, le gaz et l'huile [20].

D'autre part, les technologies à grande échelle durables sont en cours d'élaboration pour capturer sources ambiantes efficacement renouvelables dans les formes de l'énergie solaire, l'énergie éolienne et de la marée.

Aux échelles inférieures, il y a aussi de petites quantités d'énergie gaspillée ou négligé qui pourrait être utile en cas de capture. Même en utilisant une petite partie de cette énergie autrement méconnu peut avoir un impact économique et environnemental important [21]. Ceci est où la récolte d'énergie entre en jeu.

Le concept de la récupération d'énergie se rapporte généralement à le processus d'utilisation des énergies ambiantes, qui sont transformés principalement en énergie électrique, afin d'alimenter de petits appareils électroniques et autonomes.

La récupération d'énergie capture de petites quantités d'énergie qui seraient autrement perdus. Cette énergie peut être ensuite utilisée soit pour améliorer l'efficacité des technologies existantes (par exemple, les coûts informatiques pourraient être considérablement réduits si la chaleur des déchets ont été récoltés et utilisés pour aider à alimenter l'ordinateur), ou pour permettre à de nouvelles technologies, par exemple les réseaux de capteurs sans fil.

La récupération d'énergie a le potentiel de remplacer les piles pour les petits appareils électroniques de faible puissance. Cela permettra sans entretien (pas besoin de changer les piles), respectueux de l'environnement (élimination des piles est problématique, car ils contiennent des produits chimiques nocifs et des métaux) et des applications distantes [21].

Nous pouvons imaginer des applications de surveillance de l'environnement de grandes infrastructures ou des endroits éloignés et difficilement accessibles tels que les glaciers ou les montagnes, les applications nécessitant plusieurs centaines de noeuds sans fil dispersés sur une vaste zone, ou les dispositifs médicaux implantés, où l'accès à remplacer les piles est gênant, voire impossible. En effet, dans de telles applications, des solutions de récupération d'énergie ont des avantages évidents [22].

Ces technologies en développement exigent une expertise dans tous les aspects de la physique, y compris la capture de l'énergie, stockage d'énergie, la métrologie, la science des matériaux,

gestion de l'alimentation et de l'ingénierie de système [21].
En outre, l'impact socio-économique des technologies de récupération d'énergie est d'une grande importance, avec un potentiel estimé du marché du € 3 milliards en 2020 et amplement l'occasion de la création d'emplois [23].

Dans ce contexte, cette thèse présente un travail expérimental dédié à la récolte de l'énergie thermique. Récolteuse de l'énergie, basé sur un système composite constitué d'un polymère de PVDF piézo-électrique en combinaison avec un alliage à mémoire de forme thermique NiTiCu, est étudié. Le but ultime est de faire de bas-batteuse flexibles de profil, capable de générer de l'énergie à partir des variations de température lents et petits, sans nécessité de la gestion de la source froide ou un radiateur. Ce serait agir comme un capteur thermique autonome de seuil, combinant détection et de l'énergie les capacités de récolte.
Le principe du composite de ce travail repose sur le fait que le PVDF a naturellement deux propriétés piézoélectriques et pyroélectriques. Lorsque la température augmente, la pyroélectricité génère une tension électrique en PVDF. Dans le même temps, l'alliage à mémoire de forme (SMA) engage une transformation de phase, ce qui induit une tension de 2 à 3 %. Cette souche est transférée au PVDF et génère supplémentaire de tension piézo-électrique en lui. Ces deux effets pyroélectriques et piézoélectriques résument et donnent lieu à une double augmentation de la sortie de l'abatteuse.
Comme nous le verrons plus loin, l'efficacité de conversion thermique à mécanique de NiTiCu peut être jusqu'à 8%. Dans un cas plus général de l'efficacité est d'environ 4%. Cette énergie mécanique est à son tour convertie en électricité par le comportement de PVDF piézo-électrique, avec une efficacité caractérisé par le coefficient de couplage k, ce qui peut être aussi élevée que 15%.
Ainsi, si l'on tient compte que la génération piézoélectrique, l'efficacité totale d'un SMA + harvester composite piézo-électrique peut être estimé à environ 0,6 %, ce qui est comparable à typique efficacité de conversion pyroélectrique ($\approx$ 1 %). Cela signifie que la combinaison de deux matériaux pyroélectriques non peut avoir théoriquement efficacité similaire à celle d'un matériau pyro-électrique par lui-même dans la conversion d'énergie thermique à électrique. L'estimation de l'efficacité est illustrée à la figure 1.1, avec un exemple de 100 J chauffage par effet Joule de NiTiCu.

Dans les paragraphes de cette thèse, nous allons présenter au lecteur les concepts de récupération d'énergie thermique, puis nous présenterons brièvement le pyroelectic et modèles théoriques piézoélectriques, et enfin nous allons donner une introduction aux matériaux de PVDF et NiTiCu avant de définir les principaux objectifs de ce travail.
Depuis PVDF est soumis à un chauffage et le stress mécanique, il est important d'évaluer comment il se comporte dans de telles conditions, d'évaluer son comportement pyroélectrique et d'étudier comment ses caractéristiques piézoélectriques sont touchés. Ces aspects seront présentés dans le chapitre 2, où nous allons effectuer la traction et de la température de PVDF commerciales afin de mesurer son coefficient de tension et d'auto-décharge dépendance piézoélectrique sur la température et de la souche.
Chapitre 3 sera consacrée aux composites PVDF + SMA; les méthodes de fabrication, la caractérisation composite et des capacités d'énergie seront explorées. Nous allons aussi les comparer avec les semi-flexibles composites piézo-électriques à base de céramique, en termes de densité d'énergie générée.

Chapitre 4 traitera du circuit impliqué dans la gestion de l'alimentation de l'énergie récoltée par nos composites. Depuis la tension générée par ces harvesters peut atteindre 400 V, un pas de deux convertisseur abaisseur personnalisé a été conçu pour réduire la tension à 1,5 à 2 V sortie stable, qui a ensuite été utilisé pour alimenter un émetteur de noeud sans fil.

La récupération d'énergie, en termes généraux, est la conversion de l'énergie a fait abstraction de l'environnement libre en une énergie électrique utile est de petites échelles, contrairement à grande échelle des énergies renouvelables fiables telles que le solaire, la production hydroélectrique ou éolienne. L'Institut de physique définit la récupération d'énergie comme un processus qui capture de petites quantités d'énergie qui serait autrement perdue[21]. L'énergie de l'environnement peut être présente sous de nombreuses formes, y compris la lumière, les vibrations, les écarts de température, de l'énergie de la radio, de l'énergie magnétique et même biochimiquement énergie produite[24]. Le principe de la récolte dépend de la forme de l'énergie disponible: il peut être récolté par un élément piézo-électrique, un thermo générateur -electric ou pyroélectrique, capturé par une antenne, etc. La principale différence de la récupération d'énergie à partir de la production d'énergie conventionnelle est qu'elle est libre frais, car il provient de l'énergie qui est autrement gaspillée (par opposition à pétrole ou le charbon de production), et fournit seulement une très petite quantité d'énergie pour l'électronique de faible énergie (par opposition aux éoliennes ou grands panneaux solaires). La récupération d'énergie cibles généralement ignoré des sources d'énergie, ce qui signifie que les sources ne sont pas fiables et petite. Principales cibles de demandes de récupération de l'énergie comprennent des dispositifs sans fil ultra-faible puissance, l'électronique portable, les réseaux de capteurs sans fil, télécommandes sans batterie, capteurs de pression de pneus de voiture et les alternatives aux petites batteries[21,25].
Tout environnement extérieur ou intérieur typique a un large éventail de sources d'énergie différentes. Parmi ceux déjà mentionnés, l'énergie solaire, thermique et cinétique sont trois énergies qui sont le plus souvent utilisés pour la récupération d'énergie à partir d'un environnement typique en plein air[22]. Il est difficile de généraliser ces sources, étant donné qu'ils sont présents dans diverses conditions, ils ne sont pas toujours disponibles et peuvent changer leur intensité dans le temps. Par conséquent, pour chaque cas particulier d'utilisation, la source ou la combinaison de plusieurs sources le plus approprié doivent être considérés, en ce qui concerne les niveaux de puissance typiques qui sont disponibles. Tableau 1.1 résume niveaux de puissance typiques théoriques pour différentes sources d'énergie. En termes de densité de puissance, l'énergie solaire dans des conditions extérieures fournit de bien meilleurs résultats. Toutefois, si utilisé à l'intérieur, il devient comparable avec d'autres sources; dans des environnements sales où les cellules peuvent devenir sombres, il ne convient pas du tout. Ainsi, le choix final des sources et des méthodes de récolte d'énergie est largement déterminée par les applications. Dans le cas de récupération de l'énergie cinétique vibrations exploiteuses, les spectres de vibration de la source varie largement pour différentes applications: par exemple, le mouvement humain est très différente de vibrations de machines, donc totalement différentes approches à la conception d'un générateur sont nécessaires. Va de même pour l'énergie thermique, qui peut être présent sous forme d'un gradient de température spatiale ou temporelle en tant que variations de température, et avec une large gamme d'amplitudes.
Energy harvesting comme il est connu aujourd'hui est apparu dans la fin des années 1990. Parmi les premiers étaient des chercheurs du MIT Media Laboratory qui ont présenté des communications sur le pouvoir de récolte dans les chaussures à l'aide de PVDF et PZT semelles et une minia-

ture rotor magnétique[26], et ont discuté de la possibilité d'alimenter un ordinateur en utilisant la puissance du corps humain juste, comme la chaleur , le souffle, ou motions[27].
En 2000, Rabaey et al.[28] proposé un réseau ultra-faible puissance sans fil avec une consommation d'énergie globale a diminué d'un facteur de 50. Ils ont également eu une vision de noeuds de réseau autonomes et auto-alimentés, en les alimentant avec une énergie de récolte des vibrations.
Aujourd'hui, avec l'intérêt mondial croissant pour l'Internet des objets[29], et le développement de nouvelles technologies de transmission de données sans fil et les appareils de faible puissance, un certain nombre de groupes académiques et industriels sont impliqués dans l'analyse et le développement de technologies de récolte d'énergie commerciale . Parmi eux sont de grands joueurs tels que Siemens avec leur entreprise spin-off EnOcean GmbH fourniture de solutions d'auto-alimentés pour la construction d'automatisation[30], mais aussi de nombreuses petites entreprises, tels que Algra avec des générateurs piézoélectriques mus par pression[31], Pavegen avec générateur tomette de traces piétonnes[32], Micropelt avec récupération d'énergie thermoélectrique[2], Perpetuum Ltd avec la vibration récolte[33], et d'autres. Dans et autour de la zone de Grenoble, INPG partenariat entre l'université et le CEA ont donné naissance à des start-ups telles Enerbee avec mouvement basé piézo générateurs -magnetic (fruits de collaborations de notre équipe avec le CEA - Leti)[34], HotBlock avec les systèmes thermoélectriques (CEA - Liten)[35], Arveni avec la récolte mécanique de l'énergie[36]. L'augmentation du nombre d'industriels et d'universitaires qui travaillent dans le domaine de la récupération d'énergie indique clairement l'intérêt et la demande de ces technologies pour l'avenir de la vie quotidienne.
L'intérêt devient encore plus évident lorsque l'on regarde l'aspect financier: la Commission européenne a signalé que, en 2009, le marché global des pêcheurs de l'énergie est élevé à €463 millions, avec 67 % étant incorporé dans les biens de consommation. En 2011, ce nombre était passé à €530 millions, avec près de €11 millions dépensés sur les pêcheurs de l'énergie dans les applications de capteurs sans fil. En 2011, la plupart des batteuses utilisés dans le marché étaient des cellules solaires, suivis par dynamos électro, qui, ensemble, sont parmi les technologies de récupération d'énergie les plus matures. Cependant, de nouvelles technologies prometteuses commencent à gagner des parts de marché, permettant l'alimentation des machines et de l'équipement dans les domaines où cela n'a pas été possible avant[23].
Les prévisions de marché varient entre 250 millions $ en 2017 par Yole[37] à plus de 4 milliards $ en 2021 par IDTechEx[38].
Depuis de nombreuses sources différentes d'énergie sont les stratégies actuelles et différents récupération d'énergie existent, il faudrait longtemps pour les décrire tous. En outre, de nombreuses excellentes critiques ont été publiés récemment, qui sous-tend l'état de l'art des technologies de récupération d'énergie[24,39–42]. Nous allons donc limiter notre discussion ici à la récolte de l'énergie thermique seul, car cela est l'énergie de l'intérêt dans ce travail.

Avant de passer aux détails techniques de récupération d'énergie thermique, nous estimons que les niveaux d'énergie sont nécessaires pour alimenter un noeud typique de capteurs sans fil autonome. D'une manière générale, sa consommation d'énergie peut être séparé entre l'énergie nécessaire pour le capteur lui-même d'effectuer des mesures physiques (température, pression, pH, l'humidité, etc.), et l'énergie nécessaire pour envoyer ces informations par l'intermédiaire d'un protocole sans fil.
Dans un examen par Dewan et al.[39] données pour la consommation du capteur varier de 0,01 mW (température, pH, les mesures d'humidité) à 85000 mW (processus océaniques, surveillance sous-

marine). Pour un capteur interne classique, nous pouvons prendre valeur de 10 mW.
Protocoles sans fil modernes ont une consommation d'énergie sous-watts, par exemple un Bluetooth émetteur linebreak consomme environ 10 mW[43]. La technologie Bluetooth Low Energy récente en charge la configuration de connexion et le transfert de données aussi vite que 3 ms[44].
Si l'on calcule maintenant l'énergie nécessaire pour la détection et la transmission, on obtient:

$$E = P \cdot T = (\ 10mW + 10mW\ ) \cdot 3\ ms = 60\ \mu J$$

Ces chiffres sont approximatifs. Il est difficile de donner des valeurs d'énergie moyennes, car elles sont très différentes et dépendent de la conception du système. En outre, de nombreux fabricants indiquent volontairement peu ou pas de données sur leurs produits car il est très dépendant des applications, par exemple le nombre de données envoyées, le protocole utilisé, planche conception, etc.
Cependant, nous pouvons estimer que les valeurs de l'énergie de l'ordre de grandeur de 100 μJ devrait être suffisant pour un seul cas de détection et de transmission de données sans fil. De notre propre expérience précédente avec le protocole sans fil ZigBee, l'énergie de 100 à 150 μJ par émission est nécessaire.

L'énergie thermique est présent dans de nombreux environnements et dans de nombreuses formes, que ce soit en tant que gradient de température spatiale ou temporelle en tant que variations de température. De nombreuses tentatives ont été faites afin d'exploiter cette énergie, qui est par ailleurs généralement gaspillée. Générateurs thermoélectriques sont généralement utilisés pour exploiter les gradients de température spatiales comme une source continue. Matériaux pyroélectriques sont généralement utilisés pour la récolte temporelles des gradients de température. Il est également possible de transformer un gradient de température en une variation de température temporelle, par exemple en utilisant un fluide calorique pompage entre les sources chaude et froide[45], ou au moyen d'un système mécanique avec un élément oscillant pyroélectrique entre les sources chaude et froide[46–48]. A l'inverse, en maintenant une température constante à une extrémité du générateur thermoélectrique, il est possible de variations de température de la récolte à l'autre extrémité[49].
Prévision du marché pour la récolte d'énergie thermique va à 100 millions $ en 2016 et à plus de 950 millions $ d'ici 2024[50], et des sociétés comme EnOcean, Micropelt et HotBlock sont déjà présents sur le marché avec leurs produits commerciaux.
Dans les prochaines sections, nous allons donner un bref aperçu de l'état de l'art pour les matériaux de récupération de l'énergie thermique. Nous allons essayer de comparer quels matériaux thermoélectriques - ou pyroélectriques - sont les plus efficaces dans des conditions données.

Le procédé de génération thermoélectrique est décrite par l'effet Seebeck. Les dispositifs se composent généralement de deux matériaux: de type n et de type p de semi-conducteurs, qui sont connectés électriquement en série, mais thermiquement en parallèle. Les deux semi-conducteurs produisent de l'électricité directement lors de leurs jonctions sont exposés à une différence de température (figure 1.2).
Générateurs thermoélectriques produisent une tension proportionnelle à la fois à la différence de température entre les côtés chaud et froid et de la différence entre les coefficients de Seebeck des deux matériaux, qui est elle-même fonction de la température.

L'efficacité des générateurs thermoélectriques est assez faible, car un matériau, pour être efficace, doit être à la fois un bon conducteur électrique et un bon isolant thermique. Malheureusement la plupart des matériaux qui sont de bons conducteurs électriques sont également de bons conducteurs thermiques, et vice versa. Pour estimer la propriété thermoélectrique d'un matériau, un facteur de mérite ZT appelé est utilisé.
Bien que théoriquement illimité, dans la pratique les valeurs ZT sont proches de 1. Figure 1.3 compare les valeurs ZT pour les thermoélectriques les plus couramment utilisés. Comme on peut le voir, l'efficacité augmente presque linéairement avec la température.
Thermoélectrique ont plusieurs avantages à savoir l'absence de pièces mobiles, un fonctionnement silencieux, la fiabilité et l'évolutivité. D'autre part, leur efficacité est faible, le prix est assez élevé et un dissipateur de chaleur massive est souvent indispensable (figure 1.2). Néanmoins, il existe de nombreux produits commerciaux qui exploitent thermoélectrique tels que les générateurs 'Micropelt' [2], applications automobiles [51,52], les piles à combustible [53,54] et montres [55].

L'énergie thermique peut également être exploité en utilisant des matériaux pyroélectriques. Comme indiqué par Sebald et al. [43], la récupération d'énergie pyroélectrique nécessite variations de température dans le temps, alors que thermoélectrique exigent spatiales gradients de température. Dans des conditions réelles de l'énergie thermique gaspillée, produite par exemple par des machines de travail, crée généralement des gradients spatiaux, favorisant ainsi thermoélectrique. Cependant, le taux de conversion peut être beaucoup plus élevé pour les générateurs d'énergie pyroélectriques, et théoriquement, il pourrait atteindre le taux de cycle de Carnot de conversion.
L'effet pyroélectrique est la propriété de certains matériaux diélectriques avec polaire symétrie ponctuelle d'avoir une polarisation électrique spontanée en fonction de la température. Quand un matériau pyroélectrique subit un changement temporel de la température, il en résulte un flux de charges, appelé courant pyroélectrique, ou à partir des surfaces du matériau. En supposant un matériau pyroélectrique homogène tout au long de laquelle la température T est uniforme, le courant pyroélectrique engendrée est donnée par equation [56].
Une illustration simple d'un système de récupération d'énergie pyroélectrique est présenté par Cha and Ju [4], à partir de laquelle nous allons fournir quelques citations. La figure 1.4 illustre un fonctionnement du cycle Ericsson, ce qui est le cycle le plus couramment utilisé pour la récupération d'énergie thermique d'exploiter deux sources de différentes températures. Il se compose de deux deux procédés de champ constant et à température constante. Lorsque la température du matériau pyroélectrique est diminuée [1 $\rightarrow$ 2] charges, sa polarisation et liée à la surface augmentent. Si le matériau pyroélectrique est connecté à un circuit externe, les charges libres sur ses électrodes seront redistribués pour compenser le changement dans les charges liées à la surface. Ces résultats responsable de la redistribution dans un flux de courant pyroélectrique dans le circuit. Plus frais seront accumuler le domaine de la polarisation externe est augmentée [2 $\rightarrow$ 3]. Ensuite, comme le matériau pyroélectrique est chauffé [3 $\rightarrow$ 4], le signe d'un courant pyroélectrique est inversé. Le cycle est complété par la réduction du champ de polarisation externe vers sa valeur initiale [4 $\rightarrow$ 1]. Les travaux d'électricité par cycle W correspond à la zone délimitée par les lignes de process 1-2-3-4, ou simplement $W = \oint EdD$.
Le phénomène de la polarisation spontanée à une différence de température est appelée pyroélectricité primaire. Il ya aussi une contribution de pyroélectricité secondaire, qui vient du fait que tous les pyroélectriques sont également piézoélectriques (bien que l'inverse est impossible en raison de leur structure cristalline polaire). Cela signifie que pendant le chauffage de la dilatation thermique

va changer la polarisation de la pyro-électrique dû à l'effet piézoélectrique.
En supposant un chauffage homogène, le coefficient pyroélectrique totale p pour la direction cristallographique *m* de pyroélectrique peut être écrite comme equation 1.5[57].
Ces coefficients pyroélectriques peuvent être présentés sous la forme de la charge pyroélectrique coefficients ρ_Q [Coul·m^{-2}K^{-1}] ou de tension pyroélectrique coefficients ρ_V [V·K^{-1}]. Ce dernier peut être calculé avec l'équation (1.6), comme indiqué dans[58].
La tension pyroélectrique développé à travers l'échantillon pour un changement de température ΔT, est donnée par l'équation (1.7).
La principale application de matériaux pyroélectriques est capteurs infrarouges passifs, principalement utilisés pour des détecteurs de mouvement. Beaucoup d'entreprises se partagent le marché, avec de grands acteurs industriels présents (Honeywell, Panasonic, Murata, etc.).
Maintenant, comme nous l'avons vu matériaux sensibles aux variations de température, nous allons continuer et présenter le matériel sensible au stress mécanique. Thèses matériaux sont appelés piézoélectrique.

Les matériaux piézoélectriques sont une sous-classe de diélectriques avec une structure cristallographique non centrosymétrique particulier. La classe piézoélectrique contient 20 sous-catégories, parmi lesquels il ya des matériaux pyroélectriques et ferroélectriques. Quand un matériau piézoélectrique est sollicité par une force extérieure, les réseaux sont tendues et les barycentres des charges électriques de cellules unitaires sont séparés. Ceci induit une polarisation du réseau comme indiqué dans la figure 1.5, et il est appelé l'effet piézoélectrique direct.
Inversement, lorsqu'une tension est appliquée à un matériau piézo-électrique, il est tendu comme représenté sur la figure 1.6. Ceci est appelé l'effet piézoélectrique inverse.

Prenons un système thermodynamique isolé avec énergie interne U, qui dépend de paramètres tels que le stress T, souche S, champ électrique E, déplacement domaine D, entropie σ et de la température θ. Depuis l'énergie totale d'un système isolé est constante (première loi de la thermodynamique), les variations de l'énergie dU peuvent provenir de variations de ses paramètres. Nous pouvons exprimer dU.
Dans les matériaux piézo-électriques, un couplage entre les composants mécaniques et électriques est introduit, ce qui signifie que le changement va nécessairement changer une de l'autre. Par exemple, la contrainte induite dépendra non seulement de la déformation appliquée, mais aussi sur le champ électrique appliqué. Nous pouvons exprimer le stress.
Nous effectuons maintenant l'intégration de l'équation (1.9) considérant le couplage électromécanique.
Voici le premier terme est l'élément mécanique, le second terme est le composant électrique et le troisième terme est le composant de couplage électro -mécanique.
La plus grande quantité possible d'énergie disponible dans le système est donnée par l'énergie libre de Gibbs G. On peut montrer qu'un changement dans l'énergie de Gibbs est donné par ΔU.
Les différentielles partielles de ΔG vont nous donner les paramètres du système.
Selon les conditions aux limites, quatre formalismes sont possibles. Par exemple, sous constante E et s, nous pouvons écrire l'equation 1.15.
Deux constantes mécaniques (C - rigidité, de la - conformité), deux constantes diélectriques (ε - constante diélectrique, β - constante de perméabilité) et quatre constantes piézoélectriques (e, g, h, d) sont utilisés pour décrire le matériau piézo-électrique. L'utilisation de ce constantes

on peut décrire le comportement du matériau lorsque l'un des paramètres a changé. Figure 1.7 résume schématiquement l'électro couplage -mécanique.
Tous les quatre piézoélectriques formalismes sont équivalentes. Cela signifie que tous les coefficients piézo-électriques sont reliés entre eux par l'equation 1.18.
Comme un facteur de qualité, les coefficient de couplage k^2 est introduite, qui montre quelle est la proportion d'une énergie mécanique d'entrée est transformée en énergie électrique utile (equation 1.19).

En raison de leur structure cristallographique particulière, les matériaux piézo-électriques sont très anisotropes, ce qui signifie que les propriétés varient en fonction de l'orientation du cristal. Pour décrire ces orientations, 3 axes et 3 rotations sont utilisés comme défini à la figure 1.8. Habituellement, l'axe 3 est placé le long de l'épaisseur de l'échantillon, et l'axe 1 est placé dans le plan le long de son côté le plus long.
Tous les paramètres mécaniques et électriques sont tenseurs d'ordres différents. Pour distinguer le piézoélectrique et coefficients d'élasticité mesurée le long de différents axes, ils sont présentés sous forme de matrice et sont notés d_{ij}, où l'indice i se réfère à la direction de tension générée et de l'indice j se réfère à la direction de la contrainte appliquée.
Pour déterminer entièrement le comportement de matériau piézoélectrique, 36 flexibilité coefficients s, 18 piézoélectrique coefficients d et 9 permittivité coefficients ε existe. Pour caractériser le comportement des matériaux piézo-électrique, il ya 63 coefficients à savoir, ce qui est un grand nombre. Néanmoins, même si les matériaux piézoélectriques sont pas centrosymmetric ils ont assez de la symétrie de réduire le nombre de coefficients. Tenant compte de cette symétrie, les matrices pour $dela$, d et ε sont présentés dans la figure 1.9[59]. Dans la pratique, la plupart du temps seulement 3 coefficients piézoélectriques sont utilisés: d_{33}, d_{31} et d_{32}. Nous parlons respectivement d'un mode "3-3", "3-1 mode" ou "mode 3-2" de fonctionnement.
Les matériaux piézoélectriques les plus couramment exploitées sont en céramique PZT ($Pb[Zr_xTi_{1-x}]O_3$, 0≤x≤1). Piézoélectricité se retrouve également dans des matériaux naturels tel que le quartz. Matériaux sans plomb sont également développés, comme métallique AIN ou $KNbO_3$. PVDF et ses copolymères sont naturellement piézoélectrique et appartiennent à l'électro polymères Active. Nous allons maintenant donner une brève introduction à PVDF polymères, y compris leurs propriétés et les applications.

Polyvinylidène fluorure, polyvinylidène difluorure ou simplement PVDF est un thermoplastique chimiquement stable polymère fluoré synthétisé par polymérisation de vinylidène difluorure. Dès 1969 Kawai[60] découvert l'effet piézoélectrique de PVDF et la première mesure de son g_{31} et d_{31} coefficients, qui étaient au moins un ordre de grandeur supérieur à ceux des autres polymères. Deux ans plus tard, l'pyroélectricité de PVDF a été découvert par Bergman et al.[61]. Depuis lors, PVDF et ses copolymères ont été étudiés pour leur utilisation dans pyroélectriques technologies et piézoélectriques. Le processus de fabrication bi-orienté PVDF a été développé plus tard[62] et a été montré pour être avantageux pour piezoelectic films[63]. Adaptation de cette amélioration technologique par Piezotech entreprise a éliminé piézoélectrique anisotropie et a permis pour la fabrication de la hausse des performances PVDF films[64].
Le semi-cristallin piézoélectrique PVDF polymère montre une structure complexe et peut présenter cinq phases cristallines distinctes: α, β, γ, δ et ε. Différentes phases sont liés à différentes conformations de la chaîne: TTT (all trans) de zigzag plane pour le β -phase, TGTG '(trans-

gauche-trans-gauche) pour le α et Δ phases et T_3GT_3G pour γ et ε phases[6]. Figure 1.10 montre les PVDF phases qui sont le plus utilisés pour les applications et étudiés, à savoir α, β et γ phases. Bon nombre des propriétés intéressantes de PVDF, en particulier celles liées à son utilisation comme un capteur ou actionneur, sont liées à la forte moment dipolaire électrique du PVDF unité monomère (5–8 $\cdot$ 10^{-30} Cm[65]) qui est dû à l'électronégativité des atomes de fluor par rapport à ceux de hydrogène et de carbone[66].

Ainsi, chaque chaîne possède un moment dipolaire perpendiculaire à la chaîne de polymère. Si les chaînes de polymère sont emballés dans des cristaux pour former des dipôles parallèles, le cristal possède un moment dipolaire net tel qu'il est le cas dans polaire β, γ et δ phases. Dans antiparallèles dipôles de la chaîne, le moment dipolaire net disparaît comme il est le cas dans la non-polaire α et ε phases[67].

Le β -phase est celui avec le plus haut dipolaire instant par cellule de l'unité (8 $\cdot 10^{-30}$ cm) par rapport aux autres phases[65], et il est celui qui donne le PVDF ses propriétés piézoélectriques. Par conséquent, la polaire β -phase a suscité beaucoup d'intérêt technologique raison de sa capacité de fournir la plus haute pyro - et la réponse piézoélectrique[67]. Par opposition aux matériaux céramiques où le mécanisme piézoélectrique est régi par dipôle réorientation, piézoélectricité en PVDF est censé être dominé en volume électrostriction; en conséquence, le d_{33} et g_{33} coefficients piézoélectriques sont négatifs en PVDF[68].

Différentes stratégies ont été développées pour obtenir le électro phase du PVDF, se concentrant principalement sur élaboration de procédures spécifiques de traitement et l'inclusion des charges spécifiques. Comme le résume Martins et al.[6] le β-phase est le plus souvent obtenu soit par étirement mécanique de α phase, ou à partir d'une masse fondue dans des conditions spécifiques telles que l'hypertension, le champ électrique externe et ultra- refroidissement rapide, ou de la solution de cristallisation à des températures inférieures à 70°C ou par l'addition de charges de nucléation tels que $BaTiO_3$, l'argile, le sel ionique hydraté, PMMA, TiO_2 ou nanoparticules tels que la ferrite, le palladium ou l'or.

Le mécanisme d'étirement est d'un intérêt particulier pour nous dans ce travail, depuis le PVDF connaîtra étirement par le SMA. Dans ce genre de β la formation de -phase, les résultats de stress appliquées dans l'alignement des chaînes de polymère dans les cristaux ainsi qu'un plan en zigzag tout-trans (TTT) conformation est intronisé. Un tel mécanisme permet d'aligner les dipôles perpendiculaire à la direction de la contrainte appliquée[67].

Le processus de transformation de α -phase de β-phase de PVDF par étirement mécanique tel que proposé par Li et al.[7] est résumé par le schéma de la figure 1.11. L'alpha sphérulites de PVDF avec des chaînes repliées est aisément obtenue dans des conditions de traitement classiques. Quand un étirage mécanique est appliquée sur le matériau, la région de transition de la structure cristalline commence à partir du milieu de la sphérulites, où les chaînes moléculaires sont étendus le long de la première direction d'étirage. Avec la déformation de la matière, des régions de chaînes longues se dilatent transversalement le long du milieu de la sphérulites. De plus en plus de longues chaînes sont formées avec l'évolution de la déformation de PVDF, jusqu'à ce que toute sphérulite de α-phase est transformé en β.

Pourtant, une autre façon d'obtenir PVDF dans son électro phase est d'utiliser PVDF de les copolymères. Ils sont élaborés et synthétisés pour améliorer matériau cristallinité, bien que le degré de polarisation de la structure de l'unité pourrait être réduite[69]. Une commun copolymère de PVDF est le poly (fluorure de vinylidène -CO- trifluoroéthylène) ou simplement P(VDF-TrFE), qui a un coefficient de piézo-électrique jusqu'à 38 pC/N[70] (jusqu'à deux fois autant que nous

PVDF).
Comme examiné par Qin et al.[69], PVDF est chimiquement inerte, comme beaucoup d'autres polymères de fluorocarbone. Sa haute résistance à l'hydrolyse, le taux de faible dégradation, et le vieillissement indépendant rigidité matérielle révèle le matériau biocompatibilité[71] (US Pharmacopeial classe VI[72]). Lorsque PVDF entre en contact avec les tissus humains, la réponse cellulaire minimale sans minéralisation, intima l'hyperplasie, ou une réaction de tissu fibreux excessif a été détecté[73]. Ainsi, PVDF peut être utilisé dans biomédicales applications, par exemple pour les structures de détection actifs dans des capteurs de pression implantables[74,75].
Les inconvénients de PVDF comprennent une mauvaise adhérence à d'autres matériaux en raison de ses propriétés non-réactifs, et son incapacité à former des films lisses[76]. Il a une relativement faible stabilité thermique des ferroélectriques propriétés (généralement jusqu'à 80°C) en raison de sa faible température de transition vitreuse[77], et une grande variation de constante diélectrique relative (de 6 à 13) dans la gamme de fréquence de 1 kHz à 1 MHz[78]. Enfin, les coûts de production sont encore relativement élevés, en particulier pour le P(VDF-TrFE) copolymères[69].
Pour ajouter aux inconvénients, le PVDF matériau est connu pour ses anisotropes propriétés de l'effet piézo-électrique[11,12,64,79]. La performance piézoélectrique selon la direction 2 de films orienté uniaxialement est inférieure à 1 selon la direction, qui vient de la anisotrope semi-cristallin structure. Ceci est attribué au processus qui se produisent dans les régions cristallines et à leurs interfaces avec l'environnement amorphes[11]. Films Toutefois, en bi-orientés axialement (un processus technologique de Piezotech entreprise) les anisotropes effets sont éliminés[64,80]. En outre, les films bi-orientés ont une épaisseur plus uniforme et une meilleure stabilité à long terme.
Ses caractéristiques thermiques, mécaniques, électriques et piézoélectriques (résumés dans le tableau 1.2) font PVDF un matériau prometteur pour capteurs[81–84] et la récolte d'énergie Combinaison naturelle de propriétés diélectriques et piézoélectriques permis la création de cellules d'auto-chargement électriques, où PVDF a été utilisé à la fois comme un séparateur et un piézo -Element[94,95]. Il a également été utilisé pour des mémoires non volatiles[96,97], transducteurs et actionneurs[98,99], et des capteurs[100–103]. De nombreuses autres applications comprennent l'isolation des fils électriques[104], les liants et les séparateurs dans les batteries lithium-ion[105], membranes[106] et même les lignes de pêche[107].
Les principaux industriels PVDF producteurs sont Spécialités société de mesure et américains groupe français Piezotech - Arkema. Dans ce travail, nous avons utilisé PVDF échantillons provenant de ces deux fabricants.

PVDF a été utilisé pour récolter différentes énergies mécaniques, y compris les vibrations[87,88], étirement[92], rain drop[86], flux d'air[90], écriture[85] et magnétiques[93] énergies. Ici, nous allons cependant se concentrer sur la récolte énergies thermiques avec PVDF et nous présenterons quelques résultats récents sur ce sujet.
Tableau 1.3 compare les pyroélectriques propriétés les plus courantes pyroélectriques matériaux, y compris PVDF. En raison de sa haute $\frac{\rho_Q}{\varepsilon}$ rapport, la pyro coefficient de tension de PVDF est d'un ordre de grandeur supérieure à celle du plomb Zirconate titanate (PZT) et le baryum titanate (Ba-TiO $_3$). Considérant cela, PVDF et de ses co-polymères ont attiré l'attention des chercheurs, et de nombreuses publications sur pyroélectrique récupération d'énergie sont apparus juste récemment. Cuadras et al.[108] rapporté en 2010 atteindre jusqu'à 15 μJ d'énergie récoltée avec un PVDF cellule mince de film pour les fluctuations de température de 300K à 360K dans une période de temps de l'ordre de 100 s. Ils ont à plusieurs reprises commerciales chauffées PVDF éléments

avec un sèche-cheveux et utilisé un circuit de redresseur de facturer 1 μ condensateur de charge de F à 5,5 V . Basé sur les tailles prévues (3×1.2 cm^2 et épaisseur 64 μm), nous estimons que la densité d'énergie produite pour être autour de 65 $\mu J/cm^3$. Auteurs proposent que, avec un circuit de gestion d'énergie propre, ce batteuse pourrait être utile pour surveiller les tuyaux chauds, où le gradient de température temporelle est suffisant pour alimenter les noeuds de capteurs autonomes.
En 2013 Lee et al.[8] proposé d'exploiter directement le fait que les pyroélectriques matériaux sont également piézoélectriques, en fabriquant ce qu'ils ont appelé un *hautement extensible Piezoelectric-pyroélectrique hybride Nanogénérateur*. Il se compose de micro-motif P (VDF - TrFE) de graphène électrodes, monté sur un micro-motifs polydiméthylsiloxane (PDMS) de carbone a nanotubes (NTC) substrat composite. Le résultat était un composite hautement étirable qui peut être étiré jusqu'à 30 % et encore produire un stable pyroélectrique tension. La tension de sortie maximale signalé était de 1,4 V lors de l'application simultanée d'un mode différent de la souche et la température appliquée de 20 ° C (gradient thermique de 120 °C/ s). Malheureusement, les auteurs ne précisent pas l'énergie récoltée. On peut estimer que ce soit autour de 24 nJ (ou 2 $\mu J/cm^3$) sur la base du PVDF épaisseur (7 μm), sa constante diélectrique, et la taille de le harvester (≈4× 4 cm^2).
Yang et al.[9] souple rapporté un multimodal cellule hybride d'énergie qui est capable de simultanément ou individuellement récolte énergies thermiques, mécaniques et solaires. La multimodal batteuse est composée d'un PVDF couche, un réseau de nanofils de ZnO et un poly(3-hexylthiophène) (P3HT) hétérojonction de cellule solaire. Le PVDF partie seule était capable de produire 3,2 V avec une différence de température de 19 °C de plus de 100 s. Basé sur le PVDF épaisseur (100 μm), sa constante diélectrique, et la taille de le harvester estimée à partir de la figure 1.13 (≈5×3 cm^2), la densité d'énergie correspondant était d'environ 0,5 $\mu J/cm^3$. Multiples récoltes d'énergie (soit + thermique piézo, solaire thermique +) ont augmenté le rendement global du système.
Wu et al.[109] a présenté en 2014 un 2 ×2 cm^2 pyroélectrique hétéro-structure du plomb zirconate titanate (PZT) particules enrobées dans P(VDF-TrFE) copolymère. En raison de combiné formabilité, faible conductivité thermique et haute pyroélectrique coefficient, les auteurs ont proposé d'utiliser le composite comme un capteur thermique infrarouge et étaient en mesure d'atteindre des valeurs élevées de détectivité. En principe, le même hétérostructure pourrait être utilisé à des fins de récupération d'énergie, et il serait très probablement obtenir de meilleurs rendements par rapport à la réponse individuelle des composants.
A titre d'exemple, lorsque Ericsson cycle de conversion est appliqué densités d'énergie plus élevés sont obtenus, mais l'application d'un champ électrique très élevé est nécessaire. Cha and Ju[4] ont démontré la faisabilité de l'utilisation d'une interface thermique à base de liquide entre le pyro-P(VDF-TrFE) couche et une source de chaleur/évier afin d'augmenter le gradient de température temporelle. L'utilisation de glycérol comme une interface liquide diélectrique a aidé à créer un contact complet entre deux surfaces et d'éliminer les couches de gaz piégé. L'évaluation de le harvester a été fait dans ce cas par l'application d'un champ électrique de polarisation tout en surveillant la pyro-électrique actuelle. Avec une différence de température de 60 ° C entre le dissipateur de chaleur et la source, l'appareil a été en mesure de récolter jusqu'à 550 mJ/cm^3 au champs électrique appliqué de 750 kV/cm. Pour les applications de la vie réelle les auteurs mais reconnaissent que le harvester ne sera pas produire une telle énergie haute car il ne sera pas possible d'appliquer ces grands champs de polarisation.
Comme nous pouvons le voir dans le tableau 1.4, la plupart des pyroélectriques pêcheurs de l'énergie thermique avec PVDF ou P(VDF-TrFE), testés dans des conditions réelles, peut produire

de 0,5 à 65 μJ/cm^3 avec des différences de température de 20 à 60°C.
Pour augmenter l'efficacité des pêcheurs, la recherche aujourd'hui se penche sur multimodal récolte ou matériaux améliorés. La façon exploré dans ce travail est la fabrication de matériaux composites pour améliorer la récupération d'énergie thermique. Arracheuse de l'énergie composites peuvent être réalisées en utilisant soit des matériaux de différentes familles, mais même fonctionnalité (par exemple la céramique + polymères), ou des matériaux de différentes fonctionnalités (par exemple pyroélectrique + forme un alliage à mémoire), ou la combinaison d'une fonction et d'un matériau non-fonctionnel. Dans la section suivante, nous allons introduire les alliages à mémoire de forme, qui ont été utilisés pour la fabrication de nos vendangeurs composites. Nous reviendrons à la récolte d'énergie composite dans le chapitre 3 où nous présenterons nos résultats sur cette question.

Alliages à mémoire de forme (SMA) appartiennent à une famille de matériaux qui ont la capacité de revenir à une forme prédéterminée lors du chauffage. L'état chaud de la SMA est appelée austénite; au cours du refroidissement, le matériau subit une martensitique transformation qui est une première transition de phase d'ordre de diffusion-moins, ce qui entraîne une déformation de cisaillement en forme de réseau cristallin. Le produit de cette transformation est appelée martensite. Si le matériau est déformé à froid et ensuite chauffé, le changement inverse dans la structure cristalline provoque son retour à sa forme initiale.
Pas tous les alliages subissant martensitique transformation effet de mémoire de forme présente (par exemple martensitiques des aciers), mais seulement ceux où cette transformation est thermoélastique, à savoir la cohérence entre les deux phases est conservée.
La fois directe et inverse des transformations se produisent dans un intervalle de température et sont caractérisées par des températures départ et d'arrivée. En outre, thermodynamiquement hystérésis thermique conditionné empêche ces intervalles de température de coïncider.
Prenons un coup d'oeil de plus près à sens unique effet de mémoire de forme, qui est l'effet le plus commun de récupération de forme, et est réalisé uniquement pendant le chauffage. Schéma d'une courbe contrainte-déformation-température est montré dans la figure 1.14. La première étape de la séquence de chargement, lorsque la souche est initialement appliquée, induit un stress linéaire dans le martensitique structure à pas de changement de forme macroscopique. Pendant la deuxième phase, la contrainte mécanique dans le martensitique en phase induit une réorientation des grains jumeaux (dite de detwinning) et des résultats en grande déformation inélastique, qui ne sont pas récupérés lors de déchargement (courbe bleue). Ensuite, le matériau est chauffé et l'inverse martensitique transformation récupère la déformation inélastique. Depuis martensite grains ont été réorientés par le stress, le retour à austénite produit une grande déformation de transformation ayant la même amplitude, mais la direction opposée à la déformation inélastique et le SMA retourne à sa forme originale dans sa austénitique phase (courbe rouge). Enfin, le matériau est refroidi et le martinsitic phase est formée à nouveau; le processus peut maintenant être répétée (courbe verte).
SMA avec bidirectionnelle effet de mémoire de forme sont différents dans la façon dont les cours du refroidissement, l'martensitique transformation est également accompagné par la souche induite. Ainsi, le matériau peut se souvenir de ses deux états chauds et froids.
Martensitique transformation se produit dans un certain thermodynamique intervalle de température Climatisé, représenté schématiquement à la figure 1.15. Pendant le refroidissement, une transformation directe a lieu dans l'intervalle de température ΔT_M: à partir de M_s et de finition au M_f.

De même, pendant le chauffage, une transformation inverse qui se passe dans l'intervalle de température ΔT_A: à partir de A_s et de finition à A_f. Les deux transformations sont décalés par ΔT_{hys} correspondant à la surchauffe nécessaire à franchir l'énergie d'interface. Intervalle de transformation ΔT_{transf} = A_f - M_f est l'amplitude minimale d'un cycle thermique nécessaire pour remplir à la fois les transformations directes et inverses.
Il existe de nombreuses familles de matériaux qui présentent l'effet de mémoire de forme, y compris l'or, le cadmium, le cuivre-zinc et des alliages métalliques à base de fer, et un polyéther - ou des polymères à base de polyester. Parmi ceux-ci, l'alliage nickel-titane (ou Nitinol, de nickel et de titane Naval Ordnance Laboratory) découvert en 1959[114] a reçu un plus grand nombre d'applications. Nitinol est moins fragile et capable de souches élevées récupérables (deux fois celle de la alliages de cuivre)[115], et il peut être produit dans des films minces[116] qui est important pour la fabrication de lots et MEMS technologie.
Il dispose également de très bonnes propriétés électriques et mécaniques, longue durée de vie, la fatigue et la résistance à la corrosion; Son principal électro propriétés -mécanique sont résumés dans le tableau1.5. Lors du chauffage NiTi alliages peuvent développer grand stress et les taches, jusqu'à 600 MPa et 10 %, respectivement. Généralement, les alliages à plus grande pression et du stress ont de plus grands intervalles de température et hystérésis. Ceci limite l'énergie qui peut être récoltée à partir d'un système donné. Par ailleurs, toutes ces caractéristiques sont nettement dépendante du SMA composition, ce qui signifie que le choix optimal d'un alliage ou l'ajustement de sa composition pour les applications de collecte d'énergie spécifique sont typiquement requis.
Pour estimer l'efficacité de la conversion de la chaleur en énergie mécanique par SMA, nous pouvons effectuer une série de calculs simples[49]. L'énergie thermique d'entrée requis par le SMA corps pour effectuer un travail mécanique se compose de la chaleur pour augmenter sa température (généralement de 20°C pour NiTi) et de la chaleur latente de transformation ($\approx$ 20 J/g pour NiTi[117,118]). Par conséquent, la valeur normale de l'énergie d'entrée est d'environ 30 J/g.
Travail mécanique spécifique qui peut être produite par SMA peut être calculée comme un produit de la contrainte mécanique générée ($\approx$500 MPa en moyenne) et de sa déformation relative ($\approx$ 3% en moyenne). De cette façon, le travail utile peut être estimé comme 15 J/cm^3 ou 2,3 J/g (en prenant la densité de NiTi 6,5 g/cm^3 [117,119]). L'efficacité, qui est le rapport de travail à la chaleur d'entrée, peut alors être estimé comme 2,3 $\div$ 30 = 8 %. Alors que les valeurs publiées varient dans 3 à 30 %[117,118], dans la majorité des publications théoriques et expérimentales de l'efficacité rapportée est <10 %.

Maintenant que nous avons présenté brièvement les principes physiques et les matériaux utilisés dans ce travail, nous pouvons définir les spécifications de notre dispositif de récupération d'énergie.
Nous voulons que notre dispositif pour être en mesure de récolter aléatoires des variations de température, donc être indépendante de la fréquence. Cela signifie que peu importe si l'événement est souvent répété ou si il arrive de temps en temps, l'énergie produite par le harvester doit être la même.
Thermoélectriques générateurs ne peuvent pas être utilisés dans de telles conditions, car ils peuvent travailler uniquement avec des gradients de température en continu. Des événements uniques de chauffage ne sont pas suffisantes pour la transmission sans fil, et les événements répétés sont nécessaires pour générer assez de puissance.
Pyroélectriques générateurs peuvent, en principe, travailler avec les événements de chauffage sim-

ples. Toutefois, la puissance générée sera toujours dépendant de la fréquence, et l'énergie générée est proportionnelle à gradient de température.
En revanche, les pêcheurs de l'énergie composites peuvent augmenter la densité de l'énergie générée par l'utilisation de deux effets complémentaires: piézoélectrique et pyroélectrique. Cette multimodal approche de la récolte permettra la détection d'événements aléatoires de chauffage dans des plages de température étroites, et de générer assez d'énergie pour la communication sans fil. En outre, l'utilisation de SMA va ajouter une fonctionnalité de détection de l'appareil: dans le ΔT_{transf} intervalle, la détection d'événements thermiques avec seuil prédéterminé sera possible. Ainsi, la machine de récolte composite sera en mesure de détecter et en même temps la production d'énergie nécessaire pour envoyer les informations sur l'événement thermique à un récepteur distant.
Le dispositif de récupération d'énergie composite se compose de PVDF films et NiTiCu rubans, couplés ensemble. La souche de la température induit des NiTiCu (2–3%) et augmentation de la température (jusqu'à 70°C) doit être compatible avec PVDF conditions opérationnelles. Enfin, avec un chauffage de la température ambiante à 50 à 70°C, le harvester devrait produire de l'énergie de production d'environ 100 μJ, assez pour alimenter un émetteur sans fil.

Habituellement coefficients piézoélectriques des films minces de céramique sont mesurées par interférométrie optique analyse des que bien que avec Berlincourt Type piézomètres[125,126]. Par conséquent l'piézoélectrique d_{33} ou d_{31} frais coefficients sont généralement extrait de la mesure, à partir de laquelle le g_{33} ou g_{31} coefficients de tension peut encore être recalculé.
Mesures Pizoelectric de films de PVDF ont été rapportés en utilisant des techniques similaires. Pour ne citer que quelques exemples, Bune et al.[127] ont mesuré les d $_{33}$ coefficient dans la gamme de fréquence de 1-100 kHz par interférométrie laser. Roh et al.[79] utilisé un bas -Fréquence surface acoustic wave méthode pour mesurer le nombre d'onde complexe K_m de laquelle le g $_{ij}$ matrice a été calculé en utilisant un numérique algorithme.Seminara et al.[128] ont mesuré le comportement dynamique d'un film de PVDF autonome dans pur flexion. Enfin, Piezoresponse vigueur microscopie (GFP) a été également utilisé pour mesurer le d_{33} coefficient[129]. Comme dans le cas de la céramique, ces méthodes sont indirects, ce qui signifie que le g_{ij} coefficients sont recalculés sur la base des autres mesurées constantes. Le couplage coefficient est habituellement recalculée à partir de l'impédance résonance fréquences[120], mais il est connu pour être un gênant méthode pour PVDF en raison de ses mécaniques élevées pertes[130]. Beaucoup expérimentale travaille sur PVDF piézo-électrique caractérisation utilisation mesures de fréquence et étudier la dépendance des coefficients piézoélectriques sur la fréquence de mesure dans la gamme haute -Fréquence[127,131]. Il serait donc intéressant de mesurer la réponse piézo-électrique dans des conditions quasi-statiques, semblable à nos applications de récolte lentes les fluctuations de température.
Il a été montré par de nombreux groupes de recherche que le contenu des piézoélectrique β triphasée en PVDF dépend sur l'allongement[7,132,133], traction souche taux[7,133,134] et chauffage[7,132,134]. Il est convenu que la contenu de β-phase augmente fortement avec l'allongement. Il augmente également avec la température de la température ambiante à environ 80°C, mais diminue en avec en outre le chauffage. Certains travaux ont montré une importante augmentation de β triphasée avec augmentation de la traction souche taux, mais d'autres travaux ont montré aucun effet du tout ou même une légère diminution[7,134]. Quoi qu'il en soit, prononcées effets ont été présentés seulement à haute contrainte gammes de 100-550 % et des températures autour de 80°C. Petite

discussion a été accordée aux effets à petites souches, et aucun effet direct de la souche sur le g_{31} piézoélectrique coefficient de tension a été mesurée. Il serait donc intéressant de directement mesurer la g_{31} la valeur et étudier sa dépendance à la contrainte appliquée et de la température, en particulier dans la gamme des applications envisagées à savoir une souche d'environ 2 % et une température de jusqu'à 70°C.
Il ont été quelques expérimentales travaux sur le comportement des piézoélectriques propriétés de PVDF sous faible appliqué stress. Une des premières oeuvres va revenir à 1985 par Hahn[11]. Il a étudié le comportement de d_{31} et d_{32} sous contrainte appliquée jusqu'à 60 MPa dans un PVDF étirée axialement uniforme. Il a noté le comportement linéaire de d_{31} et une diminution non linéaire inhabituelle de d_{32} qu'il croyait dû à des effets intrinsèques liés aux changements d'orientation de dipôle. La grande différence entre le d_{31} et d_{32} valeurs (d_{31} a été mesurée à environ 20 fois plus élevés à chambre décrit que le piézo-électrique réponse le long de la direction 1 est principalement déterminée par une déformation des régions amorphes, tandis que les deux sens dépend également de la déformation des régions cristallines
En 1993 Lynch[135] mesuré coefficients piézoélectrique de stress e_{31} et e_{32} à petites déformations. Il n'a pas observé de souche dépendance considérable, et a suggéré que tous les non-linéarités de la d_{ij} coefficients proviennent des non-linéarités du module d'élasticité.
En 20002 Lanceros-Mendez et al.[136] étudié PVDF films au cours de la déformation processus au moyen de diélectriques mesures et FTIR (Fourier Transform Infrared Spectroscopy) et plus tard par SEM (Scanning Electron Microscope)[137]. Les auteurs rapportent une réorientation de le β phase chaînes de parallèle à perpendiculaire à la contrainte orientation à l'intérieur de la matière plastique région. Aussi une diminution dans le taux de cristallinité due à la déformation a été observée. Basé sur les résultats de ce travail, on peut s'attendre à la diminution de la piézoélectriques propriétés au sein de la matière plastique région de la matière due à la continue réorientation de chaînes et diminution de cristallinité.
Sencadas et al.[12] en 2004 a effectué des tests de traction sur métallisé 28 μm d'épaisseur β PVDF films long de la direction 2. La réponse électrique générée a été mesurée en circuit ouvert sous un taux de déformation constante à la température ambiante. Le (extrait des résultats présentés dans la figure2.2) a montré que la tension en circuit ouvert développé par l'échantillon dans une déformation uniaxiale augmenté non linéairement avec la contrainte appliquée dans la zone pré - cédant et a diminué dans l'après - cédant. zone Le expérimentale idée est similaire à notre travail, qui est de déterminer l'évolution de g_{ij} coefficients avec l'appliqué stress. Malheureusement, des valeurs précises ou pas d'informations sur la façon dont le coefficient g_{ij} a été calculé sont donnés, et que le g_{32} comportement général a été interprété.
On peut résumer ainsi que le g_{ij} coefficient piézoélectrique est rarement étudiée directement, même si elle est une caractéristique importante de la matière pour les applications de récupération de l'énergie ou de générateurs. Compte tenu de cela, nous avons concentré nos efforts sur la mesure directe de la g_{ij} coefficients, et effectuer les mesures conformément à nos conditions opérationnelles ciblées, à savoir une situation de quasi-statique et contrainte appliquée élevé.

Pour estimer la tension de sortie théorique et la densité de l'énergie produite en un matériau piézoélectrique utilisé en tant que générateur, nous allons décrire les équations analytiques correspondants et couplage matrice. Ensuite, en utilisant connu Fiche mécaniques et piézoélectriques constantes nous allons calculer la maximale théorique des performances de PVDF et comparer avec d'autres communes piézoélectriques.

Nous avons déjà vu qu'il est possible de décrire le comportement d'un piézoélectrique matériau utilisant le piézoélectrique couplage matrice, qui est donné dans sa forme générale par l'équation (1.15). Selon la façon dont le matériau est utilisé, et donc les conditions aux limites, la forme fondamentale peut être réécrit en conséquence. Pour le cas des générateurs, le couplage matrice devrait être réécrite comme pour donner le produit électrique champ sous appliqué le stress ou de la souche. Dans le cas d'un -standing gratuitement composite couplé avec SMA, PVDF subit la contrainte appliquée pendant qu'il reste mécaniquement libre, ce qui signifie que la contrainte T est constante. Pendant les mesures, le PVDF est relié à un circuit électrique ouvert, ce qui signifie qu'il n'y a pas de déplacement de charge et le champ de déplacement électrique D est constante. Si nous considérons ces conditions limites, la matrice de l'équation (1.15) peut être réécrite sous la forme suivante:
Dans les conditions expérimentales de circuit ouvert, D est égal à zéro, de sorte que la matrice se simplifie en:
L'indice ^{D} indique que la valeur a été mesurée sous constante D. Toutefois, ces conditions de mesure ne sont pas toujours possible ou pratique, et les valeurs sont parfois mesurée sous constante E. Dans le cas de la souplesse de , les valeurs mesurées dans différentes conditions sont reliés par l'équation suivante:
bigskip
En fonction de la matière, la s^D et s^E peuvent être très différents, ce qui conduit à différents élastiques propriétés de la piézoélectrique matière, lorsqu'elle est mesurée sous différentes expérimentales conditions, telles que en circuit ouvert ou en circuit fermé mesures. Par exemple, des artefacts tels que des dents de scie un contour de la courbe de dilatation thermique du PZT, ont été rapportés pour être causé par ce phénomène[138]. Aucun de ces artefacts ont été rapportés pour le PVDF à notre connaissance.
Pour comprendre cet impact des conditions expérimentales sur les propriétés mécaniques d'un piézo-électrique, nous estimons les valeurs des premier et second termes de la somme de l'équation 2.3 en utilisant les constantes matérielles standard de PVDF, et comparer à PZT Pour ce faire, nous devons prendre en compte que s^E = YM^{-1} pour 1-1 et 3-3 les directions, $\beta^T = (\varepsilon^T)^{-1}$ et $d^t_{33} = d_{33}$. Les principales étapes de calculs sont montré dans tableau 2.1.
Nous pouvons voir que pour PZT, le second terme ($d^t \cdot \beta^T \cdot d$) est d'environ 30 % de la première période (s^E); par conséquent, la valeur du s^D est d'environ 30 % plus élevé que la valeur du s^E. D'autre part, pour le PVDF le second terme est 43 fois plus petite que la première et peut donc être tout simplement négligé, donc les valeurs de s^D et s^E sont à peu près équivalente. Cette est l'un des importants avantages de PVDF sur PZT, depuis sa mécanique respect s ne pas dépendre sur en circuit ouvert ou en circuit fermé conditions.
Revenons maintenant plus loin et extraire la tension piézo-électrique à partir de la seconde expression de l'équation eqref eq:piézo matrice SE forme simple Il peut être exprimé en fonction de l'épaisseur du matériau t, son piézoélectrique constant g_{ij} et la contrainte appliquée T.
Du point de vue de l'échantillon la géométrie, nous pouvons voir que, lors de l'examen de la même façon homogène appliqué le stress, la sortie piézoélectrique tension ne doit être dépendante sur le matériau d'épaisseur et devrait être indépendante sur de l'échantillon de la longueur et la largeur.
Pour une utilisation pratique l'équation (2.4) peut être réécrit alors en fonction de la souche S, appliquée à la matière Cependant, cette équation ne serait valable que dans la gamme élastique de PVDF, où la souche et le stress sont linéairement proportionnel.
La représentation graphique de la tension de sortie théorique pour un 30 μm d'épaisseur PVDF

dans les différents modes de travail en fonction de l'équation (2.5) est représenté dans la figure 2.3. Comme prévu par les -coefficients piézo correspondant, le mode 3-3 doit donner une tension de sortie plus élevée. Cependant, comme nous le verrons plus loin, ce ne est pas toujours le cas, car expérimentalement, il est beaucoup plus compliqué à appliquer une contrainte homogène sur minces échantillons flexibles en mode 3-3 pure.

PVDF, en raison de sa flexibilité, est généralement considéré comme une haute énergie matérielle de densité[140]. Pour estimer son électrique de sortie de l'énergie que nous avons à faire plusieurs hypothèses: lorsque le matériau est mécaniquement déformé par un externe vigueur, sa mécanique l'énergie peut être caractérisé par la densité d'énergie élastique de $U_{mcanique}$.

La conversion de la mécanique de l'énergie en énergie électrique l'énergie est représentée par l'électromécanique couplage coefficient k exprimé en %:

Nous pouvons exprimer la densité d'énergie électrique en fonction des contraintes mécaniques ou de stress.

Depuis PVDF et ses copolymères sont disponibles par différents fournisseurs et avec différentes compositions, nous avons résumé certains des plus populaires commerciale grades dans tableau 2.2 pour estimer leur théorique disponible densité d'énergie. Nous avons calculé les densité d'énergie des valeurs à l'aide de l'équation (2.8) à 2 % de déformation, car il est notre valeur de déformation ciblée qui est possible de réaliser en utilisant des alliages à mémoire de forme Nous avons également ajouté à titre de comparaison les données de l'état non commerciale - de - les nanofibres -Art, produites par électrofilage PVDF, et d'un matériau PZT classique. Pour PZT, souche de 0,08 % est prise pour les calculs, car il est la souche de rendement moyen de la matière (plus élevés souches conduisent à l'échec de la matière).

De ces simples calculs, nous pouvons voir que PVDF possède une très souche de rendement élevé, qui essentiellement signifie qu'il peut être déformé élastiquement à plutôt grandes déformations. Il est une caractéristique habituelle des biens pour les polymères, mais pas commun pour tous les matériaux piézoélectriques, où la limite élastique est généralement inférieur à 0,1 %, comme il est le cas pour PZT.

Dans le meilleur des cas, 2 % souche, qui pourrait venir de coupler un SMA avec des nanofibres de PVDF de[141] possédant une haute électro - mécanique de couplage coefficient, nous pourrions théoriquement récolter jusqu'à à 30 mJ cm ^{3}, ce qui est une très forte et prometteuse. valeur Pratiquement cependant, il va être beaucoup plus faible, autour de 10 mJ/cm ^{3}, parce que l'électro - mécanique de couplage coefficient d'un PVDF commune teneur est inférieure, et il ya toujours des pertes dans les interfaces composites.

Les considérations ci-dessus seront utiles pour nous pour la mesure des coefficients piézoélectriques. Par exemple, à partir des résultats expérimentaux où la tension en circuit ouvert est mesurée en fonction de la contrainte appliquée, nous pouvons obtenir directement l'g_{ij} coefficient moyen de l'équation eqref. eq:tension vs g, T De même, à partir d'un rapport d'énergie informations de stress, nous pouvons calculer le coefficient k ^{2} en utilisant l'équation (2.8).

Nous avons vu des calculs théoriques pour estimer la tension de sortie et l'énergie de PVDF. Maintenant, nous allons aller de l'avant pour le côté pratique et de voir comment les mesures de tension sont effectuées dans ce travail.

La précision de mesure de la tension générée a un impact direct sur la précision finale des coefficients piézoélectriques; il est donc crucial.

Caractérisations piézoélectrique direct classiques peuvent être entravés par de grandes pertes électriques et les fuites de charge non contrôlé dans le circuit pendant les mesures, ce qui peut entraîner

à plus faible détecté tension et possible sous-estimation des propriétés du matériau.
Compte tenu de la faible permittivité (donc la capacité) de polymères piézoélectriques par rapport à la céramique, ce problème devient encore plus critique.
Habituellement, les mesures de réponse piézoélectrique direct de polymères sont faites avec un oscilloscope standard dans une connexion Circuit fermé[86,144], ou en utilisant un amplificateur de charge plus sophistiqué circuits[88,145]. Pour minimiser les pertes et les fuites, il est préférable d'effectuer des mesures à des fréquences élevées, mais même alors, la tension mesurée reste généralement faible (elle dépasse rarement 10 V).
Dans notre travail, nous nous concentrons sur la récolte des événements lents dans des conditions quasi-statiques. Par conséquent, une technique de mesure est nécessaire qui seraient en mesure de donner des mesures fiables dans de telles conditions. En l'absence d'une technique existante fiable, nous avons récemment proposé une méthode simple et précis pour mesurer la tension piézo-électrique de films organiques souples, travaillant dans des conditions de circuit ouvert réels, et donc avec pratiquement aucune fuite de charge[146]. . Conditions composition non de circuit sont obtenus par l'introduction d'un commutateur mécanique dans le circuit de mesure pour séparer la partie piézoélectrique (batteuse) à partir de la partie de mesure (collecteur) Ceci permet l'accumulation des charges produites sans leur dissipation immédiate à l'intérieur du circuit de mesure; une fois accumulée, ils sont alors dissipée dans le collecteur lorsque l'acquisition de la tension est effectuée. Le commutateur est maintenu dans sa ouverte Etat pendant la mécanique de déformation de l'élément piézoélectrique matériau tout les produits frais accumulent sur les électrodes. Lorsque la déformation est terminée, la interrupteur est fermé et toutes les charges sont transférées à la fois dans le circuit de mesure. Une représentation schématique du circuit décrit est montré dans la figure 2.4.
Pour collecter et mesurer les charges accumulées pendant la déformation, nous avons proposé deux possibilités à l'aide de différents équipements:

- oscilloscope standard (Agilent DSO1014A).

  Dans ce cas, alors que l'interrupteur est ouvert l'oscilloscope détecte pas charges, de sorte que la tension reste zéro. À la clôture de l'interrupteur piézoélectrique échantillon est déchargé dans le connu interne résistance, et la tension observée augmente instantanément de zéro à sa valeur maximale. Ensuite, l'interrupteur reste fermé et à dissiper les charges dans le circuit de mesure, et la tension décroît à zéro.

- non-contact voltmètre électrostatique (TREK 370).

  Ce type de voltmètre mesure électrostatique surface potentielle de l'échantillon sans physique de contact, rendant l'impédance de tels système pratiquement infinie, et éliminant ainsi régulière - oscilloscope fuites de charge. Dans ce travail, un voltmètre TREK 370 a été utilisé, qui a été connecté en parallèle à l'échantillon et à une résistance externe, séparés par un interrupteur. TREK 370 est capable de mesurer en gamme 0-3 kV avec une résolution V
  .

  Le sans contact voltmètre set-up permet en temps réel la surveillance de l'accumulation de tension au cours de la demande de la mécanique stress. La tension comportement est différent dans ce cas: avec le commutateur étant ouvert la tension monte à sa valeur maximale et reste à cette valeur car il n'y a pas de dissipation dans le circuit de mesure. Une fois que

l'interrupteur est fermé, la décharge dans la résistance externe intervient et que la tension tombe à zéro.

Dans la figure 2.5 les courbes de tension de sortie obtenus avec les deux méthodes sont présentés. Une mesure classique avec un oscilloscope dans un -Circuit fermée pour fins de comparaison, à partir de laquelle nous pouvons voir que la tension maximale détectée est 6 fois plus faible que toutes les propositions de procédés à 0,5 % souche. L'énergie qui a été produite par le piézo-électrique peut être calculée comme un équivalent à l'énergie dissipée dans la résistance extérieure. D'une manière générale, à partir de Joule première loi, nous pouvons affirmer que le puissance P dissipée à partir électrique énergie thermique énergie est égale à la tension$V$ déposer à travers l'élément multiplié par la résistance$R$[147].
La décharge de piézoélectrique échantillon prend lieu sur quelques dizaines de millisecondes au cours de laquelle plusieurs centaines de mesure des points sont prises, donc l'intégration est nécessaire de calculer la valeur réelle d'énergie:
En pratique, l'intégration numérique est réalisé par la sommation de tous les points de mesure acquises avec un Δt constant, ce qui est caractéristique de l'appareil de mesure.
Les limites de sommation sont fixés à partir du moment du début de la décharge (l'interrupteur est fermé, le point$A$ dans la figure 2.5) à l'instant où la décharge est terminé (point de$B$).
Depuis PVDF métallisé peut également être présenté comme un condensateur de plaque simple avec un matériau diélectrique, son énergie peut également être estimée par l'énergie maximale d'un condensateur avec une telle capacité peut stocker (équation (2.13)).
Analysant à la fois le comportement de décharge dans la figure 2.5 et les valeurs dans tableau 2.3, nous pouvons observer que l'énergie la plus élevée la valeur peut être obtenue par l'intégration de la tension de la contact- moins voltmètre et l'oscilloscope dans circuit ouvert conditions. Cela rend ces méthodes, les préférés mesure méthodes pour nos applications. L'énergie calculée par la capacité est légèrement inférieure dans les deux cas, ce qui peut venir de sous-estimer la capacité valeur (La RCL - mètre utilisé pour la mesure de capacité est actionné à une fréquence de kHz, tandis que la capacité quasi-statique peut être plus élevé).
D'un autre côté, à la fois la tension et l'énergie des valeurs obtenues par la classique oscilloscope installation sont beaucoup plus bas, ce qui peut être expliqué par continu la charge de fuite dans le système, ce qui, entre autres le fait tension sortie dépendant de la dose d'application de contrainte, à savoir lorsque l'échantillon est tendue lentement la tension sera moindre que si l'échantillon est tendue rapidement.

En outre, la durée de décharge de tension (constante de temps) dans tous les cas sur la capacité dépend fortement matériau et sur la figure 2.5, où les décharge temps augmente avec l'augmentation de la résistance. D'autre part, physiquement parlant de la valeur de l'énergie produite ne devrait dépendre de la capacité matérielle et non sur le circuit de la résistance. Il est néanmoins un équipement de mesure d'erreur qui apparaît à faible résistance des valeurs et conduit à une erreur de calcul de l'énergie. Ce qui se passe est que, à des résistances de circuit inférieur la constante de temps de la décharge ne sont pas régies par la capacité de PVDF plus, mais plutôt par la vitesse du voltmètre de réponse. Ce phénomène est illustré à la figure 2.6 et comprend an increased energy value observed by electrostatic voltmeters and decreased energy observed by an oscilloscope at resistances < 10 kOhm .
Ce phénomène est particulièrement prononcé pour l'électrostatique voltmètre. Pour souligner cela, séries de mesures ont été fait en utilisant une autre marque de électrostatique voltmètre (244A Iso-

probe électrostatique voltmètre de Monroe Electronics), qui a une réponse plus faible vitesse de Trek, et qui est en mesure de donner des mesures correctes qu'à résistances> 10 MOhm. Pour le voltmètre Trek et l'oscilloscope Agilent la résistance pourrait être aussi bas que 10 kOhm sans des variations considérables dans l'énergie. Au cours de ce travail la plupart des mesures piézoélectriques ont été réalisées avec la résistance de 1–10 MOhm.

Maintenant que nous avons vu comment précisément mesurer la tension, nous avons besoin de savoir comment la souche du PVDF dans le but de générer que la tension. Voilà, nous devons trouver un moyen pour déformer mécaniquement le matériau d'une manière précise, contrôlable et quasi-statiques. Dans ce manuscrit, nous vous proposons et développer des quatre approches à appliquer la déformation d'échantillons de PVDF. Premièrement, faible déformation mécanique a été appliqué avec la presse, flexion quatre points et cintrage de tubes. Ces méthodes sont relativement rapide à effectuer dans l'échelle du laboratoire, et permettre aux simples expérimentales mesures de piézoélectriques coefficients. Puis, haute souche a été appliqué avec traction linge, qui exige plus sophistiqué set-up et l'automatisation de l'expérience. Depuis PVDF peut être soumis à assez élevés souches dans des structures composites avec SMA, et le peu de renseignements sur son comportement dans de telles conditions, nous avons pour la première fois étudié directement son g_{31} coefficient sous appliquée haute tension.
Toutes ces approches expérimentales ont été adaptés spécialement aux polymères souples flexibles, et a permis l'application de la souche contrôlable et quasi-statique.
Une fois les méthodes de mesure ont été établis, nous avons mesuré différents PVDF commerciale et P(VDF+TrFE) échantillons pour obtenir une évaluation directe des coefficients de tension (g_{33} et g_{31}.) Habituellement g_{ij} est calculé à partir d_{ij} coefficient par l'équation (1.18) et pas mesurée directement. Nous avons donc comparé nos directement mesurées valeurs avec celles de du fournisseur les fiches techniques. Nous avons utilisé 30 μm épaisses pré - assemblé éléments piézo - de Measurement Specialties (nom de code LDT1 [148]) et PVDF métallisé et P(VDF+TrFE)films of different thicknesses from PiezoTech [80]. Les matériaux et leur piézo-électrique et les propriétés mécaniques sont résumés dans tableau 2.4.
Nous allons maintenant décrire les trois méthodes d'application faible déformation et de faire une brève comparaison entre eux.
Pour cette première méthode, une presse mécanique a été utilisé, comme le montre la figure 2.7. Il permet de compresser un film piézoélectrique le long de son épaisseur, en exploitant le 3-3 Mode. Le échantillon a été pressé entre deux plats métalliques surfaces, avec le poids appliqué étant mesurée avec une jauge en poids. Lorsque la pression est appliquée à l'échantillon, une déformation mécanique ε est induite Les valeurs deε peuvent être calculées en utilisant une approche standard de la mécanique des solides avec l'équation (2.14).
Le tension de sortie correspondant V_{33} a été mesurée simultanément, et un exemple de V_{33} vs charge est présentée dans la figure 2.8. Après une certaine charge la sortie tension chute considérablement, ce qui suggère que la rupture mécanique de l'échantillon a été atteint.
En théorie, la presse set-up est facile et l'expérience elle-même est simple à réaliser. Toutefois, dans la pratique, cette méthode présente de nombreux inconvénients. Tout d'abord, la jauge de charge a une très large gamme d'échelle et la précision limitée, ce qui rend difficile à détecter et de lire les petits changements de pression. En outre, le mécanisme de déformation de l'échantillon est pas clair, que de grandes forces statique friction apparaissent entre la surface et métalliques entourant les disques de l'échantillon, qui ne permettent pas la libre circulation de la matière le

long de son sens de la longueur . Cela a pour conséquence le fait que la longueur et la largeur de l'échantillon restent pratiquement inchangés tandis que son épaisseur est obligé de diminuer, ce qui est pas le cas lorsque le matériau est capable de se déformer librement. Enfin, la pression appliquée à la presse est pas uniformément distribué à l'échantillon, mais à la place il est appliqué sur les disques métalliques environnantes. Ceci conduit à une la situation où la vigueur effectivement appliquée à l'échantillon est beaucoup plus faible que la vigueur mesurée par la jauge. Cette dernière question peut être partiellement résolu en utilisant de petites métalliques plaques bien adaptées à l'échantillon taille (figure 2.7b).

La comparaison entre la tension de sortie expérimentale de LDT1 et le rapprochement théorique pour le mode 3-3 selon l'équation (2.5) est présenté dans la figure 2.9. Un assez grand décalage entre les valeurs expérimentales et théoriques est observée.

En fait, le rapport entre l'aire de surface de l'échantillon et la surface de presse jouent un rôle critique au cours des mesures. Par exemple, si les disques de presse sont trop grands par rapport à l'échantillon, ils peuvent toucher sur les côtés, et seulement une petite une partie de l'appliqué la pression va effectivement affecter l'échantillon, donnant une surestimation de l'échantillon souche selon d'équation (2.14). Lorsque les intermédiaires plus petits disques sont utilisés, l'appliqué la pression est distribué dans de façon plus homogène sur la surface de l'échantillon, de sorte que les valeurs de déformation calculées deviennent plus proches des valeurs réelles. Mais même dans ce cas, comme le montre la figure 2.9, les courbes de tension expérimentales sont encore en dessous de la courbe théorique; ce qui conduit à une sous-estimation du coefficient g_{33} selon l'équation (2.15).

Bending permet de filtrer le film le long de sa longueur, faisant usage du mode 3-1. Quatre points de flexion et de cintrage de tubes ont été utilisés pour plier les échantillons.

Procédé de cintrage dans le tube, un échantillon métallisé est collée à un substrat en plastique flexible et est repliée autour d'un tube de diamètre connu. L'échantillon est déformé le long de sa longueur, en utilisant le mode de 1/3. La mise en place de l'expérience est représenté sur la la figure 2.10. Lorsque l'échantillon est plié par lui-même, son neutre axe est situé dans le milieu de l'échantillon, et la déformation totale est égale à zéro. Lorsque l'échantillon est monté sur un substrat beaucoup plus épais, l'axe neutre efficace résultant est complètement déplacé en dehors de l'échantillon et la souche calculation peut être avec une certaine hypothèse simplifiée pour equation (2.16)[149].

Cette méthode permet des mesures rapides et faciles et une large gamme de déformations peut être réalisé simplement en utilisant des tubes de différents diamètres Il est très reproductible, comme l'a confirmé par la série de mesures effectuées avec un échantillon:. Tension variation mesurée à des déformations fixes était autour de ± 5 %. Au cours de l'expérience six différents métalliques tubes de diamètres allant de 20 à 100 mm ont été utilisés, ce qui donne des déformations de l'échantillon de PVDF de 0,2 % jusqu'à 0,7 %. Sur chaque tube a été mesurée de l'échantillon trois fois et les valeurs moyennes de la tension de sortie et de l'énergie ont été prises.

La comparaison entre la tension de sortie de LDT1 expérimental et le rapprochement théorique du mode selon l'équation (2.5) est présenté dans le figure 2.3. Valeurs de déformation positives correspondent à un allongement de PVDF et négatifs des valeurs de compression, lorsque l'échantillon avec un substrat a été retourné et plié dans la face direction. Les deux valeurs théoriques et expérimentales ont un très bon match, confirmant la pertinence de cintrage pour la caractérisation piézoélectrique direct. Dans ce cas, le g_{31} coefficient peut être calculé par l'équation (2.17).

Néanmoins, il existe certains inconvénients de cette méthode: l'épaisseur précise de la fois le

substrat et la couche de colle sont nécessaires pour le calcul de la déformation; also, higher levels of strain are difficult to achieve , since either very thick substrate is necessary , which naturally limits its flexibility , ou très petits diamètres de tubes doivent être utilisés, ce qui les rend difficiles à manipuler.

La présentation schématique de la machine de pliage en quatre points et une photo de l'actuel dispositif expérimental est montré dans la figure 2.12. Pour effectuer ces expériences, un échantillon de PVDF métallisé était collé à un substrat en plastique ayant une épaisseur h par le biais de colle commerciale.

La charge F est proportionnelle au déplacement vertical de la machine, qui est enregistrée par un capteur de déplacement d'in- construit. Le fichier de sortie de la machine après chaque essai de pliage est fourni en force en fonction du déplacement, comme le montre dans la figure 2.13, à partir de laquelle la valeur maximale F est extrait.

Quatre-point de flexion est un test mécanique permettant des calculs précis de stress. Dans nos conditions expérimentales, le stress est induit initialement dans le substrat, et la souche est transféré vers le PVDF. Par conséquent, la nature du substrat aura un impact sur les mesures (par exemple de contrainte maximale et contrainte) et le module du substrat de Young est nécessaire de calculer la souche transféré à PVDF. Dans notre cas, l' de g_{31} coefficient a été calculé par l'équation (2.19).

Les résultats expérimentaux des expériences de flexion à quatre points et expériences tubes de flexion pour un échantillon d'LDT1 sont présentés dans la figure 2.14. Les deux méthodes présentent une excellente match, thus confirming the possibility of using either of them depending on availability and experimental conditions. Based on our experience the tube bending method is more convenient for measuring samples with larger surface areas , et il devient très difficile de manipuler et de mesurer des échantillons que leur taille diminue. En revanche, la flexion quatre points set-up est plus adapté pour les petits échantillons; la taille maximale de l'échantillon est limité à 2,75 cm ^{2} en raison de la géométrie de la machine.

La tension de sortie et correspondant généré densité d'énergie électrique en fonction de la déformation appliquée pour tous les échantillons sont présentés en chiffres 2.15 et 2.16 respectivement La souche de tension linéaire classique - de la dépendance (comme de l'équation (2.4)) est confirmé pour tous les échantillons, avec des valeurs de haute tension remarquables jusqu'à 120 V Les pentes des courbes reflètent au premier ordre les différences d'épaisseur du film et also g_{31} coefficients. Ainsi, les échantillons avec grand épaisseur et/ou supérieur g_{31} coefficient produisent une tension plus élevée pour les mêmes valeurs de contrainte.

Compte tenu de la densité de l'énergie électrique, des résultats expérimentaux sont en accord aussi avec la dépendance de déformation parabolique prévu comme prédit par l'équation (2.8). Etant donné que la densité d'énergie est indépendante de la géométrie de l'échantillon, une corrélation directe entre les valeurs de g_{31} et la pente de paraboles est observée. Constamment, avec des tensions élevées, nous avons observé des valeurs élevées remarquables de densité d'énergie électrique avec environ 0,5 à 1 mJ/cm^3 pour les souches de $\approx$1 %. Ces valeurs sont du même ordre de grandeur que les valeurs théoriques calculées pour 2 % de déformation (représenté en tableau 2.2), ce qui confirme la bonne adéquation entre nos mesures et de calculs techniques proposées, leur pertinence et leur exactitude.

Enfin, g_{31} coefficient de tension and k_{31} facteur de couplage mécanique ont été calculées à partir des courbes de production d'énergie résultant de l'équation (2.8) comme un rapport de l'entrée mécanique et des énergies électriques générés Les résultats de ces calculs sont présentés dans le tableau 2.5 et comparées à celles des fiches techniques.

On peut noter que le g_{31} coefficients sont plus élevés que ceux des fiches techniques, en particulier pour la "Piezotech P(VDF-TrFE)" échantillon de copolymère. Lors de l'examen de la de k_{31} facteur de couplage, les valeurs expérimentales are Dans la gamme de la fiche, à l'exception du "Piezotech PVDF (40μ m)" échantillon. Une Telle Valeur Faible Peut indiquer Une valeur incorrecte du module de de Young Dans CAS CE. Pour exemple, en utilisant une valeur de 1,4 GPa au lieu de 2,5 GPa, qui est toujours dans l'intervalle de confiance de la fiche technique, le k_{31} calculée est de 10%, en accordance de valeur de la Fiche technique.

Pour conclure, nous avons proposé une méthode spécialement adaptés pour mesurer la tension piézoélectrique direct et de l'énergie de polymères flexibles. Le stress est appliqué avec une haute précision-quatre points du système et la tension de flexion est mesurée avec des conditions de circuit ouvert réels en utilisant un interrupteur mécanique. Cette technique permet d'explorer l'effet piézoélectrique direct dans des conditions quasi-statiques, sans utilisation ni d'équipements de haut hrecision ni circuits de mesure sophistiquée. Comme une caractéristique claire, nous rapportons inhabituelle grande souche. Tension induite et de la densité d'énergie électrique pour le PVDF et les copolymères remarquablement élevé et la densité d'énergie des valeurs allant jusqu'à 120 V et 1,2 mJ/cm^3 ont été obtenus pour 40 μm de PVDF avec la souche 0,7 % dans le mode 3-1. Nous pouvons conclure que la méthode proposée permet évaluations de coefficient piézoélectrique direct, ce qui est suffisant pour des considérations de générateur ou batteuse. Les résultats expérimentaux suggèrent que les coefficients de tension habituelles de PVDF et P(VDF-TrFE) copolymères pourraient être sous-estimés.

Le système de pliage en quatre points permet une mesure directe de la g_{31} coefficient de PVDF, mais elle repose sur les valeurs fournisseur de fiche technique de module de Young, qui sont souvent donnés avec une faible précision (intervalle de confiance $\pm$20% pour les films Piezotech[80] et $\pm$30% pour les films MeasSpec[13]). En outre, seulement de petites valeurs de déformation sont accessibles par flexion quatre points (<1 %, comme on peut être vu de la figure 2.15) en raison des limitations mécaniques de la machine avec cintrage de tubes, légèrement plus grandes souches sont possibles avec des tubes de petits diamètres, mais il finit par devenir peu pratique pour effectuer des mesures sur de petits tubes.
In order to improve the accuracy of the measurements , it is thus desirable to assess with higher confidence the Young's modulus of the samples prior to piezoelectric measurements . The use of the tensile machine will let nous une mesure directe du module de Young pendant les mesures piézoélectriques, ainsi que direct control of the applied strain . This should greatly improve the precision of calculated piezoelectric coefficients et diminuer l'incertitude due à des estimations analytiques faites pour la souche et de l'énergie sur les calculs de flexion.
Nous avons donc décidé de développer une méthode de mesure in-situ de la tension coefficients g_{31} en fonction de la déformation de traction, effectué dans des conditions de quasi-statique et en circuit ouvert, indépendamment des paramètres de fiche technique, qui permette de caractériser PVDF aussi près que possible des conditions opérationnelles ciblées avec des souches appliqués élevés.
Pour cela, nous avons utilisé une machine de traction commerciale avec des colliers personnalisés fabriqués à la souche PVDF, et directement étudié pour la première fois de g_{31} coefficient sous haute contrainte appliquée.
On discutera la dépendance de g_{31} sur la contrainte appliquée ainsi que l'isotropie de propriétés piézoélectriques lorsque l'on compare coefficients g_{31} et g_{32}.

Une machine de traction de MTS a été utilisé pour filtrer les films. Il a permis à des vitesses de chargement dans la gamme de 0,1 à 10 mm/min, avec un capteur de force jusqu'à 125 N avec environ 0,001 N sensibilité. Ce type de machines sont utilisé pour la caractérisation mécanique des matériaux en vrac (détermination du module de Young, la limite d'élasticité, etc.). Pour mince films characterization il y a un standard ISO[151] qui suggère des paramètres géométriques des échantillons ainsi que leurs conditions de test. Il est également nécessaire d'accorder une attention particulière aux pinces qui retiennent l'échantillon en place pendant les mesures, comme les films minces glissent facilement sur les pinces. Habituellement, pneumatique[152] ou hydrauliques[153] poignées sont recommandés pour une utilisation dans ces cas, mais ils sont grands et très coûteux. Par conséquent, nous avons décidé de développer nos propres fixations, adapté pour les films très minces et qui nous permet d'effectuer des mesures précises piézoélectriques.
Pour la conception de nos pinces nous avons amélioré le travail original de Thompson[154], qui a proposé de coller deux blocs petites métalliques directement sur l'échantillon Puis les placers Dans Le Fond des Nations Unies d'étrier de forme particulière avec une petite ouverture. L'échantillon était ainsi fixée fermement les pinces et dans aucun glissement était possible. L'inconvénient de cette approche est la quantité de temps nécessaire pour monter soigneusement et coller chaque échantillon, et l'alignement parallèle des blocs d'extrémité métallique qui devaient être très précis pour maintenir le film non faussée pendant l'étirement.
Nous avons amélioré la conception de Thompson, et fait une fixation qui serait facile à monter et qui seraient naturellement compenser un alignement imparfait du film dans les pinces Notre pince, comme indiqué dans la figure 2.17, se compose de trois parties. Partie 1 est un parallélépipède rectangulaire avec une ouverture de fente dans le milieu d'un côté où le film de PVDF est inséré et collé avec de la colle cyanoacrylate. La partie 2 a un "C" - forme une partie à laquelle est reliée par l'intermédiaire d'une tige de goupille cylindrique, qui fait partie 3. Partie 2 est alors relié directement à la machine de traction au moyen d'une vis. La conception des pinces permet de cabinet fixation des échantillons de PVDF minces sans glisser.
La liaison entre les parties 1 et 2 en utilisant une broche permet une rotation libre de la partie 1, collé au film, dans la partie 2 autour de l'axe perpendiculaire à la surface du film. Ceci permet une compensation de tout défaut d'alignement éventuel du film de PVDF à l'intérieur des pinces. En conséquence, la résistance à la traction est appliquée de manière homogène le long de la section transversale du film et pas de forces de cisaillement apparaissent, gardant ainsi les films non faussée pendant l'étirement. L'inconvénient, toutefois, est la quantité de temps nécessaire pour monter avec précaution, de la colle et connecter les électrodes de chaque échantillon.
Les parties 1 et 2 ont été fabriquées dans une imprimante 3D à partir de plastique ABS, et une partie 3 est une tige d'acier solide.
Le capteur de force intégré dans la machine de traction permet le calcul direct de la contrainte dans le film. Pour une distribution de force/contrainte uniforme, le stress σ est donné par l'équation[155]. La souche de film ϵ est calculé à partir du capteur de déplacement linéaire de la machine.
Un échantillon de PVDF métallisé non monté dans la machine à l'intérieur des pinces de traction, tendu et à la déformation plastique est représenté sur la figure 2.18.
Films de PVDF de deux fournisseurs ont été utilisés: orientation axiale films 110 μm d'épaisseur uniformes de Measurement Specialties ayant encre argent métallisation, et bi - orientées axialement 40 μ m films épais de Piezotech sans métallisation Les échantillons rectangulaires. ont été coupés manuellement à partir d'une grande feuille de matériau à l'aide d'un cutter, conformément à la norme ISO 527-3: 1995[151] , qui indique la géométrie et d'essais par sondage conditions

échantillons de forme rectangulaire avec des longueurs variant de 20 à 40. mm et des largeurs entre 5 et 15 mm ont été préparés (voir le résumé dans le tableau 2.6).. Ils ont ensuite été collées dans les bornes avec de la colle cyanoacrylate et ont été laissés à sécher pendant au moins 12 heures pour mesurer la tension produite, un fil métallique mince a été collé à l'époxy conducteur de chaque surface de l'échantillon, si cela est métallisé ou non. Pour les échantillons non métallisées, une mince layer de graisse d'argent conductrice (CW7100 CircuitWorks) a été appliqué. L'utilisation de graisse conductrice permet d'effectuer des mesures jusqu'à 10 % de la souche sans aucune dégradation des électrodes.

L'idée principale pour la mesure est assez simple: pour appliquer un bien - contrôlée et un puits - le stress mesurable à l'échantillon de PVDF et d'obtenir simultanément la tension en circuit ouvert généré. En pratique, il nécessite une bonne synchronisation de l'heure entre la contrainte/déformation appliquée et la capture de tension générée, ainsi que la possibilité de décharger les échantillons à ramener la tension retour au niveau zéro. For these reasons , the measurement procedure was automatized by a LabView script, which synchronized mechanical force et filtrer la sortie de la machine de traction avec des mesures de tension et ouvert/fermé états de commutation. Acquisition de données de force et de contrainte a été fait via un port BNC de la machine de traction par carte d'acquisition USB (National Instruments USB -6009). Le script recueillies et recalculé les données pour obtenir des courbes de contrainte et de tension-stress au stress. Figure 2.20 montre le panneau avant de LabVIEW pendant la mesure.

La tension de sortie a été mesurée par le voltmètre électrostatique sans contact (Trek 370), relié directement à l'échantillon. Un relais de mercure a été utilisé pour mettre le circuit sur une charge de résistance et de décharger l'échantillon PVDF lorsque cela est nécessaire. Le relais a été fermé et ouvert périodiquement, ce qui signifie que la tension observée serait répétée élever à un certaine valeur, puis tomber à zéro. Pour la plupart des échantillons de la période de commutation a été réglé sur 2 secondes, ce qui est un compromis entre la génération de tension piézo-électrique et voltage decay due to self- discharge.

Le taux déformation est maintenue constante pendant la mesure, et a été réglée entre 0,5 et 1,5 mm/min, en fonction de la longueur de l'échantillon. Étant donné que certains polymères amorphes sont connus pour modifier leurs propriétés mécaniques en fonction de la vitesse de déformation[156], nous avons mesuré le module de PVDF Young avec des vitesses de déformation de 0,5 à 100 mm/min afin de vérifier si elle est le cas pour le PVDF (figure 2.21). On n'a pas observé de variations de module de Young dans la plage de mesure, et peut supposer que, pour nos conditions expérimentales, la vitesse de déformation ne modifie pas les propriétés mécaniques PVDF.

Un script Matlab a été faite pour effectuer les calculs de tension-stress pente à chaque fois que le relais était en état ouvert g_{31} a ensuite été calculé par l'équation (2.22) et tracée en fonction de stress.

Les mesures ont été effectuées à la température ambiante de 23°C et relative humidity of $\approx 46\%$. L'épaisseur des échantillons a été mesurée avant la mesure de la tension et a été supposé constant pendant l'étirage , que ses variations dues à coefficient de Poisson seraient moins de 2 % dans la gamme de mesure.

Strictement parlant, afin de comparer avec les valeurs de la littérature, le g_{ij} coefficient ne doit être calculé dans la région élastique linéaire de la courbe de contrainte-déformation. Cependant, puisque notre objectif ici est d'étudier le comportement de PVDF à haute tension, nous avons exploré les valeurs de souche qui vont au-delà de la région élastique linéaire. Nous allons néanmoins

toujours référer à la "g coefficient "en tant que coefficient de proportionnalité entre la tension appliquée et le champ électrique induit, même au-delà de la limite élastique du matériau.

Tension mesurée typique en fonction de stress est montré dans la figure 2.22. La contrainte est augmentée en continu et ainsi la tension monte également en continu, ce qui correspond à l'état de relais ouvert, en bleu sur le graphique. Toutes les 2 secondes environ, le relais est fermé pendant un court laps de temps indiqué en rouge dans le graphique, au cours de laquelle la tension tombe à zéro et reste proche de zéro jusqu'à ce que le relais est de nouveau ouvert.
Les résultats présentés dans les figures 2.23 à 2.29 montrent à la fois des valeurs de coefficient g_{31} calculée en fonction de la tension appliquée sur l'axe vertical de gauche, et la souche induite sur l'axe vertical de droite. Nous allons comparer les échantillons de géométries différentes, provenant de fournisseurs différents et à différentes orientations cristallographiques.
Les résultats pour Piezotech échantillon P6 sont présentés dans la figure 2.23 La valeur donnée par le fournisseur (g_{31} = 0,056 Vm N) est encerclé sur l'axe vertical gauche et l'intervalle de confiance ($\pm$20%) est ombragé. Le valeur g_{31} calculée à faible niveau de stress et la fatigue sont environ 0,04 Vm/N qui est inférieur à la valeur de fiche technique et hors de l'intervalle de confiance indiqué. Avec l'augmentation du stress, g_{31} augmente jusqu'à atteindre un maximum de 0,065 Vm/N puis diminue progressivement à zéro. Remarquablement, la valeur maximale de g_{31} est situé dans le milieu de la région élastique , et la diminution correspond à la variation de la souche pente stress, représentant le début de la transition entre les régions élastiques et plastiques, dans ce cas, à 25-30 MPa et 1-1,5 % de déformation. Dans l'intervalle de tension entre 0,5 et 2 % de déformation, de g_{31} valeurs de rester à l'intérieur de l'intervalle de confiance de fiche de 0,056 Vm/N $\pm$20%.
Figure 2.24 montre g_{31} coefficient contre le stress pour les trois échantillons Piezotech P4, P6 et P8 Indépendamment des paramètres géométriques, la tendance principale est visible pour tous les échantillons: au faible niveau de stress et de tension g_{31} est un peu inférieure à la valeur de la fiche technique, mais elle augmente avec le stress jusqu'à ce qu'il atteigne sa valeur maximale de l'ordre de 0,065 Vm/N, puis diminue progressivement tout. trois échantillons atteignent leur g_{31} valeur maximale à environ 25 MPa et la souche 1,5 %, ce qui correspond au milieu de la zone de déformation élastique. Le maximum est suivie d'une courte plateau où de g_{31} la valeur reste constante La longueur du plateau est visuellement indépendant de rapport L:W de l'échantillon. Une fois dans la région plastique, le comportement de g_{31} coefficient est clairement influencée par des paramètres géométriques de l'échantillon: plus le L: W rapport, le ralentissement de de g_{31} coefficient diminue le stress. Les courbes de contrainte-déformation sont également légèrement différente pour les échantillons de géométries différentes, mais aucun changement significatif dans le module de Young et la valeur limite élastique est observée.
Les valeurs des coefficients mesurés sont situés à l'intérieur de l'intervalle de confiance de la souche de 0,5 % à environ 2%. Au souches inférieurs Cependant, une fois de plus les valeurs mesurées de la sont plus faibles que prévu, ce qui indique que pour des applications pratiques, il serait souhaitable d'effectuer une pré- déformé le matériau de PVDF à présenter efficacement sa performance piézoélectrique prévu.
Si l'on compare maintenant les échantillons Piezotech avec beaucoup plus faible L:W ratios à 1,3 (montré dans la figure 2.25) nous pouvons voir distinctement l'influence de la géométrie sur de g_{31} coefficient valeurs et les comportements apparents Depuis échantillons plus larges à faible ratios L:W (donc plus proche d'un carré que d'un rectangle) ne respectent plus les exigences de la

géométrie dans les expériences traction[151] pour la distribution de contrainte homogène, certaines parties du tendues échantillon pourrait subir un stress plus élevé que d'autres, et l'équation (2.22) mènera à faux et surestimé valeurs de g_{31}.

Les échantillons à faible L:W ratios montrent leurs valeurs de g_{31} à partir de 0,06 Vm/N et jusqu'au 0.14 Vm/N. Leurs courbes de contrainte au stress sont nettement plus élevés, ce qui signifie qu'ils subissent de la même souche appliquée le stress beaucoup plus faible que les échantillons précédents. A basse L: W ratios, le module d'Young diminue, et la transition entre les zones élastiques et plastiques sont beaucoup moins visibles.

En revanche, le 110 μm MeasSpec PVDF a un comportement tout à fait différent (figure 2.26) avec une augmentation plus prononcée de g_{31} la valeur avec le stress. g_{31} augmente avec le stress et une fois de plus atteint son maximum vers le début de la transition entre les régions élastiques et plastiques à 60 MPa et 3 % de déformation . L'influence de la géométrie de l'échantillon est moins visible que sur les échantillons Piezotech: large et échantillons étroites avoir similaire g_{31} valeurs and similar stress dependence . Les valeurs maximale de g_{31} des échantillons M8 et M6 sont près de la valeur de la fiche technique. Car l'intervalle de confiance pour g_{31} ne sont pas fournis par le fournisseur, nous ne pouvons pas affirmer que ce que souligner les valeurs de Raisonnables Sont mesurées.

En contraste avec les échantillons Piezotech, les valeurs de g_{31} au faible niveau de stress pour les échantillons MeasSpec sont nettement inférieurs à la valeur de fiche et ils restent faibles jusqu'à relativement élevé souche est appliquée. En d'autres termes, pour atteindre la valeur déclarée Fiche du coefficient piézo-électrique, l'échantillon doit être pré - tendues à environ 3 %, ce qui se rapproche de la limite de la région élastique linéaire.

Tableau2.7 résume les coefficients g_{31} mesurés et les modules d'Young pour différents échantillons, et la figure 2.27 l'illustre graphiquement. Comme une tendance générale, les échantillons longs et étroits avec élevé rapport L:W sont plus proches des valeurs de fiche que les échantillons courts et plus larges. Si nous considérons de g_{31} coefficients, échantillons MeasSpec avec des géométries de L:W de 2 et plus ont plus ou moins similaires valeurs, qui sont proches de la fiche échantillons Piezotech besoin d'avoir L:W de 4 et plus être dans l'intervalle de confiance de fiche Considérant le module de Young, des échantillons Piezotech de L:W de 3 et plus, mais un seul échantillon MeasSpec mesurée avec L:W 8 ne tombe dans l'intervalle de confiance.

Ces résultats montrent l'importance d'un choix approprié de la géométrie de l'échantillon pour les procédures d'essai ainsi que pour l'avenir la fabrication de prototypes, de veiller à ce que les hypothèses de travail, dans cette répartition des contraintes homogène de cas dans les échantillons, sont valables.

Les résultats expérimentaux présentés de mesures directes in situ, de la piézo-électrique g_{31} de coefficient de tension des films commerciaux PVDF indiquent pour la première fois une forte dépendance de apparente de g_{31} coefficient sur la souche et l'échantillon géométrie appliquée. Bi -orienté PVDF a montré une valeur maximale de g_{31} coefficient au milieu de la région élastique de la matière. Uni- PVDF orientation axiale a montré une maximale de g_{31} valeur près de la transition from elastic to plastic deformation regions . La longueur: largeur rapport des échantillons rectangulaires influencé de façon significative le g_{31} mesuré, qui était apparemment plus élevée pour les échantillons plus larges et plus courts (plus petit rapport L: W). L'importance d'un choix approprié de la géométrie de la matière pour les mesures piézoélectrique direct est également démontrée.

Les résultats obtenus indiquent que les valeurs de fiche technique de la tension piézo-électrique coefficients, fournie par les fabricants de matériaux, pourrait être surestimée au faible niveau de

stress. Cela peut être connecté à la différence entre les méthodes de mesure utilisées ici et par les fabricants. Lorsque tendues, le g_{31} est augmentée, suggérant que pré-contrainte est an paramètre important pour les applications. Les deux qualités commerciales de PVDF de Piezotech et MeasSpec devaient être tendues de 0,5 à 3 % afin de respecter les valeurs de la feuille Data- annoncées. Sans micro-structurelle des études supplémentaires, il est difficile d'argumenter on the origins of the observed phenomena of the decreased g_{31} dans la zone plastique. Réorientation des chaînes de phase β de l'orientation perpendiculaire à parallèle à des contraintes à l'intérieur de la région de matière plastique et une diminution du degré de cristallinité[136,137] peut contribuer à la réduction globale des propriétés piézo-électriques. Aussi non-linéarités du module d'élasticité pendant l'étirement peuvent conduire à des non-linéarités des coefficients piézoélectriques[135]. Ceci est cependant une importante résultat expérimental, car elle souligne les avantages de la pré-contrainte de PVDF pour obtenir une sortie de tension plus élevée depuis dans nos composites est prévu la souche délivrée par le SMA pour être en ordre de 2 %, ce qui crée une condition de travail presque idéale pour maximiser la sortie de PVDF.

Comme nous l'avons déjà mentionné plus haut, le matériau de PVDF est connue for its anisotropic piezoelectric properties[11,12,64,79]. La performance piézoélectrique selon la direction des 2 films Orientes axialement uniformes is lower according to direction 1, qui vient de la structure anisotrope semi-cristallin de PVDF. Ceci est attribué au processus qui se produisent dans les régions cristallines et dans leurs interfaces avec le entourant amorphe[11] . Dans les films bi-étirés les effets anisotropes sont éliminés[64,80].
Pour étudier l'anisotropie directionnelle de l'effet piézo-électrique, des échantillons supplémentaires ont été découpés dans les mêmes feuilles de PVDF dans deux directions perpendiculaires. Cela permet l'extraction de coefficient g_{32} en plus de g_{31}.
Figures reffig:g piezotech iso et 2.29 montrent g_{31} et g_{32} coefficients en fonction de la contrainte pour les échantillons Piezotech et MeasSpec respectivement.
Les échantillons Piezotech sont bi - axialement étiré par le fabricant, qui est spécifiquement mentionné dans la fiche technique[80], ce qui signifie que l'anisotropie intrinsèque devrait être pas moins prononcés ou pas visible de tous. En effet, les mesures effectuées ne présentent aucun anisotropie, avec le g_{31} et g_{32} coefficient étant pratiquement identiques le long de la plage de mesure complète.
Pendant ce temps, MeasSpec ne donne pas d'informations sur l'échantillon fabrication conditions. On suppose donc qu'ils ont été étirés seulement uni- axialement et qui anisotropie doivent se produire . Effectivement, les resultats montrent un niveau élevé d'anisotropie dans ces échantillons, avec g_{32} étant jusqu'à 10 fois plus faible que g_{31}. Le comportement de g_{32} est complètement différent, car il ne possède pas un maximum valeur, mais diminue la place à zéro rapidement avec le stress, et puis même le change signer.
Ce comportement peut être expliqué par la dépolarisation réversible induit mécaniquement cite Hahn1985. Zéro et négatif $g_{32}valeursde$ seront obtenus dès que la polarisation globale est réduite au stress mécanique accrue. Deux mécanismes différents peuvent expliquer ce phénomène:

- taille globale échantillon effet dû à des changements dans les propriétés mécaniques,
- effet intrinsèque liée aux changements d'orientation dipolaire.

La caractéristique d'anisotropie du matériau est étroitement liée à son g_{31} de la sensibilité de la géométrie. Lorsqu'il est étiré dans une direction, le matériau est comprimé dans des directions

perpendiculaires raison de l'effet de Poisson. Pour un matériau piézo-électrique, cela signifie que le g_{31} observé est toujours un coefficient sum de g_{31} , g_{32} et g_{33}. Le MeasSpec PVDF a beaucoup plus faible g_{32}, ce qui le rend moins sensible à la géométrie facteur de forme d'échantillons. En revanche, le Piezotech PVDF a des valeurs équivalentes de g_{31} et g_{32}, ce qui le rend très sensible à la géométrie échantillon.
Pour résumer, le bi-orienté PVDF de Piezotech a montré un comportement totalement isotrope, avec g_{31} et g_{32} étant identique dans la gamme de mesure.
Le PVDF mono-orienté de MeasSpec a montré une forte anisotropie piézoélectrique, avec g_{32} à basse souche étant 5 fois plus faible que le g_{31}, et 10 fois plus faibles que la valeur de g_{31} de datasheet.

Résumé

Les travaux de cette thèse portent sur la caractérisation de polymère piézoélectrique PVDF et de ses composites avec un alliage à mémoire de forme pour des applications de récupération d'énergie thermique. Des techniques de caractérisation adaptées sont introduites pour caractériser le PVDF et son aptitude à la récolte de l'énergie thermique. Puisque le PVDF est un matériau très souple, la flexion à quatre points, la flexion sur tube, et la machine de traction sont utilisé pour étudier sa réponse piézoélectriques en mode quasi-statique, ainsi que les changements de propriétés piézoélectriques sous contrainte. Des mesures d'auto-décharge sous différents champs électriques appliqués, températures et contraintes sont effectuées pour étudier la stabilité du matériau.

Un concept de récupération d'énergie utilisant des composites de matériaux de familles différentes est introduit. Ici, couplage entre un matériau piézo-/pyroélectrique et un alliage à mémoire de forme est proposé. Le voltage pyroélectrique simple est combiné avec un voltage piézoélectrique induit par transformation de l'alliage à mémoire de forme, pour augmenter l'énergie totale générée par le système en chauffant. Une preuve de concept est presentée d'abord pour un matériau semi-flexible basé sur une ceramique PZT, et ensuite pour le PVDF qui est entièrement flexible.

Enfin, un circuit de gestion d'énergie a été conçu et intégré au recuperateur d'énergie en PVDF. Les hauts pics de tension générés lors du chauffage sont abaissés par un convertisseur type buck à deux étages jusqu'à une tension de sortie utile stable. L'energie de sortie est utilisée pour alimenter une carte d'émission sans fil. Ainsi, une chaîne complète de génération d'énergie, exploitant des variations de température et allant jusqu'au l'émission de données est présentée.

Les résultats de ces travaux concernent un large spectre d'applications potentielles, particulierement les réseaux de capteurs autonomes sans fil, et des objets de Internet of Things, avec une flexibilité mécanique élevée et un faibles coûts de maintenance.

Abstract

This work deals with the characterization of piezoelectric polymer PVDF and its composites with shape memory alloy, for thermal energy harvesting applications. Custom characterization techniques are introduced to characterize PVDF piezoelectric properties and its suitability for thermal energy harvesting. Since PVDF is a very flexible material, four-point bending, tube bending and a tensile machine are used to study its piezoelectric response in quasi-static mode, as well as changes in piezoelectric properties with increased strain. Self-discharge measurements under various applied electric fields, temperatures and strains are performed to study the stability of material.

A concept of composite energy harvesting, utilizing two materials of different family, is introduced. Here, we propose the coupling of piezo-/pyroelectric material and shape memory alloy. The pure pyroelectric voltage is combined with piezoelectric voltage, induced by shape memory alloy transformation, to increase the total energy generated by the system during heating. The proof of concept is shown first for ceramic PZT-based semi-flexible material and then for fully flexible PVDF.

Finally, a power management circuit was designed and integrated with the PVDF energy harvester. High generated voltage peaks at heating are lowered by a two-step buck converter to a useful stable output voltage. Output energy are used to power a wireless emission card. Thus, a complete power generation chain from temperature variations to data emission is presented.

The results of this work concern a wide range of applications, especially modern autonomous wireless sensor node networks and Internet of Things objects, with high mechanical flexibility and low maintenance costs.